UNIVERSITY OF CAPE TOWN

Modelling the Oceanic Circulation in the Delagoa Bight

Obadias J. Cossa

Thesis presented for the Degree of Doctor of Phylosophy

in the Department of Oceanography

Supervisor: Prof. Chris Reason

Co-supervisors: Dr. Stéphane Pous and Dr. Pierrick Penven

Declaration

I declare on my honour that the present academic work was done by me. I have not resorted into other sources, besides of those referred to and properly identified and cited herein, in compliance with the academic conventions of the University of Cape Town. I declare that this thesis has not been presented for the purposes of evaluation or publication in any institution or entity. The content of the printed and electronic versions are entirely coincident.

Supervisors:

Prof. Chris Reason: Department of Oceanography, UCT.

Dr. Stéphane Pous: Sorbonne Universités (UPMC, Univ Paris 06)-CNRS-IRD-MNHN, LOCEAN Laboratory, Paris, France.

Dr. Pierrick Penven: LMI ICEMASA, Laboratoire de Physique des Océans, UMR 6523 (CNRS, Ifremer, IRD, UBO), Plouzané, France.

Publications Based on this work:

Cossa, O.J. and Pous, S. and Penven, P. and Capet, X. and Reason, C.J.C., "Modelling cyclonic eddies in the Delagoa Bight region", Continental Shelf Research 119 (2016), pp. 14-29.

In preparation: Effect of improvement of resolution in the modelled Delagoa Bight Circulation

Abstract

The Regional Ocean Modeling System (ROMS) is used to investigate the oceanic circulation in the Delagoa Bight region, near the southwestern end of the Mozambique Channel. The model is initially configured at a horizontal resolution of $\frac{1}{10}^{\circ}$ (9.9km) over the domain $30.1 - 43°E, 22.13 - 30.8°S$. Subsequent configurations nested an inner grid of resolution $\frac{1}{30}^{\circ}$ (3.3km) over the region $32.43 - 36.43°E, 24.09 - 27.71°S$.

Several sensitivity experiments were performed with and without the inner grid or with or without tidal forcing. Using only the outer coarse resolution grid, the first experiment (DELAG- I) does not include tidal forcing whereas tides are included in the second (DELAG-II) experiment. DELAG-III and DELAG-IV both use the inner higher resolution grid but exclude and include tidal forcing respectively.

The model was evaluated against observations, namely the Word Ocean Atlas (WOA), Pathfinder Sea Surface Temperature (SST) and Archiving, Validation and Interpretation of Satellite Oceanographic Data (AVISO) Sea Surface Height (SSH). The results showed that ROMS adequately resolves the oceanic features in the region, namely the pathways of the anticyclonic eddies from the northern Mozambique Channel and from Madagascar, and the instances when the Delagoa Bight Lee Eddy (DBLE) is present or absent. The model is also able to reproduce the main water masses and their sources in the region. Water masses found in the centre of the Bight enter through the northeastern sector, either by intrusion of pulses or instabilities of the southwards flowing current. When the DBLE is well established, upwelling is likely to contribute to the water masses in the lower layers. The transport of water towards the Bight from the east was found to be less than that from the north. The model also succeeds in representing the thermocline structure of the DBLE but it fails to capture the local salinity maximum.

When tidal forcing is included, the speed of the flow close to the coast increases. The model also revealed the influence of the Inhambane Cyclone on the Delagoa Bight as well as on the region to its south. This cyclone, which is generated in the flow near Inhambane, is similar to Natal Pulses which occur in the Agulhas Current.

An eddy detecting and tracking system was used with both the model outputs and AVISO SSH to determine the statistics of the DBLE, namely its dimensions, amplitudes and life-times. A maximum radius of 59.52 km, life span of 126 days and an amplitude of 27.27 cm were found.

It was also demonstrated that this feature is generated northeast of the Bight. When the inner grid was included in the simulations, anticyclonic features were generated within the Bight with a maximum diameter of 85.4 km and life span of 12 day. These anticyclonic features dominate the circulation when the DBLE is absent (less than 30 percent of the total period of the simulation). The possibility of several cyclonic cores existing simultaneously in the Bight was also demonstrated. Two cores were found with life spans of more than 12 days. When the number of cores is greater than two, they tend to be short lived. Analysis of energy conversion rates showed that the generation of both the DBLE and the Inhambane cyclones is mainly by barotropic instabilities, although in both regions of their generation, weak baroclinic instabilities were also found.

Acknowledgements

I would like to thank God, for His love that sustained me along the whole period I devoted to this work. Secondly I thank my main supervisor for having accepted me to initiate this course, which has improved considerably my technical limitations, catapulting me into a level of confidence to challenge the future. To Doctor Stéphane Pous and Doctor Pierrick Penven, I'm essentially grateful for transmitting to me their modelling experience, that turned this investigation possible. My sponsors, namely Ministério do Ensino Superior e Tecnologia (MTC) and Instituto Nacional de Hidrografia e Navegação (INAHINA), were also determinant for the success of this work, specially the latter who kept me in the effective staff of the institution, until the end of the studies.

To all my colleagues in the Department of Oceanography, first to those I shared the same office, such as Jérôme Guiet, Majuto, Katherine, Majambo and Daneeja, I'm quite grateful for their support and friendship demonstrated in a daily basis, which made me feel home even though 2000 km away from my home land. To the new office members namely Keneilwe and Jeremy I do extend this thankfulness. Secondly, to Doctor Issufo Halo, Bernardino, Malawene, Clousa, and all the members of this department, I'm entirely humbled of their sympathy and friendship.

I do feel from the bottom of my heart that I should recognize all my people at the Fountain of Redemption Church for their prayer and material support, specially the senior Pastor Reverend Ralph Mandawala, who in many occasions advised me to continue even when the financial situation was not favorable.

Finally I thank my family for their constant and unconditional support, along the whole period of my studies. To my daughter who has endured my absence without understanding the reason, I hope to have time for the due compensations from now on.

List of Acronyms and Glossary

Mean Mean over 8 years of model simulations or satellite observations

mean mean over 8 years of model simulations or satellite observations

AAIW Antarctic Intermediate Water

AABW Antarctic Bottom Water

ASW Arabian Sea Water

ADCP Acoustic Doppler Current Profilers

ACSEX Agulhas Current Sources Experiment

AVHRR Advanced Very High Resolution Radiometer

AGRIF Adaptive Mesh Refinement Package

AVISO Archiving, Validation and Interpretation of Satellite Oceanographic Data

BBW Bay of Bengal Water

CARS CSIRO Atlas of Regional Seas

CDW Circumpolar Deep Water

CTD Conductivity, Temperature and Depth

COADS Comprehensive Ocean Atmosphere Data Set

CZCS Coastal Zone Colour Scanner

DBLE Delagoa Bight Lee Eddy

EKE Eddy Kinetic Energy

EGS Department of Environmental and Geographical Sciences

ENSO El Niño Southern Oscillation

Envisat ESA Environmental Satellite

EPE Eddy Potential Energy

ERS European remote sensing satellite

HYCOM Hybrid Coordinate Ocean Model

IEW Indian Equatorial Water

INAHINA Instituto Nacional de Hidrografia e Navegação

IOGOOS Indian Ocean Global Ocean Observing System

IIOE-I International Indian Ocean Experiment

IIOE-II International Indian Ocean Experiment

IIW Indonesian Intermediate Water

IW Internal Waves

ICW Indian Central Water

IOD Indian Ocean Dipole

IUW Indonesian Upper Water

JASON Joint Altimetry Satellite Oceanography Network

JGOFS Joint Global Ocean Flux Study

KPP K Profile Parameterization

MADT Absolute Dynamic Topography

MTC Ministério do Ensino Superior e Tecnologia

MKE Mean Kinetic Energy

MPE Mean Potential Energy

MDT Mean Dynamic Topography

MJO Madden Julian Oscillation

NCEP National Centers for Environmental Prediction

POM Particulate Organic Matter

PSD Power Spectral Density

NASA National Aeronautics and Space Administration

NASA-S NASA Scatterometer

NOAA National Oceanic and Atmospheric Administration

PGF Pressure Gradient Force

PDF Probability Density Function

ROMS Regional Ocean Modeling System

RSIW Red see Intermediate Water

RSW Red Sea Waters

RSPGIW Red Sea-Persian Gulf Intermediate Water

SCRUM S Coordinate Rutgers University Model

SOMS Self Organized Maps

SAR Synthetic Aperture Radar

seasonal mean over 8 year of model data, determined with data from specific season

SLA Sea Level Anomaly

SODA Simple Ocean Data Assimilation

SSH Sea Surface Height

STW Subtropical Surface Water

SST Sea Surface Temperature

SSS Sea Surface Salinity

SICW South Indian Central Water

SWIM South West Indian Ocean Model

TSW Tropical Surface Water

UCT University of Cape Town

WOA Word Ocean Atlas

WOCE World Ocean Circulation Experiment

WHP WOCE Hydrographic Program

XBT Expendable bathythermograph

Contents

List of Figures

List of Tables

Chapter 1

Introduction

The Delagoa Bight, on the south-east African coast, is one of the largest coastal indentations in the south-west Indian Ocean (Lamont et al., 2010) and is located right offshore of the Mozambican capital, Maputo [Figure 1.0.1]. Situated on the southwest end of the Mozambique Channel, it is influenced by oceanic features traveling through the Channel and those coming from the southern tip of Madagascar (Lutjeharms, 2006a). This is also the region where the merger of two of the contributors to the Agulhas Current, the largest western boundary current in the southern hemisphere and of global climatic importance (Lutjeharms, 2006a), takes place.

The flow in the Delagoa Bight is dominated by a topographically trapped cyclonic mesoscale circulation, the Delagoa Bight Lee Eddy (DBLE), which is generally centered around $26°S, 34°E$ (Lutjeharms and Jorge da Silva, 1988; Lutjeharms, 2006b; Lamont et al., 2010). Typically, the DBLE has a diameter of 180 km (Lutjeharms and Jorge da Silva, 1988). While Lutjeharms and Jorge da Silva (1988) have described it as a quasi permanent feature, observations by Lamont et al. (2010) revealed its intermittency. The also known as Delagoa Bight Cyclonic Eddy is dominated by high levels of mixing over the upper levels (around $50-75\,m$), (Lutjeharms and Jorge da Silva, 1988; Lamont et al., 2010) and shows temperature-salinity characteristics completely modified from those prevalent in the Mozambique Channel. Equatorial Surface Waters and Subtropical Waters are mixed out in the eddy, whereas the core of the eddy contains the Antarctic Intermediate Water (AAIW) which upwells from depths of around $1000\,m$ (Lutjeharms and Jorge da Silva, 1988).

Based on in-situ data and infra-red satellite imagery, Lutjeharms and Jorge da Silva (1988) gave an insight into Delagoa Bight circulation, including possible mechanisms of generation of the DBLE

by the Mozambique Current. A sediments records study by Martin (1981), associated the lee eddy with the deep currents in this region. The prevalence of the Mozambique Current as a continuous jet (covering the whole coast of Mozambique) has been questioned (Lutjeharms, 2006a; DiMarco et al., 2002; Piton et al., 1991; Sætre and Jorge da Silva, 1984). Indeed, modelling studies and satellite altimetry analyses showed the dominance of a southward transport mainly composed of a train of anticyclonic eddies (Biastoch and Krauss, 1999; Schouten et al., 2003), the Mozambique Channel rings (Halo et al., 2014a). More recently, Roberts et al. (2014) described a southward propagating eddy dipole (less strong cyclone to the south of an anticyclone) along the western slope of the Mozambique Channel and its interaction with the western continental shelf, leading to slope upwelling and offshore export of chlorophyll-enriched shelf water. Lamont et al. (2010), used in-situ and satellite observations to investigate the impact of the passing anticyclones on the Delagoa Bight Cyclonic Eddy.

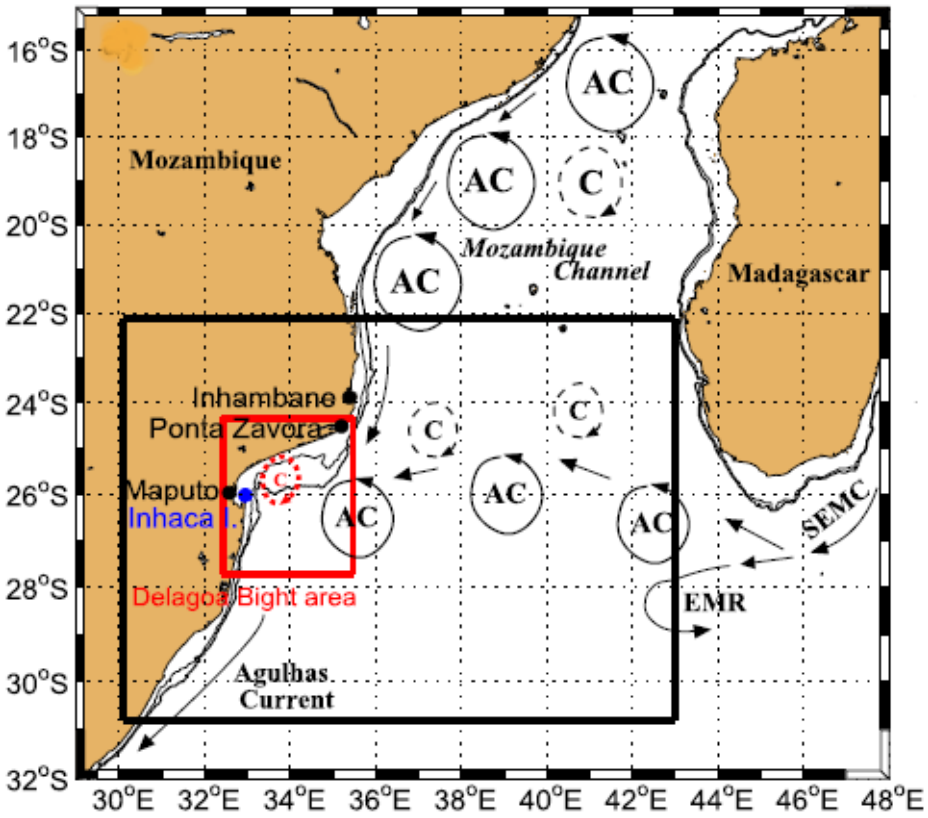

Figure 1.0.1: General schematic of the circulation in the Delagoa Bight area and neighbourhoods (adapted from Hancke et al. (2014)). The black line represents the ocean model domain whereas the red indicates the center of the Bight. (AC) represents the anticyclones whereas (C) indicates the cyclones. EMR represents the South East Madagascar Current (SEMC) retroflexion.

Cyclonic eddies are generally associated with the vertical pumping of nutrients, and consequently with enhancement of oceanic primary productivity (McGillicuddy and Robinson, 1997). In Delagoa Bight, the high levels of productivity offer a suitable environment for the development of a

rich marine ecosystem (Lamont et al., 2010). Indeed, it is deemed as one of the most important areas in commercial fisheries in Mozambique, after the Sofala Bank (Dove, 2015). The lifespan of the Delagoa Bight Cyclonic Eddy is supposed to be crucial for holding the productivity. This assumption leads us to investigate the DBLE using a numerical model. In another hand, the tidal activity in this region is considerable. Huge internal tides have been seen in satellite images propagating towards the shore in this region, (Jackson et al., 2004). The relatively broad and shallow shelf, generates substantial tidal signals with 3.3 and 1.5 m average spring and neap tidal variations, respectively MacNae and Kalk (1969). Indeed, Cossa (2005) mapped the hot spots of semi-diurnal internal tides in the Bight, whereas Da Silva et al. (2009) found similar hot spots farther north in the Sofala Bank. The mixing processes associated with the internal tides are known in the global ocean (Zhao et al., 2012; Garrett, 2003; Sangrá et al., 2001).

Tew-Kai and Marsac (2009), investigated the patterns of variability of Sea Surface Chlorophyll in the Mozambique Channel. They divided the whole Channel in three sub-areas: the northernmost part located between $10 - 16^oS$, the central region between $16 - 24^oS$ and the southern $24 - 30^oS$. They noted that the Chlorophyll variability on both the northern and southern regions was strongly affected by seasonality, while on the central part the seasonal signal had a minor impact. Although their study was focused on the offshore coupling of physical processes with chlorophyll concentration, these authors noted that along the shelf, to the western side of the Mozambique Channel in Delagoa Bight, the southward passage of eddies causes a cyclonic cell there, and possibly nutrient inflow into the surface waters enhances the primary productivity. Tew-Kai and Marsac (2009), indicated that the spatial pattern of chlorophyll in Delagoa Bight region shows a seasonal pattern.

Omta et al. (2009), simulated seasonal variability of plankton biomass and chlorophyll in the Mozambique Channel using various plankton population models coupled to physical models. Their results were compared with satellite-derived chlorophyll observations, to show that the variations in cellular chlorophyll content has strong impact on the seasonal chlorophyll cycle in the Mozambique Channel.

The circulation in the Delagoa Bight is complex, (Lutjeharms and Jorge da Silva, 1988; Lamont et al., 2010). Based on level two images of the satellite Nimbus-7 Coastal Zone Colour Scanner (CZCS) Gründlingh et al. (1989) found a well defined anticyclonic eddy located at $25.9^oS, 32.5^oE$, with an average diameter of $70\,km$. They justified that the presence of such a feature, was caused

by the instabilities of the southwards flowing warm current, which sometimes lies much farther west (Quartly and Srokosz, 2004). The DBLE has been recognized as a semi-permanent feature, (Lutjeharms and Jorge da Silva, 1988; Lamont et al., 2010). In fact a relatively recent study of Lamont et al. (2010), demonstrated that the lee eddy could be absent in the Bight. Several mechanisms of generation have been proposed for the DBLE. Lutjeharms and Jorge da Silva (1988) associated the DBLE generation with the southwards flowing Mozambique Current, whereas more recent works linked it with the southwards passage of anticyclonic eddies (Lamont et al., 2010; Quartly and Srokosz, 2004). In another assertion, Martin (1981) argued that it was not likely that in a so large terrace a single cyclonic eddy could exist, such as the Delagoa Bight Cyclonic Eddy. The results of a regional oceanic model configuration which was designed specifically to resolve the local oceanic circulation and the tidal impact in the Delagoa Bight, are presented in this thesis. Although in-situ observations have been collected in the region (Lamont et al., 2010), the utilization of an oceanic model can help in the understanding of the dynamical oceanic processes in action in the Bight, and provide a more complete description of the DBLE and associated dynamics. This model simulation is also able to identify new processes of importance such as the generation of cyclonic eddies by interaction of the Mozambique Channel rings with the topography north of Delagoa Bight.

The thesis incorporates seven chapters. After this introduction, the second chapter presents the literature review of the Southwest Indian Ocean dynamics relevant to the Delagoa Bight area. The third chapter consists of the methodology. It presents the ROMS principles, its numeric schemes, and the relevant data sets used to force the model. It is finalized by the presentation of the eddy detecting and tracking system, the tool used to investigate the mesoscale processes and their statistics. In the fourth chapter, the mean state is discussed using the available sensitivity experiments. In the fifth chapter, the cyclonic features of the Delagoa Bight region are analysed. Chapter sixth was conceived to tackle the mechanisms of generation of the mesoscale features in the Bight, while the last chapter is devoted to the synthesis and conclusions of the thesis.

Throughout the thesis, the whole zone covered by the large scale coarse resolution grid $22.13 - 30.8°S, 30.1 - 43°E$, will be referred to as the Delagoa Bight region, whereas the Delagoa Bight proper is the area limited by $24.09 - 27.71°S, 32.43 - 36.43°E$ as illustrated in Figure 1.0.1, and is mainly covered by the child domain in these simulations. Overall, the analyses of composites will be used to tackle the thermocline structure of the DBLE and its neighbourhood.

Chapter 2

Literature Review

2.1 General oceanographic aspects affecting Delagoa Bight

2.1.1 Circulation of the South West Indian Ocean

2.1.1.1 Geographical settings and topography

The Indian Ocean is the smallest oceanic basin of the world oceans. According to the SP-23 IHO (1953) on the north it is bounded by the southern limits of the Arabian Sea, and the Laccadive Sea, as well as the Southern limit of the Bay of Bengal and the southern limits of the East Indian Archipelago, and the southern limit of the Great Australian Bight. On the west, it stretches southward from Cape Agulhas by the $20E$ longitude, where it separates from south Atlantic, and extends along this meridian towards the Antarctic Continent. On the east, it extends from the South East Cape, in the southern point of Tasmania down the meridian $116"55'E$ to the Antarctic Continent. On the south it is bound by the Antarctic Continent. Its north-southward extension, estimated from the Bay of Bengal to Antarctica is $9600\,km$, whilst its west-eastern width spans $7800\,km$ between Southern Africa and western Australia. Its total area is estimated as $74.1 \times 10^6\,km^2$ if the portion in the Southern Ocean is included (Tomczak and Godfrey, 2003). Three major topographic features, each of different geologic origin, are known to dominate the seafloor topography of the western Indian Ocean, (Parson and Evans, 2005). To the east, lies the Chagos–Laccadive Ridge, stretching southward by more than $2000\,km$ from the western margin of the Indian subcontinent, representing a relic trace of persistent local and excessive magmatism and extrusive volcanic construction on the spreading ocean floor plate, (Parson and Evans, 2005).

In the mid Indian Ocean, lies the mid-ocean-ridge system, known to partition the floor this ocean in three distinct parts, separating the tectonic plates of East Africa, Arabia, Antarctica and India/Australia, along three actively spreading plate boundaries (Parson and Evans, 2005). Finally the Mascarene Plateau, is one of the most prominent shallow bathymetric features of the Indian Ocean (Parson and Evans, 2005).

According to Parson and Evans (2005) these topographic features divide the western Indian Ocean into several basin complexes. The major bathymetric features namely the Chagos–Laccadive Ridge, the Mascarene Plateau, the Madagascar Ridge and the Indian Ocean mid-oceanic ridge system (comprising the Central, Southwest and Southeast Indian ridges) divide the whole area into a number of smaller isolated basins, (Parson and Evans, 2005). In Figure 2.1.1, a topographic map mainly covering the Mozambique Channel and its neighbourhoods is presented. The Mozambique and the Madagascar basins, containing maximum depths over $5000\,m$ respectively are very well depicted in the map. The Madagascar Ridge to the south of Cape Saint Marie, separates both basins. Several bathymetric features are also visible inside of the Mozambique Channel. To the north, lies the Comores Basin, with maximum depth of $3600\,m$, (Halo, 2012). The seafloor topography within the Mozambique Channel is very irregular. It follows a north-south orientation. Overall, in the northern part are found the Islands of Comores and Gloriousa, as well as the Banks of Geyser and Leven, (Halo, 2012). In the southern part lie the Islands of Europa and Bassas da India, whereas at the center are found the Davies Ridge and the Island of Juan Nova. In the coast of Mozambique the Sofala Bank and the Delagoa Bight, are characterized by shallow depths of approximately $500\,m$. The whole ocean has an average depth of $3890\,m$, which is approximately equivalent to the average world-ocean depth (Demopoulos et al., 2003).

2.1.1.2 Hydrography

The rim of the Indian Ocean is mainly surrounded by relatively poor countries. Therefore, until 4 to 5 decades back, it had not benefited from considerable research. The huge distance in relation to the main oceanographic institutions compromised the research in this ocean, specially in the South Indian Ocean (Schott and McCreary Jr., 2001; Schott et al., 2009). The International Indian Ocean Experiment (IIOE-I) carried out on the period 1962-1965, was the first international program to give much attention to the Southwest Indian Ocean. The result was the compilation of the *Atlas of the Indian Ocean*, (Wyrtki, 1971). Before this project, only very few research

expeditions had entered the region. Amongst such expeditions, one may refer to *HMS Challenger* (1872-1876), the *Valdivia* (1888-1889), the *John Murray Expedition* 1930, the *Swedish Deep Sea Expedition* (1947-1948) and the *Galathe*a (1950-1952), (Demopoulos et al., 2003).

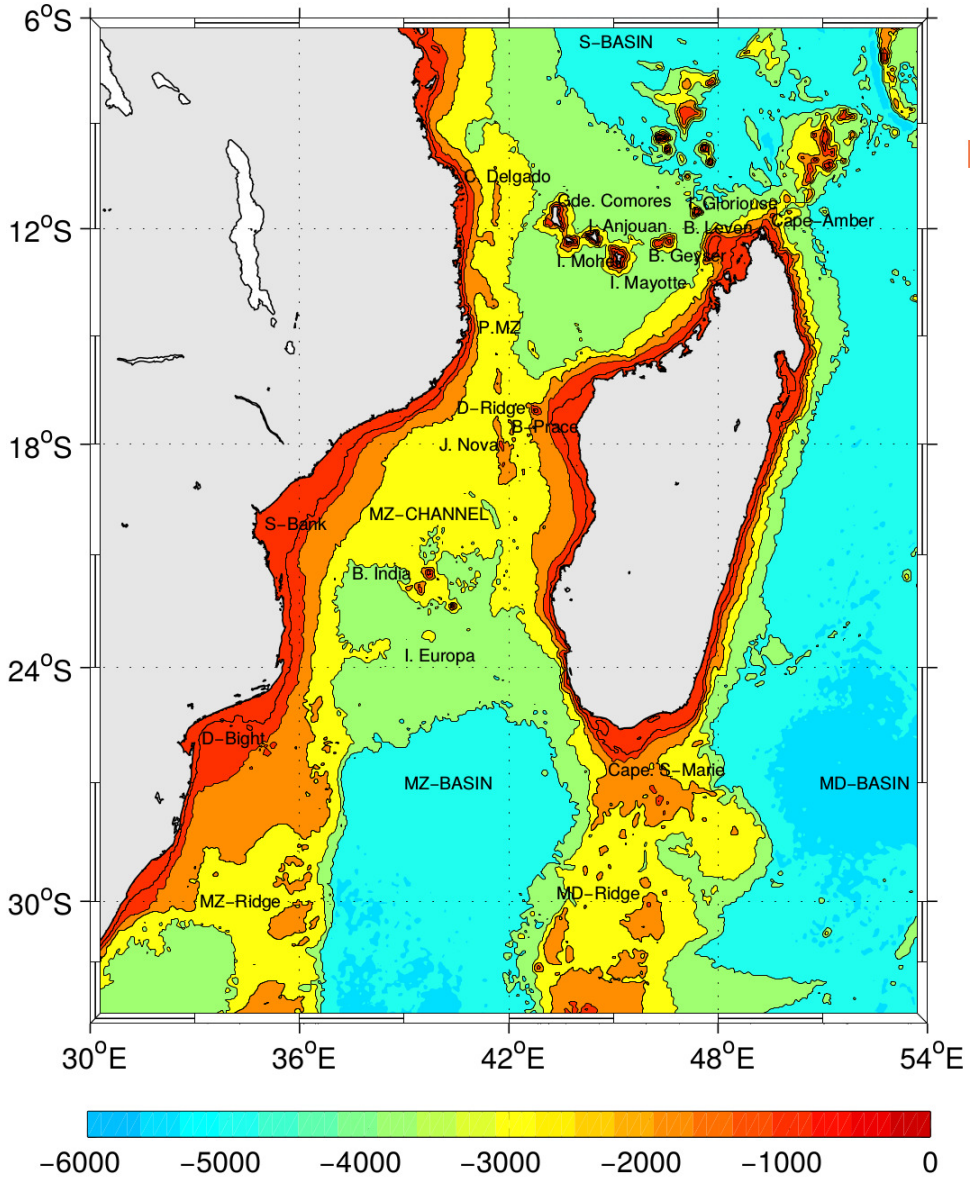

Figure 2.1.1: Topography Of the Mozambique Channel and surroundings. Meaning of the acronyms: Somali Basin (S-BASIN), Mozambique Basin (MZ-Basin), Mozambique Channel (MZ-Channel), Madagascar Basin (MD-Basin), Sofala Bank (S-Bank), Ponta Mozambique (P. MZ), Davie Ridge (D-Ridge), Madagascar Ridge (MD-Ridge), Delagoa Bight (D-Bight), Juan de Nova (J. Nova), Bank Pracel (B. Pracel), Bassas da India (B-India), Islands (I). The colours indicates the ocean depths. Halo (2012))

Following the IIOE-I, the long term current meter moorings taken during the *INDEX Campaign* (1976-1979), constituted a crucial measure towards understanding the full depth oceanic hydrography of the Indian Ocean. In fact, analyses of its dynamics prior to this phase was based on the ship drift data, (Tomczak and Godfrey, 2003). Similarly, the World Ocean Circulation Experiment (WOCE) (1990-1998), the most ambitious global oceanographic program ever undertaken (Ffield, 1997), offered a more broader coverage of this ocean, with stations spanning the

whole basin, in both the north-south and west-east extensions. The profiling of the whole water column using XBTs, CTDs, ADCPs, current meters, profiling floats, subsurface floats etc., allowed a relative improvement in comparison with the previous expeditions. Technically, WOCE Indian Ocean expedition surpassed by far its predecessor, the IIOE-I effort (Ffield, 1997). The set of stations and transects of the WOCE project are presented in Figure 2.1.2.

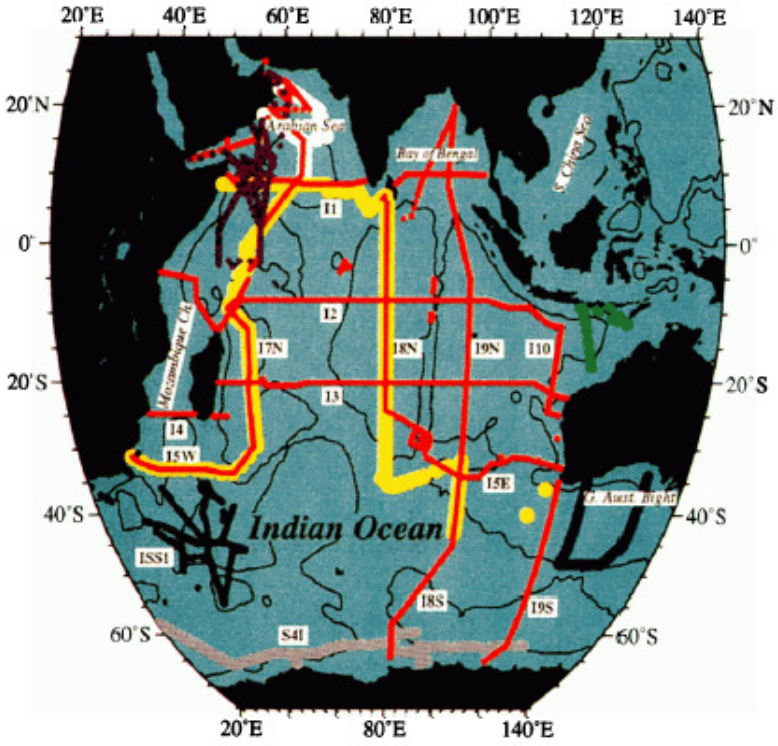

Figure 2.1.2: Map of the Indian Ocean showing the location of the WOCE hydrographic stations. Thin black lines indicate the smoothed 4000 m bathymetry contours. (Courtesy of Ffield (1997)).

Some other isolated hydrographic projects have been carried in the Indian Ocean. In the Southern Hemisphere for instance, one may refer to the Agulhas Current Sources Experiment (ACSEX), carried out over the last decade (de Ruijter et al., 2006), whereas in the northern hemisphere the Joint Global Ocean Flux Study (JGOFS) during (1994-1996) was settled to study the response of the Arabian Sea mixed layer to monsoonal forcing (Weller et al., 1998).

A new expedition, the International Indian Ocean Experiment (IIOE-II) is expected to be carried out over the (2015–20) period (IOC, 2013). Born out from the voluntary community group under the auspices of the Indian Ocean Global Ocean Observing System (IOGOOS), on the celebration of the 50^{th} anniversary of the IIOE-I of the 1960s, the IIOE-II is hoped to improve the sampling in a region that is still recognized to be poorly investigated in comparison with the major oceanic basins. This effort will considerably improve our understanding of the geologic, oceanic and atmospheric processes and their interactions in the Indian Ocean, and determine how these

dynamics affect climate, marine bio-geochemical cycles, ecosystems, and fisheries both regionally and globally, (Hood et al., 2015).

2.1.1.3 The Monsoon regime and the large scale circulation in the Southwest Indian Ocean

A unique characteristic of the Indian Ocean is the presence of the Eurasian continent at its northern boundary, which results in its oceanic circulation and the wind forcing north of about 15^oS being very different from the tropical Atlantic or Pacific oceans (Schott and McCreary Jr., 2001; Demopoulos et al., 2003; Schott et al., 2009). A full picture of the monsoon circulation expressed by wind stress field determined from seasonal-mean climatologies of the National Centers for Environmental Prediction (NCEP) data sets overlaid on the thermocline depth from Simple Ocean Data Assimilation (SODA), is presented in Figure 2.1.3, for January, June, August and November. The regions of considerable upwelling are marked by a relatively shallow thermocline. From wind stresses, one may clearly observe that south of 10^oS the southeast trades persist throughout the year, but their seasonal maximum is in the boreal summer, (Schott and McCreary Jr., 2001; Schott et al., 2009). At this time, the flow over the western tropical Indian Ocean is mostly southwesterly, and draws air towards the Asian continent, strengthening the Findlater Jet (Findlater, 1971), (Figures 2.1.3b,c). In Austral summer, this condition is reversed (Figure 2.1.3a,d). The wind reversal exerts a great impact in the circulation of the whole Indian Ocean, with dramatic influence in the northern hemisphere, and over the equatorial sector (Schott and McCreary Jr., 2001; Schott et al., 2009). The seasonal changes in the winds over the South Indian Ocean are much smaller than those over the North Indian Ocean and lead to typical subtropical gyre similar to those found in the Atlantic and Pacific oceans, (Demopoulos et al., 2003; Kantha et al., 2008). The surface large scale wind driven circulation over the whole basin is depicted in Figure 2.1.4. In Figure (2.1.4a) is portrayed the circulation during the southwest monsoon (boreal summer monsoon). During the southwest monsoon, the Findlater Jet is robust and the East African Coastal Current, a continuation of the Northeast Madagascar Current, gets strengthened with transports around $23\,Sv$, (Schott and McCreary Jr., 2001). On crossing the equator the East African Coastal Current meets the Somali Current which deflects eastwards, generating the Southern Gyre centered around the equator, in Figure 2.1.4a). At the surface, the Northeast Madagascar Current consists of speeds of $70\,cm.s^{-1}$ that decay monotonically to depths of $1000\,m$, (Schott and Mc-

Creary Jr., 2001). Manyilizu et al. (2016) associated this current with an annual mean volume transport of 25–35 Sv, whereas Swallow et al. (1998) based on situ data estimated it to vary in the range $29.6 \pm 8\,Sv$. The remainder of the East African Coast Current is diverted towards the east, feeding the North Equatorial Counter Current and the Southwest Monsoon Current, which consists in transports of $8\,Sv$, in the opposite season (Schott and McCreary Jr., 2001).

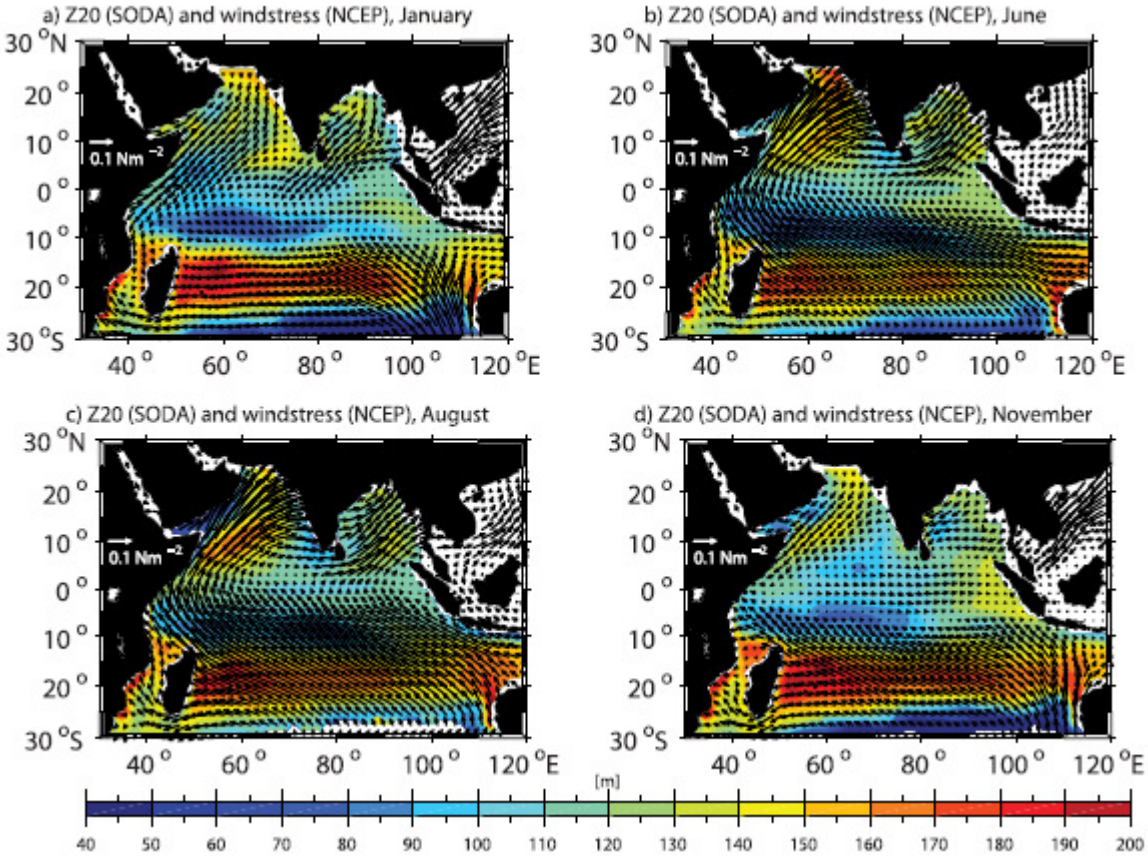

Figure 2.1.3: Monsoon wind stress fields from the 1990–1998 National Centers for Environmental Prediction (NCEP) climatology (vectors) and depths of 20°C isotherm (Z20) from Simple Ocean Data Assimilation (SODA) (mean for 1992– 2001, color shaded) for (a) January, (b) June, (c) August, and (d) November, (Courtesy of Schott et al. (2009)).

Near the tip of Somalia, an anticyclonic feature known as the Great Whirl is observed with a smaller anticyclonic eddy, the Socotra eddy to the north of it. Northwest of the Arabian Sea, a strong jet, the Ras al Hadd Jet forms off the northeastern tip of Arabia. A southward return current, the West Indian Coastal Current forms off the west coast of India, and feeds the South Monsoon Current south of Sri Lanka. Part of this current flows on the east coast of India, forming the East India Coast Current, which is driven by the southwest winds, that are still strong here, (Schott and McCreary Jr., 2001). On the west coast of India a cyclonic feature known as the Laccadive Low is prominent during this season. On the eastern side of the equatorial zone, the southeastward Java Current flows along the Sumatran coast as an extension of the North equatorial Counter Current. The estimations of the transports of these currents according to

Schott and McCreary Jr. (2001) are given in (red) in Figure 2.1.4.

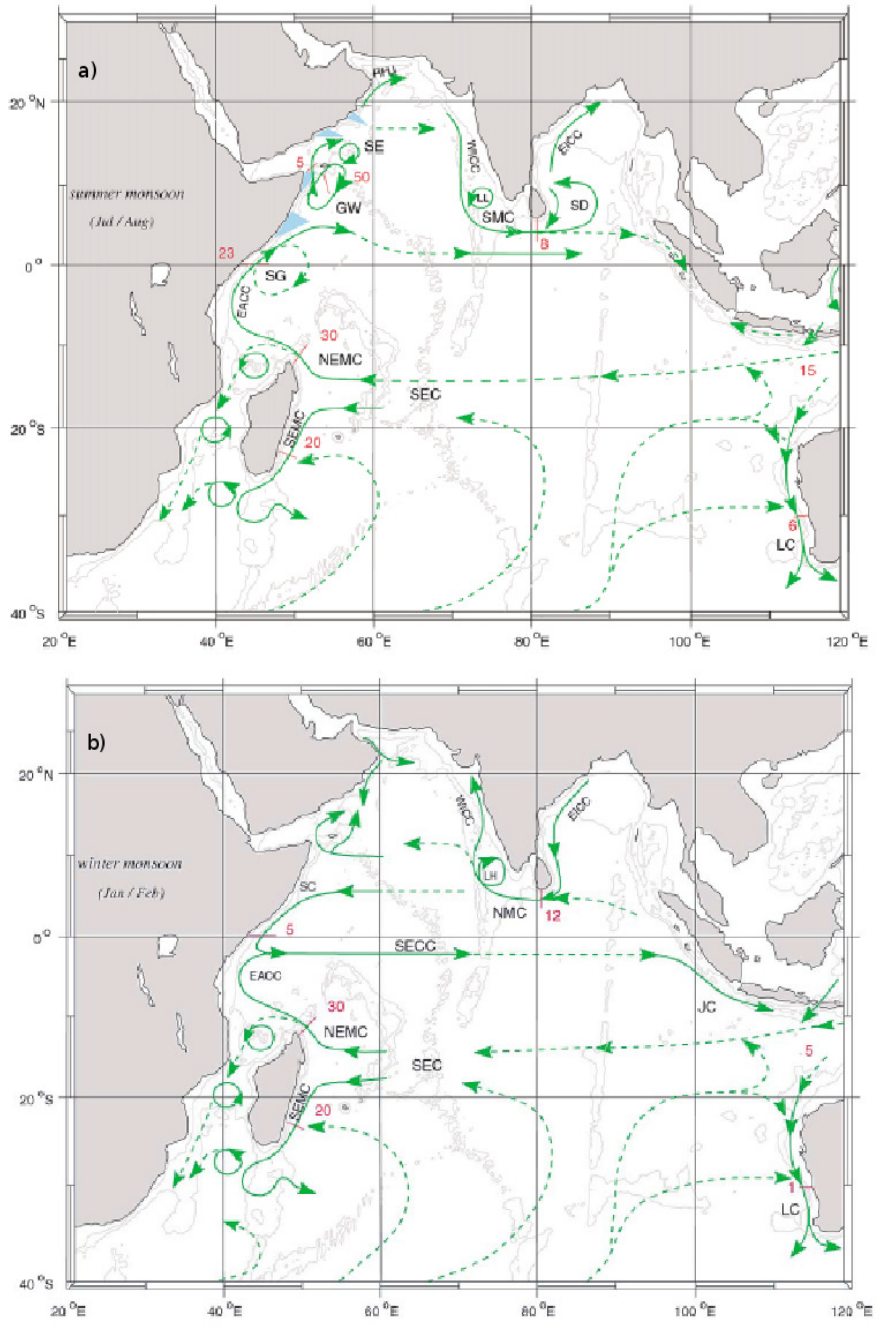

Figure 2.1.4: The large scale oceanic circulation of the Indian Ocean, including sections (red) where the transports were estimated. South Equatorial Current (SEC), South Equatorial Counter-current (SECC), Northeast and Southeast Madagascar Current (NEMC and SEMC), East African Coastal Current (EACC), Somali Current (SC), Southern Gyre (SG) and Great Whirl (GW) and associated upwelling wedges, Socotra Eddy (SE), Ras al Hadd Jet (RHJ) and upwelling wedges off Oman, West Indian Coast Current (WICC), Laccadive High and Low (LH and LL), East Indian Coast Current (EICC), Southwest and Northeast Monsoon Current (SMC and NMC), South Java Current (JC) and Leeuwin Current (LC), (Courtesy of Schott and McCreary Jr. (2001)).

During the boreal winter (Figure 2.1.4b), most of the currents north of about 15^oS change direction in response to the wind reversal (Northeast Monsoon). The Somali Current, and both the West Indian Coast Current and the East Indian Coast Current reverse direction. The connection between the Bay of Bengal and the Arabian Sea is established by the North East Monsoon Current. The Laccadive Low shifts into an anticyclonic eddy, the Laccadive High. Both the Somali

Current north of the equator, and the northward flowing East African Coastal Current south of the equator, turn eastward and feed the South Equatorial Counter Current, south of the equator. Off Java the southeastwards current disappears with the Northeast Monsoon Current, north of the equator. To the south, the South Equatorial Current feeds a well established current south of the equator, the South Java Current, which feeds into the Indonesian seas and the South Equatorial Current during this season.

The equatorial sector in the Indian Ocean differs considerably from those of the Pacific and the Atlantic, in which the westward blowing winds dominate. The monsoonal wind shifts during the transitional seasons (April to June and October to December), exerts a very important role on the dynamics of equatorial sector. They drive eastwards surface currents along the equatorial band, which are known as the Wyrtki Jet (Wyrtki, 1973). This jet, acts to remove waters from the western side of the ocean, lowering the sea level and decreasing the mixed-layer thickness in the west, but increasing them on the eastern side of the basin. The absence of sustained easterly winds, explains why the Equatorial Undercurrent occurs only during part of the year, generally from February to June, although it can appear in other seasons as well, when anomalous easterlies occur, (Kantha et al., 2008; Schott et al., 2009).

The equatorial Indian Ocean is dynamic, because it displays variability from few days up to inter-annual, whereby the intra-seasonal variability seems to play a considerable role (Senguta et al., 2007). The intra-seasonal variability of the zonal winds and currents is influenced by large scale seasonal variations of the tropical atmosphere and ocean (Senan et al., 2003; Senguta et al., 2007). Wind bursts, with $10-40\,days$ or $30-60\,days$ periods, are reported in several articles (Senan et al., 2003; Han, 2005; Senguta et al., 2007). These westerly winds are considered to be of importance in the equatorial wave guide of the Indian Ocean (Senguta et al., 2007), because they cause rapid changes in the zonal pressure force via equatorial waves. Kelvin waves generated by wind bursts over the central equatorial Indian Ocean, are able to create swift changes in the zonal pressure gradient, generated by the westerlies. These Kelvin waves may reach speeds of around $2\,ms^{-1}$, and act to lower the sea level on the east, counteracting the sea level rise associated with the jets (Senguta et al., 2007).

Another intra-seasonal variability in the equatorial Indian Ocean is the Madden Julian Oscillation (MJO), a striking planetary-scale mode of tropical variability at periods around $30-60\,days$. Reported for the first time by Madden and Julian (1972), MJOs are characterized by the devel-

opment of convection over the western tropical sector, that propagates slowly eastwards across the equatorial ocean and its maritime continents in winter, to decay around the east of the international date line, (Schott and McCreary Jr., 2001). Despite their eastwards progression and connection with the westerly winds, and their associated wind bursts in winter, they are not able to generate surface jets in the ocean (Senan et al., 2003).

One of the key elements of the circulation in the southern hemisphere is the South Equatorial Current (Figure 2.1.4). It is mainly fed by the water originated in the South Indian Ocean (Schott and McCreary Jr., 2001; Tomczak and Godfrey, 2003), as well as by the less saline waters from the Pacific Ocean through the Indonesian Throughflow, (Gordon, 1986). It is composed of narrow jets that split and coalesce at locations marked by steep topographic formations, (Matano et al., 2002).

The southernmost part of the South Equatorial Current around 15^0S, bifurcates on reaching Madagascar forming the northward branch of the East Madagascar Current, of the order of $30\,Sv$ (Schott and McCreary Jr., 2001). On reaching the northern tip of Madagascar, this branch deflects northwestwards forming the North East Madagascar Current. The southward flow of the order of $20\,Sv$ forms the southern branch of the East Madagascar Current, the Southeast Madagascar Current (Schott and McCreary Jr., 2001). Over the past, the Northeast Madagascar Current was thought to bifurcate to form the Mozambique Current, a southward boundary current along the Mozambican coast, (Quartly and Srokosz, 2002). Today, a chain of anticyclonic eddies are recognized to originate from instabilities of this current as it interacts with topography, north of the Channel (Backeberg and Reason, 2010). The North East Madagascar Current feeds the East African Coastal Current, also known as Zanzibar Current, flowing northward. The southward branch of the East Madagascar Current diverts westward on reaching the Cape Saint Marie south of Madagascar, merging later to the formerly named the Mozambique Current around the southwestern ends of the Mozambique Channel. For an extensive review of the estimations of these currents, the reader if referred to Matano et al. (2002), who lists several historic attempts based on literature.

In contrast with the northern sector of the ocean, where the wind dynamics is responsible for swift changes in the large scale circulation, this sector tends to resemble its counter parts of the other oceanic basins, which are characterized by anticyclonic gyres. However, the currents are known to vary seasonally and inter-annually. Based on WOCE in situ and satellite altimetry, Ffield and

Toole (1997) estimated the seasonal variability in the South Indian Ocean gyre. They found that the mean annual curves derived from altimeter and wind data, revealed a strengthening of the anticyclonic gyre in March and September, and weakening in June and December. From ship drift data Lutjeharms et al. (2000) concluded that the Southeast Madagascar Current and the current formerly known as the Mozambique Current reached their maximum speeds during winter and spring, with the minimums in summer.

Ridderinkhof et al. (2013) demonstrated that the Southeast Madagascar Current after separating from the southern coast of Madagascar flows southwestward and breaks into pairs of symmetric vortices in counter-rotation. They associated the formation of these vortices, which mainly propagate towards the Agulhas Current, with the El Niño Southern Oscillation (ENSO). Palastanga et al. (2006), linked the low-frequency mesoscale eddy variability around Madagascar with the large-scale Indian Ocean variability. Their findings pointed out that the SSH field in the Mozambique and East of Madagascar contains a significant inter-annual oscillation, to which they related with the large anomalies propagating eastwards in the band of $10 - 15^{o}S$. The positive (negative) anomalies were coined to positive (negative) Indian Ocean Dipole (IOD) phases (Palastanga et al., 2006), and were also considered to induce a shift in the intensity and positioning of the tropical and subtropical Indian Ocean gyres. Schouten et al. (2005) documented a case of subtropical water intruding into the tropical water north of Madagascar during 2001 austral summer. The westwards jet of subtropical origin reaches the Comoros Basin as a continuation of the South Equatorial Current. These authors conjectured that this phenomenon is a common characteristic of the austral summer.

2.1.2 South-west Indian Ocean Water Masses

The uniqueness of the Indian Ocean in the wind regimes and the large scale circulation is determinant in the water properties distribution, (Tomczak and Godfrey, 2003). Two factors are crucial in the abnormal behaviour of the water masses distribution in the Indian Ocean, namely the closure of the northern subtropic region and the blocking of the equatorial currents system by topography (Tomczak and Godfrey, 2003). The topography is a controller of the water masses distribution in the ocean (Tomczak and Godfrey, 2003). Although the monsoonal winds exert a considerable impact on surface circulation, they are not the most determinant aspect on the hydrology of the Indian Ocean as a whole. The direct monsoonal impact is restricted to the surface mixed layer

and the western boundary currents (Tomczak and Godfrey, 2003).

Up to date, the atlas of Wyrtki (1971) remains as the most important in the distribution of water properties in the world oceans. Based on published material Emery and Meincke (1986), gave a synthesized distribution of water masses in the global oceans. They considered that the ocean is divided vertically in three layers: the upper ocean from $0 - 500\,m$, the intermediate ocean $500 - 1500\,m$ and the deep and abyssal water from $1500\,m$ up to the bottom. In Table 2.1 are presented the characteristics of the water masses of the whole Indian Ocean.

In the upper layer, is found the Arabian Sea Water (ASW) on the north-westernmost side of the basin (Arabian Sea) and the Bay of Bengal Water, occupying the Bay of Bengal (East of India), extending farther south-eastwards in the northern Indian Ocean, as indicated in Figure 2.1.5a). The Indian Equatorial Water (IEW) covers the area within the parallels $20.0^oS - 5^oN$ but it reaches the Horn of Africa to the northwest, where it meets the Arabian Sea Water. Around the Central Indian Ocean the IEW, reaches the southern part of India, whereas to the eastern side it is limited by the Bay of Bengal Water (BBW) and the Indonesian Upper Water (IUW). This is an authentic limb in the Indian Ocean to the west of Java and Sumatra entering the Indian Ocean from equatorial Pacific, (Emery and Meincke, 1986). The South Indian Central Water, also called the Indian Central Water (ICW) is generated by subduction in the central Indian Ocean (Tomczak and Godfrey, 2003). It is spread along the subtropical band of the basin, from the west coast of Australia towards the east Coast of Africa, (Emery, 2001; Emery and Meincke, 1986).

Table 2.1: Southwest Indian Ocean water masses. Adapted from Emery and Meincke (1986).

Layer	**Water masses**	**Characteristic**
Upper Water	BBW	$25.0 - 29°C$ and $28 - 35psu$
	ASW	$24.0 - 30°C$ and $35.5 - 36.8psu$
	IEW-TSW	$8.0 - 23°C$ and $34.6 - 35.0psu$
	IUW	$8.0 - 23°C$ and $34.4 - 35psu$
	SICW-STW	$8.0 - 25.0°C$ and $34.6 - 35.8psu$
Interm. Water	AAIW	$2 - 10°C$ and $33.8 - 34.8psu$
	IIW	$3.5 - 5.5^oC$ and $34.6 - 34.7psu$
	RSPGIW	$5.0 - 14 \circ C$ and $34.8 - 35.4psu$
Deep and Abysal Water	CDW	$0.1 - 2 \circ C$ and $34.62 - 34.73psu$

According to Emery and Meincke (1986) the intermediate layer in the Indian Ocean comprises three water masses, the AAIW, the Indonesian Intermediate Water (IIW), also a limb in the eastern

side of the ocean, lying below the Indonesian Upper Water, and finally the Red Sea-Persian Gulf Intermediate Water (RSPGIW), (Figure 2.1.5b). The AAIW occupies the hole ocean in medium depths, up to around 10^oS, while the RSPGIW covers the northern sector of this ocean. The bottom layer is composed of the Circumpolar Deep Water (CDW), under which lies the Antarctic Bottom Water (AABW). The AABW reaches some areas in the equator through the open passages of the bottom topography, while over the east coast of Africa it is blocked by the Mozambique strait (Tomczak and Godfrey, 2003). An attempt to describe the route of the intermediate water circulation from their source in the Indian Ocean was carried out by You (1998), who again considered that the whole ocean at intermediate level is dominated by three water masses, namely the AAIW, the Red see Intermediate Water (RSIW) and the IIW. He showed that the AAIW can propagate farther into the northern Indian Ocean.

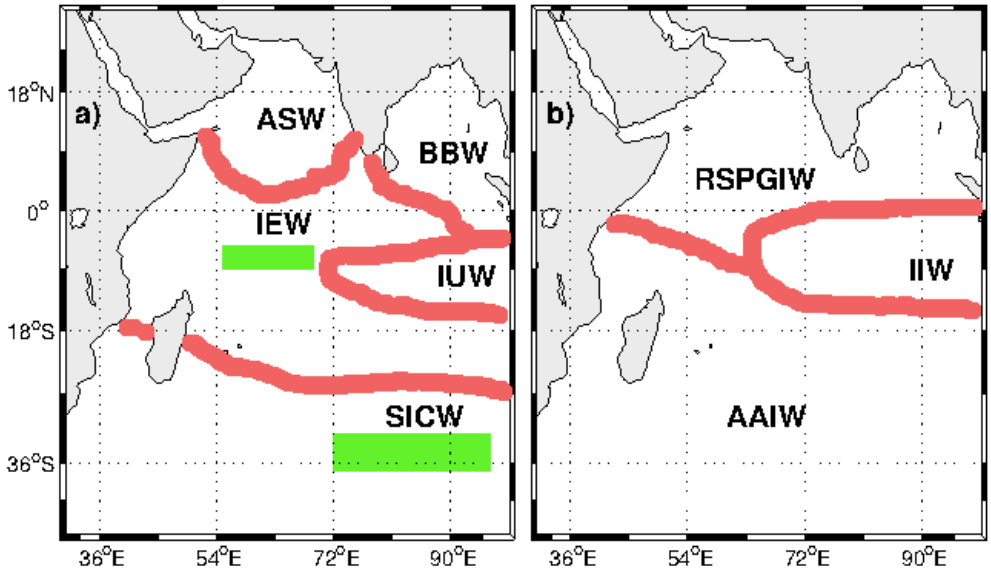

Figure 2.1.5: Distribution of water masses in the Indian Ocean. In a) are given the upper ocean waters, namely the Arabian Sea Water (ASW), Bay of Bengal Water (BBW), Indian Equatorial Water (IEW), Indonesian Upper Water (IUW) and the South Indian Central Water (SICW). In b) are shown the intermediate waters, namely the Antarctic Intermediate Water (AAIW), the Indonesian Intermediate Water (IIW), and finally the Red Sea Persian Gulf Water (RSPGIW). The green rectangles represent the areas of water masses formation, whereas the purple line indicates the borders between distinct water masses. Picture adapted from Emery and Meincke (1986).

The intrusion of the Red Sea Waters (RSW) into the South Indian Ocean, has been noted by several papers, (Wyrtki, 1971; Morales et al., 1996; Beal et al., 2000). Nevertheless, the physical processes behind its intrusions is unknown, (Beal et al., 2000). Beal et al. (2000), mapped the intrusion of this water mass over the whole sectors of the Indian Ocean using data from WOCE Hydrographic Program (WHP) for the Indian Ocean. Another intruder, the Banda Sea Intermediate Water, also known as the IIW (You, 1998), is well recognized and separated. This distinction is possible because this water is characterized by a salinity minimum, in contrast with the RSW that contains

a salinity maximum, (Beal et al., 2000). On investigating the water masses properties in Aldraba, within the area defined by the geographical coordinates $46^o20'E - 47^o30'E$ and $9^o25'S - 9^o45'S$ Morales et al. (1996), also recognized the intrusion of RSW in that area. Beal et al. (2000), demonstrated that the RSW propagates preferentially in the western boundary of the Mozambique Channel, whereas part of it reaches the Agulhas Current from the subtropical gyre. They also concluded that the RSW is important in the salt exchange into the Atlantic Ocean.

In the Delagoa Bight the most important water masses debated in literature are the AAIW, Tropical Surface Water (TSW) and the Subtropical Surface Water (STW) (Lutjeharms and Jorge da Silva, 1988; Lamont et al., 2010). In this study their reproducibility in the model outputs is assessed. Furthermore, their sources are also reexamined. The classification of Emery and Meincke (1986) incorporates the TSW in the IEW, whereas the STW is in the SICW. The SICW lies immediately below the STW, (Tomczak and Godfrey, 2003).

2.1.3 Ocean Dynamics in the Mozambique Channel

2.1.3.1 General Description

According to IHO (1953) the oceanic region that falls within the geographical coordinates $10.482 - 6.8472^oS$ and $32.5872 - 49.2583^oS$ is known as the Mozambique Channel. It is bordered by the Mozambique main land on the west and Madagascar on the east. At the northern border of the Channel is located the Comoros archipelago, whereas its southern limit is topographically dominated by the Mozambique ridge. The Channel is a seismically active region thought to be an offshore continuation of the Tanzanian Basin, (Kapilima, 2003). From Cape Amber at the northern tip of Madagascar to its southern tip at 26^oS, there is an extension of $1600\,km$. At the narrows, the Channel is about $430\,km$ wide but at 20^oS it reaches a maximum width of about $1000\,km$. The continental shelves on the Mozambican and Madagascar sides of the Channel are in general narrow, and bordered by steep continental slope, (Swart et al., 2010). The tidal ranges in the coastal areas of the Channel may reach $7.3\,m$ (Sete et al., 2002), whereas the SST and Chlorophyl Concentrations vary seasonally according to the region of the Channel, (Tew-Kai and Marsac, 2009). The behaviour of the flow, which is entirely dominated by eddies moving southward (Biastoch et al., 1999; Halo et al., 2014a) reflects a complex ecosystem whereby the biologic productivity is linked with eddy shelf interactions (Roberts et al., 2014). In Figure 2.1.6, is presented the map of the Mozambique Channel.

Figure 2.1.6: The Mozambique Channel map including the surrounding countries. The red star indicates their capitals, whereas the small dot refers to smaller special locations. Picture of the World atlas (www.wordatlas.com/aatlas/infopage/mozchann.htm).

2.1.3.2 Mozambique Channel Eddies

In a region where a western boundary current was considered to prevail, Biastoch and Krauss (1999) used an ocean model, to shed light on the prevalence of anticyclonic eddies and their morphology. The Northeast Madagascar Current splits in two parts around the northwest tip of Madagascar (Cape Amber). The northern branch flows towards the east African coast, forming the East African Coastal Current, whereas the second branch is an anticyclonic loop in the northern Mozambique Channel, (Figure 2.1.7). This loop pinches off anticyclonic eddies that propagate southwards with the mean flow along the Channel, (Biastoch and Krauss, 1999). South of the Channel, Biastoch and Krauss (1999) eddy permitting model reproduced another set of anticyclonic eddies traveling southwestwards from the southernmost tip of Madagascar, which although were bound to the east coast of Madagascar, these investigators speculated that they were formed in the central South Indian Ocean. Interestingly, these anticyclonic eddies travel southwestwards and merge with those of the northern Mozambique Channel, around 27^oS (Biastoch and Krauss, 1999).

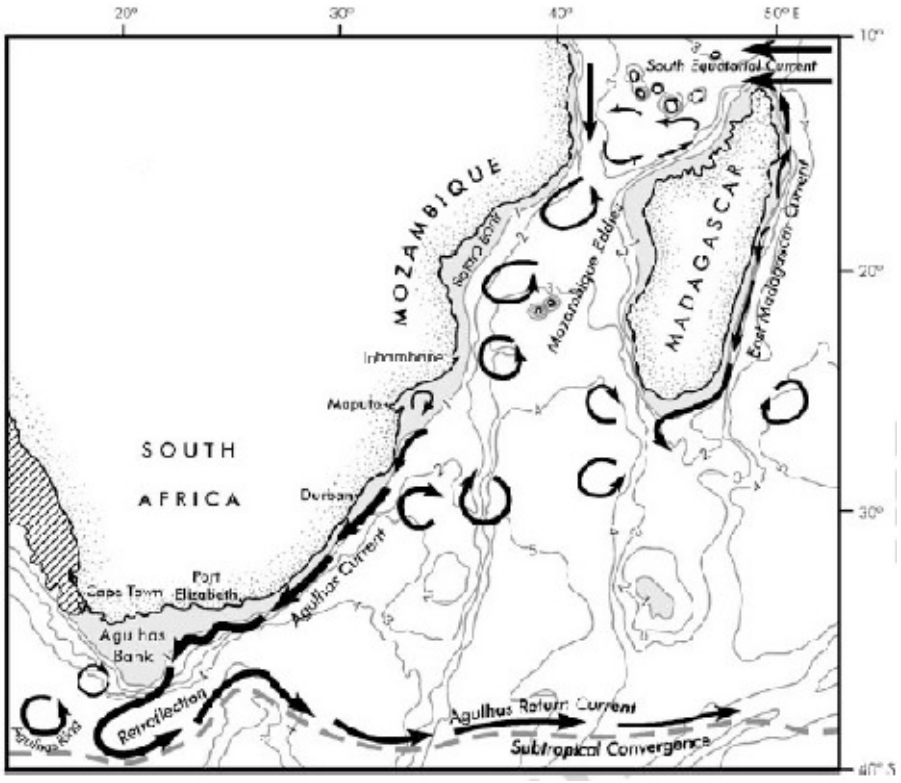

Figure 2.1.7: The main circulation features of the region of Mozambique Channel. The cyclonic feature in the Delagoa Bight is well presented. Courtesy of Lutjeharms (2006a).

The rate of formation of anticyclonic eddies in the northern Mozambique Channel has been documented to be around 4 to 5 eddies per annum (Biastoch and Krauss, 1999; Schouten et al., 2003). Their pathway is rather uniform and generally, they advect along the African coast shelf (Schouten et al., 2003). Their average speed has been demonstrated to vary according to the area they are traveling on. Between $12-27^oS$, the speed was estimated to be $6\,km/day$, but it grows faster around $27-35^oS$, while between $18-21^oS$ they slacken to around $3-4\,km/day$ (Schouten et al., 2003). Biastoch and Krauss (1999), coined the formation of the northern Mozambique Channel anticyclonic eddies with barotropic instabilities of the South Equatorial Current north of Madagascar. These eddies are characterized by a strong barotropic component, that reaches speeds of $10\,cm.s^{-1}$ at around $2000\,m$ depth (Schouten et al., 2003), in contrast with their $400\,m$ prevalence modelled by (Biastoch and Krauss, 1999). More recently (Swart et al., 2010; Halo et al., 2014a), gave detailed characterization of these eddies and their impact downstream of the Agulhas Current.

Schouten et al. (2003), linked the Rossby waves (from the east), with a 4 year forcing considered to be crucial in the westwards elongated anomalies over the meridional extent of the Mozambique Channel, whose associated fluctuations, constitute the large scale modulation of the SSH that controls the reduced number of eddies that enter the Channel. In fact, only about $4-5$ strong

anomalies do enter the Channel from the north as associated with the signal fluctuation due the Rossby waves (Schouten et al., 2003).

The morphology of the southeast Madagascar eddies is linked to the dynamics of the South East Madagascar Current, as it separates from the southern tip of the island, forming a typical western boundary current associated to the subtropical gyre of the South Indian Ocean. It runs out of the boundary on reaching the southern tip of Madagascar (de Ruijter et al., 2004). From in situ observations carried out during the ACSEX experiment de Ruijter et al. 2004, identified a dipolar structure around the southwest coast of Madagascar. These eddies have been shown to drift in a west or southwest direction towards the African coast (Gründlingh, 1995; de Ruijter et al., 2004). Indeed, Siedler et al. (2009) identified two basic modes in the South East Madagascar Current extension, with anticyclonic motion favouring retroflexion in the northern Mozambique Basin, when the current is flowing in a southwestward direction and cyclonic motion located farther north, occurring when it flows westwards along the southern Madagascar slope.

Although the East Madagascar Current had been assumed as a western boundary current similar to the greater Agulhas Current, including the concept of retroflexion also similar to that of the Agulhas (Quartly et al., 2006), the new view of the local circulation points to a prevalence of pairs of contra-rotating eddies south (east) of Madagascar. These symmetric circular structures in which the anticyclonic (positive vorticity) is located to the west (inshore), with the cyclonic (negative vorticity) on the offshore side of the downwards flowing East Madagascar Current (de Ruijter et al., 2004; Quartly et al., 2006). The eddy-pair formation southeast of Madagascar according to Quartly et al. (2006) starts with the generation of the anticyclones. These are mainly caused by the increase of potential vorticity due to the shallowing of the bottom topography in the Madagascar Plateau and the beta effect which induce positive vorticity in the jet, stimulating positive vortex formation, whereas the negative (cyclonic) vorticity is thought to originate in the inshore side of the jet as it separates from the main land, due to friction against Madagascar. Quartly et al. (2006) also found that the bipolar trains from the South of Madagascar, are able to stimulate early retro-reflection in the Agulhas Current. This view is concomitant with the evidence of the impact of these eddies in Agulhas ring formation (Schouten et al., 2002; de Ruijter et al., 2004; Quartly et al., 2006; Ridderinkhof et al., 2013). However, a recent paper by Ridderinkhof et al. (2013) considers the impact of the dipoles on early retroflexion, a low frequency process.

Applying an eddy detecting and tracking system on satellite observations and model outputs of

ROMS and the Hybrid Coordinate Ocean Model (HYCOM), Halo et al. (2014a) gave a new light into the morphology and behaviour of the Mozambique Channel eddies. Their finding, showed that the anticyclonic eddies are formed at around 12^oS, by the western side of Cape Amber between Madagascar and Mozambique in agreement with Biastoch and Krauss (1999). However a second location, which they considered to be less discussed in literature was also found, south of the narrows of the Channel at $20^oS, 43^oE$. Regarding the cyclonic eddies, they concluded that they were generated at the eastern side of the Channel, although they are ubiquitous all over the Channel.

Roberts et al. (2014), investigated the mechanisms involved in the shelf and offshore interaction associated with the rings. They used Sea Level Anomaly (SLA) data, aided by in situ data and drifters to track a southward propagating dipole. They inferred that this dipole, in which the cyclone is to the south of the ring, in contact with the western side of the Channel induce slope upwelling due to horizontal and vertical divergence at the shoreward leading edge of the anticyclone. They also indicated that the up-welled water moves onto to the shallow shelf ($20\,m$), but doesn't generally reach the surface, elevating the subsurface chlorophyll maximum against the slope, a key condition in enhancing surface Chlorophyl Concentration within the dipole divergence zone, (Roberts et al., 2014).

2.1.4 The Delagoa Bight

2.1.4.1 Geographical features

The Delagoa Bight is one of the largest coastal indentation along the east cost of Africa, (Lamont et al., 2010). It is situated in the south-westernmost part of the Mozambique Channel, south of Mozambique main land. It is the second large in the region after the Bank of Sofala. For the purpose of this study, the Delagoa Bight falls within the latitudes $24 - 28^oS$ and longitudes $32 - 36^oE$. The configuration of the continental terrace provides a suitable condition for the existence of cyclonic features, (Martin, 1981; Lutjeharms and Jorge da Silva, 1988; Lamont et al., 2010). Several studies demonstrated a relative impact of the topography in the generation of the DBLE, a key element of the local circulation (Lamont et al., 2010; Lutjeharms, 2006b; Lutjeharms and Jorge da Silva, 1988). Martin (1981), identified 5 important elements of Delagoa Bight bottom topography, namely the Limpopo cone, the Inharime terrace, the continental shelf, the Almirante Leite bank and the Central Terrace (Figure 2.1.8).

According to Martin (1981), the Limpopo cone is a smooth surface feature 300 km long, extending from the Limpopo river mouth southward. It is smoother on its northern side. To the south, it deepens on reaching the Central Terrace at around 800 m of depth. The Inharime Terrace, is a smooth convex curvilinear sedimentary feature located to the eastern side of the Limpopo cone, with an extension of 140 km towards the southwest from Ponta Závora (Martin, 1981). Two slopes are recognized on this terrace, with one descending eastwards in two steps towards the northern end of the Mozambique ridge, whereas the second, a sedimentary lobe, curves towards Maputo, (Martin, 1981). The Almirante Leite Bank, is composed of 80 rocky peaks and sea mounds, the shallowest of which is only 71 m. It spreads out over 130 km in an northwest-southwest trend, (Martin, 1981; Lutjeharms and Jorge da Silva, 1988). The largest sea mounts are flanked deep moats whereas several small channels and sedimentary mounds are distributed asymmetrically among the smaller pinnacles (Martin, 1981). The Central Terrace lies on the southeastern side of Delagoa Bight (western Mozambique ridge), northeastern Natal. The Central Terrace slopes gently down from 1300/1400 m to 2000 m, with its southern extension flanked to west and east by prominent valleys, separating it from the continental slope and the Mozambique ridge (Martin, 1981). The Central Terrace is characterized in general by a smoothed area which slopes gently in two convex axes curving towards the southeast (Martin, 1981).

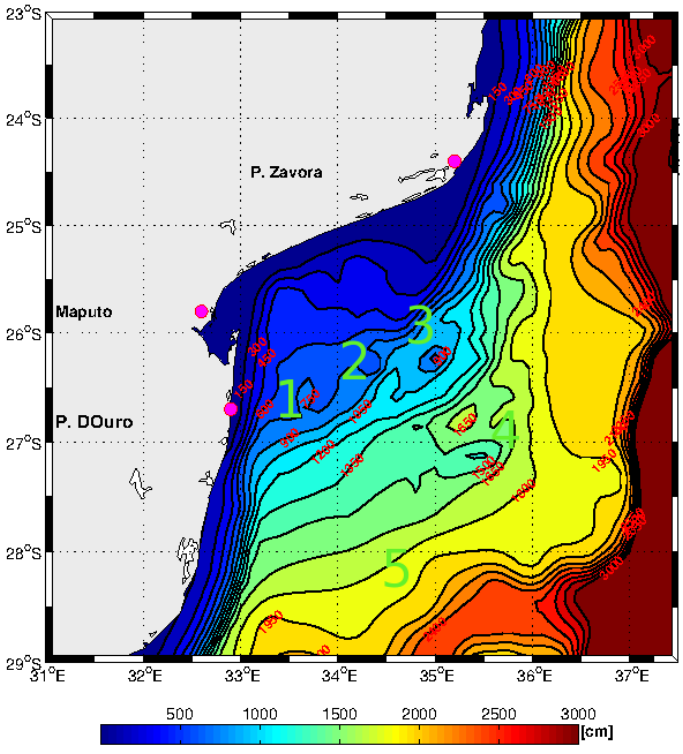

Figure 2.1.8: Delagoa Bight Topography. The black lines represent the contours of topography. (1) is the Limpopo cone, (2) the Inharime terrace, (3) the continental shelf, the (4) Almirante Leite bank and (5) the Central Terrace.

Between 28^oS and Ponta D'Ouro the shelf is very narrow $2-7\,km$ (Figure 2.1.8), but it widens from there towards the north, until Ponta Závora, where it bulges seawards as an expression of the Inharime Terrace, (Martin, 1981). Near Maputo, the slop descends up to the depths of $350\,m$, probably in response of sedimentary infill of the Limpopo Cone (Martin, 1981). This bathymetric configuration has been considered to be of great importance in the formation of the Delagoa Bight Lee Eddy (Lutjeharms and Jorge da Silva, 1988).

2.1.4.2 The Delagoa Bight Lee Eddy

The DBLE, is the most prominent feature of the Delagoa Bight oceanic circulation and the work of Lutjeharms and Jorge da Silva (1988) appears as the first to establish most of the recognized aspects and concepts of the Delagoa Bight circulation so far. These authors, documented the presence of a semi-permanent cyclonic feature generated topographically, whose shore-wards current was bound to the shallow shelf, and propagated northward, hence the name counter-current, in opposition of the southward flowing current, historically known as the Mozambique Current. Also, they indicated the prevalence of the AAIW in the lower layers and the Tropical Equatorial waters in the surface.

From analysis of hydrographic and satellite imagery, Lutjeharms and Jorge da Silva (1988) demonstrated that the DBLE is found in the same position most of the time. Their study supported for long the concept of a semi-permanent cyclonic feature with the center located around $26^oS, 34^oE$. Recently, Lamont et al. (2010) used hydrographic and satellite altimetry data to demonstrate that the DBLE, is not a permanent feature. It some times disappears. Furthermore, they state that the passage of anticyclonic eddies impacts the water masses in the Bight by inducing upwelling onto the shelf.

Over the past, the DBLE was known to be generated by the Mozambique Current, as it is constrained topographically in the narrow and steep continental shelf of the northern Natal Valley (coast of Ponta D'Ouro) (Martin, 1981; Lutjeharms and Jorge da Silva, 1988). The wide terrace and the large continental shelf off Maputo, were considered to facilitate the DBLE inception and dynamics (Lutjeharms and Jorge da Silva, 1988; Quartly and Srokosz, 2004; Lamont et al., 2010). A theoretical study by Gill and Schumann (1979) applied to the Agulhas Current, on the extension between Port Eduard and Natal Bight (where the current is known to be fast and uniform), demonstrated the importance of a jet of uniform vorticity (inertial boundary current), on a shallow

topography. These authors used a two layers model in which the boundary current flows on top. They found that changes in the shelf topography may cause substantial changes in the structure of the current. Also, a minimum in the shelf width could exert a hydraulic control on the current, which is characterized by reversal of the jet on its upstream side (bifurcation), outcropping cold water near the shore downstream of the reversal point, (Gill and Schumann, 1979).

The model of Gill and Schumann (1979) that was successfully applied in the Natal Bight has been a key element for Lutjeharms and Jorge da Silva (1988) to sustain the results of their study based on observation and satellite data. This helped them to understand and explain the origin of the coastal counter current, for the landward border of DBLE, which is observed often advecting warm water northward. Lutjeharms and Jorge da Silva (1988) concluded that the DBLE is generated topographically because its core is found locked in a flat area of the shelf most of the time.

Regarding the water masses distribution, Lutjeharms and Jorge da Silva (1988) concluded that the DBLE T-S characteristics are completely modified in comparison with those of the Mozambique Channel. The Sub-Tropical Water is completely mixed into the eddy due to upwelling. Possible movement of the core southward has been suspected (Lutjeharms and Jorge da Silva, 1988), whereas the presence of various cyclonic cores was conjectured by Martin (1981). During the present work, the mechanisms behind the DBLE generation will be reassessed, including the whole dynamics over the region.

Quartly and Srokosz (2004) showed that cyclonic eddies from south of Madagascar have variable directions of propagation, with some reaching the east African coast around the Kwazulo Natal, and others reaching the Delagoa Bight region. The Mozambique Channel eddies propagate southward and impact Delagoa Bight circulation (Lutjeharms, 2006a). Lamont et al. (2010) found that these anticyclonic eddies were important in the DBLE development as well as in the characteristics of the water masses in this region. Despite the recent establishment of the concept of DBLE present and absent by Lamont et al. (2010), there is no statistics available regarding the timing of the lee eddy, its radius variations and life-spans. Gründlingh et al. (1989), found an anticyclonic circulation covering completely the whole Bight, to which they linked with the instabilities of the former Mozambique Channel. These authors refuted completely the possibility of prevalence of a cyclonic eddy in Delagoa Bight. The modelling study presented here, is an opportunity to tackle these problems, and shed more light into the complex dynamics of the Bight.

2.1.4.3 Eddy and tidal induced enhancement of primary production

By exploring SeaWiFS Satellite color imagery, Quartly and Srokosz (2004) carried out the first investigation of the interaction of the anticyclonic eddies with the shelf over the sources of the Agulhas Current. They underlined the importance of both the sluggish north of Mozambique anticyclonic eddies (speed of around $6\,km/day$) and the relatively fast south of Madagascar anticyclones ($10\,km/day$), in the dynamics of the region. The former drive the nutrients from the shelf towards offshore, whereas the latter drive nutrients from offshore towards the African slope (Quartly and Srokosz, 2004). Also, they noted that Delagoa Bight was one of the most productive regions in the southwestern Mozambique Channel, (Quartly and Srokosz, 2004).

Delagoa Bight is a location of formation of a cyclonic eddy, (Lutjeharms and Jorge da Silva, 1988; Lamont et al., 2010). Cyclonic eddies are generally associated with high level of vertical transport (pumping) of nutrients and increased productivity (Tew-Kai and Marsac, 2009; Kolanski et al., 2012). Although several recent studies on productivity and distribution of chlorophyll concentrations induced by eddy dynamics were carried out in the region (Tew-Kai and Marsac, 2009; Omta et al., 2009; Kolanski et al., 2012; Roberts et al., 2014), such studies refer to the Mozambique Channel as a whole, while relatively few are dedicated to the Delagoa Bight (Kyewalyanga et al., 2007; Barlow et al., 2008).

Kyewalyanga et al. (2007), performed an investigation with the aim of assessing variations in the phytoplanktonic biomass and primary production in Delagoa Bight. They concluded that the variability in the Bight was very high due to the local hydrography, which is very dynamic. Furthermore, Kyewalyanga et al. (2007) concluded that the highest levels of productivity was found between the latitudes $24.5 - 25^{o}S$, in the northeastern area of Delagoa Bight (south of Ponta Závora). They associated this levels of productivity, with the dynamics of the eddies and also to the impact of the incipient Agulhas Current and the East of Madagascar Current. They also suspected that the Limpopo River that debouches in the western side of the Bight could be contributing, especially over the rainy seasons (Kyewalyanga et al., 2007).

Barlow et al. (2008), investigated both the Natal and the Delagoa Bight. For the Delagoa Bight, they concluded that the area where the DBLE is usually found is dominated by an intermediate level of productivity (mesotrophic), whereas the northeastern part of the Bight is highly productive (eutrophic), concomitant with Kyewalyanga et al. (2007). The high levels of productivity at the northeast sector, made one conjecture that other unknown mechanisms might have a role on the

generation of productivity there, since the lee eddy is generally found centered slightly southward at $26^oS, 34^oE$.

Another intriguing fact is the recent result of Lamont et al. (2010), indicating that the Delagoa Bight eddy is not a permanent feature, because it vanishes occasionally. This enforces the need of more studies towards the understanding of the dynamics in the Bight, and this has been carried out in this PhD, recurring to a regional oceanic model (ROMS), a powerful tool which has already been successfully used in the Indian Ocean (Penven et al., 2006; Halo et al., 2014a).

The very high activity of the eddies in the Mozambique Channel, make this region a preferential place for the investigation of the eddy induced transport processes that affect some sources and sinks (Kolanski et al., 2012). These researchers used stable isotope tracers sampled from the local environment, to capture the sources and sinks of Particulate Organic Matter (POM), in association with the dynamics of a mesoscale eddy dipole, located around Sofala Bank but moving southward. Their study suggests firstly that the eddies in the Mozambique Channel may be directly associated with the sites of upwelling and production inside the cyclones, and secondly with the coupling between the coastal and pelagic systems through entrainment as the eddies interact with the shelf. They consider this to be crucial to explain the high diversity and biomass of pelagic consumers observed there.

Another important factor of productivity in the region might be the presence of internal tides in the region. The region of the western Indian Ocean (mainly the Mozambique Channel) was rated at 11 in a total of 28 regions all over the globe in therms if dissipation of M2 tidal energy, (Egbert and Ray, 2001). In a similar type of rating Bains (1982), estimated the energies involved in the generation of internal tides, having considered that the region of the Mozambique Channel lies within the 12 most active regions in the world. Jackson et al. (2004), presented a global scale atlas, containing images of Internal Waves observed by Synthetic Aperture Radar (SAR) on board of the ERS satellite, registered over the whole global ocean, and the region of Delagoa Bight showed very prominent signatures of Internal Waves (IW). Huge tidal amplitudes have been recorded in coastal areas in this region, (Sete et al., 2002).

The importance of internal tides induced mixing and associated impact in primary production in the ocean is well known over the global oceans, and this is expressed by the existence of extensive publications of the subject (Zhao et al., 2012; Hall et al., 2011; Garrett, 2003; Sangrá et al., 2001) Although they were initially considered of great influence along the continental shelf, their impact

in the deep sea is now recognized (Garrett, 2003; Garrett and Laurent, 2002). Due to the challenge to resolve internal tides at horizontal and vertical resolution (Nash et al., 2012; Buijsman et al., 2012; Garrett, 2003), this study will be limited to the analysis of the effect of tides in the local dynamics, whereas the IW will be left for the future.

2.1.5 Summary

This review has shown that the most prominent oceanic features of the region are the anticyclonic eddies generated north of the Mozambique Channel and south of Madagascar. These eddies impact the circulation in the Delagoa Bight, as they move towards the Agulhas Current farther south.

In Mozambique, the Delagoa Bight region is very important in fisheries industry, one of the most important income sources in the country, until recent decades. Following the Sofala Bank in central Mozambique, Delagoa Bight is the second most productive region in Mozambique. However, the scarcity of research in the region (Quartly and Srokosz, 2004; Lutjeharms, 2006b, 2007), hinders the improvement of the fisheries management in the country. As previously indicated, the highest levels of primary productivity in the Bight is found in the north-easternmost sector of the Bight. The reason of this behaviour is not understood. Although the aim of this work is not to determine productivity, the attendant dynamics will be assessed.

The DBLE has been considered for long as a semi-permanent feature, but recently it has been demonstrated that it occasionally disappears (Lamont et al., 2010). It is not clearly known why, neither if that follows a specific seasons or not. Other researchers suspected that the topographic configuration in the Delagoa Bight was capable of sustaining more than one cyclonic eddy, (Martin, 1981). Currently, only the DBLE is known. Furthermore, the impact of the passing anticyclones from the north of Mozambique Channel in the Bight is not well understood. Here, a high resolution experiment is carried out to investigate the complex oceanic dynamics in the Bight.

The anticyclonic feature found occupying the whole Bight by Gründlingh et al. (1989) is also intriguing, in a region where the circulation is deemed complex. This study will investigate the possibility of occurrence of such feature, and its characteristics.

Although several rivers drain waters into the Bight, on the south-westernmost part of the Bight (Maputo Bay), and also by the northwestern part where the Limpopo River debouches, their effect will not be included due to the paucity on available river data. The research questions to be answered during this study are the following:

1. Is our ROMS configuration able to resolve the mean regional circulation in the Delagoa Bight region?
   (a) Are the presences and absences of the Delagoa Bight lee eddy represented by ROMS?
   (b) Are the main water masses in the Bight represented? What is their source?
   (c) What is the impact of the offshore passing cyclonic and anticyclonic eddies?
   (d) What is the effect of improvement of resolution?
   (e) Are there other relevant aspects of the regional circulation resolved by ROMS?
2. What are the mechanisms controlling the DBLE generation?
   (a) Is the cyclonic eddy generated by the southwards flow, or by the passing mesoscale featues from the north of Mozambique Channel or of the east of Madagascar?
   (b) Is the lee eddy generated by the cyclones intruding into the Bight?
   (c) Where is the location of generation of the DBLE and what is the mechanism involved?
   (d) What is the mechanism involved in the generation of anticyclonic features in the Bight?

Chapter 3

Material and methods

3.1 The Regional Ocean Modeling System (ROMS)

ROMS is a three-dimensional, free-surface, terrain-following primitive equations model, designed to tackle oceanic and coastal processes at a relatively high resolution, (Shchepetkin and McWilliams, 2015). It solves the barotropic and baroclinic momentum equations separately, (Shchepetkin and McWilliams, 2015). It features high order numerical schemes for space and time differencing, to optimize the effective resolution of the model (Soufflet et al., 2016). Therefore, ROMS is a good tool for modeling mesoscale, approximately geostrophic balanced flows and eddies, as well as non-linear gravity and inertial waves at high resolution, (Shchepetkin and McWilliams, 2009). The model has been used to investigate large basin scale simulations with success (Haidvogel et al., 2000).

The choice of ROMS AGRIF version 3.2 for this study, is based on the great success achieved by several configurations designed for specific issues in this region, (Collins et al., 2014; Halo et al., 2014a; Nehama and Reason, 2015). Furthermore, its advanced numeric schemes have been considered adequate in solving regional oceanic problems, applying a generalized vertical sigma coordinates (Shchepetkin and McWilliams, 2015; Shchepetkin and McWilliams, 2009). This Chapter is organized in the following manner: In section 3.2 the model momentum equations and the surface and bottom boundary conditions are discussed. The generalized coordinate system, as well as the Open Boundary Conditions are also presented in this section; In section 3.3 the numeric schemes are explained. This section discusses the model horizontal and vertical discretizations before dealing with some aspects of the model parametrization. In section 3.4, the Delagoa Bight

model configuration and all the sensitivity experiments carried out are given. The description of all the data sets used in model initialization follows in section 3.5. In section 3.6 the description of the eddy detecting and tracking system is discussed, whereas the Power Spectral Density is described in section 3.7. Finally, the synthesis of the chapter is given in section 3.8.

3.2 General equations

ROMS solves the momentum equations in a rotating frame following the hydrostatic and the Boussinesq approximations, as illustrated below:

$$\frac{\partial u}{\partial t} + \vec{v}.\nabla u - fv = -\frac{\partial \phi}{\partial x} - \frac{\partial}{\partial z}\left(\overline{u'w'} - \nu\frac{\partial u}{\partial z}\right) + F_u + D_u \tag{3.2.1}$$

$$\frac{\partial v}{\partial t} + \vec{v}.\nabla v + fv = -\frac{\partial \phi}{\partial y} - \frac{\partial}{\partial z}\left(\overline{v'w'} - \nu\frac{\partial v}{\partial z}\right) + F_v + D_v \tag{3.2.2}$$

$$\frac{\partial \phi}{\partial z} = \frac{-\rho g}{\rho_o} \tag{3.2.3}$$

with the continuity equation expressed as:

$$\frac{\partial u}{\partial x} + \frac{\partial v}{\partial y} + \frac{\partial w}{\partial z} = 0 \tag{3.2.4}$$

while the scalar transport is given by:

$$\frac{\partial C}{\partial t} + \vec{v}.\nabla C = \left(\overline{C'w'} - \nu_\theta\frac{\partial C}{\partial z}\right) + F_C + D_C \tag{3.2.5}$$

Finally, the equation of state is expressed by:

$$\rho = \rho\left(T, S, P\right) \tag{3.2.6}$$

The Reynolds stresses and turbulent tracer fluxes, are parameterized as:

$$\begin{cases} \overline{u'w'} = & -K_M \frac{\partial u}{\partial z} \\ \overline{v'w'} = & -K_M \frac{\partial v}{\partial z} \\ \overline{C'w'} = & -K_C \frac{\partial C}{\partial z} \end{cases} \tag{3.2.7}$$

The prognostic variables presented in the equations [3.2.1 - 3.2.7] are described as: C represents scalar quantities such as temperature, salinity. D_u, D_v and D_C are optional horizontal diffusive terms. F_u, F_v and F_C represent the forcing terms. $f(x, y)$, is the Coriolis parameter, g is the acceleration due to gravity, $h(x, y)$ is the depth of the sea floor below the mean sea level. $[\nu, \nu_\theta]$, are the molecular viscosity and diffusivity respectively, while $[K_M, K_C]$ represent the vertical eddy viscosity and diffusivity, respectively. P represents the total pressure, and is given by the hydrostatic equation $P = -g\rho_o z$. The dynamic pressure is described by $\varphi(x, y, z, t)$. The total in *situ* density is $\rho_o + \rho(x, y, z, t)$, where t is time. $T(x, y, z, t)$ is the potential temperature, $S(x, y, z, t)$ is the salinity, and both are represented by $C(x, y, z, t)$ in these equations. (u, v, w) indicate the components of velocity along the x, y, z coordinates, while $\zeta\,(x, y, t)$ is the sea surface elevation.

Equations 3.2.1 and 3.2.2 describe the momentum balance in the x and y directions. The temporal evolution (advection and diffusion) of the tracers (temperature, salinity and scalar concentration fields) is expressed by equation 3.2.5. The equation of state of sea water is given in 3.2.6, whereas the hydrostatic balance is in equation 3.2.3. Finally the Boussinesq approximation, according to which all perturbations in the density are negligible except in the buoyancy, is considered in the resolution of these equations.

The boundary conditions at the surface and bottom are expressed by the system of equations 3.2.8 and 3.2.9, respectively.

$$\begin{cases} a) \;\; K_M \frac{\partial u}{\partial z} = \tau_s^x\,(x, y, t) \\ b) \;\; K_M \frac{\partial v}{\partial z} = \tau_s^y\,(x, y, t) \\ c) \;\; K_C \frac{\partial C}{\partial z} = \frac{Q_C}{\rho_o c_P} \\ d) \;\; w = \frac{\partial \zeta}{\partial t} \end{cases} \tag{3.2.8}$$

$$\begin{cases} a) \quad K_M \frac{\partial u}{\partial z} = \tau_b^x (x, y, t) \\ b) \quad K_M \frac{\partial v}{\partial z} = \tau_b^y (x, y, t) \\ c) \quad K_C \frac{\partial C}{\partial z} = 0 \\ d) \quad -w + \vec{v}.\nabla h = \frac{\partial \zeta}{\partial t} \end{cases} \tag{3.2.9}$$

In equations [3.2.8 and 3.2.9] Q_C represents the surface concentration heat fluxes, τ_s^x and τ_s^y, are the horizontal components of the surface wind stresses while τ_b^x and τ_b^y represent the bottom stresses. C_p is the heat capacity of the sea water. Since Q_C is a strong function of the ocean surface temperature, this variable is determined from SST and atmospheric fields according to an atmospheric bulk parametrization. On the bottom $z = -h(x, y)$, the horizontal velocity is affected by a bottom stress of linear, quadratic or logarithmic form. The vertical concentration flux at the bottom, is generally prescribed to zero, but it may be attributed a specific value, as detailed by Hedstrȯm (2009).

To account for the sensitivity of Q_C to the SST variations a correction is added to the flux in the form:

$$Q_C = Q_{net}^{clim} + \frac{\partial Q_C}{\partial SST_{clim}} (SST_{model} - SST_{clim}) \tag{3.2.10}$$

where Q_C is the corrected heat flux, Q_{net}^{clim} is the net climatological heat flux, and depends on the climatological sea surface temperature, SST_{clim}. The factor $\frac{\partial Q_C}{\partial SST_{clim}}$ is the correction determining the influence of the SST following the linearization of the net heat flux bulk formula, (Barnier et al., 1995; Chassignet et al., 2000).

The terms in the net non-climatological heat flux consist of four components, and may be expressed as:

$$Q_C = Q_S + Q_{IR} + Q_H + Q_E \tag{3.2.11}$$

where, Q_S is the solar short waves heat flux at the surface of the ocean, Q_{IR} is the net long wave radiation, Q_H represents the latent heat flux and finally Q_E, is the sensible heat flux. Equation 3.2.11 can be expressed in terms of the climatological SST as:

$$\frac{\partial Q_C}{\partial SST_{clim}} = \frac{\partial Q_S}{\partial SST_{clim}} + \frac{\partial Q_{IR}}{\partial SST_{clim}} + \frac{\partial Q_H}{\partial SST_{clim}} + \frac{\partial Q_E}{\partial SST_{clim}} \tag{3.2.12}$$

Since the solar heat flux at the ocean surface does not depend on model SST, only three components contribute to the correction, (Barnier et al., 1995). Therefore, equation 3.2.12 is reduced to

$$\frac{\partial Q_C}{\partial SST_{clim}} = \frac{\partial Q_{IR}}{\partial SST_{clim}} + \frac{\partial Q_H}{\partial SST_{clim}} + \frac{\partial Q_E}{\partial SST_{clim}} \tag{3.2.13}$$

The individual terms of 3.2.13, are presented in 3.2.14, in which σ is the Stefan-Boltzmann constant ($5.6697 \times 10^{-8}\, W.m^{-2}.^oK^{-4}$), ρ_A is the air density, C_P is the specific heat of the atmosphere at the sea surface ($1004.8\, J.kg^{-1}.^oK^{-1}$), C_H is the sensible heat transfer coefficient ($0.66 \times 10^{-3}\, W.m^{-}2.^oC^{-1}$), C_E represents the latent heat transfer coefficient, L is the latent heat of vaporization ($2.5008 \times 10^6\, J.kg^{-1}$), U_A is the wind speed at the level of the anemometer and q_s is the specific humidity at the sea level.

Because of the poor quality of the evaporation and precipitation data, the terms of equation 3.2.13 are expressed as:

$$\begin{cases} a)\ \frac{\partial Q_{IR}}{\partial SST_{clim}} = -4 \times \sigma \times SST^3_{model} \\ b)\ \frac{\partial Q_H}{\partial SST_{clim}} = -\rho_A C_P C_H U_A \\ c)\ \frac{\partial Q_E}{\partial SST_{clim}} = -\rho_A C_E L U_A \times 2353 ln10 \times \frac{q_s(SST^{clim})}{(SST^{clim})^2} \end{cases} \tag{3.2.14}$$

The model salinity would be diverted from the climatologies if a due correction of the fresh water fluxes on account of the air-sea interaction was not carried out. The corresponding equation is given below, and relates with equation 3.2.9c):

$$K_S \frac{\partial S}{\partial z}|_{z=0} = \frac{(E_r - P_r) \times SSS_{clim}}{\rho_o} + \frac{1}{\tau}(SSS_{clim} - SSS_{model)} \tag{3.2.15}$$

In 3.2.15, ρ_o is the density of sea water, $(E_r - P_r)$ expresses the difference between evaporation and precipitation, whereas SSS_{clim} and SSS_{model} represent the climatological and model Sea Surface Salinity (SSS), respectively. The constant $\frac{1}{\tau}$ is the relaxation constant (corrector). It prevents the model from drifting to far away from the climatological value. This constant is usually kept equivalent to $\frac{\partial Q_H}{\partial SST_{clim}}$, and falls in the range of $[30 - 40\, days]$.

The observed fluxes used to force the model at the sea surface include wind stresses, heat and fresh water fluxes, from a monthly climatology at $\frac{1}{2}^o$ resolution, derived from the Comprehensive Ocean Atmosphere Data Set (COADS), (Da Silva et al., 1994).

ROMS uses a generalized terrain-following sigma coordinate (s), for the discretization of the momentum equation. This coordinate system is characterized by the transformation:

$$z = z(x, y, \sigma) \tag{3.2.16}$$

In 3.2.16 z represents the vertical cartesian coordinate, and σ refers to the non-stretched vertical coordinate, usually taken as a fractional part of the depth of the whole water column. It varies in the range $-1 \leq \sigma \leq 0$, according to the system given below:

$$\begin{cases} z = \zeta \ \text{ if } \ \sigma = 0 \\ z = -h(x, y) \ \text{ if } \ \sigma = -1 \end{cases} \tag{3.2.17}$$

This coordinate system is non-orthogonal. The horizontal derivative are treated using the chain rule $\frac{\partial}{\partial x}|_z = \frac{\partial}{\partial x}|_\sigma - \frac{\partial z}{\partial x}|_\sigma . \frac{\partial}{\partial z}$, (Shchepetkin and McWilliams, 2015). Equation 3.2.16, can be reduced to the classical case of non-stretched sigma coordinates of Phillips (1957), according to the following equation.

$$z(x, y, \sigma) = \sigma \times h(x, y) \tag{3.2.18}$$

Combining 3.2.18 with the nonlinear vertical transformation $S(\sigma)$, a more generalized coordinate system s is developed, as presented in 3.2.19. Our model follows the original S Coordinate Rutgers University Model (SCRUM) approach developed by Song and Haidvogel (1994) for both z and the stretching function. In this case 3.2.16 behaves like 3.2.18 in shallow waters, whereas in deep waters, it emulates 3.2.19.

$$z(x, y, \sigma) = S(\sigma) \times h(x, y) \tag{3.2.19}$$

In Appendix A, a complete expression for 3.2.19 is given, including the formulation of the $S(\sigma)$ and the stretching function $C(\sigma)$, which may vary according to the ROMS implementation, (https://www.myroms.org/wiki/Vertical_S-coordinate).

Despite the advantages of this coordinate system, it presents an inherent problem, which is due to the error that may appear in the calculations of the horizontal (x) component of the pressure gradient force, (Song, 1998; Shchepetkin and McWilliams, 2003):

$$-\frac{1}{\rho_o}\frac{\partial P}{\partial x}|_z = -\frac{1}{\rho_o}\frac{\partial P}{\partial x}|_s + \frac{1}{\rho_o}\frac{\partial P}{\partial z}\frac{\partial z}{\partial x}|_s \tag{3.2.20}$$

where P is the pressure, $\rho_o = const$ is the mean density of the water and z is the vertical coordinate. The subscript z in the left hand side derivative of 3.2.20, indicates that this term is determined at a constant geopotential surface $z = const$. Likewise the subscript s on the right hand side of equation 3.2.20, indicates that the derivatives are calculated along the transformed coordinate $s = const$. Close to topographic features, the terms on the second hand side, tend to grow to the same order of magnitude and cancel, in association with the non-alignment of the isosurfaces of the vertical coordinate with either the geopotential surfaces or isopycnals. The errors in the pressure gradient force calculation is due to the discretization of these terms, and also to the non-orthogonality of the coordinate system, and to the non-uniform stretching of the vertical coordinate (Shchepetkin and McWilliams, 2003). In ROMS, the algorithm used to minimize these errors was developed by Shchepetkin and McWilliams (2003). It is an extension of the second-order Jacobian scheme investigated by Song (1998). Such algorithm, consists of the reconstruction of both the density field and the physical z coordinate as continuous functions of the transformed coordinate, with subsequent analytical integrations to compute the pressure gradient force, (Shchepetkin and McWilliams, 2003). The advantages of this scheme consists of allowing high order accuracy while retaining important symmetries of its prototype developed by Song (1998). Furthermore, it contains a built-in monotonicity constraining algorithm, designed to prevent spurious oscillations of the polynomial interpolants, assuring numerical stability and robustness of the model, (Shchepetkin and McWilliams, 2003). This scheme also incorporates a method to treat the compressibility of the sea water in the equation of state (EOS), in such a way that it does not appear in the calculation of the gradient pressure force, (Shchepetkin and McWilliams, 2003).

In the horizontal, ROMS code is written in a curvilinear coordinate system. This representation is advantageous in real ocean applications, especially where topographic constraints (mainly in coastal regions) exert an influence over the flow, or when frontal disturbances and or boundary currents dominate the fluid flow. In these situations both a boundary-following coordinate and

a laterally variable grid resolution are needed. In ROMS this requirement is met by introducing a curvilinear coordinate system, (Hedstrȯm, 2009). In such a system, the coordinates relate to the horizontal coordinates (x, y) through the referential (ζ, η), where the relationship between the length of the arc and the differential distance is given by:

$$\begin{cases} (ds)_\xi = (\frac{1}{m})d\xi \\ (ds)_\eta = (\frac{1}{n})d\eta \end{cases} \tag{3.2.21}$$

where $m(\xi, \eta)$ and $n(\xi, \eta)$ are the scale factors that link the differential distances $(\triangle\xi, \triangle\eta)$ to the lengths of the physic arcs, $(\triangle S)_\xi$ and $(\triangle S)_\eta$ as illustrated in Figure 3.2.1. In appendix A.2, the whole set of ROMS momentum equations, is presented for the case of curvilinear coordinates.

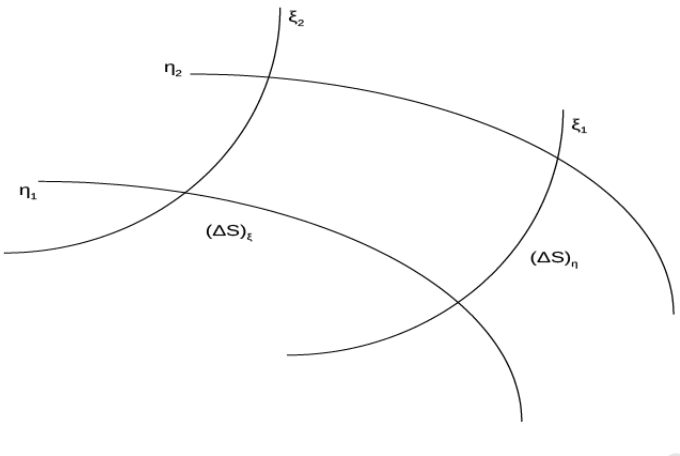

Figure 3.2.1: Representation of the Orthogonal-Curvilinear coordinate, Hedstrȯm (2009).

3.2.0.1 Open Boundary Conditions

The problems involving the exchange of information along the open boundaries in modelling of oceanic and meteorologic processes have been a subject of several studies (Roed and Cooper, 1986; Palma and Matano, 2000; Marchesiello et al., 2001). These problems entail the need to find good numerical schemes along the open boundaries to allow the inner model solutions to move out of the domain without causing reflection (under-specification). Likewise, the external ocean should bring information into the inner domain without problems (over-specification). The solution of these problems is a continuous area of investigation, and may vary according to the

models, (Marchesiello et al., 2001). The approach used in ROMS to deal with the open boundary conditions was suggested by Marchesiello et al. (2001). It uses an adaptive numerical algorithm method to combine both the active (outwards) and passive (inwards) characteristics of the fluxes through the open boundary. It checks whether the open boundary is passive or active. When the boundary is passive, the radiation condition is used. Otherwise, if the boundary is active, the solution is nudged (relaxed) towards external data (Marchesiello et al., 2001). To deal with the barotropic motion (tidal waves) in ROMS, the Flather (1976) condition, which is described by the equation below is implemented:

$$\overline{u_n} = \overline{u_n^{ext}} - \sqrt{\frac{g}{h}}\left(\eta - \eta^{ext}\right) \tag{3.2.22}$$

where $\overline{u_n}$ is the normal component of the barotropic velocity, $\overline{u_n^{ext}}$ represents the velocity of the external data, and h is the local water depth. This equation is used in ROMS to estimate the difference between the predictions and external data, allowing the difference to propagate outwards and improve model performance, (Marchesiello et al., 2001).

The Delagoa Bight regional simulations are initialized with gridded data at 1^o resolution, derived from *in situ* global monthly climatology of WOA, (Conkright et al., 2002). This data set is described in section 3.5, as the open boundary condition for the model. A depth of $1500\,m$, was defined to calculate the geostrophic velocities at the open boundaries. This choice is motivated by the fact that the motions below this level are generally slow.

3.3 Numerical aspects in ROMS

The horizontal discretizations of the dynamics equations in ROMS are performed using a curvilinear coordinate system described above, on a staggered Arakawa - C grid (Arakawa and Lamb, 1977). In ROMS, prognostic variables such as the tracers, and the SSH are discretized in ρ points (green), whereas the horizontal components of velocity are discretized in v points (blue) and u points (red), as in Figure 3.3.1.

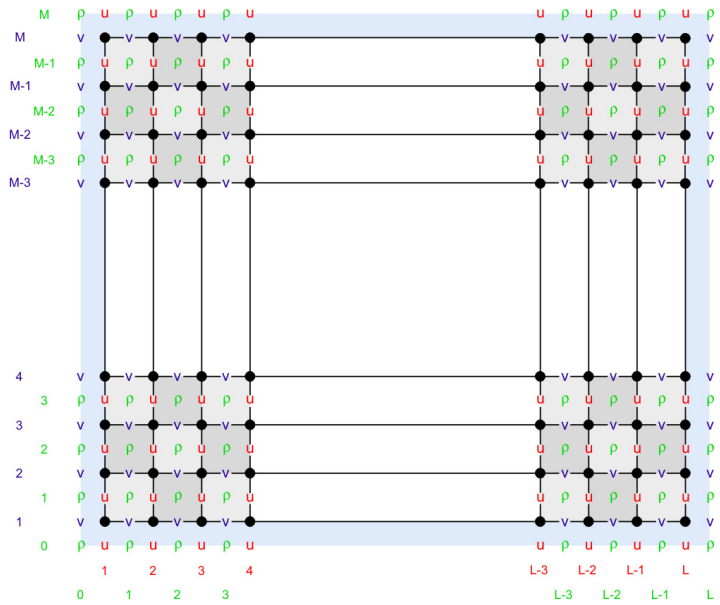

Figure 3.3.1: Diagram of the Arakawa - C grid used in the horizontal discretization of ROMS. The tracers, the SSH, the Coriolis force and the density are computed in ρ points (green at center of the grids), whereas the components of horizontal velocity are calculated at v points (blue) and u (red) points, respectively. Picture from, (https://www.myroms.org/wiki/).

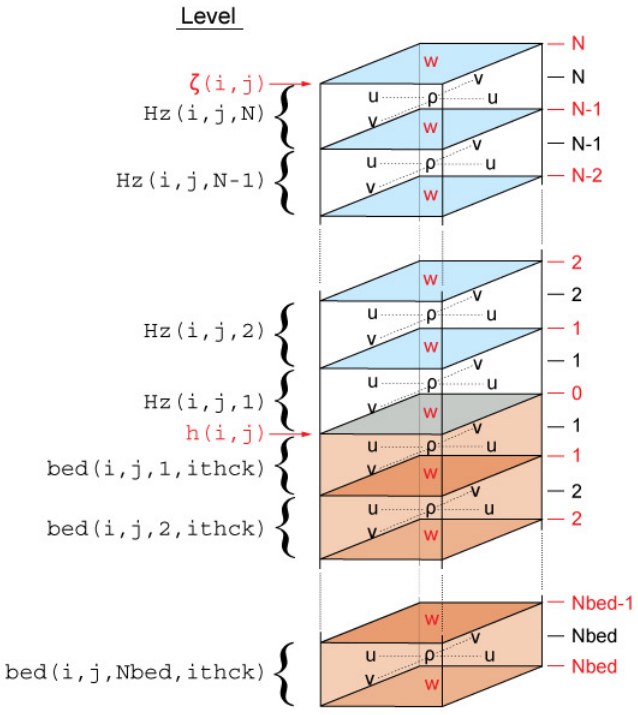

Figure 3.3.2: ROMS vertical discretization. H_z is the height of the water stencil, ζ is the SSH, w represents the vertical velocity and *bed* is the height of the sediment stencil. Picture from (https://www.myroms.org/wiki/)

The dynamics equations in ROMS, are solved in separate stages (mode splitting). The baroclinic mode (slower), is separated from the barotropic mode (faster). For each baroclinic time step, a certain number of barotropic time steps is performed in order to advance the free surface height, whilst the vertical momentum equation is integrated using the shorter time step. To optimize the performance and numerical accuracy, a specific algorithm, which guarantees conservation of mass and tracers simultaneously, has been developed, (Shchepetkin and McWilliams, 2015).

A temporal filter centered over the different stages of the baroclinic time step is used in the computation of the averages of the barotropic variables necessary for the coupling. The generalized predictor corrector algorithm allows a relatively larger time step with an increased internal stability, without sacrificing the precision (Shchepetkin and McWilliams, 2015). The precision of the mode coupling is improved by considering the variations of the density terms of the barotropic pressure gradient (Shchepetkin and McWilliams, 2015).

In ROMS the advection terms for tracers and momentum, were usually treated using a high order (third order upwind scheme), (Shchepetkin and McWilliams, 1998). This scheme is less diffusive and more accurate than the former second order centered schemes, that were associated with a Laplacian and bi-harmonic operators with spatial filters, to remove the noise introduced by numerical dispersion and turbulent cascades, (Shchepetkin and McWilliams, 1998). In this thesis the simulations are based on a modification of this scheme introduced by Marchesiello et al. (2009). Such a scheme has the ability to reduce the spurious diapicnal mixing problem arising in terrain following coordinate models.

In ROMS, the parametrization of the vertical turbulent mixing at sub-grid scales, is carried out by the non-local K Profile Parameterization (KPP) turbulent closure scheme (Large et al., 1994). It was introduced to handle the parametrization of the surface boundary layer and the interior ocean, in numerical ocean models. The depth of the ocean boundary layer in this model depends on the external forcing, the buoyancy and the vertical profile of velocity. It is estimated by equating the bulk Richardson number (a measure of relative importance of stratification to the destabilizing shear) to a critical value. Within the interior layer, the vertical mixing is regarded as a superposition of three distinct processes namely: the local Richardson number instability vertical shear, the internal wave breaking and double diffusion. Within the ocean boundary layer, the model is formulated in accordance with the Monin-Obukov similarity theory. At the base of the ocean boundary layer, the diffusivity and its gradient, are equated in order to match the interior ocean at that depth (h). It is relatively insensitive to the vertical resolution and performs very well in cases of coarse grid resolution. Furthermore, it has been demonstrated to simulate events including the convective boundary layer deepening, the diurnal cycle and storm forcing (Large et al., 1994).

3.4 Delagoa Bight model configuration

In the horizontal, the Delagoa Bight ROMS configuration was designed to cover the whole area in the south-western part of the Mozambique Channel within the latitudes $22.13 - 30.8^oS$ and longitudes $30.1 - 43^oE$, at $\frac{1}{10}^o$ resolution, which is equivalent to approximately $9.9km$. In the vertical, 50 sigma layers were defined. The vertical stretching control parameters, were set at $\theta_s = 5.5$ and $\theta_b = 0$, for the surface and bottom, respectively. The shallowest depth above which the highest resolution is required was set to $h_c = 50\,m$, and the reader is recommended to Hedstrȯm (2009) for the full description of these terms.

The smoothing of the topography is set at $r = 0.2$. This parameter is very important in the reduction of the errors associated to the Pressure Gradient Force (PGF), normally known to persist when realistic bathymetry is used (Beckmann and Haidvogel, 1993; Haidvogel et al., 2000). It is estimated by the equation $r = \frac{\triangle h}{2h}$ which relates the model resolution with the slope of the topography (Beckmann and Haidvogel, 1993). For the Delagoa Bight ROMS configurations, the internal domain was set to cover the whole Bight within the latitudes $24.09 - 27.7^oS$ and longitudes $32.43 - 36.43^oE$, with a resolution of $\frac{1}{30}^o$, equivalent to approximately $3.3\,km$. The whole set of the vertical parameters defined for the mother domain, remain the same. Sub-grid scale vertical mixing is parameterized using the KPP boundary layer formulation (Large et al., 1994), for both the surface and the bottom boundary layers. The model domain (black square) and child (blue square) used in this study are presented in Figure 3.4.1.

Although a myriad of modelling approaches have been implemented in the region (Biastoch and Krauss, 1999; Penven et al., 2006; Backeberg and Reason, 2010; Lutjeharms et al., 2012; Halo et al., 2014a), the majority of such studies were aimed at understanding the large scale processes and dynamics of the Agulhas Current. More recently however, some ROMS high resolution configurations, were used with the objective of resolving relatively smaller scale processes in specific locations of the Channel, (Halo et al., 2014b; Collins et al., 2014; Nehama and Reason, 2015). In the present study, a high resolution model is implemented in the Delagoa Bight, where the few studies performed so far, are based on satellite and in situ data highlighted the complexity of the circulation there (Lutjeharms and Jorge da Silva, 1988; Lamont et al., 2010). Therefore, a modelling approach is expected to shed more light into the local dynamics.

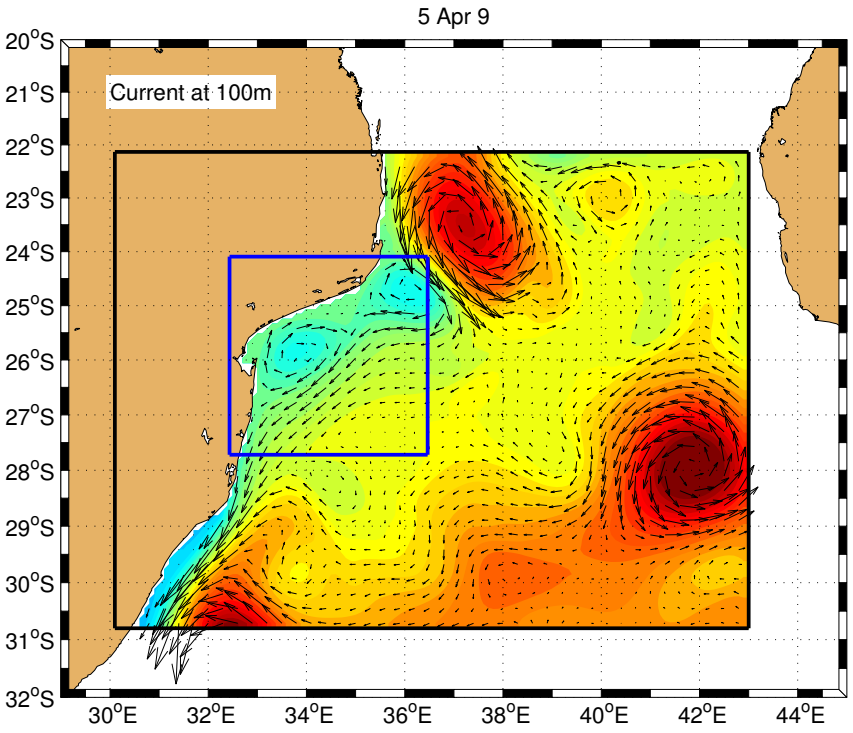

Figure 3.4.1: Grids of the Delagoa Bight mother domain (black) and child (blue). The currents at 100 m depth (black arrows) are overlaid on SSH.

The nesting capability of ROMS - Adaptive Mesh Refinement Package (AGRIF) (Blayo and Debreu, 1999; Debreu and Blayo, 2008), is used to define the child domain, which is intended to resolve the relatively small scale inshore processes (Penven, P. and Debreu, L. and Marchesiello P. and McWilliums, J.C., 2006). The objective is to better understand the small scale processes in the Delagoa Bight, including the mechanisms driving them. These simulations use a two-way nesting approach in which the highest resolution child grid is embedded in the coarser domain, with the flow of information occurring in a way that, the coarse grid provides the boundary conditions for the child grid, and the high resolution solutions is used to update the coarse grid solutions in zones of common domain (Debreu and Blayo, 2008). The advantage of such an approach consists of providing accurate boundary conditions for the incoming information along the boundaries of the child domain, whereas the update steps (feedback steps), enable the outgoing information to leave the finer grid, in a better way than in the case with the one-way approach, (Debreu and Blayo, 2008).

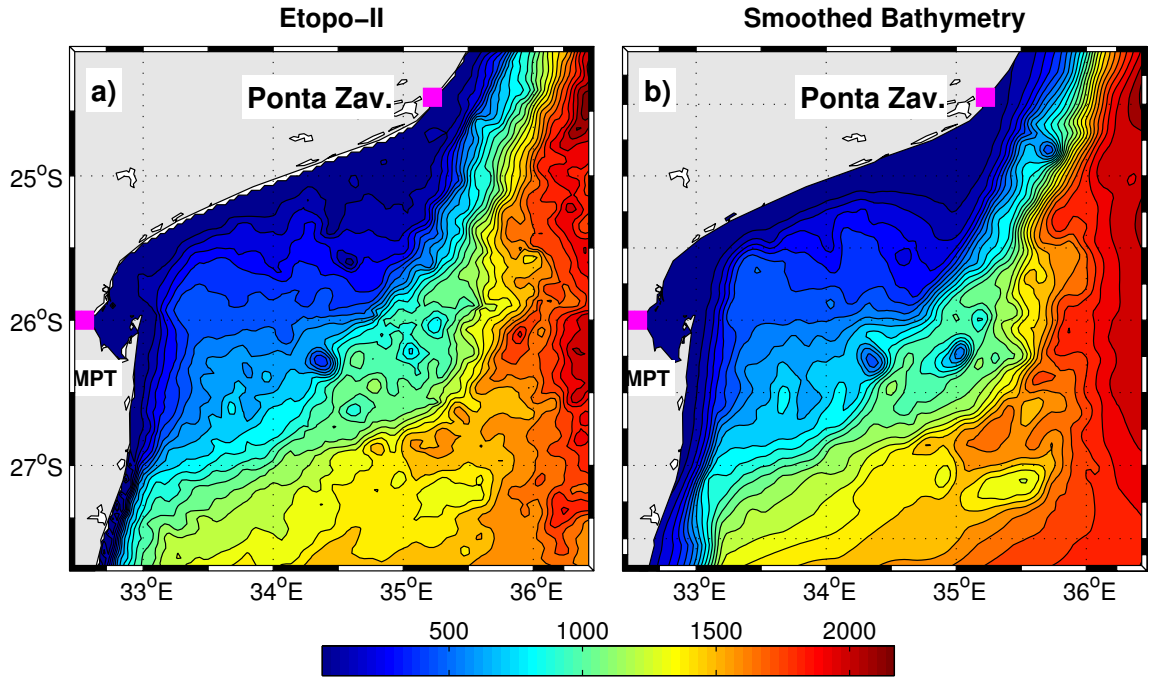

Figure 3.4.2: Comparison between original Etopo II topography (a), and the same but smoothed ($r = 0.2$) and be-linearly interpolated to the child grid. The isolines represents the isobaths.

The importance of the bottom topography in controlling the water flow in the ocean is unequivocal. Therefore, understanding the difference of the realistic bathymetry with the one used in the model is relevant in the interpretation of the model results. In Figure 3.4.2, the original topography (Etopo-II) in 3.4.2a (http://www.ngdc.noaa.gov/mgg/global/etopo2.html), is compared with the topography of the child domain 3.4.2b, after a linear interpolation and smoothing of $r = 0.2$. This rate of smoothing is needed to guarantee model robustness (Beckmann and Haidvogel, 1993; Haidvogel et al., 2000), and reduce the well known pressure gradient errors close to the coast, (Song, 1998; Shchepetkin and McWilliams, 2003). In both pictures the wide terrace at $34^oE, 26^oS$ is well represented. The sea mounds found between the meridians of $34 - 35^oE$ in Figure 3.4.2b, represent the Almirante Leite banks (Lutjeharms and Jorge da Silva, 1988; Martin, 1981).

3.4.1 Sensitivity experiments

To carry out this research, five climatological sensitivity experiments were performed. The first experiment is forced with WOA climatologies. It is referred to as DELAG-0. Its associated misrepresentation of the regional circulation, led us to the utilization of the $\frac{1}{5}^o$ resolution ROMS outputs of the South West Indian Ocean Model (SWIM) configuration of Halo et al. (2014a) to force the lateral boundary condition, for the Delagoa Bight configuration. SWIM has been created to investigate mesoscale activity in the region, and its full description is in section 3.5. Our model

was forced with high frequency SWIM data sets at the boundary to guarantee the entrance of the mesoscale features into the model domain.

The first experiment forced with SWIM is referred to as DELAG-I. Due to its associated better representation of the regional circulation, it was considered as the reference experiment along this work. The third experiment is the DELAG-II. It differs from DELAG-I, by the addition of ten tidal components, ($M2$ $S2$ $N2$ $K2$ $K1$ $O1$ $P1$ $Q1$ Mf Mm), estimated from a global tidal model (TPXO), (Egbert and Erofeeva, 2002). The fourth experiment consists of the addition of a child domain in the reference (DELAG-I), using a two way nesting approach, and is referred to as DELAG-III. The last experiment (DELAG-IV), is equivalent to the second (DELAG-II) in the sense that it includes tides, except that it contains a child domain. Like the fourth experiment (DELAG-III), it uses a two way nesting approach, (Debreu et al., 2012). The Delagoa Bight experiments used in this work, are illustrated in Table 3.1.

Table 3.1: Delagoa Bight ROMS sensitivity experiments.

EXPERIMENT	NAME	FORCING	2 WAY NESTING
Exp-0	DELAG-0	WOA	-
Exp-I	DELAG-I	WOA + SWIM	-
Exp-II	DELAG-II	WOA + SWIM + TIDES	-
Exp-III	DELAG-III	WOA + SWIM	YES
Exp-IV	DELAG-IV	WOA + SWIM + TIDES	YES

The Delagoa Bight configuration was run on CORE, a computer cluster based in the Department of Environmental and Geographical Sciences (EGS) at the University of Cape Town (UCT). The model was run for a period of 10 years, using 24 processors. Monthly files were created, containing 3 days averages of output data each.

The spin-up time is estimated from several variables as indicated in Figure 3.4.3. From both the surface kinetic energy and volume integrated kinetic energy, the reference experiment (DELAG-I) reaches an equilibrium state at the end of the first year of the simulations. The volume averaged temperature, the vertical velocity and the rest of the parameters, reach the quasi-equilibrium at same the period. However, the salinity needed one year more to reach an equilibrium state. Therefore, the analysis of the output is performed from a range of years 3-10, equivalent to 8 years, for all the sensitivity experiments.

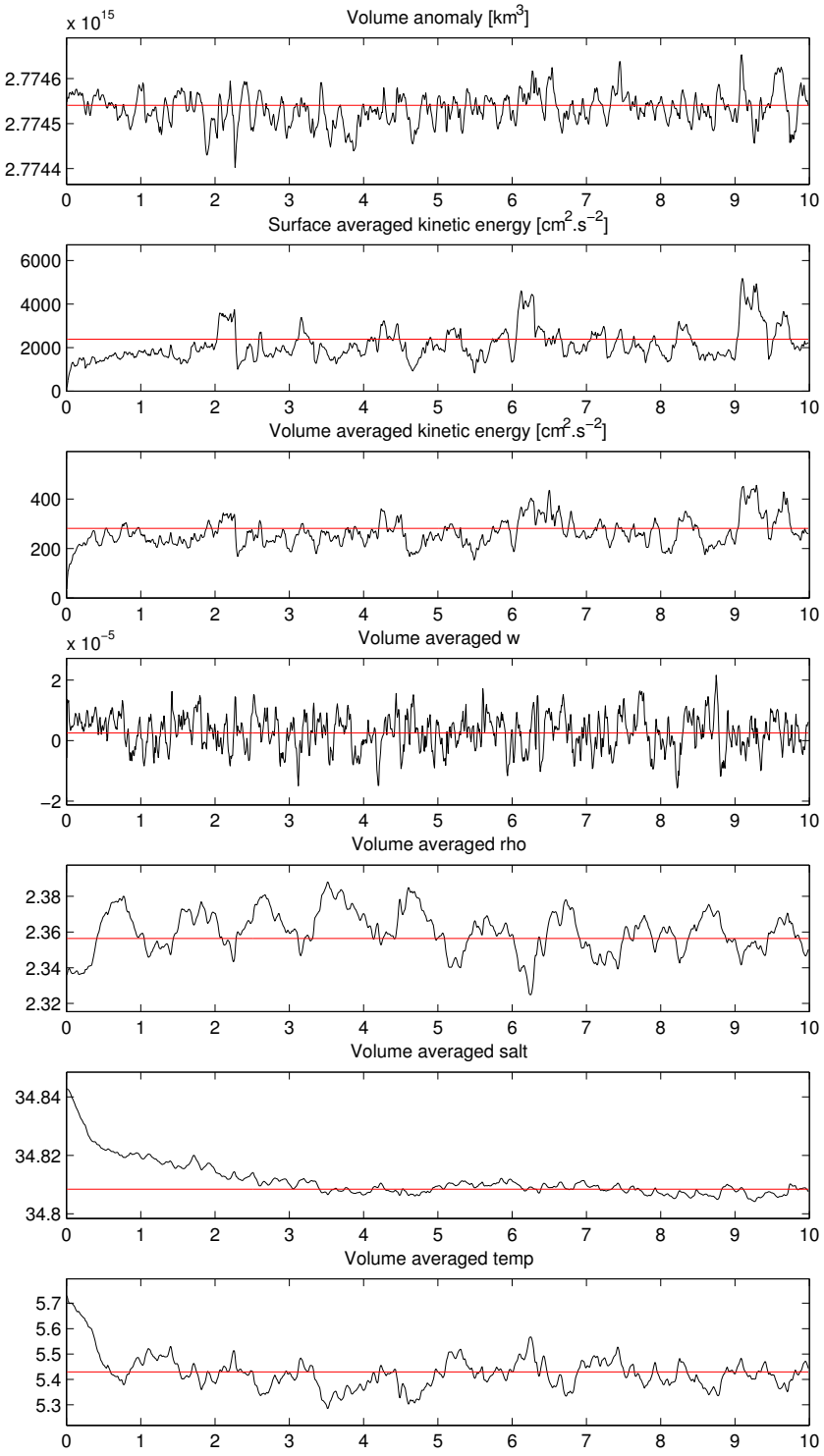

Figure 3.4.3: Integral volume properties showing that the Delagoa configurations with SWIM reaches equilibrium before the end of the second year

3.5 Description of the data sets

The model is forced by WOA data set, which consists of observed oceanic variables (Temperature, salinity, dissolved oxygen, etc) interpolated to standard depths (33 levels) distributed through the water column, from the surface down to 5500 m depth. It is a global product at 1° resolution,

distributed by the National Oceanic and Atmospheric Administration (NOAA). It exists at annual, seasonal and monthly for all the global oceans. Its full description is given by (Conkright et al., 2002).

The wind stresses utilized to force ROMS at the sea surface is from the National Aeronautics and Space Administration (NASA) Quick Scatterometer (QuikScat satellite) wind products, a quick recovery mission launched in June 1999 to fill the gap created by the unexpected loss of the NASA Scatterometer (NASA-S) after 9 months of operation. Basically, the sea wind Scatterometer consists of a scanning microwave radar which measures the electromagnetic back scattered radiation from wind roughened ocean surface at multiple antenna look angles, to infer the wind stresses magnitude and its direction (Chelton and Freilich, 2005). The used wind stress is a monthly climatology at $\frac{1}{2}^\circ$ resolution, created from Quickscat data, covering the period from 2000 to 2007, (Risien and Chelton, 2008) which is provided with $ROMS - TOOLS$, (Penven et al., 2008). In summer and spring the sea surface wind is generally southeasterly, whereas in winter and autumn it tends to weaken and shift to easterly, (Figure 3.5.1).

The heat and fresh water fluxes at the sea surface are $\frac{1}{2}^\circ$ gridded climatological fields from COADS05 (Da Silva et al., 1994), whereas the lateral boundaries are forced by the 1° gridded climatology from WOA05 (Conkright et al., 2002). The climatological boundary conditions for the prognostic variables used here is part of the ROMS - AGRIF , (Penven et al., 2008).

The Pathfinder SST data set, is a global oceanic product distributed by NOAA at 1° spatial resolution on a weekly basis, which is obtained using an Optimum Interpolation Method (Reynolds and Smith, 1994). This method allows the combination of situ data (ships and buoys), with satellite data derived from the Advanced Very High Resolution Radiometer (AVHRR) sensor of NOAA series.

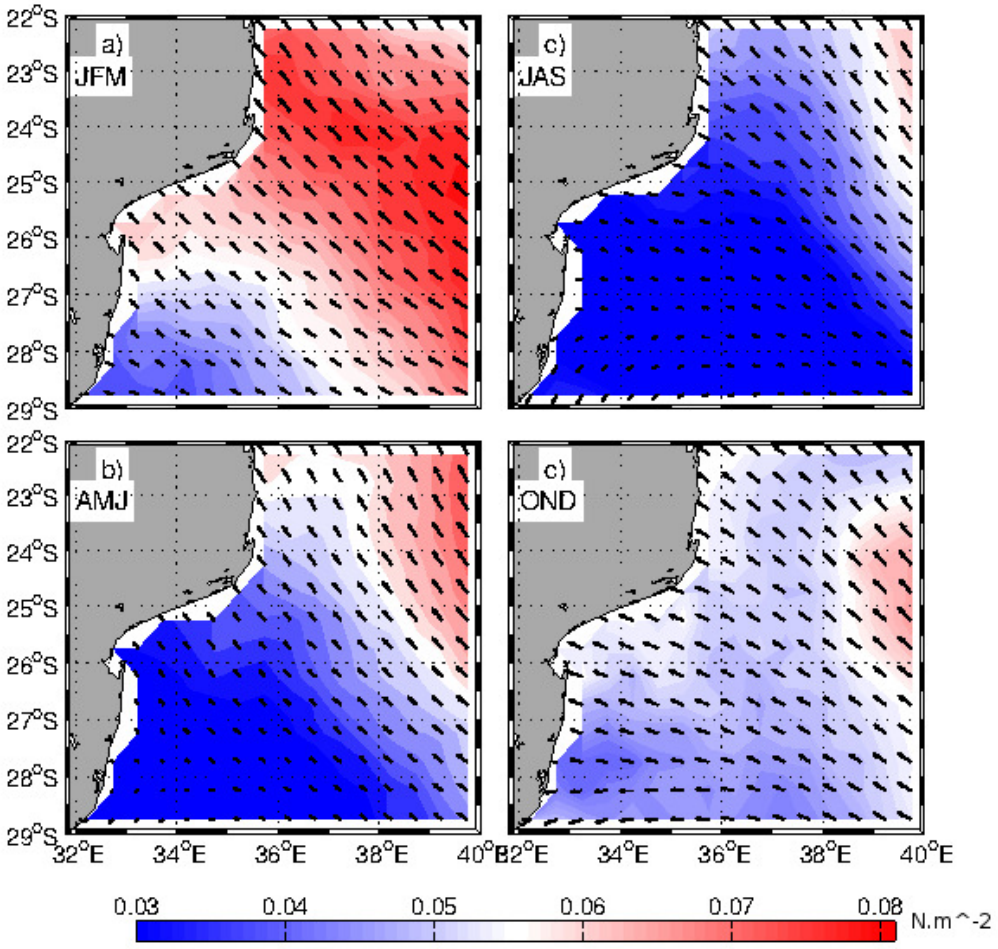

Figure 3.5.1: Climatological wind stresses determined from 2000-2007 Quick Scat sea surface winds, for summer a), autumn b), winter c) and spring d).

AVISO data set is made up of maps of Absolute Dynamic Topography (MADT) produced by Ssalto/Duacs, and distributed by AVISO, with support from the Center national d'études spatial at http://aviso.oceanobs.com/duacs/. The product is constructed by combining measured sea level anomalies from several altimeters (Topex/Poseidon, European remote sensing satellite (ERS), ESA Environmental Satellite (Envisat) and Joint Altimetry Satellite Oceanography Network (JASON)), with mean dynamic topography in a $\frac{1}{3}^o$ spacial resolution every 7 days. This product is compared with the model to evaluate its outputs.

The SWIM data set, is a ROMS simulation created by Halo et al. (2014a) to investigate the mesoscale activities in the source region of the Agulhas Current. Its domain covers the area defined by $0 - 77.7^oE$ and $2.8 - 47.5^oS$. The horizontal resolution is $1/5^o$, with 45 vertical σ - layers. The stretching parameters were set to $\theta_s = 5.5$ for the sea surface, and $\theta_b = 0$ at the bottom. The transition depth between the horizontal surface layers and the bottom σ levels, has been set to $hc = 5m$. These model data have been used as the lateral boundary condition, to improve the DELAG-0 experiment initialized by WOA data.

CSIRO Atlas of Regional Seas (CARS) is an atlas of seasonal oceanic water properties, composed of gridded fields of mean ocean properties and averaged seasonal cycles covering the period of modern ocean measurements. It is derived from historical ocean subsurface data based on research vessel, instrument profiles and autonomous profiling buoys, and it is found at http://www.marine.csiro.au/. The version used for the model evaluation here is the CARS2009, which covers the full global oceans in a $\frac{1}{2}^{\circ}$ grid.

3.6 Eddy detection and tracking schemes

An automated eddy detecting and tracking system is used to assess the DBLE dynamics. The algorithm of such system combines both geometric and dynamical properties to detect the eddies from SSH (Halo et al., 2014a,b). It uses a method in which an eddy consists of a closed contour of SSH and a negative okubo-weiss parameter (Okubo, 1970; Weiss, 1991) defined by equation: $W = S_n + S_s - \xi^2$. The first two terms in this equation represent the shear strain and the normal strain, respectively. The third term is the relative vorticity. These terms are given by $S_n = \frac{\partial u}{\partial x} - \frac{\partial v}{\partial y}$, $S_s = \frac{\partial v}{\partial x} + \frac{\partial u}{\partial y}$ and $\xi = \frac{\partial v}{\partial x} - \frac{\partial u}{\partial y}$, with u and v representing the meridional and zonal components of the flow.

The use of W for the detection of eddies from altimeter SSH, was initiated by Isern-Fontanet et al. (2003). Various problems were identified in association with such types of eddy detection systems. The first problem consists of the need to define a threshold value for W. A high (lower) value tends to induce a failure on the detection of smaller (larger) eddies, that may encompass multiple vortices, sometimes with opposite polarities. The second is linked to the fact that the determination of W from geostrophic velocities based on SSH, requires the numerical computation of the products of the second derivatives of the SSH field, causing high levels of noise in the result. The second detection criterion uses geometric properties, such that, the eddies are detected by the contours of SSH alone. This detection system was introduced by Chaigneau et al. (2008) and its goal was to find a threshold-free identification of the SSH field without further computation, or smoothing of the SSH field. Various authors have stated that this method is relatively advantageous by comparison with the previous method (Chaigneau et al., 2008; Chelton et al., 2011; Souza et al., 2011). Nevertheless, Kurian et al. (2011) argue that a third criterion based on the eddy shapes is still required.

In this study, both detection systems are merged into one algorithm, which was demonstrated to be better than using a single method alone (Halo et al., 2014a). Furthermore, two passes of the Hanning filter are applied on the Okubo-Weiss field to minimize the grid-scale noise, common in Okubo-Weiss based methods Halo et al. (2014a).

To avoid ambiguities in the identification of the eddies, the system is adopted with a minimum of tunable parameters; the intervals between the SSH closed contours are set to $2\,cm$, while the maximum closed loop of SSH is set to $600\,km$ (Halo et al., 2014b). The threshold value for the Okubo-Weiss parameter is set to zero. The tracking period is also tunable, and for these analysis a minimum period of $6\,days$ was chosen. This choice is due to the fact that the eddy detecting and tracking system uses three days average model outputs to determine the positions of the features. In fact, to track the eddies in time the system uses the method proposed by Penven et al. (2005), in which an eddy detected at a given time, is the same as the eddy detected in the subsequent time-step if a generalized distance in a non-dimensional property space is a minimum, as expressed by equation 3.6.1 below:

$$X_{e1,e2} = \sqrt{\frac{\Delta X}{X_0} + \frac{\Delta R}{R_0} + \frac{\Delta \zeta}{\xi_0}} \tag{3.6.1}$$

Here, ΔX is the spacial distance between the centres of the eddies e_1 and e_2. ΔR and $\triangle \xi$ are the changes in diameter and vorticity, respectively. X_0 is the characteristic length scale $25\,km$, R_0 is the characteristic radius, and ξ_0 the characteristic vorticity $10^{-5}S^{-1}$. To preserve the polarity of the eddies, $X_{e1,e2}$ is considered infinite if there is a change of sign in vorticity (such that a cyclone do not become an anticyclone and vice-versa). The detection method described in this section is coded in matlab and can be found at http://www.simocean.org.za/tooleddy.php. The whole system consists of MATLAB scripts for detection, selection, tracking and animation of eddies.

3.7 Power Spectral Density

The possibility of representing any function $f(t)$ in terms of linear combinations of trigonometric functions is usual in mathematics. Introduced by Fourier, it has been thoroughly studied and it finds application in analysis of temporal series and electronic signals. Its foundation is based on the idea that any function can be expressed using trigonometric series according to the equation below:

$$f(t) = \sum_{k=1}^{\infty} a_k cos(kx) + b_k sin(kx) \tag{3.7.1}$$

Although the Fourier equation 3.7.1 was conceived to handle continuous functions, nowadays an extension of the theory is used to handle discreet time series. In this case, $f(t)$ is given by equation:

$$f(t) = f_d(t_d) = \sum_{k=-\infty}^{\infty} u(t_d - kt_s) f(t_d) \tag{3.7.2}$$

In equation 3.7.2, t_d represents the discreet time, t_s is the sampling time and k is an integer assuming positive and negative values. The purpose of the discreet Fourier function is to facilitate the representation of the signal in form of exponential functions, (Proakis and Dimitri, 1996).

Although many options exist for the investigating of time series, in this case the Power Spectral Density (PSD) is chosen. This statistic is useful in the representation of energy variations as a function of frequency. Is is able to show the region of the the spectrum in which the frequency variations are stronger by comparison with its environment, (Stoica and Randolf, 1997; Proakis and Dimitri, 1996).

The problem of the nonexistence of a Fourier transform when a random signal doesn't have finite energy turns it difficult to determine the PSD. But because such signal possesses an average (mean) power, it is possible to determine the mean PSD, of the signal (Stoica and Randolf, 1997; Proakis and Dimitri, 1996). Therefore, if a given signal $y(n)$ with $n \in Z$, has an expected value $E(y(n)) = 0$, the covariance function of the this signal is defined as:

$$r(k) = E\{y(n)y^*(n-k)\} \tag{3.7.3}$$

where $y^*$is the complex conjugate of y. In this way, the power spectral density of a random signal is defined as

$$\phi(\omega) = \sum_{k=-\infty}^{\infty} r(k) e^{-\omega k} \tag{3.7.4}$$

whose inverse operation is given by:

$$r(k) = \frac{1}{2\pi} \int_{-\pi}^{\pi} \phi(\omega) e^{i\omega k} d\omega \tag{3.7.5}$$

Two important concepts are used with the PSD, namely the band width, which is the range of frequencies encompassing the minimum and maximum for a given signal, whereas the essential band is defined as the modulus of the difference between the extreme values of the frequency.
In this study the PSD, is used to assess the variability of the transports of both the branches of the lee eddy, including the processes that affect the circulation in the Bight, such as the passing anticyclones. A MATLAB routine is used to compute PSD and the frequency from the discreet time of our sample, and finally plot the frequency as a function of the power spectral density.

3.8 Summary

In this chapter the ROMS ocean model was presented, including the motivation behind its election for this study. That is followed by the presentation of the model numeric formulation and description of the boundary and initial conditions utilized. All the individual data sets necessary for this step were described, with emphasis to their characteristics and sources. A description of the performed simulations and their characteristics is included in this chapter. The chapter is finalized by the presentation of the tools used for the model output treatment. The first is the eddy detecting and tracking system, whereas the last is the power spectral density analysis.

Chapter 4

The Delagoa Bight Circulation: Mean State and Seasonal Cycle

4.1 Introduction

Previous studies in the Delagoa Bight indicated a predominance of a cyclonic semi-permanent lee eddy, generally occupying the center of the Bight (Lutjeharms and Jorge da Silva, 1988). Its generation was linked with the prevalence of a southward boundary current, formerly known as the Mozambique Current (Lutjeharms and Jorge da Silva, 1988). Early observational studies in the Channel, mainly during the eighties, have put into question the prevalence of a boundary current in the Mozambique Channel (Sætre, 1985; Sætre and Jorge da Silva, 1984). The circulation in the Channel was considered to be complex and seasonally dependent (Sætre and Jorge da Silva, 1984).

Based on model simulations, Biastoch and Krauss (1999) demonstrated that the Mozambique Channel was dominated by anticyclonic eddies moving southward. Several authors associated their formation with barotropic instabilities in the Northeast Madagascar Current (Backeberg and Reason, 2010; Harlander et al., 2009). Analysis of in situ observations by de Ruijter et al. (2002) confirmed these results, establishing in this way the modern perspective of the local circulation. According to that view, the Mozambique Channel is dominated by a train of bottom reaching large anticyclonic eddies that propagate southward along the shelf of Mozambique (de Ruijter et al., 2002; Biastoch and Krauss, 1999). Although the way they interact with the shelf was recently investigated by Roberts et al. (2014), their impact in Delagoa Bight is not well known.

The circulation in the Bight is complex and quite dynamic (Lamont et al., 2010; Lutjeharms and Jorge da Silva, 1988). Indeed, Lamont et al. (2010) associated the presence and absence of the DBLE with the passage of the anticyclones. Nevertheless, the proper dynamics involved in its behaviour seems to require further research.

The circulation in the Mozambique Channel is like wise complex. It is believed that the available techniques of observation are unlikely to have highlighted completely all the relevant aspects of the local circulation (Hancke et al., 2014). Nevertheless, it is thought that the mesoscale features dominate the circulation over the whole Channel (Halo et al., 2014a). The large Mozambique rings propagating southward along the shelf of Mozambique are generally generated in the northern sector, (Harlander et al., 2009; Backeberg and Reason, 2010; Halo et al., 2014a) whereas cyclonic eddies are typically found all over the area (Halo et al., 2014a). Ternon et al. (2014) recognized that anticyclonic anomalies are also common in the eastern sector of the Channel. Based on analyses of drifter trajectories, Hancke et al. (2014) noted that there is a considerable connectivity between the various sectors of the Channel through the interstitial zones of the mesoscale features and during their propagation. According to Hancke et al. (2014), drifters launched in the southern tip of Madagascar showed the predominance of northwestwards transport toward the African coast. This transport reaches the Sofala Bank and Delagoa Bight region (Hancke et al., 2014). The SSH variability in this region shows a clear link between the southern tip of Madagascar and Delagoa Bight (de Ruijter et al., 2005; Quartly and Srokosz, 2004). This chapter presents the local mean oceanic circulation, its seasonal variability, and finally the link between the east and the center of the Bight, through analyses of tracked mesoscale features and analysis of water masses.

The chapter is organized in the following manner: section 4.2 addresses the mean oceanic circulation based on the mean SSH, eddy kinetic energy, and mean thermocline structure and water masses. The seasonal variability is assessed in section 4.3, by exploring model outputs. Time series of SSH and tracers taken in the center of the Bight, are also analyzed to assess the relationship of their variability with the lee eddy presences and absences. In section 4.5 the effect of forcing the model with tides on the local circulation is addressed. In the last section a discussion and the synthesis of the chapter is provided.

4.2 Mean oceanic circulation

The mean oceanic circulation in the Delagoa Bight region and surrounding is inferred using the means, of several parameters. In Figure 4.2.1, the mean dynamic topography for two models namely DELAG-0 and DELAG-I, and satellite observations (AVISO) are used to track the main geostrophic currents in the region. For the model forced with WOA (DELAG-0) (Figure 4.2.1a), the current is characterized by a closed cyclonic loop at the northern side of the domain. Along the $24^o - 29^o S$ band, the flow is from the east, and corresponds to the continuation of the southern extension of the Southeast Madagascar Current. As it reaches the shelf along the African slope it bifurcates. One branch flows southward and joins the Agulhas Current. The northwards branch flows northwards along the shelf of Mozambique, to feed the cyclonic closed loop north of this domain. This loop is not apparent in the satellite MDT, as discussed below.

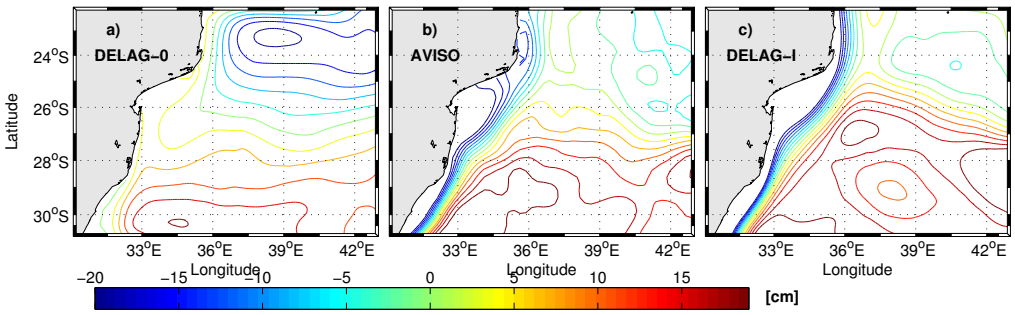

Figure 4.2.1: Mean geostrophic currents derived from MDT for (a) DELAG-0, (b) AVISO and c) DELAG-I. The contours are 3 cm each in all pictures.The positive values (red) show the pathways of the anticyclones.

In AVISO observations (Figure 4.2.1b), the MDT shows the extension of the Southeast Madagascar Current flowing westwards along the $26^o - 28^o S$ band. On reaching the shelf of the African continent, it merges with the southward flowing current. After the merger, the flow is toward the northern Agulhas Current, (Lutjeharms, 2006a). Overall, the southward flowing current reveals the consistency of a boundary current in this region. In Figure 4.2.1c), the local circulation according to the configuration forced with SWIM (DELAG-I) is illustrated. In this case, the extension of the Southeast Madagascar Current flows northwestwards toward the north-eastern part of the Delagoa Bight. Here, it merges with the southward flowing current, which is found on the shelf of Mozambique main land. It is more uniform and organized by comparison with AVISO observations, that show slight meandering in association with the local mesoscale activity. North of this current (north of the domain), a cyclonic loop dominates the circulation, whereas southward an anticyclonic loop is prominent. Both model and satellite representations are relatively closer to

the mean local circulation as suggested in several studies (de Ruijter et al., 2005; Quartly et al., 2006).

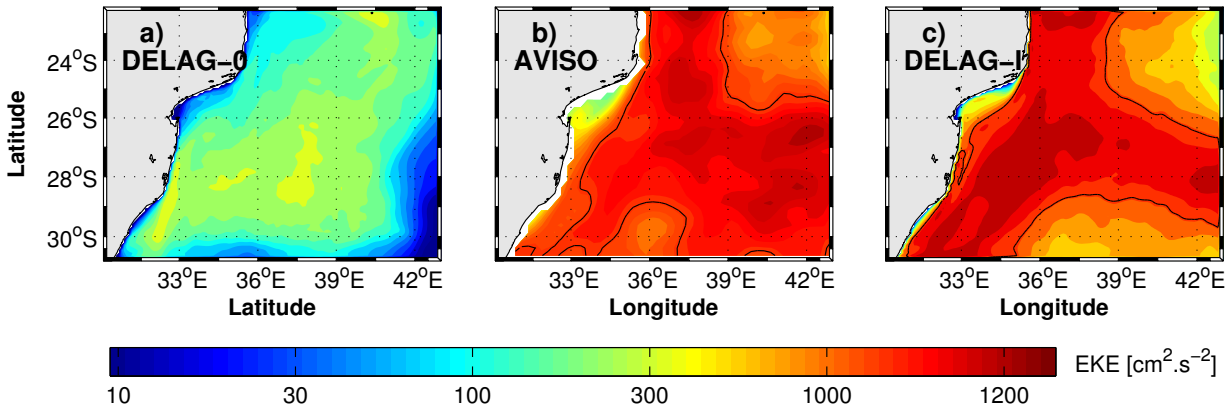

Figure 4.2.2: Mean EKE derived from the model DELAG-0 in a), observations (AVISO) in b) and DELAG-I in c), for 8 years model outputs and an equivalent extension for the observations. The black line represents the 500 $cm^2.s^{-2}$ contour.

The impact of the eddies in the region is evaluated using the mean EKE (Figure 4.2.2), which is determined using the equation given in appendix A.3. This parameter is commonly used to investigate the eddy activity in the ocean. The first experiment (DELAG-0) was not able to simulate the usual pathways of the mesoscale features in the region, (Figure 4.2.2a). Instead, it shows weak eddy activity in the center of the domain. The EKE values in this simulation are very low by comparison with those in AVISO observations and model. The highest values of approximately $300\,cm^2/s^2$ are concentrated in the center of the domain. In (Figure 4.2.2b-c), the $500\,cm^2/s^2$ contour encompasses the known pathways of the anticyclonic eddies, which are characterized by very high activity of mesoscale features, with EKE above $1300\,cm^2/s^2$. The northeastern and southeastern outer areas of the zone dominated by the transiting mesoscale features, portray relatively lower levels of eddy activity, characterized by EKEs below $500\,cm^2/s^2$, in both observations and model (Figure 4.2.2b-c). Along the slope, the EKE is below $500\,cm^2/s^2$ but it shows more consistency in AVISO than in the model, where the $500\,cm^2/s^2$ contour is much locked to the coast. The most conspicuous difference between satellite observation and DELAG-I (Figure 4.2.2b-c), consists in a northwestwards tilting of the pathway of the mesoscale features in the model, and westwards pathways in the latter. Accordingly, the merger in AVISO is found slightly to the south off Delagoa Bight.

The mean geostrophic velocity was also estimated applying the equations in appendix A.3, on the mean SSH for both DELAG-I and AVISO, (Figure 4.2.3). In AVISO, (Figure 4.2.3a) the southward flowing current is found along the $500 - 1000\,m$ isobaths. It is locked to the slope,

except in the center of the Bight where the shelf if wider. Between $24^o - 26.5^oS$, it widens possibly in response to the merger of currents from the north with those from the southeast of Madagascar. In Delagoa Bight, the strong northwards flowing coastal counter-current forms the inshore branch of the Delagoa Bight cyclonic eddy. In the model (Figure 4.2.3b), the current is characterized by a region of intense geostrophic velocities, tilted toward the northwest of the Bight where it merges with the southward flowing boundary current. In the observations (AVISO), this current is westwards and flows parallel to the zonal band formed by the $26^o - 28^oS$ latitudinal strip. It merges with the southward flowing boundary current off Delagoa Bight. It is dominated by several meanders, suggestive of strong mesoscale activity inside this strip.

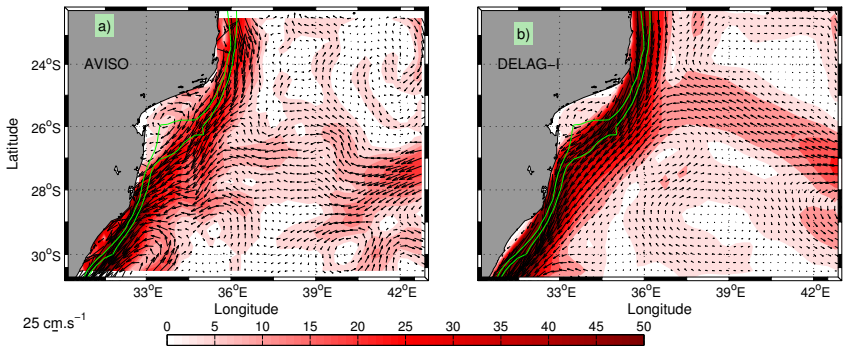

Figure 4.2.3: Mean geostrophic velocities overlaid on modulus of velocity (black arrows) for Satellite a) and model (DELAG-I) in b). The green contours represent the 500 and 1000 m isobaths.

The strong southward flowing mean geostrophic current in Figure 4.2.3, seems to contradict the concept of non-existence of a boundary current discussed in the literature (Ridderinkhof and de Ruijter, 2003; Harlander et al., 2009), at least in this region. Indeed, the recent paper of Lutjeharms et al. (2012) refers to the possibility of existence of a boundary current. Therefore, in Figure 4.2.4 such current is illustrated in individual snapshots of surface geostrophic currents, for both model and satellite (Figure 4.2.4a-b), for the model date May year 7 ($3May7$) and satellite 09 June 2007, respectively. In the model, (Figure 4.2.4a) this current follows the slope with its western edge allowing instabilities to fill the whole Bight, indicative of DBLE absence portrayed by (Lamont et al., 2010). The eastern part of the domain coincides with a huge anticyclonic feature. In AVISO (Figure 4.2.4b) the current is well organized and cohabits with small cyclonic cores at its western edge, and anticyclonic features to the east. The likelihood of occurrence of cores in the Bight is discussed in the next chapter.

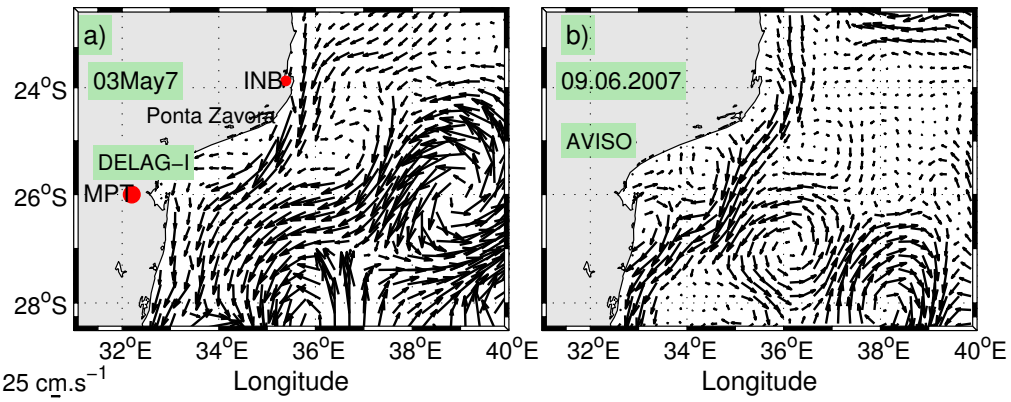

Figure 4.2.4: Model (DELAG-I) a) and AVISO b) individual snapshots illustrating the surface geostrophic currents, and the consistency of a boundary current in this region.

Analysis of 8 years of model 3-days averages allowed one to infer the consistency of such organized southward flowing current similar to the one historically known as the continuous Mozambique Current (Figure 4.2.5). Behaving like a boundary current, it is found aligned with the $500-1000\,m$ isobaths, in more than 94% of the model times. Its short lived intermittency is caused by the activity of mesoscale features in a region characterized by mutual interaction of eddies and of these eddies with the bathymetry. These features are capable to modify the normal course of the current, by causing quick meanders and short lived shifts from its usual position (picture not shown).

In Figure (4.2.5a), times series of the along coast velocities taken from six locations along the $100\,m$ isobath (Figure 4.2.5b) are shown. Overall, their means vary from $42 \pm 26\,cm.s^{-1}$ south of the Delagoa Bight (green triangle) in Figure (4.2.5b) to $76.7 \pm 32.9\,cm.s^{-1}$ at 30^oS (pink triangle in Figure 4.2.5b). The Probability Density Function (PDF) in Figure (4.2.5c) shows that from north to south, the along isobath velocities are southward, except in 2.0, 2.9, 5.8, 2.9, 0.8 and 2.6% of the total length of the simulation, respectively. This northwards flow is associated with the northwards branches of transient cyclonic features (pulses) intrinsic of this region (Cossa et al., 2016). There is scarcity of observations in this region for comparison. Nevertheless, the modelled value of $62.5 \pm 28.3\,cm.s^{-1}$ for the southward flowing current, black triangle in Figure 4.2.5b), lies in the same order of magnitude with the $50-75\,cm.s^{-1}$ measured using an Acoustic Doppler Current Profilers (ADCP) along the shelf edge between 9-Mile Reef and Leven Canyon around $(27.4-28^oS)$ (Roberts et al., 2006).

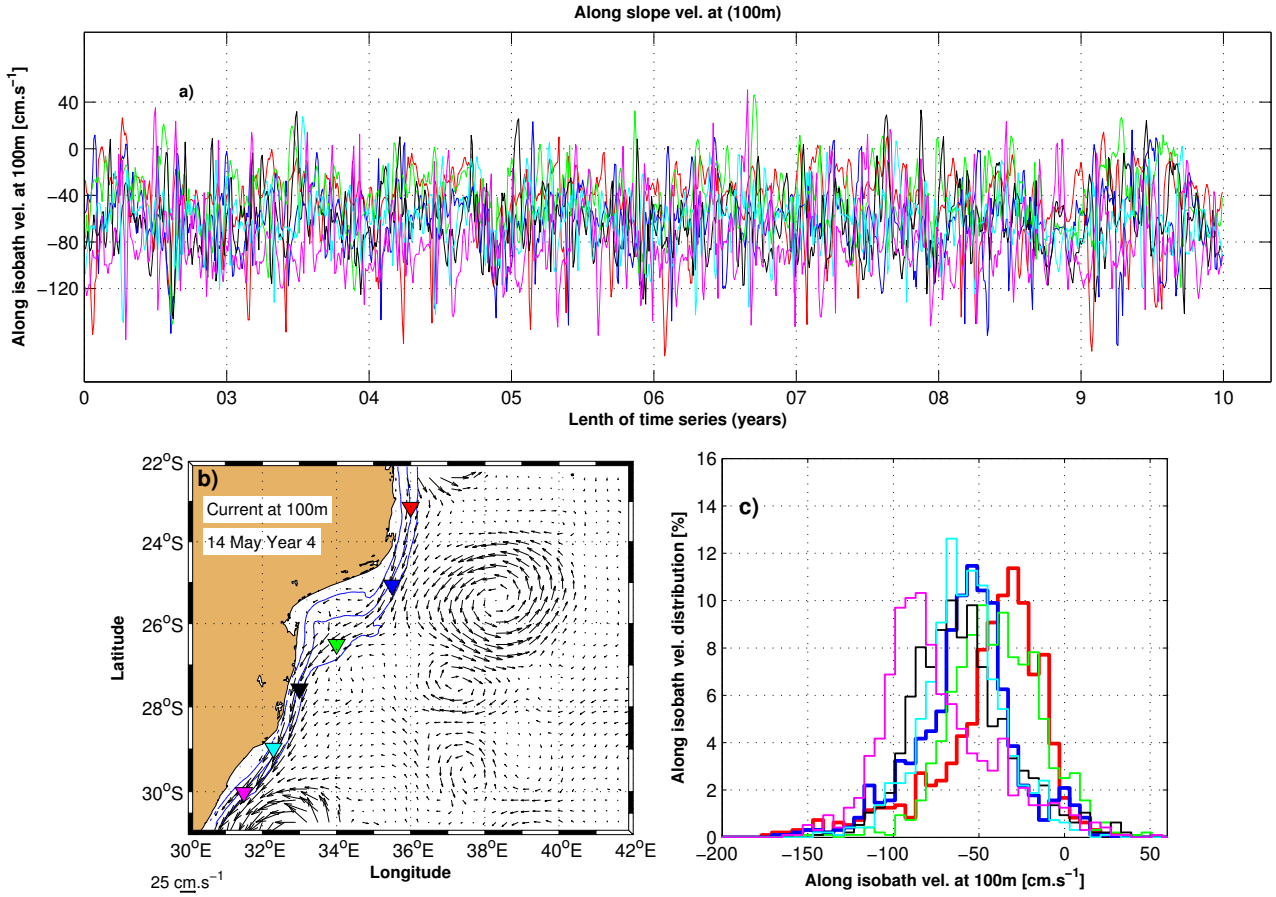

Figure 4.2.5: Times series of along $100\,m$ isobath velocities a), estimated in the positions indicated by triangles in the map b), for the reference experiment (DELAG-I). In c) are shown the PDFs, with the colours corresponding to the positions of the velocity estimations given in b).

In Figure 4.2.6, is presented the mean SST from model and observations. In the model (DELAG-0) (Figure 4.2.6a), it consists of two distinct regions, one cooler south of 26^oS and the other warmer with SST above 24^oC toward the north. There is no signature of the southward flowing boundary current represented. In the model (DELAG-I) (Figure 4.2.6b) this feature is reproduced (Figure 4.2.6b), but with relatively warmer temperatures. In the satellite observations (Pathfinder) (Figure 4.2.6c), the signature of the boundary current is also conspicuous. It links into the northern Agulhas Current along the south-westernmost part of the Mozambique Channel. This seems to be indicative of its relevance as a continuous flow in this region of the Channel.

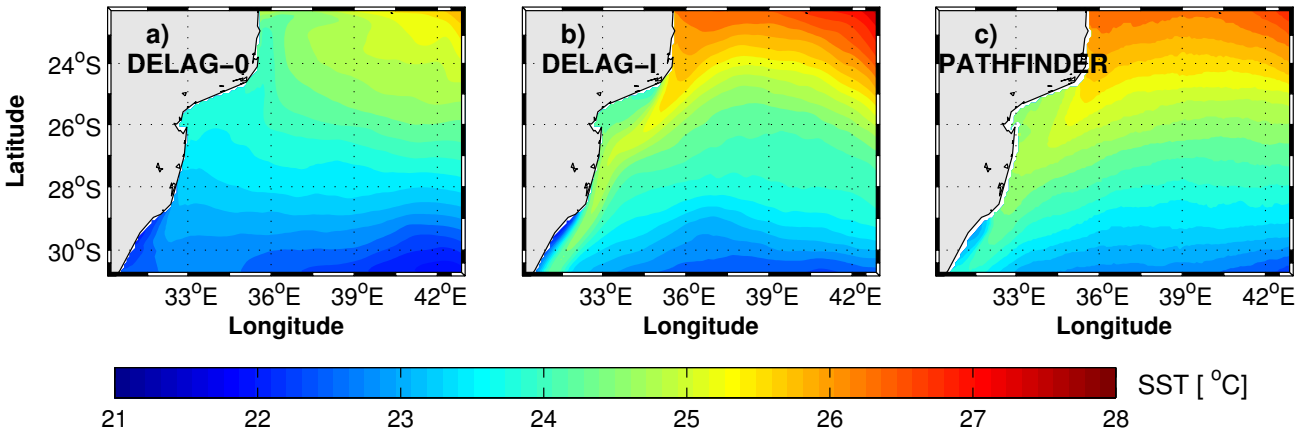

Figure 4.2.6: Sea Surface Temperature (SST) in [°C] from the model (DELAG-0) in a), the experiment forced with SWIM (DELAG-I) at boundaries in b) and satellite (Pathfinder) in c). The red shows areas of high SST whereas blue represents the lowest values.

In Figure 4.2.7, are shown the differences between the model DELAG-0 and Pathfinder. This difference was named (DIFF-0) and is represented in Figure (4.2.7a). The second difference (DIFF-1), calculated from the reference experiment DELAG-I and Pathfinder, is given in Figure (4.2.7b). The difference (DIFF-0) shows that the model DELAG-0 was not capable to reproduce the strong signature of the boundary current that characterizes the satellite climatology in this region, (Figure 4.2.7a). Furthermore, in most of the domain, the model is characterized by a positive bias. By contrast, the difference (DIFF-1) in Figure (4.2.7b), shows that the modelled boundary current is stronger than the one of Pathfinder. Nevertheless, in the middle of the region the model DELAG-I, has shown a negative bias. Despite this, the model DELAG-I seems to represent approximately well the characteristics shown by the satellite observations as portrayed above.

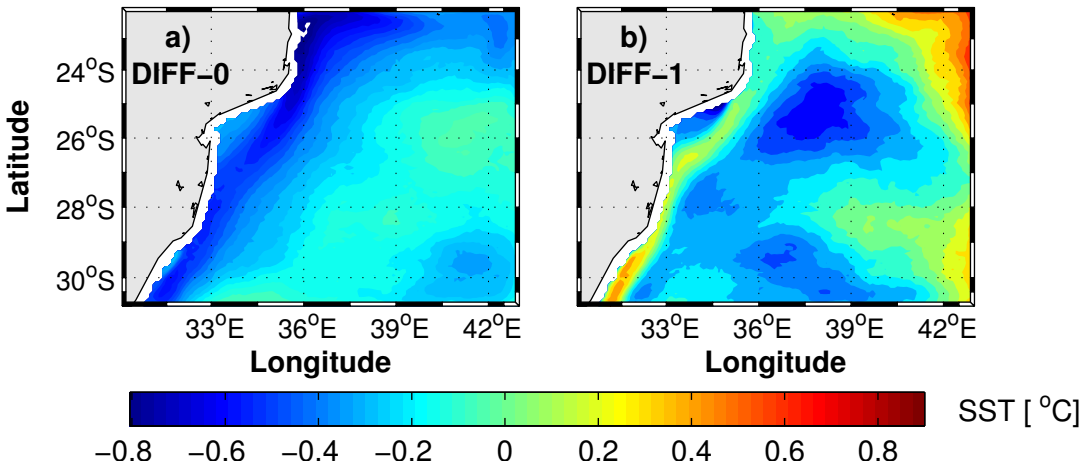

Figure 4.2.7: SST differences between model DELAG-0 and Pathfinder (DIFF-0) in a), and between (DELAG-I) and Pathfinder in b). In both blue indicates where differences are negative while red shows positive bias.

Cross sections of SST from both experiments (DEALAG-0 and DELAG-I) and satellite (Pathfinder)

were plotted along the main Delagoa Bight section at 26^oS, Figure 4.2.8. The SST values from the WOA forced experiment (DELAG-0), are too cool and show an under-estimation of the SST over the whole section, from the coast toward offshore, except around 40^oE where values greater than those from DELAG-I are found. Both DELAG-I and Pathfinder satellite observations contain the signature of the boundary current, which is characterized by a peak of SST at around 34.8^oE, in agreement with the transport of warmer water masses from the equator, by the southwards current in this location. The core of the boundary current lies within $40 - 50\,km$ offshore of the center of the classic lee eddy investigated by (Lutjeharms and Jorge da Silva, 1988). As already seen in Figure 4.2.6, the model DELAG-I under-estimates SST in the middle of the domain. Nevertheless, because it shows reasonable performance in comparison with the observations it will be considered as the main experiment henceforth, while DELAG-0 is rejected for further analyses.

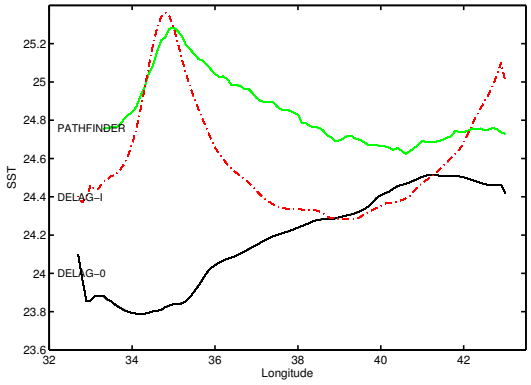

Figure 4.2.8: Transect over the mean SST from Satellite (full green line) and model configurations DELAG-0 (in black) and DELAG-I (in red), respectively.

Once (DELAG-I) had been validated as the reference experiment, the analyses were continued through the estimation of the mean thermocline structure and the mean water masses in the region, using its outputs and WOA observations (Figure 4.2.9). The map in Figure (4.2.9a) shows the mean current at $100\,m$, overlaid on the mean SSH for this experiment. The black line represents the usual Delagoa Bight section. The edge of the southward flow, sweeps the usual location of the DBLE at $26^oS, 34^oE$, (Lutjeharms and Jorge da Silva, 1988; Lamont et al., 2010). Near the coast, the coastal counter-current is very weak in this mean, by comparison with its realistic representation in the composite maps analyzed by (Cossa et al., 2016). The southward current gets strengthened by the westwards flowing extension of the Southeast Madagascar Current as both merge off Delagoa, consistent with the results based on the SSH variability presented in several studies (de Ruijter et al., 2005; Quartly et al., 2006).

The main water masses along the Delagoa Bight section (Figure 4.2.9a) are depicted in Figure

(4.2.9b), for DELAG-I (black T-S) and (WOA) (red T-S). All the water types determined using *in situ* data by Lutjeharms and Jorge da Silva (1988), namely the TSW, STW, ICW and the AAIW are well represented in both. WOA gives a better representation of the minimum salinity associated with the TSW and the AAIW, (Figure 4.2.9b). The modelled ICW is almost coincident with WOA, whereas the STW is underestimated. In the horizontal, the mean temperatures at $100\,m$ depth is below $18\,^oC$ inside the Bight, (Figure 4.2.9c). It does not form a closed contour in this mean. However, the relatively low temperature to the western side of this isotherm shows a prevalence of cooler up-welled water, which results from the lee eddy activity. Farther offshore, the isotherms in the range $19-21^oC$ are parallel to the coast, and follow the 500 and $1000\,m$ isobaths. This behaviour indicates the prevalence of a southward flow. Near $27^oS, 37^oE$, the 22^oC isotherm traces the confluence of both the pathways of the mesoscale features from the north and east, (Figure 4.2.9c). In the Bight, the salinity is relatively fresher, possibly due to the impact of the upwelling of the AAIW which is known to dominate further offshore at $900\,m$ depth, (Lutjeharms and Jorge da Silva, 1988). The 35.25 and $35.3\,psu$ isohalines separate the most saline southeastern side of the region from its western side, which is relatively fresher, firstly due to the upwelling and secondly due to the input of fresher water masses from the north, (Figure 4.2.9d). The input of water masses from the north into Delagoa Bight area has not been discussed in literature. The available studies attribute the fresh content of the water masses to the upwelling induced by the lee eddy in the center of the Bight and to the river inputs (Lutjeharms and Jorge da Silva, 1988; Lamont et al., 2010).

This same parameters were plotted at $250\,m$ (Figure not shown). It has been noted that the eastern side of the domain is saltier and the intrusion of fresher water masses in the Bight is from the north, whereas the signature of the lee eddy is not consistent at this level. Several processes seem to have a role on the transmission of water masses from the north into the Bight, as it is discussed along the next chapters of this manuscript. However, *in situ* measurements are also required to confirm the veracity of the model results.

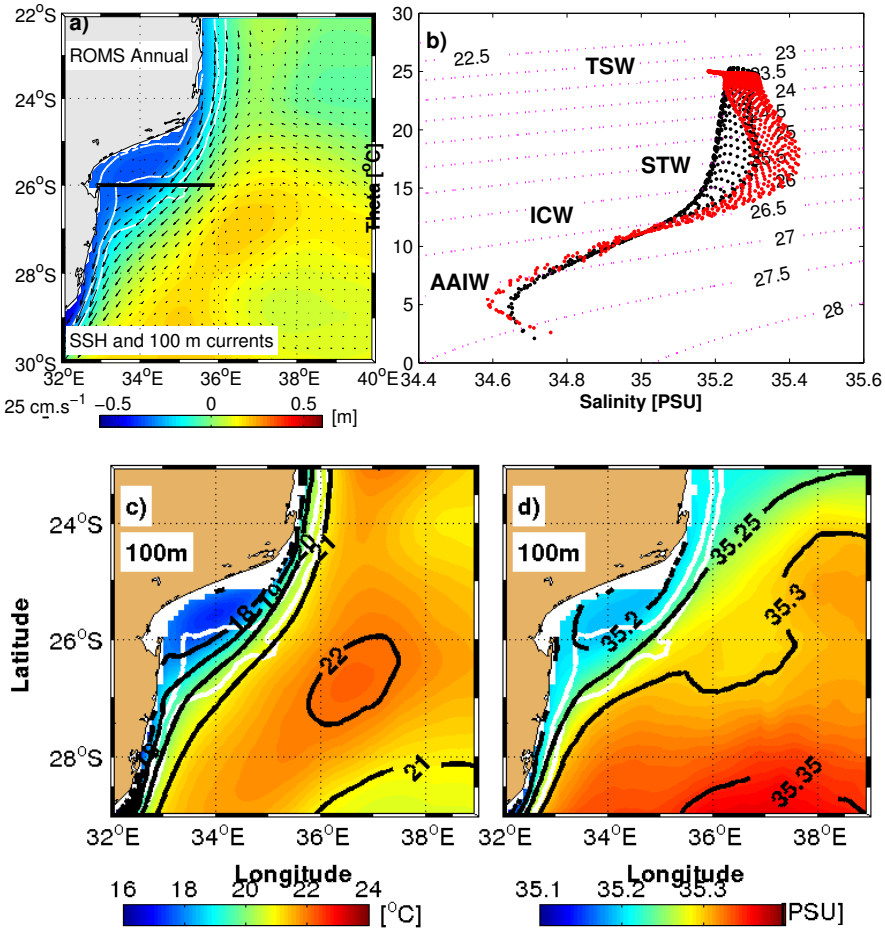

Figure 4.2.9: Mean currents at at 100 m depth, overlaid on SSH in a). The white contours indicates the 500 and 1000 m isobaths, whereas the black horizontal line represents the main Delagoa Section. T-S diagram based on DELAG-I (black) and WOA (red) are in b). In c) and d) are presented the temperature and salinity at 100 m depth respectively. The white contours in both are similar to a).

The mean vertical structure in the Delagoa section is addressed using the reference experiment and WOA data sets, Figure 4.2.10. In WOA, the 16^oC isotherm at 200 m depth (black) is flat, suggestive of the absence of the lee eddy in this relatively coarse climatology. It separates the warmer surface water from the cooler in the bottom. The 10^oC isotherm (black) lies further down and offshore of the usual center of the lee eddy, which normally is found between 100 km and 140 km, (Figure 4.2.10a). In (Figure 4.2.10b), the salinity is uniform along the whole section, with the 35.2 psu not well represented on the surface, whereas the 34.9 psu lies further down and crosses the 300 m depth. In ROMS, the 16^oC isotherm lies at 100 m and shows a slight doming by comparison with WOA, whereas the 10^oC isotherm is found close to the bottom, also with a slight doming that suggest the impact of the lee eddy, (Figure 4.2.10c). The 34.9 psu and 35.2 psu isohalines tend to mimic the temperature (Figure 4.2.10d). As a remark, it can be said that the model mean shows the impact of the lee eddy, but not WOA. This might be due to the relatively coarse resolution of the WOA climatology.

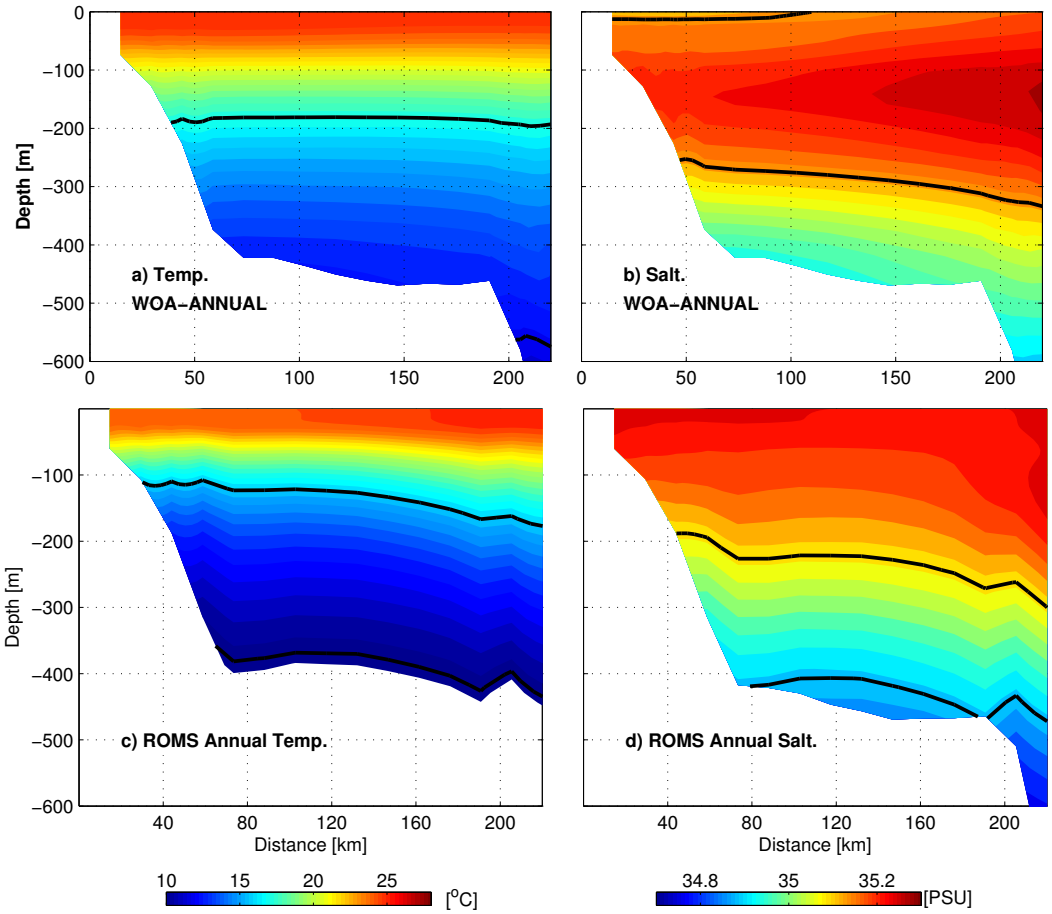

Figure 4.2.10: Mean vertical structure plotted from the main Delagoa Bight section at 26^oS. In a,c) is presented the WOA and DELAG-I temperature, while in b,d) is shown the salinity. In temperature the black contours indicate the 10 and 16^oC isotherms, whereas for salinity the 34.9 and 35.2 psu represent the isohalines.

4.3 Seasonal cycle

Above 50 m depth there is a considerable seasonal variability in the region (Figure 4.3.1). In summer, a long band of warmer water flows southward within the 24^oC isotherm. It covers mostly the whole domain from the north up to the Agulhas Current region (Figure 4.3.1a). The DBLE is marked by the 22^oC isotherm. This temperature pattern is similar to that observed in autumn, with the exception that the lee eddy in this season, is not obvious at this level (Figure 4.3.1b). In winter the 24^oC isoline is only present in the far north of the domain, and the southward flow occurs within the 22^oC isotherm. The lee eddy is not present (Figure 4.3.1c). In spring, the southward flow is characterized by a wider band, traced by the 24^oC isoline. The lee eddy is marked by the 22^oC, and like in the previous case, it is again relatively narrow (Figure 4.3.1d). This large band draws warmer water from the north toward the Bight, whereas offshore it mixes with the flow from the east.

The salinity field at 50 m, shows the 35.25 psu and 35.3 psu isohalines, separating a region of saltier

water occupying the whole southeastern side of the region in each season, with a slight difference in the extension of the band of fresher water (less saline) (Figure 4.3.2). This band is wider in warmer seasons (Figure 4.3.2a,b), but it reduces in cooler seasons (Figure 4.3.2c,d). The lee eddy is not consistent, but it is visible in summer (Figure 4.3.2a) and spring (Figure 4.3.2d). The intrusion of fresher water masses from the north is also noted in the mean (not shown). Therefore, the main water masses in the Bight are predominantly from the north.

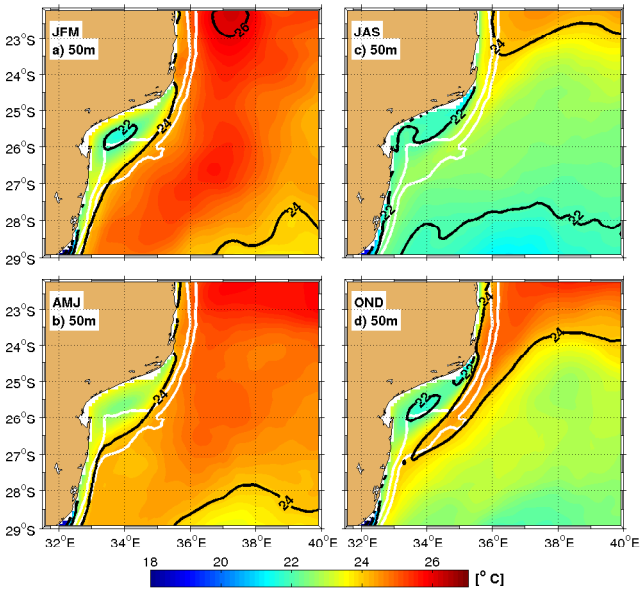

Figure 4.3.1: Seasonal variability of temperature at 50 m, for Summer (JFM) in a), Fall AMJ b), Winter (JAS) c) and Spring (OND) d). The white contours show the position of the 500 and 100 m isobaths. The black contours are the isotherms.

Temperature seasonal averages at 100 m depth tend to represent the usual pathways of the anticyclones and their confluence zone discussed in the previous sections (Figure 4.3.3). The 22^oC isotherm encloses the regions of warmer water, mainly in summer and autumn (Figure 4.3.3a,b). The lee eddy is traced by the 18^oC isotherm. In most seasons, this isotherm and that of 20^oC are aligned to the 500 and 1000 m isobaths. The area of the domain, away from the pathways of the anticyclones is cooler in these averages, (Figure 4.3.3). The upwelling zone, which is characterized by cooler temperature, is apparent in the shelf, mainly in the center of the Bight.

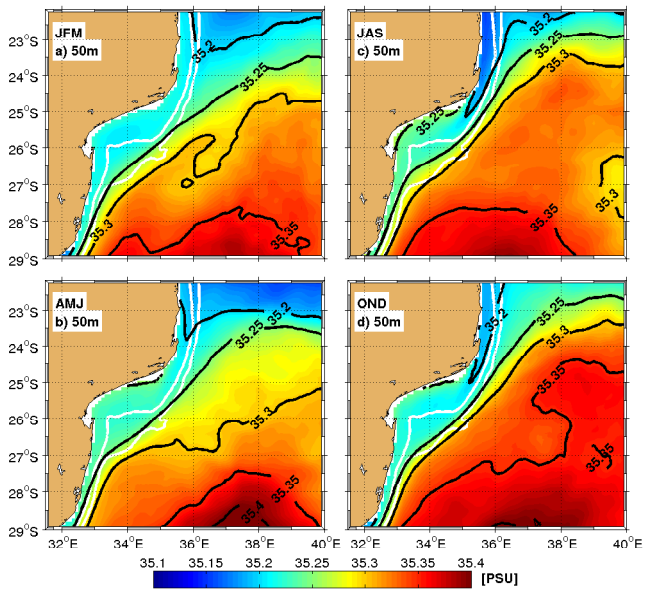

Figure 4.3.2: Seasonal variability of salinity at 50 m, for Summer (JFM) in a), Fall AMJ b), Winter (JAS) c) and Spring (OND) d). The white contours show the position of the 500 and 1000 m isobaths. The black contours are the isohalines.

In Figure 4.3.4, the summer and the autumn climatologies tend to present a wider zone of fresher water near the coastline, (Figure 4.3.4a,b). This pattern indicates the intrusion of fresher water masses from the northeast into the Bight. The southeastern side of the domain indicates the usual high salinity, that dominates this regions in all seasons. In winter and spring, (Figure 4.3.4c,d), the southeastern sub-region is dominated by higher salinity. It is hypothesized that this is due to the influence of the winds, that favour the intrusion of water masses from the south-eastern region into the Bight (winds are more easterly), during these seasons, as shown in the previous chapter. This also appears to portray the impact of the large scale oceanic circulation in this area. Lutjeharms (2006b), shows a clear link between the winds and the large scale oceanic circulation from Delagoa Bight latitudes towards the south.

At 250 m and below (Figure not shown), there is no significant seasonal changes of the temperature and salinity with depth. Near the coast there are lower values of both tracers, while the eastern side of the domain shows higher values. The pathways of the anticyclonic eddies are noticeable in the temperature field but not in the salinity. This is possibly due to the salinity mixing at lower levels, by contrast with the temperature that responds quickly the solar radiation. The lee eddy in the Delagoa Bight is preeminent, but it is not a regular structure, instead it is narrow and inconsistent. This highlights the impact of both situations of presence and absence of the lee eddy as noted by (Lamont et al., 2010). If the lee eddy was always present the signature in the averages could be a consistent circular feature in these fields.

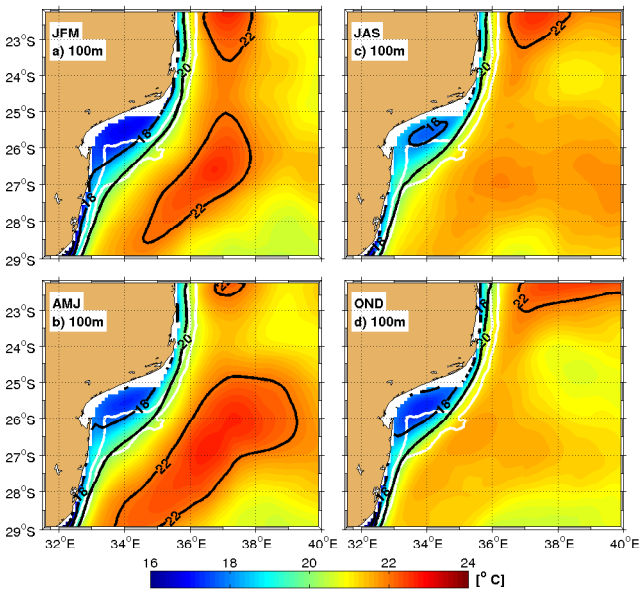

Figure 4.3.3: Seasonal variability of the temperature at 100 m in the Delagoa Bight region. JFM, for summer a); AMJ for Autumn b); JAS for winter c) and OND for spring d). The white contours show the position of the 500 and 1000 m isobaths. The black contours represent the isotherms.

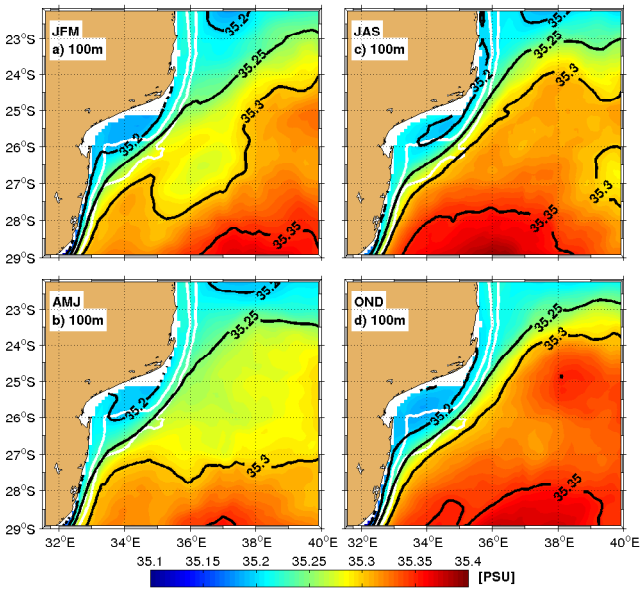

Figure 4.3.4: Seasonal variability of the salinity at 100 m in the Delagoa Bight region. JFM, for summer a); AMJ for Autumn b); JAS for winter c) and OND for spring d). The white contours show the position of the 500 and 1000 m isobaths. The black contours represent the isohalines.

Seasonal mean vertical cross sections show prevalence of an inconsistent lee eddy, together with a weak coastal counter-current of 5 cm/s, as indicated in the first column of Figure 4.3.5. This current is found throughout the whole water column along the coastal area of the Bight. Offshore, the southward flowing current is consistent with speeds above 40 cm/s throughout the year. In both temperature and salinity, second and third columns respectively, the slight doming of the contours account for the presence of the lee eddy in Delagoa Bight. Although the model succeeds in simulating situations in which the DBLE is absent, this average highlights their insignificance

in the seasonal mean. Along the next chapter it will be shown that the lee eddy absences are short leaved.

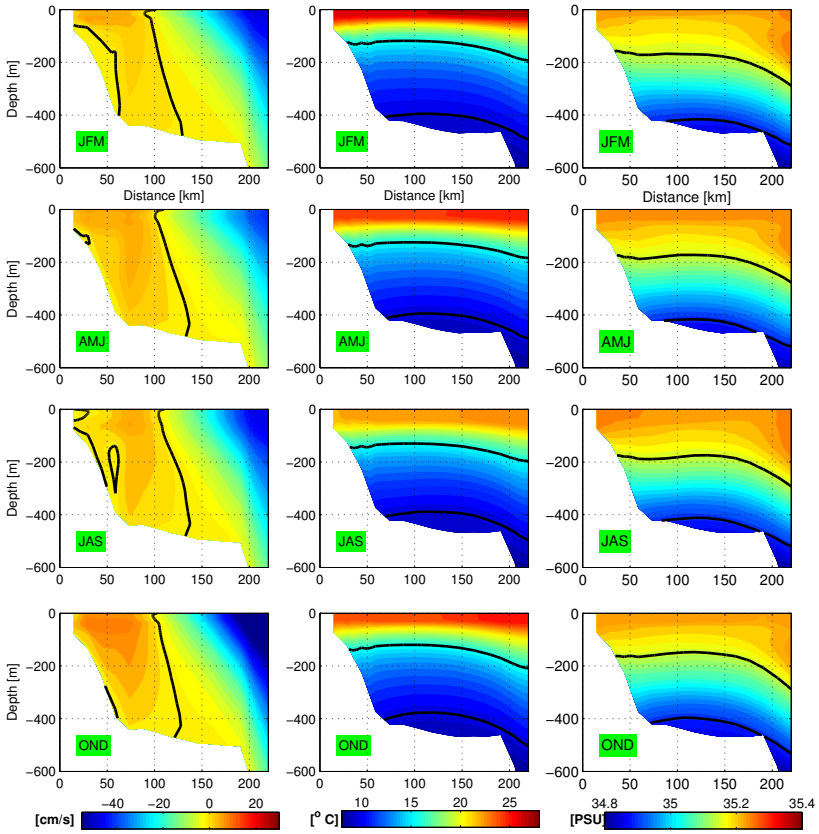

Figure 4.3.5: Cross sections of tracers and meridional velocity, showing seasonal variability in the Delagoa Bight. The black line in the first column indicates the isotach of zero cm/s. In the second column it represents the 10^oC and 16^oC isotherms, while in the last column it refers to the 34.9 and $35.2psu$ isohalines.

To determine the seasonal variability within the Delagoa Bight, monthly mean time series of the tracers in the upper layer ($25\,m$) were also computed inside of the usual location of the lee eddy at $34E, 26^oS$ (Lutjeharms and Jorge da Silva, 1988). This was performed by creating a box delimited by the meridians of $33.5 - 34.5^oE$ and latitudes $25.6 - 26.5^oS$. Model and satellite time series of SSH were also derived for the same box. For temperature (Figure 4.3.6a), a seasonal cycle with a peak in the local summer and winter is evident, and it is due to the seasonal variation of the insolation in this region. The temperature error bars are very small, indicative of a consistent seasonal behaviour of temperature in the upper layer. However, salinity presents a quasi semi-annual cycle. The corresponding error bars are very large, implying more variability of seasonal salinity from one year to another (Figure 4.3.6b). The model SSH variability in (Figure 4.3.6c), also shows a semi-annual signal with large error bars, possibly due to the passage of anticyclonic eddies. The SSH monthly data derived from satellite observations, (Figure 4.3.6d) also show a semi-annual signal but with the extremes shifted from those of the model as illustrated in (Figure 4.3.6c).

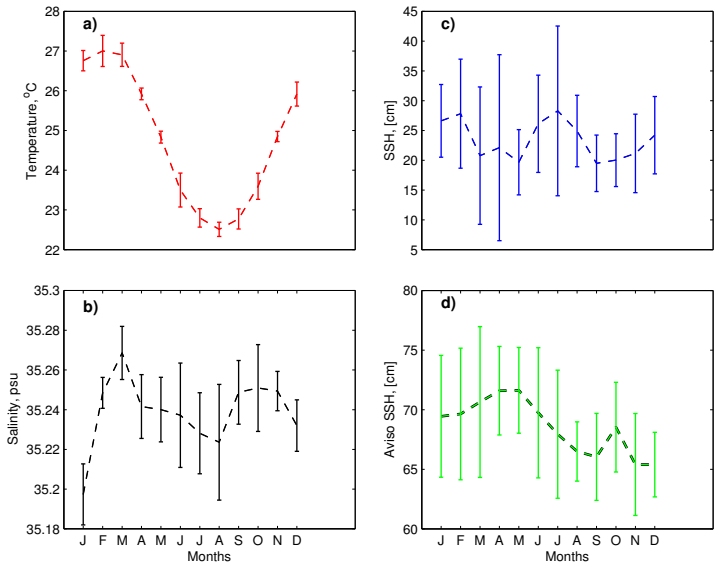

Figure 4.3.6: Variability assessed based on (DELAG-I) model time series of temperature in a), salinity b), and SSH c), and finally from AVISO SSH in d) taken from the box in the Delagoa Bight lee eddy usual location.

The temperature amplitude according to our model time series, shows that DELAG-I configuration, varies from approximately 21^oC in winter to 27^oC in summer (Figure 4.3.6a), in analogy with the values determined from in situ observations in the Delagoa Bight (Kyewalyanga et al., 2007; Barlow et al., 2008). The salinity varies from a minimum of 35.19 to 35.28 psu in the upper layer (Figure 4.3.6b), while the model SSH varies in the range of 7 cm to 42.5 cm inside of the Delagoa box, (Figure 4.3.6c). In the satellite, the SSH shows a minimum of 62 cm and maximum of 77 cm, (Figure 4.3.6d). Indeed, model and AVISO SSH, do not indicate the same seasonal variability, which is in both cases not significant.

Comparisons of seasonal T-S diagrams of DELAG-I (black) and WOA (red) in Figure 4.3.7, show considerable variability in the surface water masses, namely TSW and STW but not in the components lying below, such as the ICW and AAIW. In JFM, the model underestimates both the salinity maximum associated to the STW, and the salinity minimum of the TSW, (Figure 4.3.7a). In AMJ, WOA is characterized by a broader spectrum, consisting of a smaller salinity minimum of 35.0 psu for the TSW and a greater salinity maximum of 35.4 psu for the STW, (Figure 4.3.7b). In JAS, the salinity minimum associated to the TSW is consistent in WOA but not so much in OND. In both seasons the model still underestimates the salinity maximum linked with the STW. Overall the diagrams presented here are similar to those presented for this section by Lutjeharms and Jorge da Silva (1988).

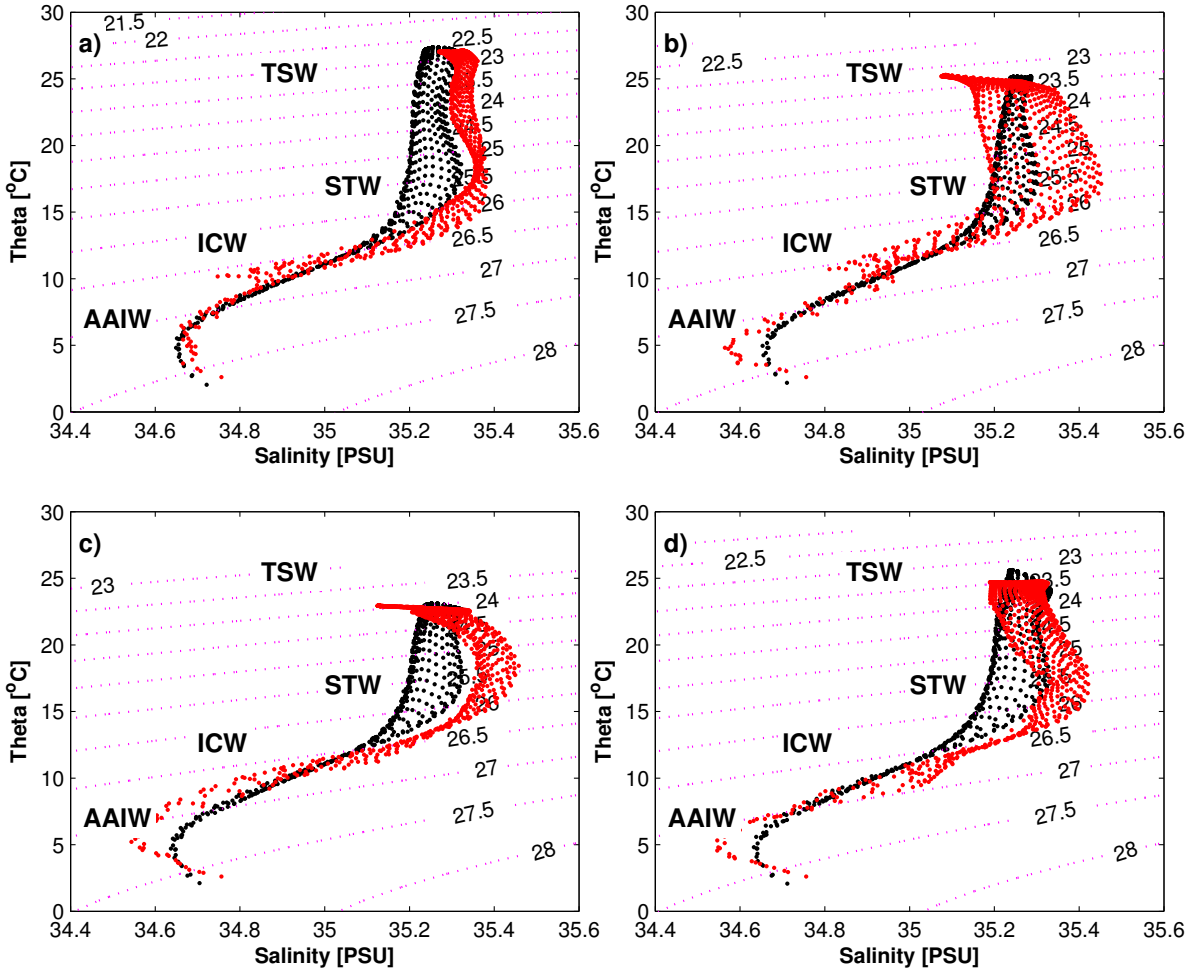

Figure 4.3.7: Model DELAG-I (black) and WOA (red) seasonal T-S diagrams for JFM in a), AMJ b), JAS in c) and OND d), showing water masses variability in the Delagoa section.

The potential temperature seasonal variations noted on the upper layers in Delagoa Bight, have been associated with the seasonal variation of insolation, (Kyewalyanga et al., 2007; Lamont et al., 2010). However, the seasonal variability of water masses illustrated in the T-S diagrams shown above, also suggest the relevance of the local dynamics in their distributions along the main Delagoa section.

4.4 Eddies Circulation in the Region

The most important features of the local oceanic circulation are the mesoscale eddies from the north and Madagascar, and the southward flowing current (Cossa et al., 2016; Lutjeharms and Jorge da Silva, 1988). According to Schouten et al. (2003), four to five anticyclonic anomalies are developed to the north of Mozambique Channel per year, whereas seven form southeast of Madagascar. The anticyclones from the north develop cyclonic eddies northeast of Delagoa Bight, as they interact with the shelf in a process that is characterized by a seasonal cycle, (Cossa et al.,

2016). Such seasonality seems to reflect the seasonality of the anticyclonic features from the north.

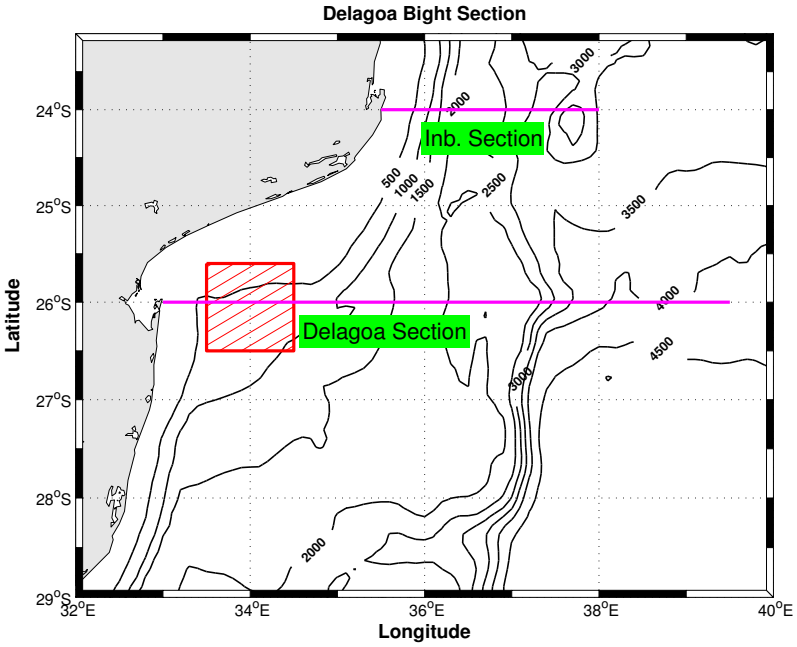

Figure 4.4.1: Inhambane section used to capture the SSH anomalies induced by the passing anticyclones from the north, and Delagoa Bight section in located to test whether the anomalies from the east are able to reach the center of the Bight, both in magenta. The red hatched square shows the areas usually filled by the DBLE.

In order to assess the impact of the flows from both the north and east, some Hovmöller plots have been made. They are plotted along two sections as indicated in the map above, (Figure 4.4.1). The first section at 26^oS (Delagoa Section) is conceived to show the influence of the mesoscale features from Madagascar in the Bight, whereas (Inb. Section) at 24^oS represents the region in which the signals of the passing anticyclones from the north are captured and accounted. For the model (DELAG-I) the results are given in the upper row (Figure 4.4.2a,b) whereas for AVISO observations are presented in the (lower row) (Figure 4.4.2c,d). Notice that the Delagoa section is represented in the first column, for both model and satellite. Indeed, at 26^oS, the SSH anomalies from the east (positive and negative) reach the center of Bight at 34^oE with a weak signal, for both model and satellite observations (Figure 4.4.2a,d). It is also noticeable that the negative anomalies reaching the Bight from the east are weaker in both the satellite and model, by comparison with the positive ones. Four to five positive anomalies per year in the model affect the center of the Bight, while the negative anomalies do not because they tend to be short lived, mainly in the model. In the model, these positive anomalies (anticyclonic) propagate at speeds of $7.4\,km/day$ against $5.5\,km/day$ in AVISO. These values are closer to the range of $5.6 - 6\,km/day$ estimated at 25^oS by Quartly et al. (2006).

The anticyclones from the north of Mozambique Channel pass through the 24^oS section in a

frequency of around 5.1 to 5.3 per year, (Figures 4.4.2b,d) and affect the Bight twofold. Firstly, as they merge with those from Madagascar, forming bigger rings that interact with the Bight. Secondly, on passing off the Bight towards the Agulhas Current, their outer edges are occasionally able to sweep the Bight impacting the dynamics there. The difference between model and AVISO is associated with the tilting on the direction of the trajectories of the anticyclones toward northwest in the model, as noted in the previous sections of this manuscript. This seems to contribute in the way the anomalies from the east along the 26^oS section reach the Bight.

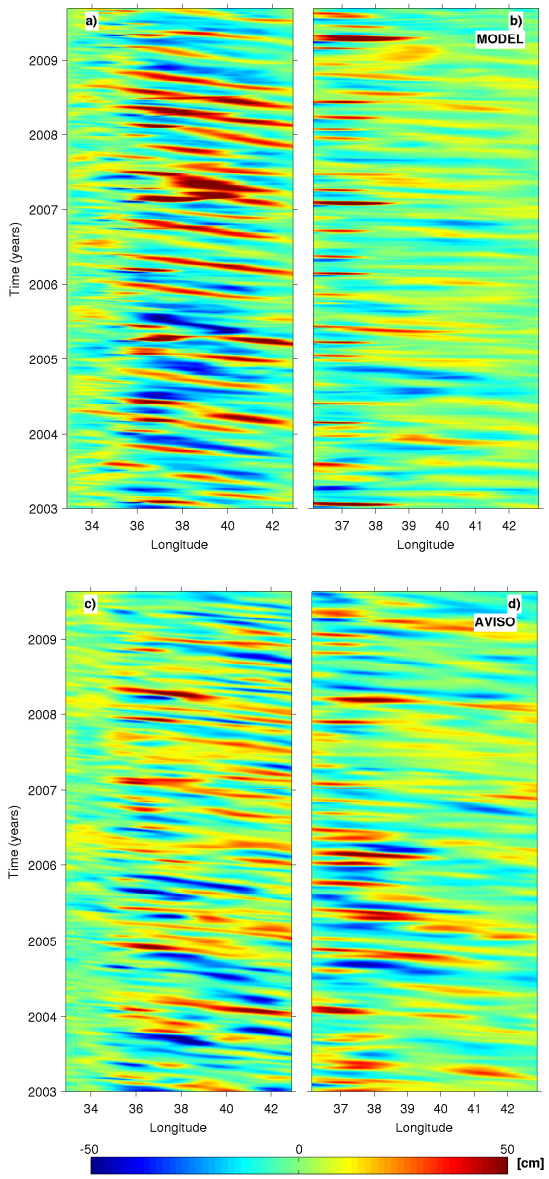

Figure 4.4.2: Hovmöller plots of SSH anomalies from model (DELAG-I) in a,b) (top row) and AVISO lower row in c,d). The first column a,c) represents anomalies along a section at 26^oS and is used to capture the signals from the east. The anomalies from north are estimated at the meridian of 24^oS, and are presented in the second column b,d).

Overall, these anomalies are weak as they reach the Bight, although the positive ones from the model are much stronger. This is because the anticyclones from the east in AVISO tend to propagate from somewhat below the latitudes of the Bight, in a way that the majority of their

edges cannot reach the Bight. In both, the small isolated positive SSH anomalies, which are not from the east, seem to be caused by the passage of the anticyclones from the north, whose outer edges are usually seen interacting with the center of the Bight in the snapshots. The transmission of SSH anomalies from the east seems to be one of the reasons that explains the seasonal variability in the upper layer water masses in Delagoa Bight, mainly the STW. Lutjeharms and Jorge da Silva (1988) found that this water mass was prevalent in stations slightly out of the Bight, while in the Bight itself it was found completely mixed with other water masses.

To shed more light on the impact of the mesoscale features from the north and east in the Delagoa Bight, the trajectories and radii distributions of anticyclonic eddies are presented in Figure 4.4.3. The anticyclones from the north of Mozambique, move generally locked to the coast and interact with the shelf, generating cyclonic features with which they form dipoles (Roberts et al., 2014). These cyclonic features have been found to behave like meandering pulses as they move southward, (Cossa et al., 2016). In this simulation, these anticyclones are characterized by an average diameter of 154 km, with maximums of 216 km. According to the literature they consist of diameters larger than 300 km, (de Ruijter et al., 2002). Their average life time is 50 day inside of the domain of this simulation. Their counterparts of the east, tend to present smaller average diameters in this simulation. Furthermore, they are longer lived. Their average life time is over 90 $days$. This life time is associated with their longer pathway inside of the domain. Indeed, they generally move northwestwards before shifting toward south off Delagoa. Their edges show a smaller likelihood to interact with the Bight, first due to their tendency of moving much offshore, and secondly because they present minor diameters in comparison with the rings of the north of Mozambique Channel. The anticyclones from the north according to the eddy detecting and tracking system have frequencies of 3.675 per year, whereas those from the east have 4.75 per year.

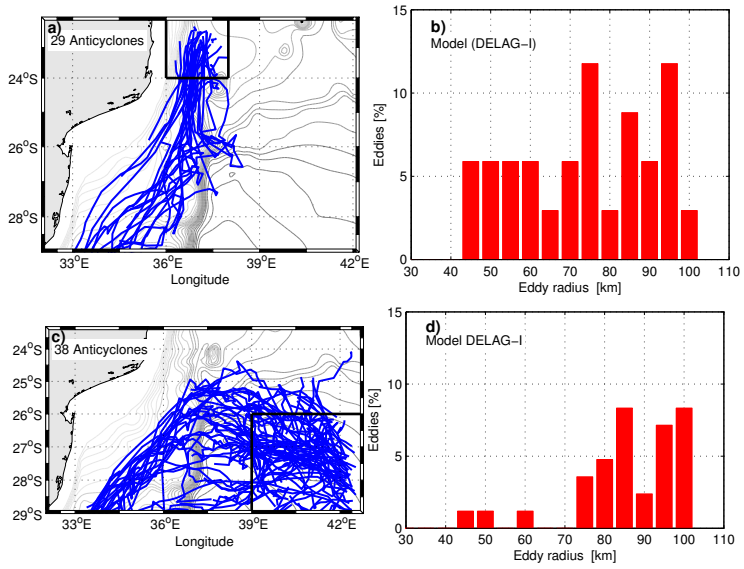

Figure 4.4.3: Trajectories of the anticyclones from north of Mozambique (blue line) in a), and Madagascar c). The gray line indicates the contours of bathymetry. The radii distributions of the anticyclones are given in b) and d), for Mozambique and South of Madagascar respectively.

The concentration of trajectories of the anticyclones from the east in the eastern side of the domain are in agreement with the high salinity and temperature found in the model climatologies in this part of the domain. The water masses from the east are more saltier due to the excess of evaporation over precipitation in their sources. The tendency of the mesoscale features from the east, of passing from far away of the Bight seems to explains the weak presence of the STW in the Bight. The tendency of the southward boundary current to strengthen in this region is another factor to consider, because in carries water masses from the north in to the Bight through its instabilities. This current is also likely to force the trajectories of the features from Madagascar southwards. Therefore, the main source of the water masses in the Bight is from the north, consistent with the findings above.

Most of the cyclones from the north that are observed in this region seem to be generated somewhere in the middle of the Mozambique Channel and do not have significant influence in the Bight. However, as stated above, cyclonic pulses originated in the northeastern side of Delagoa Bight have an impact in the local dynamics according to Cossa et al. (2016), and will be discussed in the next Chapter. Cyclonic mesoscale features coming from the east, are depicted in Figure 4.4.4. The eddy detecting and tracking system found 29 *cyclones* on model (DELAG-I), with an average radius of 46.2 km and life spans varying between 15 and 72 *days*. Their amplitudes fall in the range of $3.7 - 11.7cm$. The modelled cyclonic features tracked from the east appear to have no significant impact in the Bight, (Figure 4.4.4a). Trajectories of the cyclones tracked in AVISO observations, (Figure 4.4.4c) show that the cyclonic features from the east have an influence in-

side of Delagoa Bight, and therefore may contribute in the import of water masses into the Bight. These features are long lived by comparison with the modelled, with life spans in the interval of 15 and 139 *days*. Their radii are greater than the modelled as given in Figures b) and d).

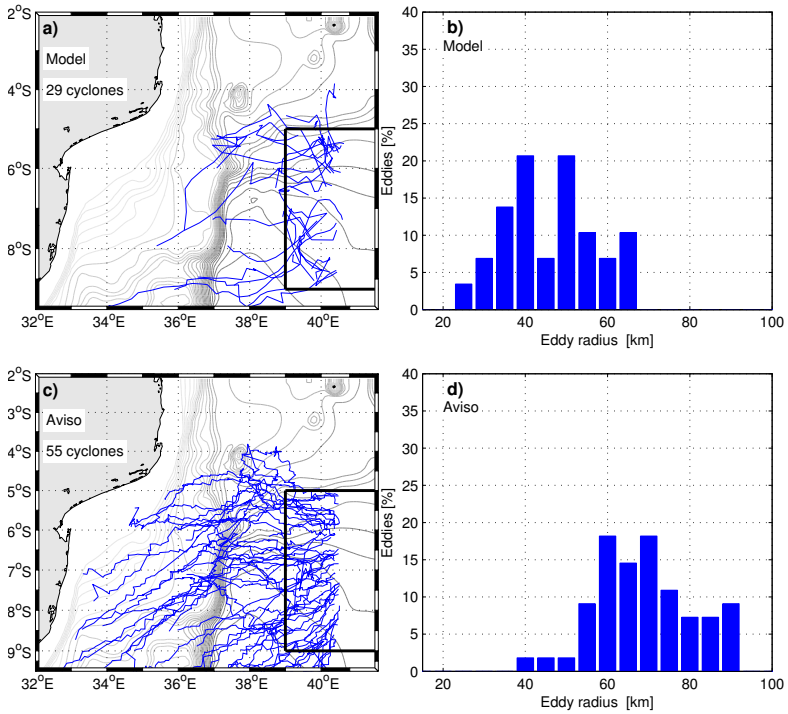

Figure 4.4.4: Cyclonic eddies tracked in the eastern side of the domain, for both model DELAG-I and AVISO. The blue lines in the maps are trajectories of the cyclones. The histograms show the radii distributions for the model (DELAG-I) and AVISO. The gray lines are contours of bathymetry.

The propagation of both cyclonic and anticyclonic features from the east in this region is in agreement with Siedler et al. (2009), who refers to two modes of vorticity in the extension region of the Southeast Madagascar Current, in which the fraction of anticyclonic motion is found in the northern part of the Mozambique Basin, whereas the cyclonic motion resides father north. It can however be argued that the model (DELAG-I) straggles to represent the cyclonic features and their impact in the Bight. These features are however well represented in the observations, in agreement with Siedler et al. (2009).

4.5 Effect of tides on the mean state

The addition of tidal forcing in the main Delagoa Bight configuration (DELAG-I), was made with the expectation of improving the various aspects of the local circulation in comparison with the observations. A total of 10 tidal components (M2 S2 N2 K2 K1 O1 P1 Q1 Mf Mm) were used to force the model. The new configuration is named Delagoa Bight with tides (DELAG-II), and

holds all of the characteristics of the reference experiment (DELAG-I). In Figure 4.5.1 the map shows the positions of the stations in (Maputo) and (obc east), a fictitious station in the east (Figure 4.5.1a). In Figure (4.5.1b) the observations (blue) are characterized by greater amplitude in comparison with the model (red) and the forcing model TPXO (dashed magenta). Overall, the model mimics the TPXO even in the offshore station (Figure 4.5.1b,c), whereas the relatively high amplitude in the observation is because these observations are from the inner Maputo harbour, where the tidal wave is more degraded.

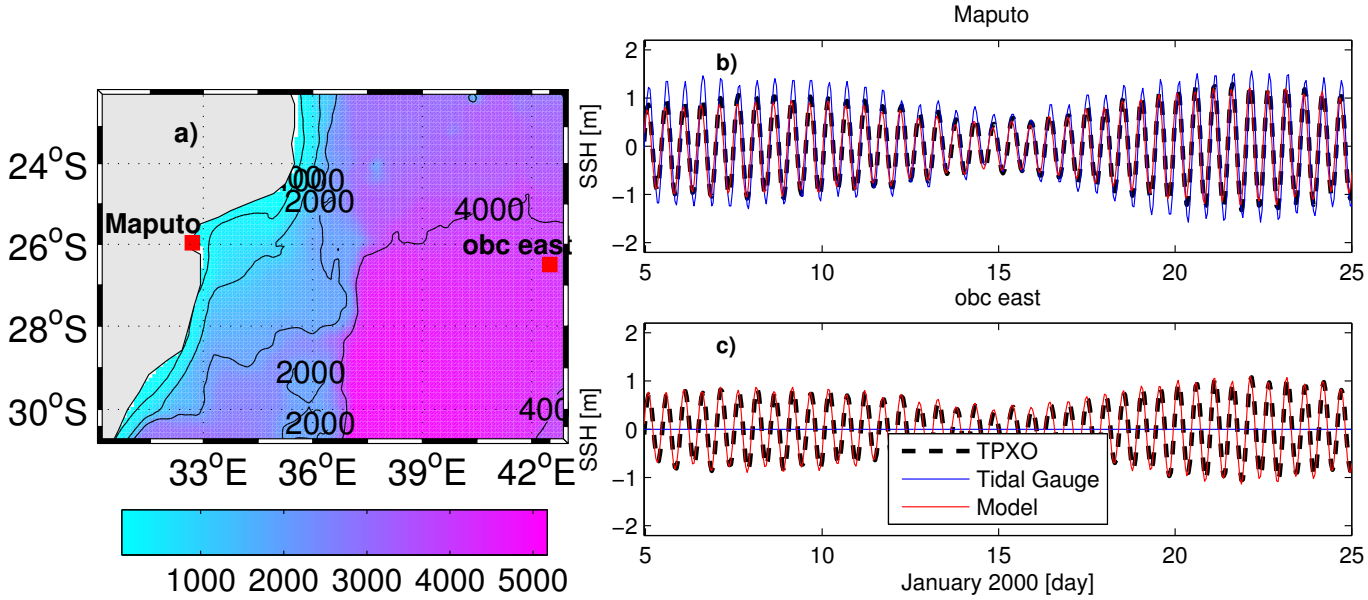

Figure 4.5.1: Map showing the location of the tidal observation (Maputo) and (obc east) in a). In b) is represented the sea surface variations in Maputo based on the tidal forcing model (TPXO) (dashed magenta), the observations (blue) and modelled (DELAG-II) (red). In c) are given the the sea surface variations in obc east.

The mean SSH contours for this simulation show an improvement in the representation of the regional circulation, Figure 4.5.2. This enhancement is characterized by reduction in the tilting of the extension of the Southeast Madagascar Current, which is toward northwest in the no-tides configuration, (Figure 4.5.2a). This reduction in the tilting of the westwards current turned the DELAG-II simulation more similar to the AVISO observations, (Figure 4.5.2b,c). The closed loops of SSH to the south and northeast of the domain are not represented in the model with tides. This is due to the increase in the speed of the southward flow along the shelf, as discussed below. Off Inhambane, the location of generation of pulses, Cossa et al. (2016) is characterized by closed negative contours in AVISO, suggestive of the importance of this feature in the oceanic circulation there.

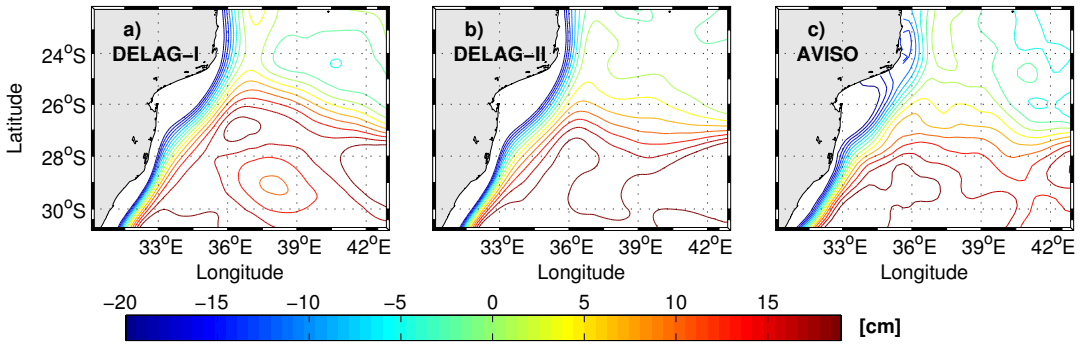

Figure 4.5.2: Mean SSH for no-tides (DELAG-I) in a), tides (DELAG-II) b) and AVISO. The SSH in these pictures follow contours of 3cm.

The effect of tides in the EKE is illustrated in Figure 4.5.3. In Figure (4.5.3b), the eddy activity based on tides (DELAG-II), shows some EKE changes along the main pathways of the mesoscale eddies in the region. This experiment highlights the activity of the rings from the north than the anticyclones from the east (Figure 4.5.3b). The $500\,cm.s^{-2}$ contour is parallel to the African coast in this simulation. Furthermore, the region of the merger of the anticyclones from both pathways is found at $28^oS, 36^oE$, (Figure 4.5.3b). In the reference experiment (DELAG-I), it lies farther north (Figure 4.5.3a). Although the pathway of the eddies from the east is weaker in this simulation, it shows similarities with AVISO, because their westwards direction is not tilted toward northwest, (Figure 4.5.3a,c). Interestingly, like no-tides (DELAG-I), AVISO also seems to give a better representation of the eddy activity for both pathways, with the region between the $500\,cm.s^{-2}$ contour (black line), showing EKEs above $1300\,cm.s^{-2}$. Overall, the distribution of variability in this simulation (DELAG-II), is similar to the satellite observations because it occupies a large extension around the center of the domain, although it appears to underestimates the EKE associated with the eddies from the east by comparison with both (DELAG-I) and AVISO.

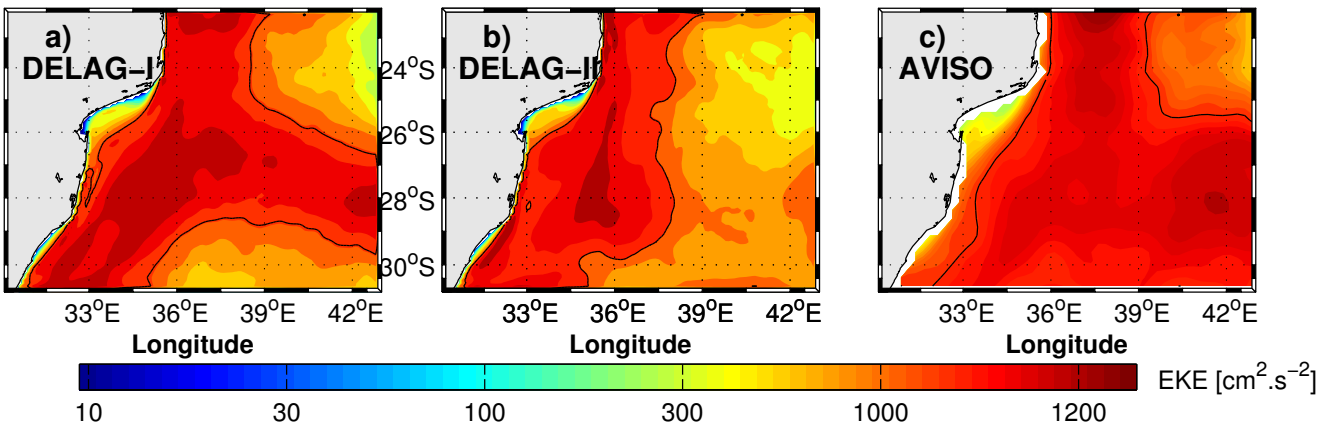

Figure 4.5.3: Mean EKE determined from (DELAG-I) in a), from tides (DELAG-II) in b) and AVISO in c). The black contour represents the $500\,cm^2.s^{-2}$ isoline.

In terms of mean geostrophic velocity, formula in A.3, the model with tides (DELAG-II) Figure 4.5.4, also shows a similar reduction in the tilting of the pathways of the currents from the east, noted in the model without tides. The currents from the east are shifted somewhat westwards in this case. There is a slight strengthening of the southward boundary current (to be discussed later) in comparison with no-tides as it flows toward the Agulhas Current. The modelled DBLE is less marked in comparison with AVISO, which is characterized by a wider feature inside of the Bight.

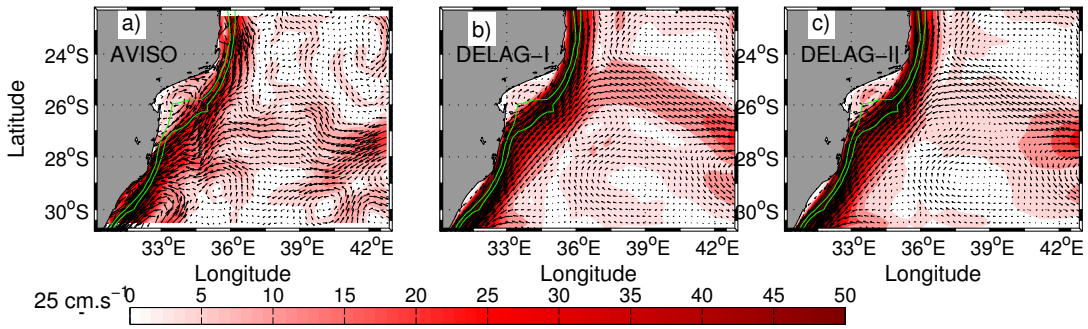

Figure 4.5.4: Mean geostrophic velocity for AVISO in a) the model (DELAG-I) in b) and (DELAG-II) in c) overlaid in the modulus of velocity.

In Figure 4.5.5 the preeminence of the southward boundary current along the shelf is reassessed based on the model with tides (DELAG-II). The along isobaths currents presented in Figure (4.5.5a), were estimated from the same positions as previously (Figure 4.5.5b) with the colour of the triangles corresponding to the lines in the plots. It is again noticeable that the flow grows from the southern part of the Bight (green triangle) $(42.4 \pm 30\, cm.s^{-1})$ to $(79.8 \pm 35\, cm.s^{-1})$ in the northern Agulhas Current, (pink triangle). This results reveals consistency of the southward flowing boundary current in this region, as well as a slight increase of intensity when tidal forcing is added, by comparison with the case without tides in the previous section. The strengthening of the boundary current is in agreement with the consistency of the Agulhas Current at this latitude as indicated by (Lutjeharms, 2006a). The along shore current is generally southward and can occasionally shift toward north in less than $2.0, 1.0, 4.0, 3.0, 1.0$, and 0.5% of the times, in those positions (Figure 4.5.5b), as evaluated from the northernmost point (red) to the southernmost (pink), (Figure 4.5.5c).

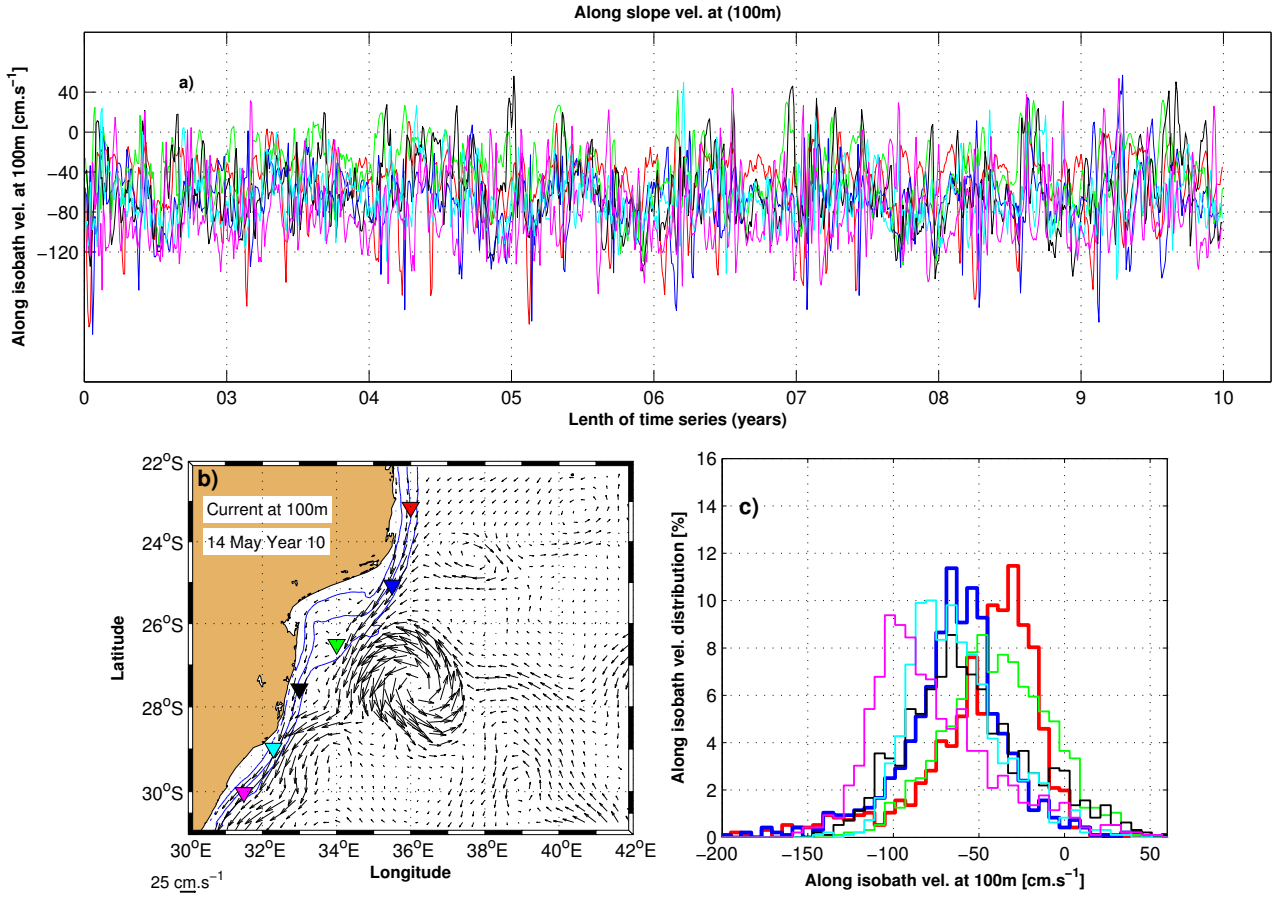

Figure 4.5.5: Times series of along the 100 m isobath velocities a), estimated in the positions indicated by triangles in the map b), for the model with tides (DELAG-II). In c) are shown the PDFs, with the colours corresponding to the positions of the velocity estimations given in b).

The profiles of the mean meridional velocity in the core of the southward flowing current at $26^o, 34.5^oE$ shows an increase of velocity in the model with tides (DELAG-II), by comparison with no-tides (DELAG-I), (Figure 4.5.6). In no-tides, the velocity presents a maximum of 5.5 cm/s on the surface, which decreases toward a minimum of 2.5 cm/s above 200 m depth. At 450 m depth it reaches a maximum of 6 cm/s, before decreasing again to the lowest velocities in the bottom. In the model with tides, the profile presents higher speeds in all depths, with oscillations around 8 cm/s. It decreases from (10.2 cm/s) at the surface to zero, in the bottom. This shows unequivocally a relative increase of the southward flowing boundary current in the model with tides.

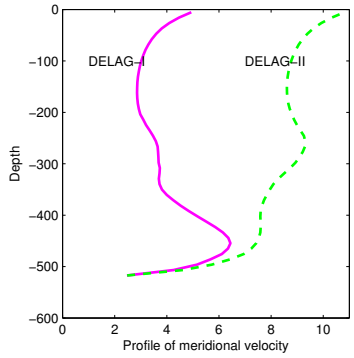

Figure 4.5.6: Profiles of meridional velocity at $[26^o; 34.5^o E]$ based on the models DELAG-I and DELAG-II, in magenta and green, respectively.

The slight increase of the meridional velocity noted above, led one to compare the mean kinetic energy close to the surface ($25\,m$) for both no-tides (DELAG-I) and tides (DELAG-II) simulations, Figure 4.5.7. In both cases, the mean kinetic energy is consistent along the shelf (Figure 4.5.7a,b), with the model with tides showing a slight intensification of the southward flowing current. This intensification is characterized by an increase of the mean kinetic energy in approximately $500\,cm^2.s^{-2}$, as suggested by the red dashed line (Figure 4.5.7c). The reason behind this increase is associated with the presence of the tidal forcing in DELAG-II simulation. Nevertheless, the tides can only affect the speed close to the coast, as suggested in (Figure 4.5.7c). In fact along the whole extension of the domain this effect is not visible, (Figure 4.5.7a,b).

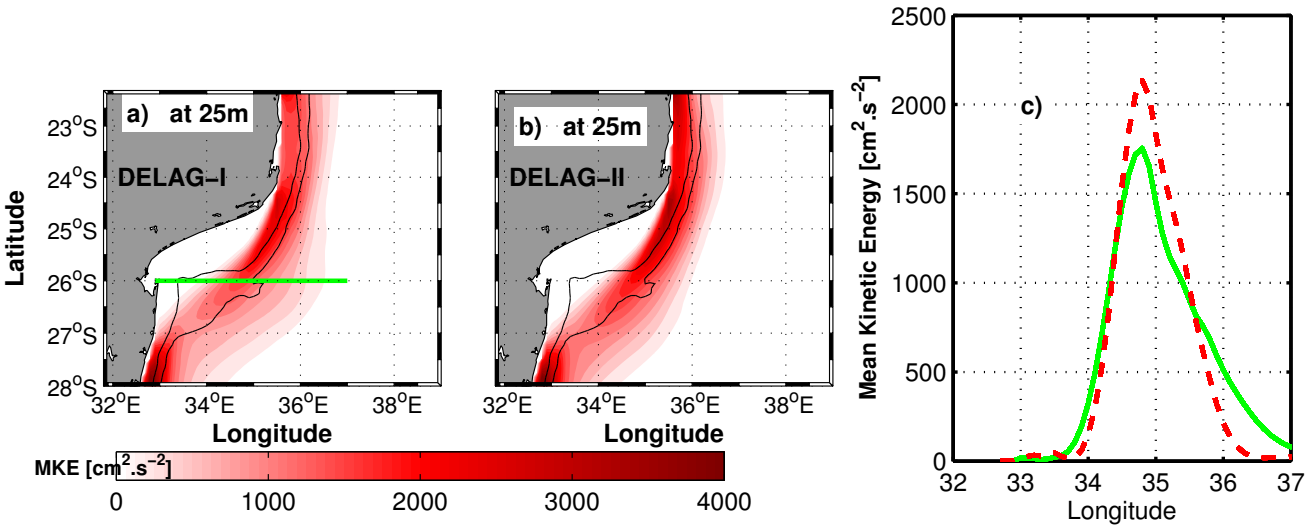

Figure 4.5.7: Mean kinetic energy for DELAG-I (no-tides) along the Delagoa section (green line) in a) and for DELAG-II (tides) in b). The black contours represent the isoline of $500\,cm^2.s^{-2}$. In c) is shown the same along the Delagoa Bight section at $26^o S$.

Cross sections of differences between model parameters for tides and no-tides, determined based on the corresponding means are presented in Figure 4.5.8. The temperature difference (DIff-1) in (Figure 4.5.8a) shows that the tidal forcing in the model does not provoke noticeable changes above $200\,m$ depth. However, below this depth a relative reduction of temperature was noted, suggestive

of an increased upwelling of cooler water in the model with tides. Likewise, salinity (Diff-2) shows no change above 200 m depth (Figure 4.5.8b), but downwards it decreases, probably because of the increase in the content of the AAIW, which is known to upwell from around 1000 m depth (Lamont et al., 2010; Lutjeharms and Jorge da Silva, 1988). The meridional velocity (Diff-3) in Figure (4.5.8c) is characterized by an increase of the southward flowing current much offshore. This coincides with an increase of the northwards coastal-counter current in the middle of the Bight. Therefore, an increase of the southward current can strengthens the coastal counter-current in the model with tides, by comparison with no-tides. In the center of the Bight there is a northwards current dominating the upper layers. This indicates an increase of the coastal counter current in more than 2 cm/s. Offshore (200 km) the southward current increases by approximately 8 cm/s in the presence of tides, indicative of the importance of tides near the coast.

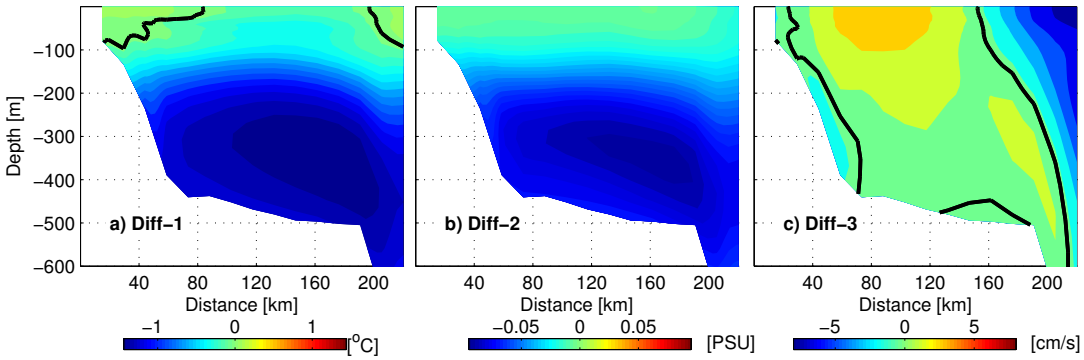

Figure 4.5.8: Cross sections of differences determined from the means of the model with tides and no-tides. a) refers to temperature, b) to salinity and c) meridional velocity. The black lines shows the isolines where the difference is null.

The water masses for the simulations with tides and no tides, are compared along the main Delagoa Bight section at 26^oS, to verify which model does better represent their properties, Figure 4.5.9. It has been noted that there is no considerable difference between these models as illustrated through the black stars for (no-tides) and red for (tides). The surface water in tides shows lower salinity ($-0.05\,psu$). Likewise the bottom water for no-tides are characterized by higher temperatures $[+0.5 - 1^oC]$. These values reveal that the difference between the thermodynamic parameters for both experiments, are small. For the central and bottom waters, there are no differences at all. Therefore, over the next chapter the analysis of the thermocline structure for the DBLE will only focus on the effect of improvement of resolution.

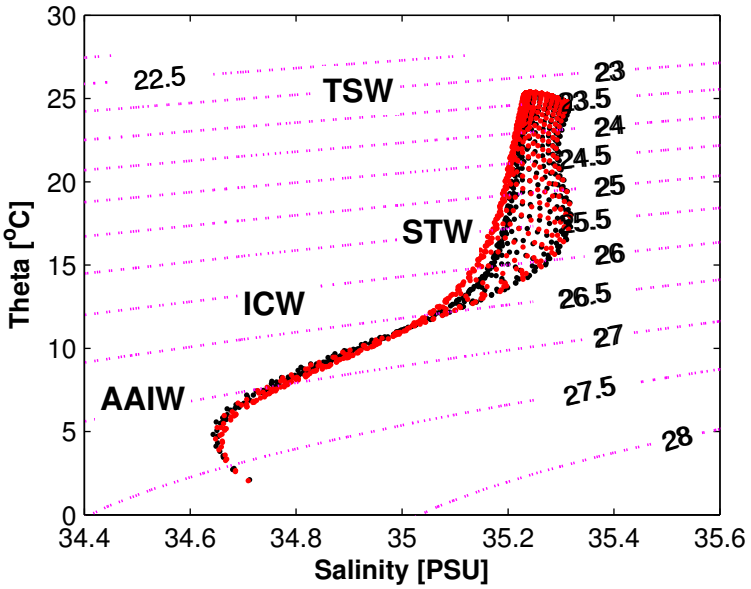

Figure 4.5.9: T-S diagram along the main Delagoa Section, for the means determined from the models no-tides (DELAG-I) in black and tides (DELAG-II) in red.

4.6 Effect of improvement of resolution in the mean state

In this section, the mean state of the regional circulation is reassessed using model data derived from the two-way nested ROMS_AGRIF experiments, namely DELAG-III (no-tides) and DELAG-IV (tides) (Figure 4.6.1). The resolution in the mother domain is approximately 10 km whereas the child is 3.3 km. The advantage of the two-way nesting over the one-way is the mutual coupling between the coarse and fine grid solutions at the barotropic level. It contains a good interface of continuity and dynamic integrity between the fine and coarse solutions, (Debreu et al., 2012).

The mean dynamic topography for the external domain of both DELAG-III and DELAG-IV are compared with AVISO in Figure 4.6.1. On the shelf, the southward flowing boundary current is well represented in both experiments. In Figure (4.6.1a) the nearly northwestwards current (extension of the Southeast Madagascar Current), merges the boundary current northeast of the Bight. This behaviour is similar to the case of DELAG-I described in section 4.2, where this current separates the region in two distinct areas, one consisting of a closed loop northeast of the domain and the other to the southern part of the domain. However, the latter consists of two small closed loops in this case. In another hand, DELAG-IV (Figure 4.6.1b), shows that the extension of the Southeast Madagascar Current flows westwards (no-tilting), to merge with the boundary current off Delagoa. It is somewhat wider in comparison with its counterpart in Figure (4.6.1a).

Its characteristics to contribute into the boundary current from around 24^oS (off Inhambane) is also noticeable in the model with tides (DELAG-IV). The closed loops of the mean SSH are not apparent in this case. This is in agreement with the results obtained using DELAG-II, section 4.5, in which the addition of tides implied an improvement toward AVISO (Figure 4.6.1c), whose representation of the westwards extension of Southeast Madagascar Current is not tilted toward northwest.

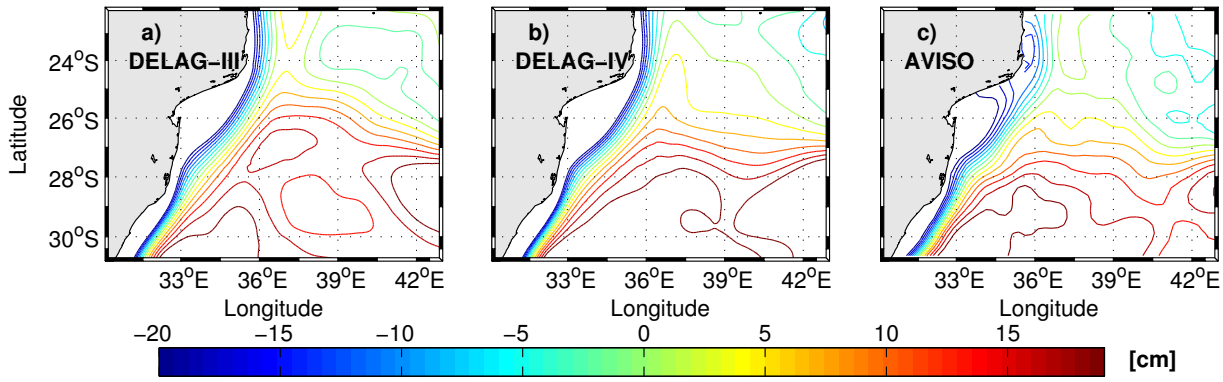

Figure 4.6.1: Mean SSH (1 contour for every 3cm), determined for the external domains of the models without tides (DELAG-III) a), tides (DELAG-IV) b) and AVISO in c).

In both the internal domains, Figure 4.6.2 the mean dynamic topography shows a closed contour inside of the Bight (Figure 4.6.2a,b). In the case of tides, this closed contour is much wider (Figure 4.6.2b). The presence of the closed contour in both experiments (DELAG-III and IV), shows the importance of nesting in the reproduction of fine structure (mesoscale) inside of the Bight, mainly cyclonic eddies, although anticyclones are also resolved, as it is shown in the next chapter. The widening of the closed loop inside of the Bight, in Figure (4.6.2b) reflects the increase of these features in the case of tides, while the boundary current is relatively narrow in this case, possibly because it gets more intensified and more constrained to the shelf in tides (DELAG-IV), as demonstrated above.

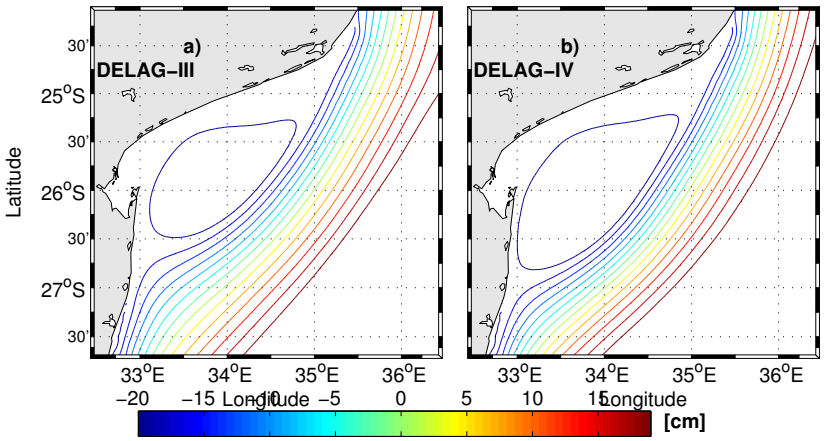

Figure 4.6.2: Mean SSH (1 contour for every 3cm), determined from the internal domains of the models without tides (DELAG-III) in a) and tides (DELAG-IV) in b).

The mean eddy kinetic energy for both external domains is shown in Figure 4.6.3. In no-tides Figure (4.6.3a) it shows similarities with that for DELAG-I portrayed in section 4.2. The $500\,cm^2.s^{-2}$ contour separates the region dominated by mesoscale processes from the rest of the domain. In tides (DELAG-IV) it is similar to DELAG-II analyzed in (section4.5), where the mesoscale activity from the east is relatively weak, with the $500\,cm^2.s^{-2}$ contour indicating the pathway of the anticyclonic eddies from the north. This contour, which follows the coast, also shows an intensification of the eddy activity inside of the Bight, with the usual path of the coastal counter-current highlighting more activity in the models (Figure 4.6.3a,b), by comparison with AVISO (Figure 4.6.3c). This apparent increase in eddies activity inside of the Bight, is possibly due to the improvement of the solution of the two-way nesting approach in the common area covered by both the internal and external domains. Likewise, it shows an increase in the eddy kinetic energy in comparison with DELAG-I and DELAG-II, non nested domains described above. Interestingly, in no-tides (DELAG-III) the coastal counter-current is marked by high values of mean eddy kinetic energy, which increases with tides (DELAG-IV). This appears to be in agreement with the increase of the intensity of the mean currents with tides, as diagnosed in (section 4.5).

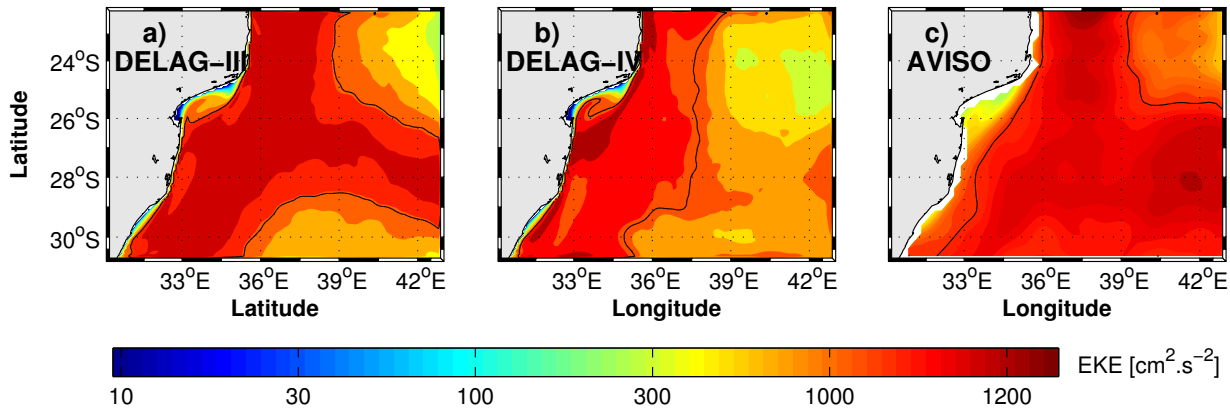

Figure 4.6.3: Eddy kinetic energy determined from the external domains of the Models: a) no-tides (DELAG-III) and b) tides (DELAG-IV). In c) is shown is presented the AVISO EKE, The black lines in all represents the $500\,cm^2.s^{-2}$contour.

The mean EKE for both the internal domains of no-tides (DELAG-III) and tides (DELAG-IV) experiments is illustrated in Figure 4.6.4. Overall, both tides and no-tides (Figures 4.6.4a,b), show all the features found in the corresponding external domains (Figures 4.6.3a,b) analyzed above, concomitant with the ability of the two-way nesting in improving the representation of the dynamics in the area with more than one level of grid points as indicated by Debreu et al. (2012). The big implications of forcing with tides was a slight increase in the eddy activity along the areas usually impacted by the coastal counter-current and the southward flowing current, with the region where the latter impinges into the African coast showing the highest rates of eddy activity (Figures 4.6.4b). In Figure (4.6.4b) the center of the Bight shows EKE around $500\,cm^2.s^{-2}$, wheres in its counterpart (Figure 4.6.4a), it is relatively lower. The tidal forcing was also able to eliminate the region of high rate of eddies activities at 35^oE meridian, seemingly around the northernmost edge of the Mozambique ridge, (Figures 4.6.4a). Further details of the impact of nesting will be presented focusing in the models without tides in the next chapters, whereas tides is relegated to future works.

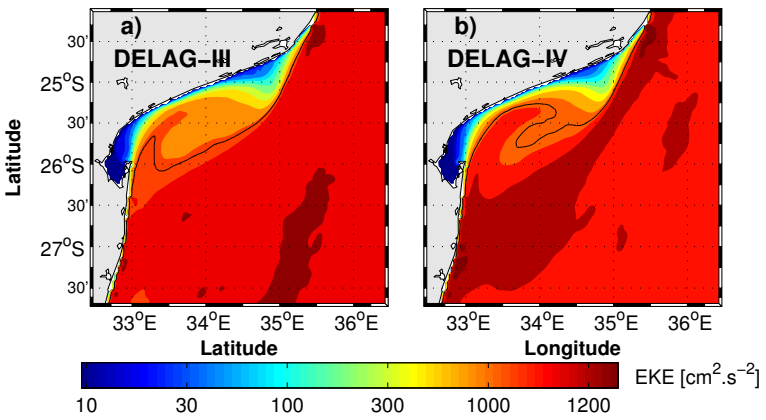

Figure 4.6.4: Mean eddy kinetic energy calculated from the child domains of the models: a) no-tides (DELAG-III) and b) with tides (DELAG-IV). The black contours represent the isoline of $500\,cm^2.s^{-2}$.

4.7 Discussions and conclusions

In this chapter, the mean state in Delagoa Bight is investigated recurring to several ROMS experiments, of the Delagoa Bight configuration. At the beginning, the (DELAG-0, I and II) are analyzed. The experiment forced with WOA (DELAG-0), was quickly rejected because of its miss-representation of the regional circulation. This problem is thought to have been caused by the low resolution of the WOA data set, used as lateral boundary condition. Its associated difficulty in reproducing accurate geostrophic currents along the open boundaries, that could represent well the dominant mesoscale features, seems to have affected this simulation. Therefore, the circulation produced by DELAG-0 was characterized by absence of eddies. The second experiment (DELAG-I), which was forced with the SWIM data set (Halo et al., 2014a), showed an improvement in the representation of the regional circulation, which was characterized by slight similarity with the observations. Therefore, further analyses are performed from this experiment along the next chapter. The third experiment as well (DELAG-II), was used to show the effect of tides in the thermohaline circulation (water masses representation), and the regional currents. Regarding the thermocline structure it shows similarity with its counter part without tides. Therefore, the experiments with tides and no-tides may be used interchangeably. Indeed, it was also noted that the experiment DELAG-II, doesn't give considerable changes in the local dynamics, although along the shelf it shows a slight increase of the mean kinetic energy (speed), by comparison with the reference experiment. Finally, the effect of improvement of resolution on the mean state was assessed, to show that both the coastal counter-current and the southward boundary current are important features in the Delagoa Bight circulation.

Concerning the thermohaline structure in the Bight, it has been noted that the properties in the upper layer, change considerably in a season to season basis. This behaviour is in agreement with the previous studies, that showed seasonal variations in the surface, in association with the changes in the insolation (Kyewalyanga et al., 2007; Lamont et al., 2010). Nevertheless, below $100\,m$ depth no significant changes occur. This result is consistent with the findings of Lutjeharms and Jorge da Silva (1988) who highlighted that the mixing in the Bight was strong in the upper layers.

The lee eddy, the most prominent feature in the local circulation, is not consistent in the mean circulation, but it may appear in both seasonal and annual means. It has been noted that in some means it appears as a very narrow feature confined to the shelf. This is due to the impact of the

anticyclones (mainly rings from the north) whose western edges sometimes affect the Bight. These anticyclones are seen in isolated events sweeping the lee eddy through the respective outermost edges. The miss representation of the lee eddy in some averages also agrees with Lamont et al. (2010), who introduced the concepts of presence and absence for the lee eddy in the Bight. The next chapter, will present the frequency of occurrence of the DBLE in all model simulations and observations.

Along the next chapter both conditions will be investigated by recurring to the composite analyses and the eddy detecting and tracking system. However, at this stage, it is important to underline that the mean circulation in the Bight is dominated by a non well organized cyclonic eddy, whose consistence improves with depth, suggestive of its persistence in the lower levels by comparison with the surface. The coastal counter-current in the seasonal averages is weaker in comparison with the observed. Its signature in the averages reveals the dominance of the lee eddy in the lower levels, in agreement the previous studies (Lamont et al., 2010; Lutjeharms and Jorge da Silva, 1988). In the mean, the upper layer (first $20\,m$) showed that a weaker southward current dominates the whole shelf for no-tides experiment (DELAG-I), with the coastal counter-current appearing below. This clearly shows that the reversals of the counter-current, is more dominant in the surface layers at least in the perspective of no-tides simulation. Addition of tides in the model showed an increase of the southward flowing boundary current speed and by consequence to the coastal counter-current. Comparison of the T-S diagram of both simulations showed that the changes induced by tides are insignificant in the thermocline structure of the region.

The consistency of the boundary current along the shelf in the region, is obvious according to the model with tides, despite its intermittency and meanderings. The meanderings are due to the prevalence of transient mesoscale eddies as it is shown in the next chapter. The presence of the Mozambique Current as a boundary current has been put into question by Sætre and Jorge da Silva (1984). These analyses showed consistency of this current along the Delagoa Bight latitudes, and that is noted in most individual model and satellite snapshots. The southward flowing boundary currents at $100\,m$, revealed its strengthening from the latitudes of the Bight toward the south. Lutjeharms (2006a) in his (Figure 3.30) highlights the importance of the Agulhas Current recirculation and the whole South Indian Ocean gyre in this region. The climatologies based on both models, the satellite SST and geostrophic currents, show consistency of the southwards currents from the Delagoa Bight latitudes. Perhaps the high resolution of the model products analyzed

here, turn it possible to infer the boundary current here. The previous studies, agree all in the consistency of the southward current in this region, (Lutjeharms and Jorge da Silva, 1988; Lamont et al., 2010). Lutjeharms et al. (2012), demonstrated that although the Mozambique Current is intermittent, it can occasionally be present as a boundary current. Here, it is speculated that the prevalence of this flow is due to the merger between the flows from the east and north. The transports associated with this boundary current will be discussed in the next chapter.

The center of the Bight is very dynamic. Based on SSH and other dynamic parameters, it has been noted that the changes in the Bight are large. This is linked with the impact of mesoscale activity namely the anticyclones from the north, whose interaction with the shelf causes variations in the center of the Bight. These variations are predominantly in the range of 1 to 1.5 months and are characterized by shifts of SSH between high and low, indicative of the presence and absence of the lee eddy, respectively. The mesoscale features from the east are also likely to import water masses into the Bight, but their observed and modelled trajectories showed that they move generally from far away of the Bight.

The region off Delagoa Bight is dominated by the merger of anticyclonic eddies. The frequency of the merger is not well known. Overall, mergers of anticyclonic eddies has been reported in the Channel (Ternon et al., 2014). Near the shelf, they are characterized by elongated anticyclones interacting with the shelf, or by big rings when the merger is away from the coast.

The seasonal averages have shown that the southeastern side of the domain is saltier, by comparison with the center of the Bight and its northeastern sector, where a clear intrusion of fresher waters masses from the north prevails in all seasons, but with slight reduction in winter and spring. This behaviour seems to be correlated with the wind stresses that tend to accumulate water toward the coast during these seasons as shown in the previous chapter (wind stresses). Analyses of trajectories of the mesoscale eddies and Hovmöller plots of SSH showed that the dominant water masses in Delagoa Bight are from the north. This is because the relatively weak SSH anomalies that reach the Bight from the east are not likely to constitute the major source of water masses in the Bight. Indeed, the modelled anticyclonic eddies from the east tend to move from far away from the Bight as they flow toward the Agulhas Current region, whereas the cyclonic features are short lived, and fade off Delagoa Bight. Despite the wide range of diameters for both mesoscale types, they are not able to transfer great content of their saltier water masses into the Bight. This, is in agreement with the previous studies (Lutjeharms and Jorge da Silva, 1988; Lamont et al.,

2010), that indicate lower contents of water masses from the east inside of the Bight.

The two-ways nesting application emphasizes an improvement in the representation of the dynamics in the Delagoa Bight region. Such enhancement is characterized by an increase in the eddy kinetic energy inside the area of the child domains. Furthermore, nesting allows a better representation of both the southward boundary current and the coastal counter-current, the northwards branch of the DBLE. Both features determine the consistency of the lee eddy in the center of the Bight. The addition of tides also shows a slight increase of the eddy activity, which is corroborated by the presence of smaller features discussed in the next chapter.

The weak signature of the lee eddy noted in the averages, and the dominance of the confluence of flows from the north and east in the Bight, resulted in the decision of introducing the concept of the classic lee eddy, to refer to the cyclonic lee eddy with characteristics of the lee eddy found in literature, whose center is located at $26^oS, 34^oE$ (Lutjeharms and Jorge da Silva, 1988; Lamont et al., 2010). The investigation of the structure of such feature in the next chapter, will be based on composite analyses with support of the eddy detecting and tracking system of (Halo et al., 2014a).

Chapter 5

Cyclonic Eddies in the Delagoa Bight region

5.1 Introduction

A weak representation of the modelled DBLE in the annual and seasonal means has been noted in the previous chapter. This behaviour suggests that the lee eddy is not a permanent feature, as demonstrated by Lamont et al. (2010). An early study alluded to the absence of a remarkable SST signature of the lee eddy in most of satellite images in the Bight, with only 10% of clear SST images showing its prevalence (Lutjeharms and Jorge da Silva, 1988). This weak representation of DBLE seems to reflect the prevalence of other regimes of circulation in the Bight, and the modelling approach used here, is expected to shed light into such dynamics.

In situ observations, indicated that the most dominant feature of the local circulation, the DBLE, generally fills most of the continental shelf and the terrace landwards of the southward flowing current, when it is present, with a relatively stronger signature below $100\,m$ depth, (Lutjeharms and Jorge da Silva, 1988). The dynamics in the Mozambique Channel is quite distinct and variable, with the mesoscale features dominating the circulation, mainly the anticyclonic eddies generated to the north of the Channel (Biastoch and Krauss, 1999; Harlander et al., 2009; Hancke et al., 2014). Likewise, the circulation in the Delagoa Bight is deemed to be complex (Lutjeharms and Jorge da Silva, 1988; Lamont et al., 2010). Nonetheless, most of the aspects of the local circulation remain hindered by the limitations in the resolution of the satellite data, such as those used by Lutjeharms and Jorge da Silva (1988), and also due to resources limitations to carry out in situ

observations in this region.

Delagoa Bight is dynamically special, thanks to its location, which is under influence of the anticyclonic eddies originated from the north and east. The former, are known to move southward locked to the African continental shelf (Biastoch and Krauss, 1999; Quartly and Srokosz, 2004). Their edges are associated with the transport of rich nutrient waters from the shelf toward the oligotrophic mid Channel waters and vice-versa (Tew-Kai and Marsac, 2009; Roberts et al., 2014). They are also deemed to influence the circulation in the Bight as they move southward (Quartly and Srokosz, 2004; Lamont et al., 2010). The latter, were not well reproduced in Biastoch and Krauss (1999) eddy permitting model but more recent studies have shown anticyclonic and cyclonic anomalies propagating from the southern tip of Madagascar towards the southwest (de Ruijter et al., 2005; Quartly et al., 2006; Cossa et al., 2016).

Tew-Kai and Marsac (2009) related the high level of productivity in the Bight with the lee eddy spawned by the passing anticyclones (Lamont et al., 2010). In the other hand, in situ measurements showed that the productivity was very high in the northeastern end of the Bight, (Barlow et al., 2008). Although that area is far from the usual location of the DBLE, the productivity there was linked to cyclonic activity, (Barlow et al., 2008). Nevertheless, there is no proof in literature of the presence of cyclonic activity there. Martin (1981) presumed that there was a likelihood of presence of more than one cyclonic features in the Bight. The wide flat area northeast of the Bight, possibly the former debouchment of the Limpopo river, is likely to hold a cyclonic circulation (Martin, 1981).

The objective of this chapter is to present the modelled Delagoa Bight lee eddy and its statistics. The effect of improvement of the model resolution will be examined by comparing results of the available simulations. The fine resolution is expected to shed light in the complex circulation in the Bight. A new feature dubbed Inhambane Cyclone will be presented, including its statistics. This cyclone, behaves like a pulse and was investigated by Cossa et al. (2016). The impact of the anticyclones and pulses in Delagoa Bight will be discussed considering that both interact with the Bight as they move southward. The chapter will be organized in a following manner: In section 5.2, the modelled DBLE is presented. This is followed by the presentation of the effect of improving the resolution in section 5.3. Both sections include the statistics of DBLE and the analysis of the thermocline structure, but section 5.3 includes the analysis of small scale features, namely, cyclonic and anticyclonic cores in the Bight, which are estimated using the same tool

(eddy detection and tracking system). In section 5.4, the Inhambane Cyclones are presented. Their thermocline structure, main trajectories and impact in the Delagoa Bight are analyzed. Finally, the synthesis and discussion is given in the last section of the chapter.

5.2 Modelled Delagoa Bight lee eddy

In this section the cases when the lee eddies in the model (DELAG-I) are present or absent, are compared with those from satellite observations. Snapshots of geostrophic velocities, overlaid on the corresponding MDT were created for both the model and AVISO to aid in the identification of the DBLE presences or absences. While the model was designed to keep the averages in each three days (ten files per climatological month), AVISO weekly data were time interpolated to guarantee the existence of data at this same interval. Therefore, $8\,years$ of data for both the model and satellite were available. For AVISO, these averages were created for the period between 2001 and 2008, whereas for the model the data result from the removal of the 2 initial years out of the $10\,years$ of the model, in association with the necessary model spin-up at the beginning of the simulations, as mentioned in chapter 3.

A total number of 960 snapshots are possible in $8\,years$, with a maximum of 80 snapshots in each climatological month. The number of presences and absences in each month are expressed in percentage, using the formula $(steps/snapshots) \times 100$, where *steps* represents the number of presences per climatological month and *snapshots* represents the total possible number of frames in each model simulation. The model experiment (DELAG-I) and satellite (AVISO) acBBLE presences are compared in Figure 5.2.1. Is has been noted that the number of presences/absences is not season dependent. In AVISO (red) the lee eddy tends to be more present than in the model DELAG-I (blue). Indeed, the reverse is true for the cases with the lee eddy absent. In the model, the lee eddy was absent during 41% of the time, as compared to 35% in the AVISO observations. The lack of seasonality in the DBLE presences led to the construction of composites to carry out the analyses of the thermocline structure of the modelled lee eddies. The classic lee eddies are usually found in the center of the Bight at $34^oE, 26^oS$ as referred to in several studies, (Lutjeharms and Jorge da Silva, 1988; Lutjeharms, 2006a; Lamont et al., 2010). Furthermore, more they are consistent below $100\,m$ (Lutjeharms and Jorge da Silva, 1988; Quartly and Srokosz, 2004; Lamont et al., 2010). This rationale, was used to develop a criterion for the selection of snapshots necessary

to form such composites. According this criterion, the classic lee eddy is centered at $26^o, 34^oE$ in a box whose size is 0.5^o. Therefore, all the eddies that temporarily or semi-permanently reside inside of this box were considered as classic DBLEs. The case of absences are those in which no lee eddy is found inside of the box.

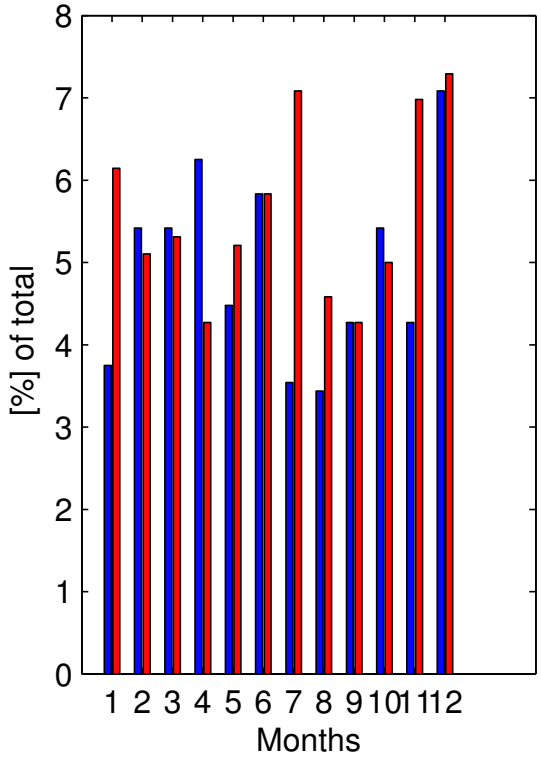

Figure 5.2.1: Percentage of DBLEs occurrence per climatological month in the model (blue) and AVISO (red).

Figure 5.2.2 shows the temperature, salinity and current fields at $50\,m$ and $100\,m$ depth, for the DELAG-I composite, in the case of DBLE presence. At $50\,m$ depth, the lee eddy is conspicuous at $26^o, 34^oE$ as suggested through the $22-23^oC$ isotherms, consistent with the previous studies (Lutjeharms and Jorge da Silva, 1988; Lamont et al., 2010). The 24^oC isotherm offshore of the Bight, shows a strip of warm water coming from the north, flowing between the $500-1000\,m$ isobaths towards the northern Agulhas Current (Lutjeharms, 2006a). The rest of the domain is cooler but not as cool as the center of the lee eddy, (Figure 5.2.2a). The salinity distribution is fairly uniform inside of the Bight and suggests efficient mixing at this depth. The southward flowing boundary current is marked by the $35.25-35.3\,psu$ isohalines (Figure 5.2.2b). It meanders southward as it reaches the coast, with part forming the coastal counter-current, the northward branch of the DBLE (Figure 5.2.2c). The southeastern part of this domain is characterized by two anticyclonic circulations, one along the 26^oS latitude with its center out of the domain, whereas the other is found along the meridian 34^oE, with its center located downstream. Due to the relative

vicinity of these structures, the whole eastern side of the domain is considered as anticyclonic in the composite.

At 100 m depth, the temperature distribution shows a well marked southward boundary current in the $19-20^oC$ isotherms, while the lee eddy is revealed in the $17-18^oC$ isotherms. The center of the eddy is cooler as expected for a cyclonic eddy (Figure 5.2.2d). The anticyclonic region in the east of the domain is warmer than 20^oC. In salinity, the 35.2 psu isohaline shows the lee eddy in the Bight (Figure 5.2.2e) while the southward flowing boundary current is marked by the $35.25-35.3\,psu$ isohalines. Thus, there is no significant changes in the salinity field between 50 and 100 m depths. The anticyclonic region is relatively saltier in comparison with the Bight.

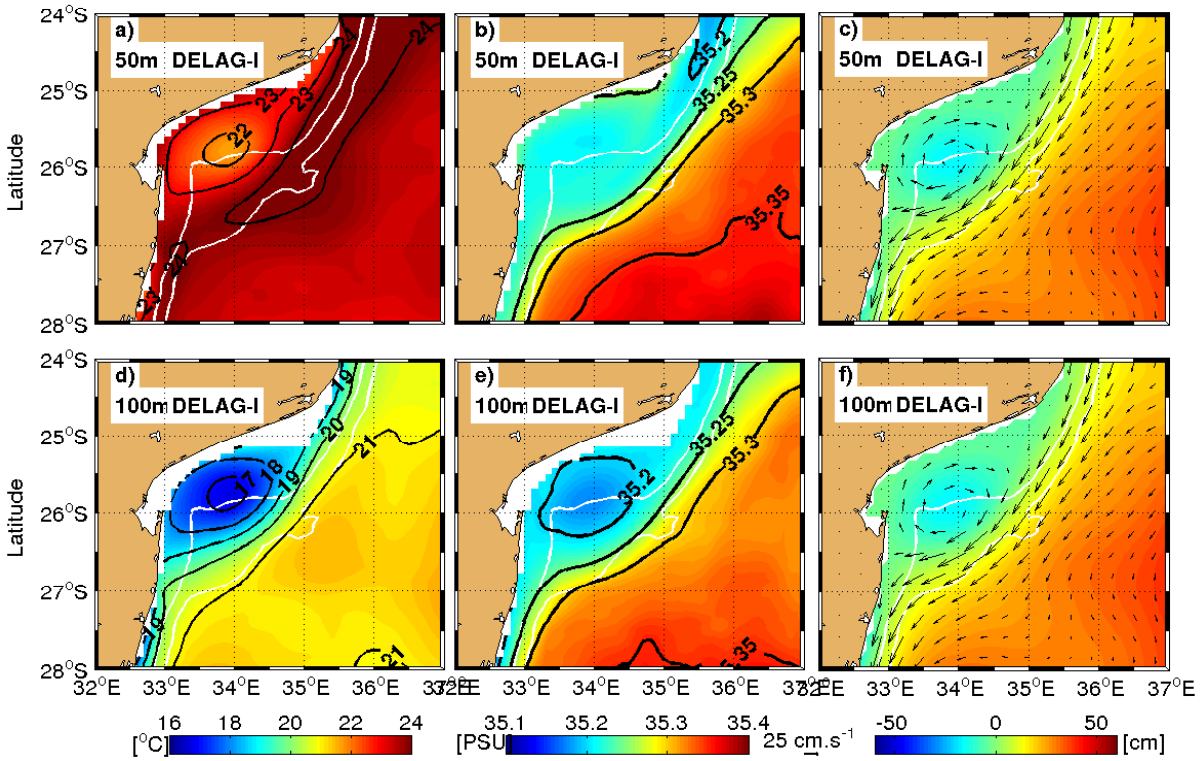

Figure 5.2.2: Composite of the classic lee eddy in the Delagoa Bight based on model (DELAG-I). Horizontal section of Temperature in a), Salinity and Currents overlaid on SSH at 50 m in c). The same variables are represented at 100 m, in d), e) and f), in the same order. The white lines are the 500 and 1000 m isobaths.

The distribution of properties at 200 and 400 m depths is given in Figure 5.2.3. The southward flowing current follows the $15-16^oC$ isotherms along the $500-1000\,m$ isobaths. The lee eddy is marked by the 13^oC isotherm in the center of the Bight. The southeastern part of the domain is characterized by temperatures greater than 17^oC (Figure 5.2.3a). For the salinity field the 35.2, 35.25 and 35.3 psu isohalines mark the southward flow, whereas the lee eddy is constricted inside the 35.1 psu isohaline. The water within the core of the lee eddy is fresher than the rest of the domain, particularly the anticyclonic region of the domain (Figure 5.2.3b). The current

distribution at both depths is very similar (Figure 5.2.3c,f). At 400 m depth the lee eddy is marked by the 10^oC isotherm, whereas the anticyclonic region is warmer than 13^oC. The southward flowing boundary current is marked by the $11 - 12^oC$ isolines, (Figure5.2.3d). In salinity, the 34.9 psu isohaline marks the lee eddy, whereas the 35.0, 35.05 and 35.1 psu isohalines mark the southward flowing coastal current. The southeastern part of the domain is saltier, (Figure 5.2.3e).

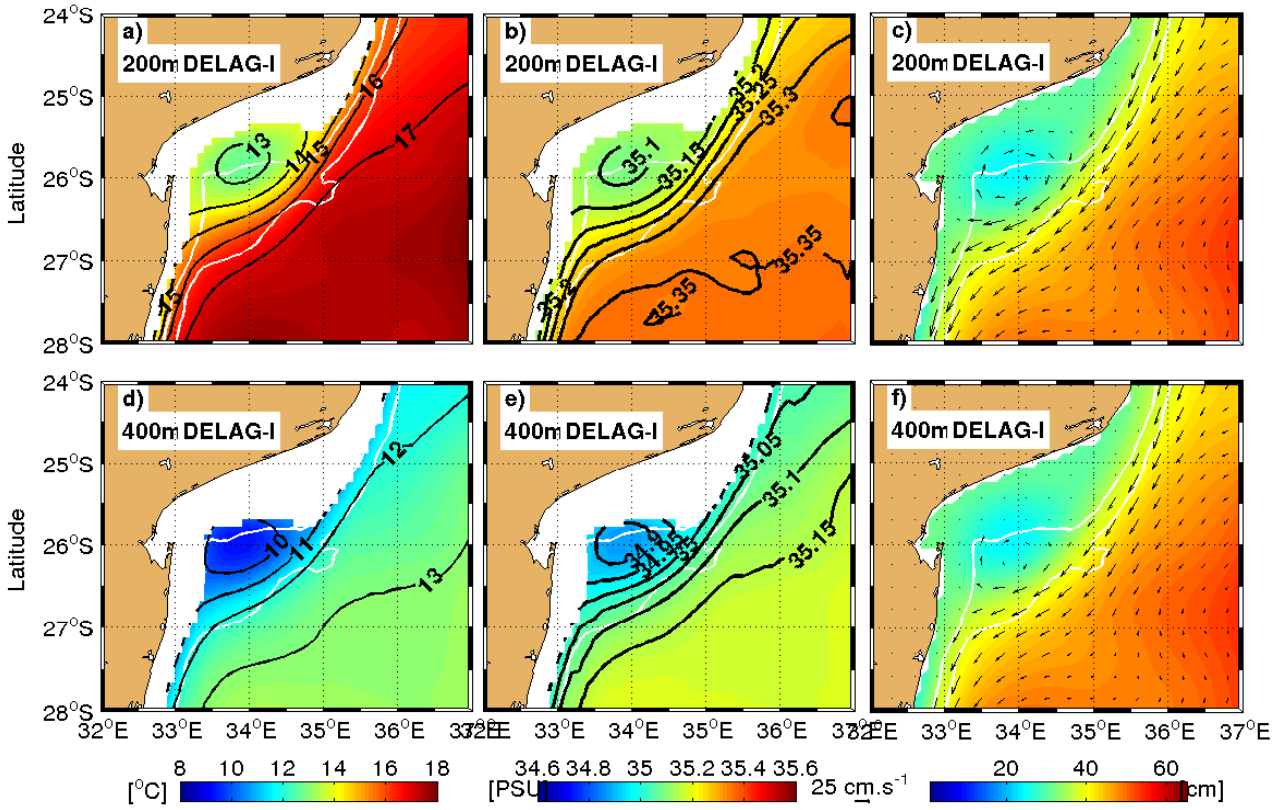

Figure 5.2.3: Composite of the classic lee eddy in the Delagoa Bight based on model DELAG-I. Horizontal section of Temperature a) Salinity in b) and Currents overlaid on SSH in c) at 200 m. The same variables are represented at 400 m, in d) e) and f), in the same order. The white lines are the 500 and 1000 m isobaths.

The composite for DELAG-I, in the case of absent DBLE at 50 and 100 m depth, is given in Figure 5.2.4. At 50 m, depth the core of the southward flowing current encompasses the $500 - 1000\,m$ isobaths and is marked by the 24^oC isotherm. It flows towards the northern Agulhas Current, with its offshore side marked by a large anticyclonic region, whose center is located at $27.5^oS, 35.5^oE$. Its temperatures in the core is greater than 24^oC (Figure 5.2.4a). The southward flowing boundary current flows across the Bight promoting removal of water towards downstream. Interestingly, the area along the shore is relatively cooler than offshore, suggestive of intrusion of cool water masses from the northeast. This is more noticeable in the salinity field, where the fresher water from the north flows along the coast (Figure 5.2.4b). It is marked by the 35.2 psu isohaline, with the band of $35.25 - 35.3\,psu$ encompassing the core of the whole southward flowing boundary current

at this depth. The eastern part of the domain is characterized by salinity greater than 35.3 psu, (Figure 5.2.4b). The SSH field shows a strip of lower values along the coast, and higher over the rest of the region (Figure 5.2.4c). At 100 m depth, the Bight is still cooler along the coast than in the rest of the region. The 18, 19 and 20^oC isotherms mark the core of the southward flowing current, whereas the anticyclonic region is dominated by temperatures greater than 21^oC (Figure 5.2.4d). For salinity, the $35.25 - 35.3\,psu$ isohalines separate the fresher coastal region from the saltier anticyclonic dominated region (Figure 5.2.4e). The currents at 100 m depth (Figure 5.2.4f), are similar to those at 50 m depth.

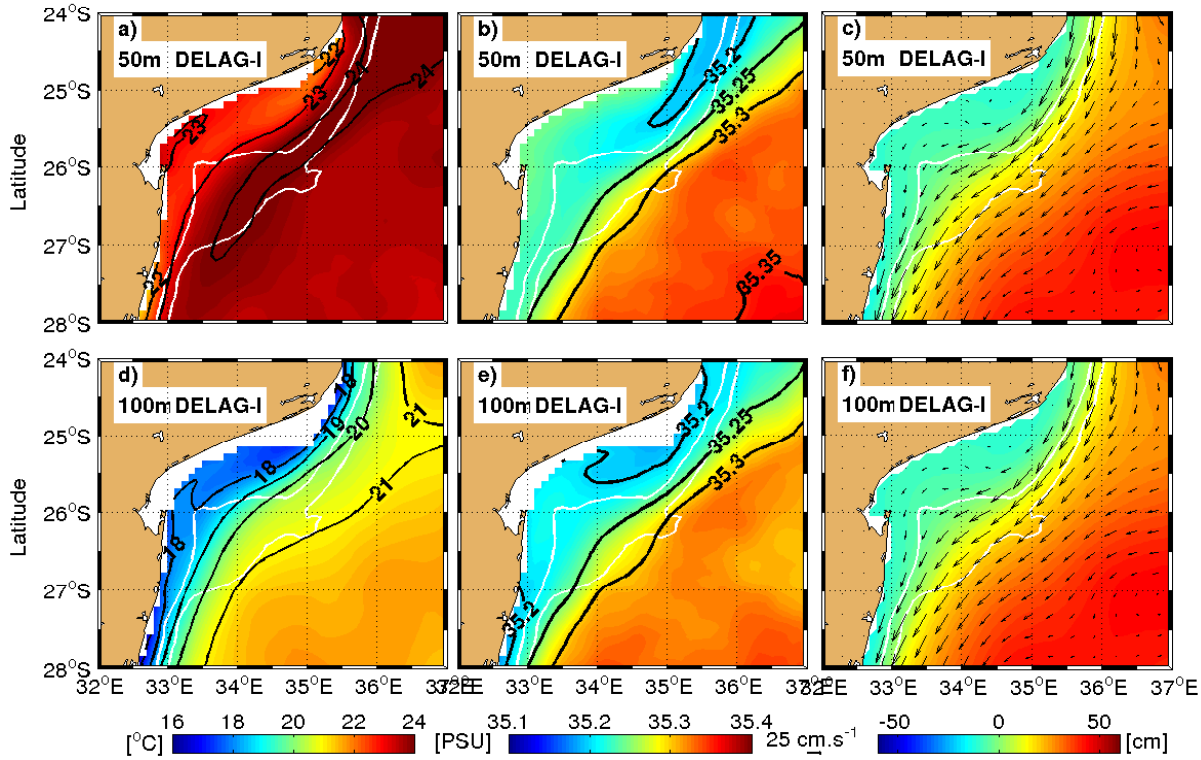

Figure 5.2.4: Composite of the lee eddy absences in the Delagoa Bight. Horizontal section of Temperature a) Salinity in b) and Currents overlaid on SSH c) at 50m. The same variables are represented at 100m, in d) e) and f). The white lines are the 500 and 1000 m isobaths.

At 200 and 400 m, the condition of the lee eddy absence for the DELAG-I composite is depicted in Figure 5.2.5. The configuration of the temperature and salinity fields are similar to those presented for 50 and 100 m depths, with an exception that the southward flowing coastal current is marked by cooler $14 - 15^oC$ isotherms. The anticyclones dominated region is warmer than 17^oC (Figure 5.2.5a). In salinity, the southward current is marked by the 35.15, 35.2, 35.25 and 35.3 psu, whereas the anticyclonic region contains values greater than 35.3 psu, (Figure 5.2.5b). The fields of currents and SSH emulate these features (Figure 5.2.5c-f). At 400 m depth, the 11 and 12^oC isotherms mark the southward flowing current, which separates the cooler coastal region

from the warmer anticyclonic region east of the Bight (Figure 5.2.5d). In salinity the southward flowing current is marked by 34.95, 35, 35.55 and 35.1psu isohalines, which separate the fresher coastal region from the anticyclonic region (Figure 5.2.5e). The presence of fresher water in case of DBLE absence appears to be due to the intrusion of fresher water from the north.

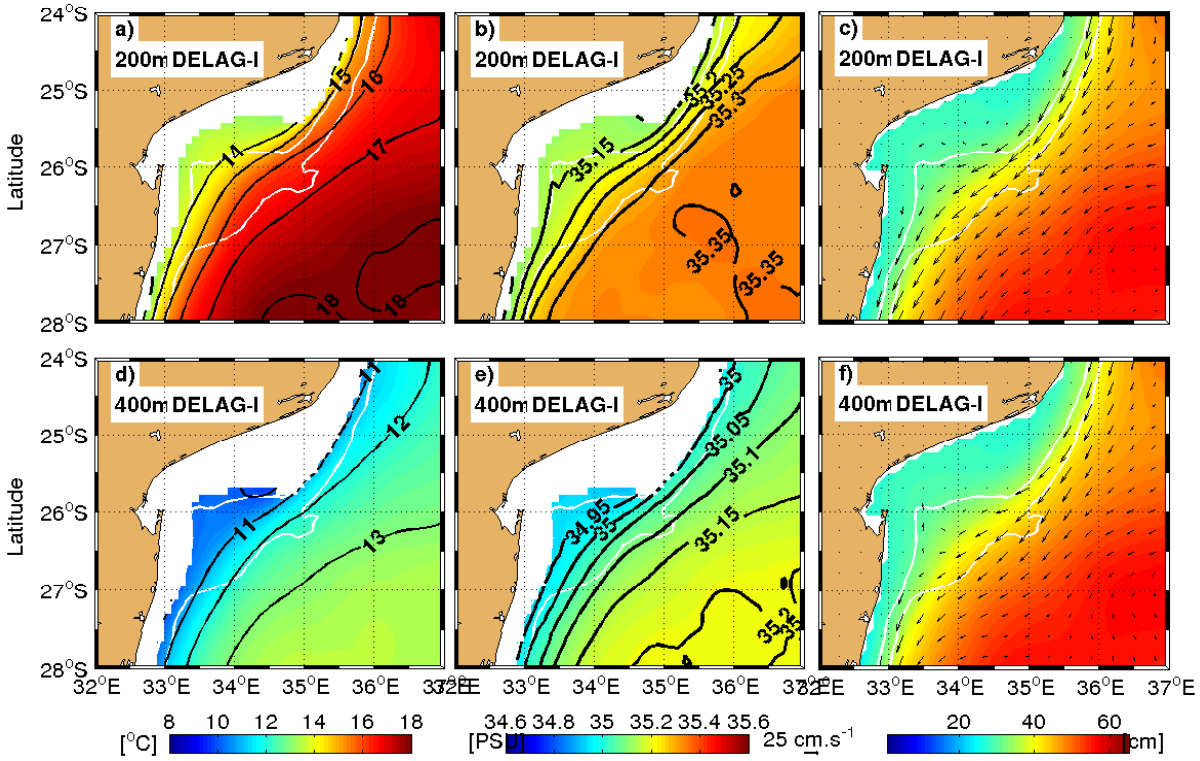

Figure 5.2.5: Composite of the lee eddy absences in the Delagoa Bight ($200-400\,m$). Horizontal section of Temperature a) Salinity and Currents over-layered by SSH at $50\,m$. The same variables are represented at $100\,m$, in d) e) and f). The white lines are the 500 and $1000\,m$ isobaths.

The difference between the composites of present and absent lee eddy for DELAG-I at $100\,m$ depth is given in Figure 5.2.6. In Figure (5.2.6a) the currents overlaid in SSH show clearly the area dominated by the lee eddy at $26^oS, 34^oE$. It is characterized by negative values and a conspicuous cyclonic circulation with the coastal counter current indicating a continuation towards the northeastern part of the Bight. South of the domain, the cyclonic feature and the negative values of SSH at $27.5^oS, 35.5^oE$ reflect the prevalence of anticyclonic circulation in the case of Delagoa Bight absent in that area. The high SSH in the coast of Ponta D'Ouro at 27^oS, shows that the positioning of an anticyclonic feature or even an increase of SSH in that location, coincides with the stability of the lee eddy in the Bight, (Figure 5.2.6a). This is noted in most of the model snapshots. In the temperature field, (Figure 5.2.6b) the center of the Bight at $26^oS, 34^oE$ is characterized by a negative difference of -2^oC. This value reflects the predominance of cooler upwelled water in the composite of lee eddy present relative to absent. At $27.5^oS, 35.5^oE$ the

negative values seem to reflect the fact that the anticyclonic features dominating the circulation under lee eddy absences there, is from the north of the Channel whereas the case of presences is governed by the cooler features from the east. In salinity (Figure 5.2.6c), the features mimic the temperature, with the region at $27.5^oS, 35.5^oE$ showing a positive difference due to the preponderance of the salinity from the east over that from the north in the composite of lee eddy presences. At this point, it is important to highlight that the eastern part of the domain will be referred to as the anticyclonic region, despite the known differences in the exact positioning of the anticyclones in both composites, as explained above.

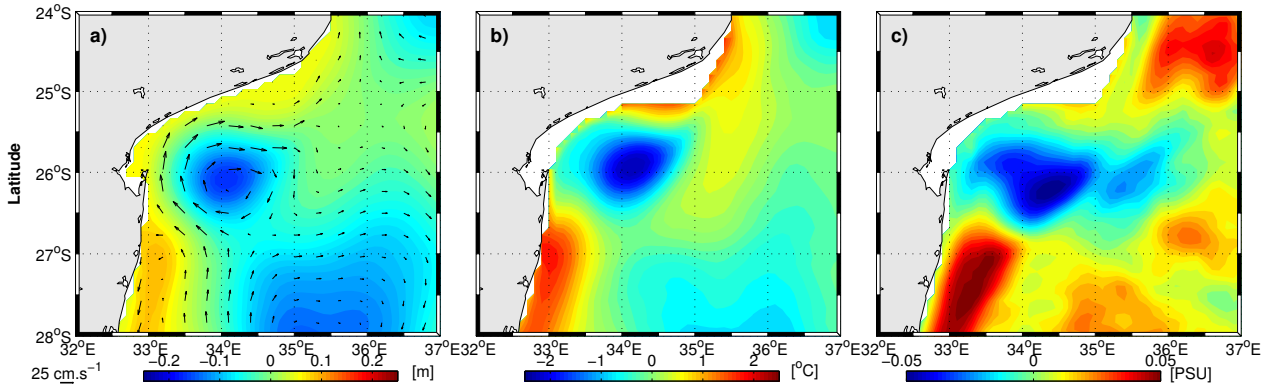

Figure 5.2.6: Difference between the lee eddy composite of presences and absences in the model (DELAG-I), at $100\,m$. In a) are presented currents overlaid on SSH, in b) the temperature, and finally the salinity in c).

The surface geostrophic currents were estimated from AVISO MDT using equations in A.3, Figure 5.2.7. The case with DBLE is shown in (Figure 5.2.7a). The southward flowing boundary current is preeminent when the lee eddy is present. It meanders to accommodate the lee eddy before bifurcation in the point it impinges into the coast at 27^oS (between the coast and the central terrace), with part of the flow reversing its direction towards the north through the coastal zones off Maputo. The other part flows towards the northern Agulhas Current (Lutjeharms, 2006a). The bifurcation of the southward flowing current seems to be promoted by the positioning of the anticyclones with the one locked to the coast around 27^oS, sustaining the meandering of the southward flowing current. In the case of DBLE absences (Figure 5.2.7b), this current flows along the center of Bight from the northeast, with its edge covering the whole coastal zone. The SSH in the Bight is lower in comparison with the surrounding environment. Again the positioning of the anticyclones seem to play a great role in the behaviour of the geostrophic circulation. In fact, under lee eddy absent in the Bight, the southwards flowing boundary current is generally parallel to the coast, and this seems to be forced by the positioning of the anticyclones, far away from the Bight.

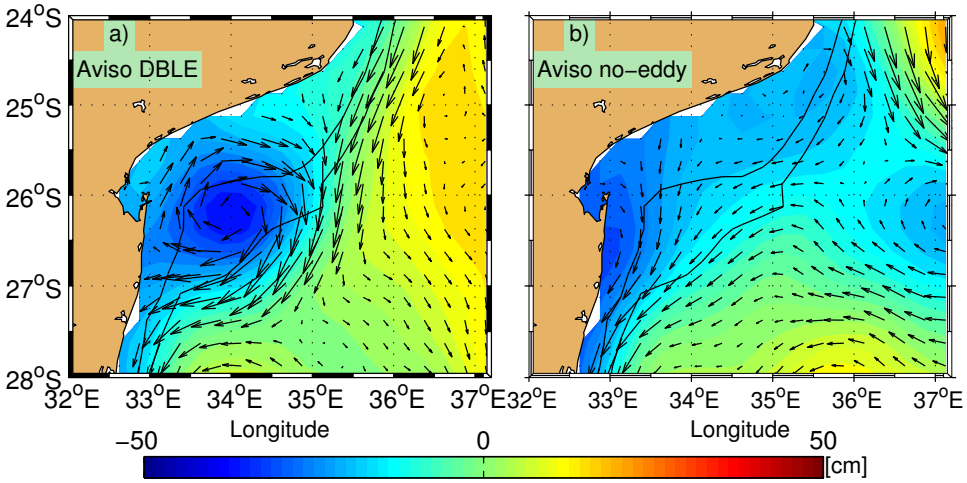

Figure 5.2.7: AVISO geostrophic currents (black arrows) calculated from the composites with DBLE present, overlaid on the corresponding SSH in a), and for the DBLE absent in b). The black lines are the 500 and 1000 m isobaths.

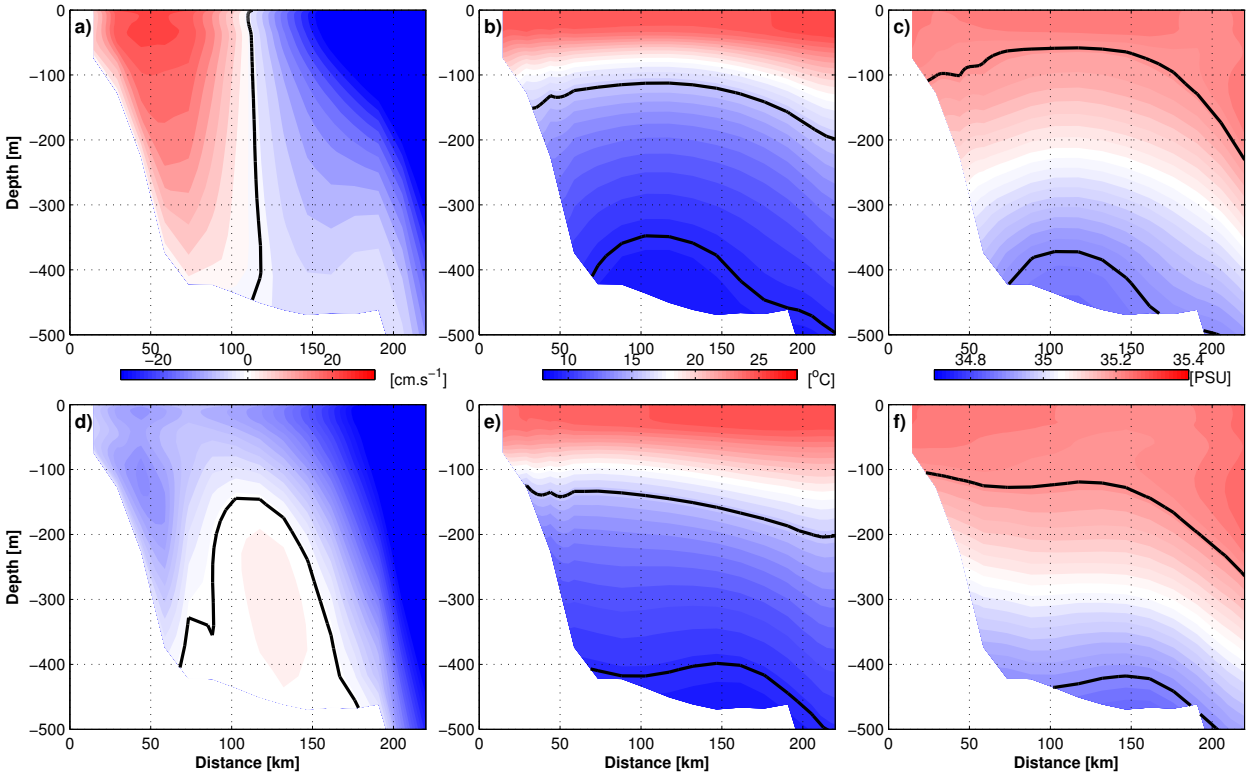

Figure 5.2.8: Vertical sections of the composites of modelled (DELAG-I) meridional currents (a and d), temperature (b and e) and salinity (c and f), across the Delagoa Bight main section at 26°S, in the case of the presence (top column) or absence (bottom). The black lines indicates the zero isotach (a and c), whereas in (b and e) it shows the 10 and 16°C isotherms and finally the 34.9 and 35.2psu isohalines in (c and f).

The vertical section for DELAG-I composite is shown in Figure 5.2.8. The meridional velocity in the case of DBLE present, shows a strong northward flow with a maximum of 25 $cm.s^{-1}$ close to the surface. This flow covers the whole shelf in the Bight and represents the coastal countercurrent, the northward flowing current which forms the coastal branch of the lee eddy when it is present. The vertical black line at 100 km from the coast, illustrates the position of the isotach of zero velocity, associated with the center of the lee eddy (Figure 5.2.8a). In the temperature field,

the black line represents the 10 and 16^oC isotherms (Figures 5.2.8b,e). In the salinity section the black line represents the 34.9 and 35.2 psu isohalines (Figure 5.2.8c,f). The presence of the lee eddy is characterized by the doming of the isolines, which reflects the upwelling associated with cyclonic eddies (McGillicuddy and Robinson, 1997). In the case of lee eddy absent, the meridional velocity shows a reversal of the coastal counter-current in all depths. The flow above 130 m is southward over the whole Bight. However, below this depth there is a residual northward flow of 5 $cm.s^{-1}$, implying an inherent difficulty in separating the presences from absences (Cossa et al., 2016), (Figure 5.2.8d). The presence of this residual northward current will be discussed later. In the tracers, the doming of the isolines still persists under condition of DBLE absent. In temperature (Figure 5.2.8e), the 16^oC isotherm for the lee eddy absent is slightly flat, but the 10^oC shows a doming at 150 km from the coast. In salinity, both the 34.9 and 35.2 psu isohalines show slight downwards doming (Figure 5.2.8f). This behavour not only highlights the difficulty in separating the presences from the absences (Cossa et al., 2016) but it also shows complexity of the circulation in the Bight.

The transport due to the southward flowing current and the coastal-counter are assessed in two sections, both at 26^oS: the first lying within $34 - 36^oE$ is made to capture the southward flowing current, whereas the second from the coast to 34^oE is to track the variability of the coastal counter-current (Figure 5.2.9). In both cases, an integration from 500 m depth up to the surface is performed using model data from year three up to year ten. The southward flowing current shows an average of 19.7 Sv, with a spread of $\pm 9.4\,Sv$, (Figure 5.2.9a), whereas the counter-current consists of an average of 0.6 Sv, with a spread of $\pm 2.2\,Sv$ (Figure 5.2.9c). Both currents are characterized by strong oscillations in DELAG-I experiment. To assess the source of this oscillations the density power spectra technique is used. For the southward flowing current (Figure 5.2.9b), several peaks with high levels of significance are noticeable. A first peak at approximately one cycle per year appears to account for the annual cycle. The origin of the second at 3.65 $cycles$ per year, is not known, whereas the last at 4.7 $cycles$ per year, seems to be related with the anticyclones coming from the north, (Figure 5.2.9c). The coastal counter-current (Figure 5.2.9d), shows some significant peaks at 3.65, 4.25 and 4.75 cycles per year. The last value is also close to the frequency of the anticyclones from the (north), whereas the first two are not understood. Despite this, the transports of both the branches of the DBLE seem to be impacted by the passing anticyclones.

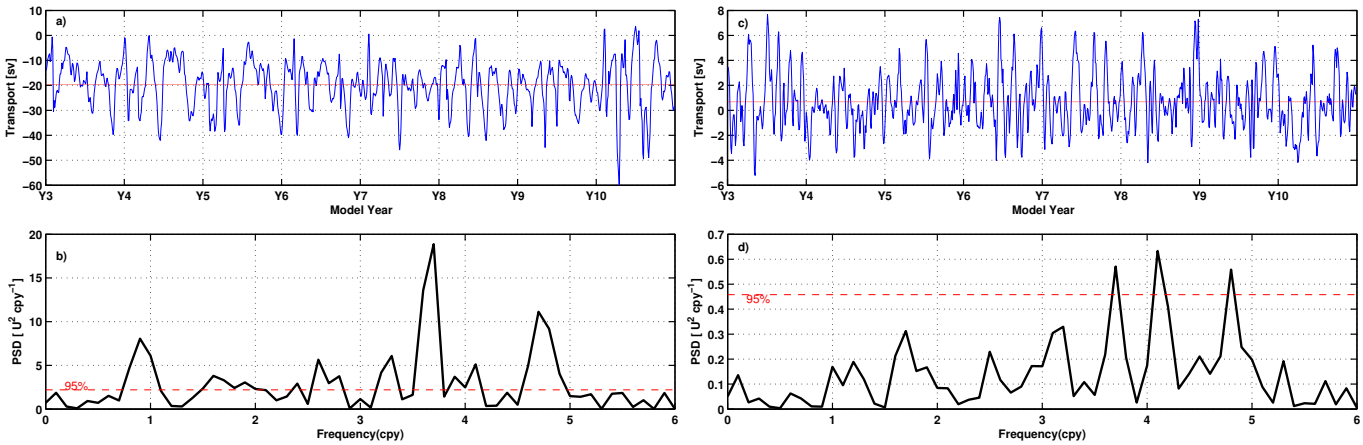

Figure 5.2.9: Upper layer transport ($500\,m$) associated with the southward current a) with the corresponding Powers Spectral Density in b). In c) and d) are given the same parameters for the Coastal-counter Current. The level of significance of the signals is set to 95%.

The eddy detecting and tracking system (Halo et al., 2014a,b) is used to estimate the characteristics of the classic DBLE, such as its radii, life-times and amplitudes (Figure 5.2.10). A total of 68 eddies were tracked on the model DELAG-I and AVISO in the Bight, along the period of 8 years of simulation, in which the model is deemed stable (Figures 5.2.10a,c). Their trajectories tend to be highly concentrated in the usual center of the lee eddy at $26^oS, 34^oE$. These trajectories also show that the lee eddy can occasionally move southward towards the northern Agulhas Current (Lutjeharms, 2006a). The radii distributions of the modelled lee eddy (DELAG-I) tend to follow a Gaussian with an average of $43.2\,km$ (Figure 5.2.10b) and Table 5.1. In AVISO observations the radii distribution also follow a normal distribution, but with a major average radius of $54.45\,km$ (Figure 5.2.10d) and (table 5.1).

Table 5.1: Lee eddies tracked in the model (DELAG-I) and (AVISO)

Model	VAR	AVERAGE	MIN	MAX	STD
DELAG-I	Radius (km)	43.2	30.4	60.0	±7.2
	Life span (days)	23.64	6	63	±15.47
	Amplitude (cm)	8.0	3.4	17.4	±3.32
AVISO	Radius (km)	54.45	33.25	73.6	±9.89
	Life span (days)	25.86	6	116	±19.92
	Amplitude (cm)	11.0	4.0	20.	±4.2

The average amplitude of the lee eddy determined from DELAG-I is $8\,cm$. It has been possible to determine a maximum of $17.4\,cm$ for this experiment. An average life time of $23.64\,days$ with a maximum of $63\,days$ was estimated. In AVISO the mean amplitude is $11\,cm$, with a maximum of $20\,cm$, whereas the life time reaches $116\,days$ (table 5.1). These variations (minimum to maximum)

reflect the fact that the lee eddy is generally generated as a small feature and grows as it remains in the Bight, before propagating unwittingly southward and dissipate in the northern Agulhas Current. Lamont et al. (2010) reported a case of a surface drifter which remained inside of the DBLE for six weeks, before moving southward in the same direction.

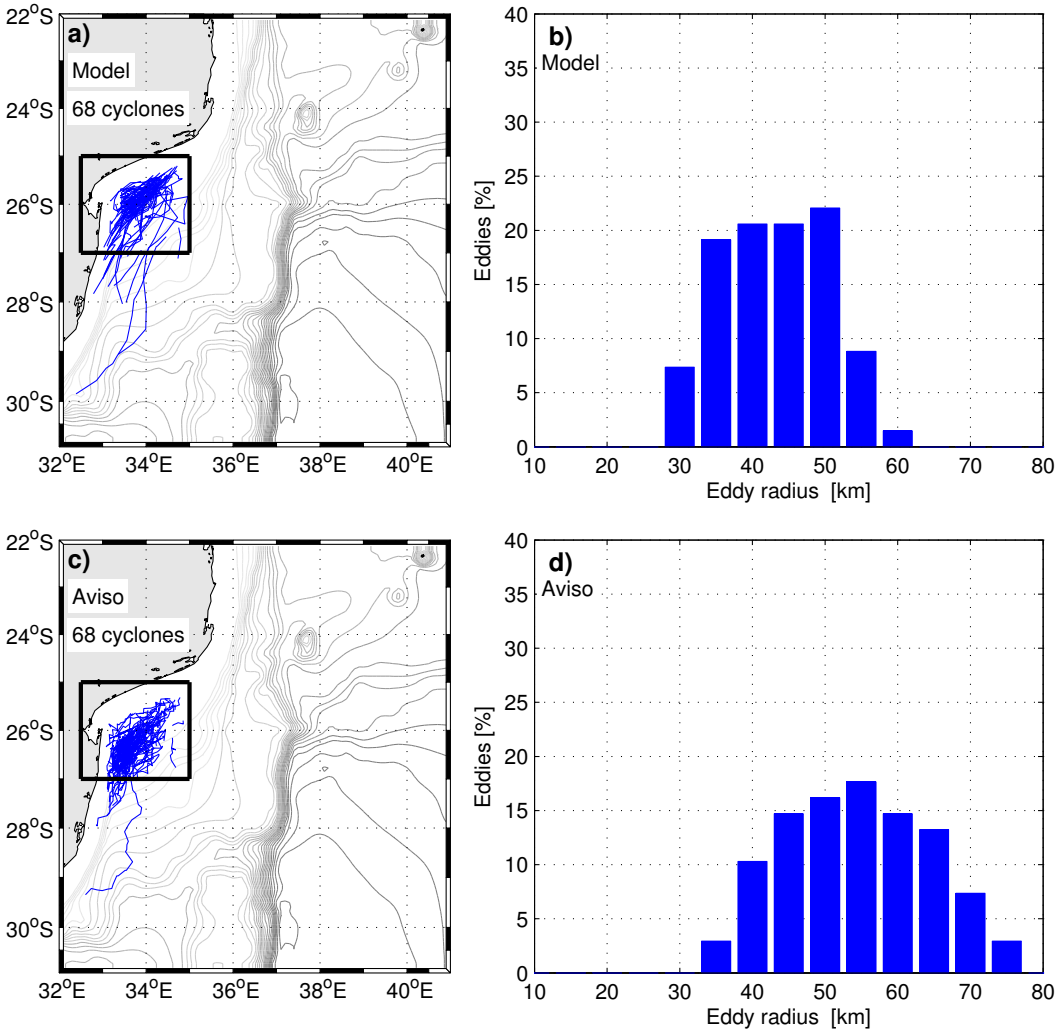

Figure 5.2.10: Delagoa Bight lee eddies tracked from Model (DELAG-I) a) and AVISO c), with the corresponding radii distribution in b) and d). The gray lines in a,c) are contours of bathymetry.

5.3 Effect of improvement of resolution in Delagoa Bight Circulation

This section is dedicated to the analyses of model data of the experiment with high resolution, without tides (DELAG-III) Figure 5.3.1. The DBLE presences in the internal domain of this simulation (blue), is compared with AVISO (red) in Figure 5.3.1. DELAG-III, shows an increase in the reproduction of cyclonic features inside of the Bight by comparison with AVISO, and DELAG-I analyzed in the previous section. Again, there is no seasonality in the DBLEs occurrences.

Therefore, the improvement in the resolution results only in the increase of cyclonic activity inside of the Bight, by comparison with the satellite observations.

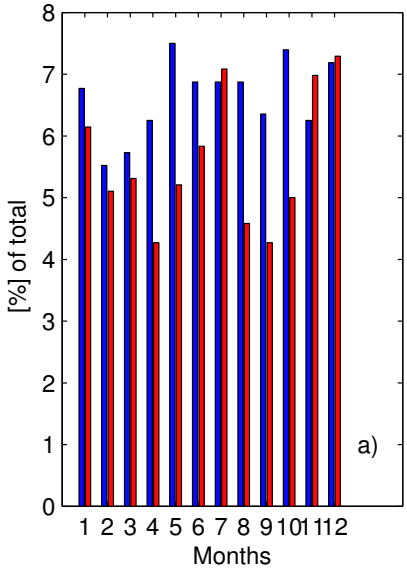

Figure 5.3.1: Percentage of DBLE occurrence per climatological month in the child domain of DELAG-III in (blue) and AVISO (red).

The thermocline structure for the model without tides (DELAG-III) is shown in Figure 5.3.2. At $50\,m$ depth, the DBLE is circumscribed in several isotherms lying in the range of 20 to 23^oC. This was not the case with DELAG-I experiment given in the previous section (Figure 5.2.2), in which only two isotherms were conspicuous. The representation of the southward flowing current improves as well (Figure 5.3.2a). The distribution of the salinity in (Figure 5.3.2b) is similar to no-tides (DELAG-I) in Figure (5.2.2b), but with slight change in terms of the way its signature is represented. The SSH and currents show an improvement in the representation of the DBLE signature in the high resolution model without tides (DELAG-III) (Figure 5.3.2c). This reflects the importance of increasing resolution in the representation of a numerical model (Debreu et al., 2012). At $100\,m$ depth, the modelled lee eddy is marked by the range of concentric isotherms from 16 to 18^oC (Figure 5.3.2d). The salinity distribution is similar to its counterpart in Figure (5.2.2e). Likewise, the currents are better represented at this depth (Figure 5.3.2f).

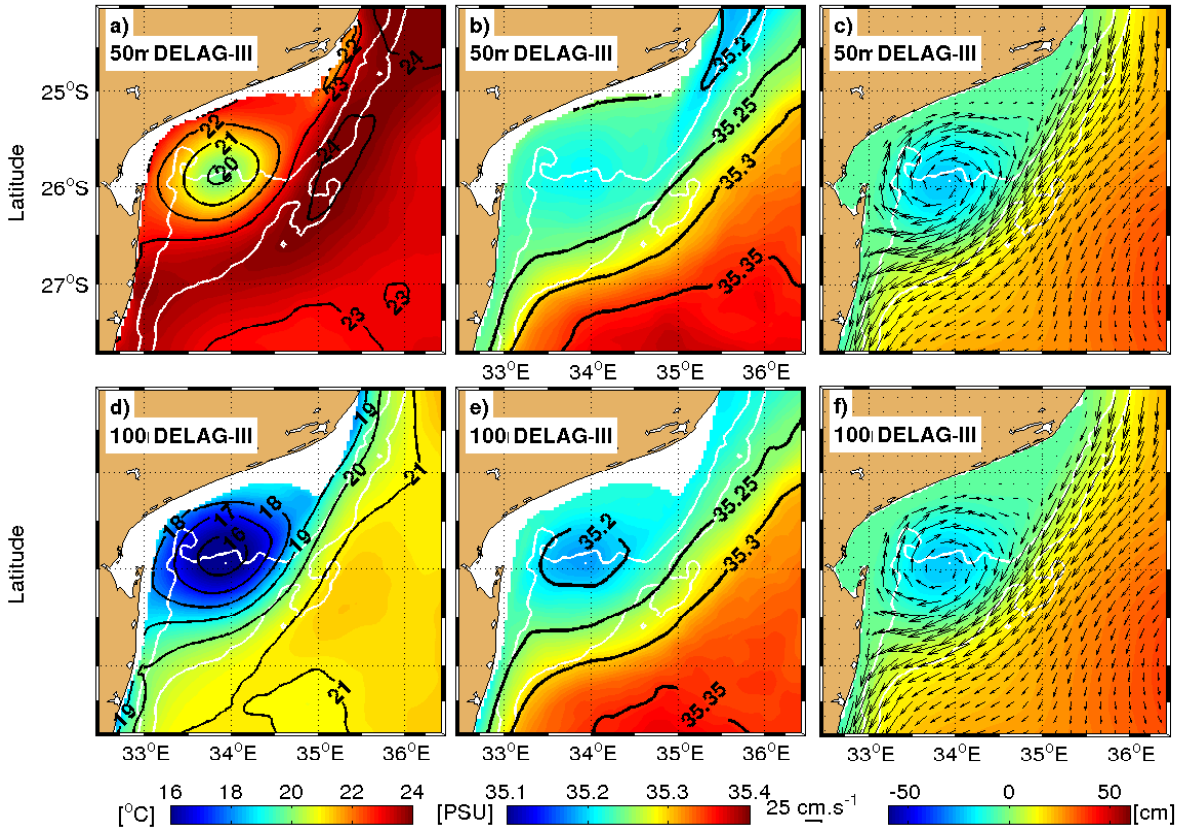

Figure 5.3.2: Horizontal sections of lee eddy presence at 50 and 100 m, based on the composite of the model without tides (DELAG-III) in the Delagoa Bight. In a) and d) is shown the temperature distribution; in b and e) the salinity; and finally the currents on SSH in c and f). The white lines are the 500 and 1000 m isobaths.

The situation during the absences of the lee eddy as portrayed by the composite created from the high resolution model without tides (DELAG-III) is shown in Figure 5.3.3. At 50 m depth, the temperature distribution highlights the strengthening of the southward flowing current, and the cyclonic feature of the northeastern part of the domain, (Figure 5.3.3a). The salinity distribution in Figure (5.3.3b) shows a better representation of the signature of the circulation by comparison with its counterpart represented in Figure (5.2.2b). The currents also highlights the consistency of the cyclonic feature northeast of the domain (Figure 5.3.3c). The southward flowing boundary current and the anticyclonic feature southeast of the domain at $27.5^oS, 35.5^oE$, are also conspicuous in this simulation. An important aspect of this simulation when the lee eddy is absent, is the representation of an anticyclonic feature centered at $25.75^oS, 33.5^oE$ inside of the Bight and off Maputo, (Figure 5.3.3c,f). This anticyclonic features not referred to in most previous studies (Lutjeharms and Jorge da Silva, 1988; Kyewalyanga et al., 2007; Barlow et al., 2008; Lamont et al., 2010), seems to be real because some individual AVISO images show high SSH in that area of the Bight (not shown here). Gründlingh et al. (1989) documented an anticyclonic eddy occupying the whole Bight, and attempted to put into cause the prevalence of a cyclonic lee eddy

in the Delagoa Bight. At 100 m depth, the cyclonic feature northeast of the domain is marked in the 17^oC isotherm (Figure 5.3.3d) whereas the anticyclonic feature at 25.75^oS, 33.5^oE is only visible in Figure (5.3.3c-d). The salinity distribution shows an enhancement in the representation of the fresher water masses from the north (Figure 5.3.3e).

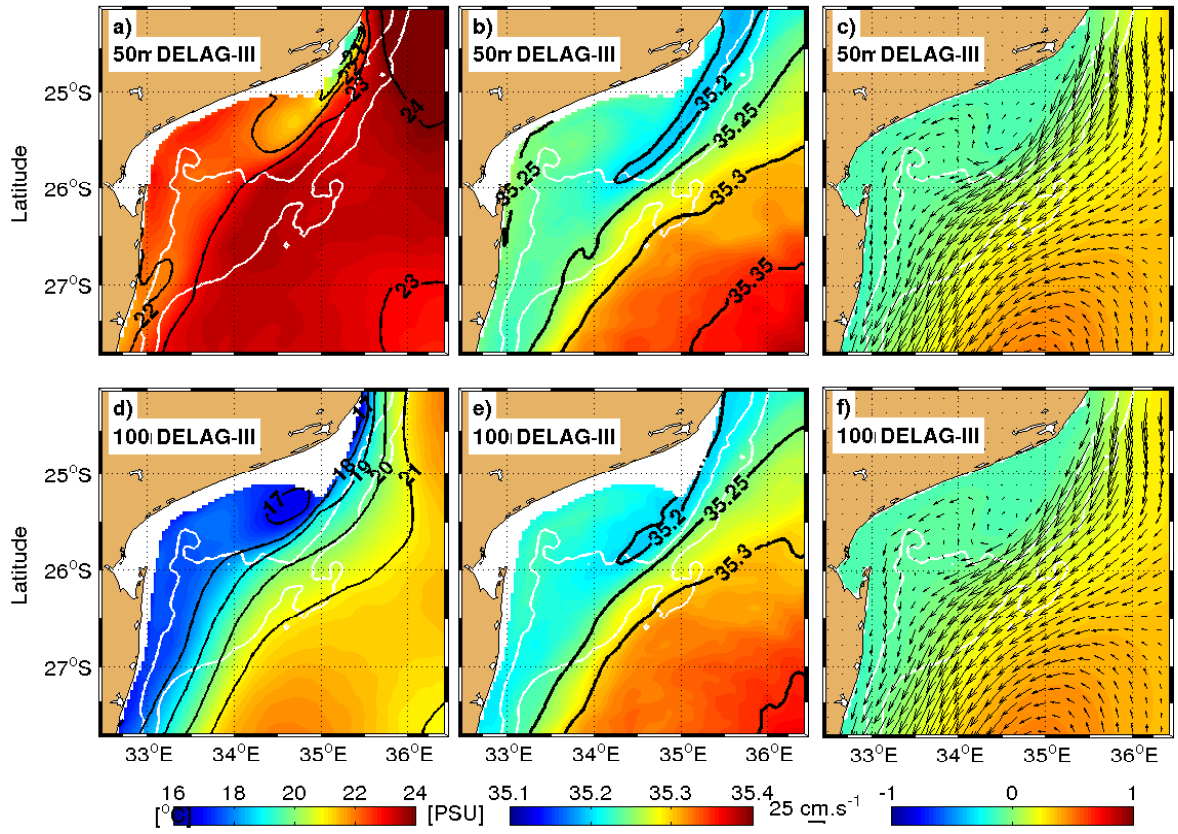

Figure 5.3.3: Horizontal sections of lee eddy absences at 50 and 100m, based on the composite of the model without tides (DELAG-III) in the Delagoa Bight. In a) and d) is shown the temperature distribution; in b and e) the salinity; and finally the currents on SSH in c) and f). The white lines are the 500 and 1000 m isobaths.

The increment of the model resolution improves the representation of the oceanic fields. Therefore, the difference between the composite with the lee eddy present and absent at 100 m depth shows an amplification of the preeminent features in the Bight (Figure 5.3.4). This can be easily seen in currents overlaid on SSH in Figure (5.3.4a), by comparison with DELAG-I (Figure 5.2.6a). This is consistent with the fact that the lee eddy absences in the center of the Bight, are characterized by relatively high SSH, in comparison with the presences. Likewise, the anticyclonic region south of the domain in the case of absences, is characterized by higher SSH in comparison with the case of presences, as previously noted. The coastal zones off Ponta D'Ouro show a stronger anticyclonic feature. This feature reflects the dominance of high SSH in the composite of lee eddy presences over the absences in that place. As indicated before, it reflects the positioning of an anticyclonic eddy during the timing of a well organized DBLE. In the west and northeast of the domain, this

difference if characterized by a stronger northward counter current locked to the coast (Figure 5.3.4a), with part of it coming from the south, precisely in the area dominated by an anticyclone under lee eddy absent. The temperature and salinity fields reproduce these features as well, (Figures 5.3.4b-c). The southward flowing current in this simulation increases, by comparison with the coarse resolution without tides. This increment is confirmed by its signature in the salinity field, which shows a strip of fresher water from the north intruding into the Bight (Figure 5.3.4c).

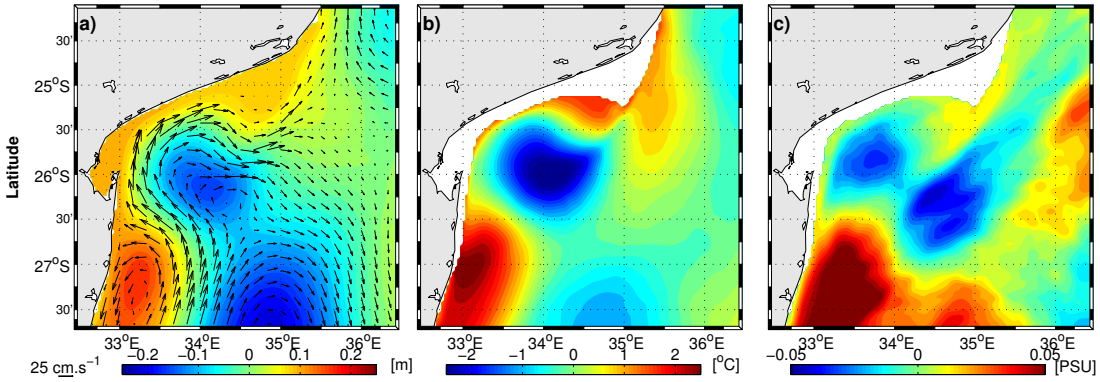

Figure 5.3.4: Difference between the composites of lee eddy presences and absences in the model (DELAG-III), at 100 m. In a) are presented the currents over-layered on SSH, in b) the temperature, and the salinity section in c).

The vertical section taken from DELAG-III composites is illustrated in Figure 5.3.5. The meridional velocity in the case of lee eddy present, shows a consistent coastal counter-current flowing northward with speeds greater that 25 $cm.s^{-1}$. It appears to be stronger in comparison with those modelled with the coarser domain. It reaches the 300 m depth with speeds of more than 20 $cm.s^{-1}$ (Figure 5.3.5a). In the coarser domain, this had been only noted up to 100 m depth. The southward flowing current in this composite shows speeds above 40 $cm.s^{-1}$. The lines of zero meridional velocity shows that the center of the lee eddy is at 100 km from the coast (Figure 5.3.5a). The 10 and 16^oC isotherms (black lines) are characterized by a stronger doming, with the former being able to reach the 320 m depth in the center of the lee eddy, whereas the latter domes up to around 95 m. The doming is stronger at the lower levels (Figure 5.3.5b), indicative of the increase of upwell in association with the lee eddy in this experiment. In salinity distribution, the 34.9 psu isohaline lies only a bit below 320 m, whereas the 35.2 psu isohaline in the upper layer lies above 95 m depth (Figure 5.3.5c).

When the lee eddy is absent, there are two lines of zero meridional velocity (black) in this composite, Figure 5.3.5. One reflects the preeminence of the anticyclonic circulation at 25.75^oS, 33.5^oE, while the other has to do with the point of interaction between the counter-current, now found in

the middle of the Bight. In the coast, the southward flowing current fills that area at all depths. It has been conjectured that the boundary current is able to generate an anticyclonic feature in the Bight, (Gründlingh et al., 1989; Quartly and Srokosz, 2004) (Figure 5.3.5d). In the coarse resolution simulation (DELAG-I), the counter current was noticeable but as an under current. When the lee eddy is absent, the reversed coastal counter-current (southwards) fills the whole coastal sector including the upper layers (Cossa et al., 2016). The characteristics of this anticyclone is investigated using the eddy detecting and tracking system. The 16^oC isotherms is flat, whereas the 10^oC isotherm shows several deformations, with the trough at $400\,m$ depth reflecting the prevalence of the anticyclonic feature (Figure 5.3.5e). In the upper level, the $35.2\,psu$ isohaline captures the southward flowing current, which is represented by a bulging in Figure (5.3.5f). The $34.9\,psu$ isohaline mimics the 10^oC isotherm.

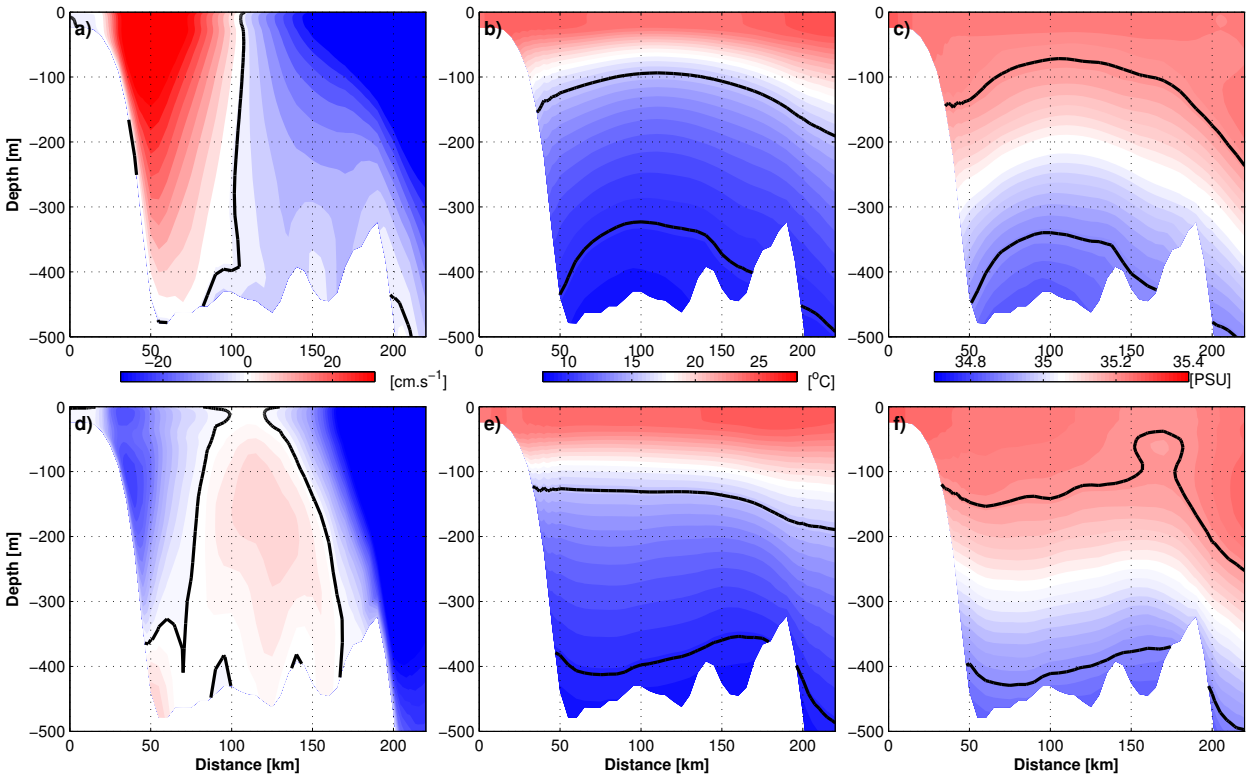

Figure 5.3.5: Vertical sections of composites of modelled (DELAG-III) meridional currents (a and d), temperature (b and e) and salinity (c and f), across the Delagoa Bight, in the case of the presence (top column) or absence (bottom). The black lines indicates the zero isotach (a and c), whereas in (b and e) it shows the 10 and $16\,^\circ C$ isotherms and finally the 34.9 and $35.2\,psu$ isohalines in (c and f).

Before moving forward, it is important to underline that forcing with tides could not bring considerable changes in the representation of the thermocline structure in all the sensitivity experiments used in this investigation. Therefore, the analysis will only focus on the higher resolution experiments, whereas the results of the experiments with tides are placed in appendix B.1.

5.3.1 Lee eddies tracked in the child domain

The effect of increasing the model resolution is reevaluated applying the eddy detecting and tracking system on the data of the internal domain from the experiment without tides (DELAG-III) in Figure 5.3.6. A total of 122 cyclones were tracked in this model (Figure 5.3.6a). An amplification of the features and reproduction of smaller cyclones has been noted. This is expected in a ROMS simulations, because the increase in the resolution implies reproduction of small scale features according to the nesting approach concepts portrayed by Debreu et al. (2012). A maximum radius of 58.78 km and minimum of 10.65 km were estimated for the cyclonic features tracked inside of the Bight (Table 5.2). This minimum radius is less than the one determined from the coarse resolution simulation in section 5.2, whose results are illustrated in Table (Table 5.1). This implies that nesting is able to reproduce smaller features than the classic lee eddy investigated by Lutjeharms and Jorge da Silva (1988). Furthermore, the amplitude and the life times of the cyclones increase in this simulation, concomitant with the improvement in the representation of the processes with the augmentation of grid resolution (Tables 5.2 and 5.1).

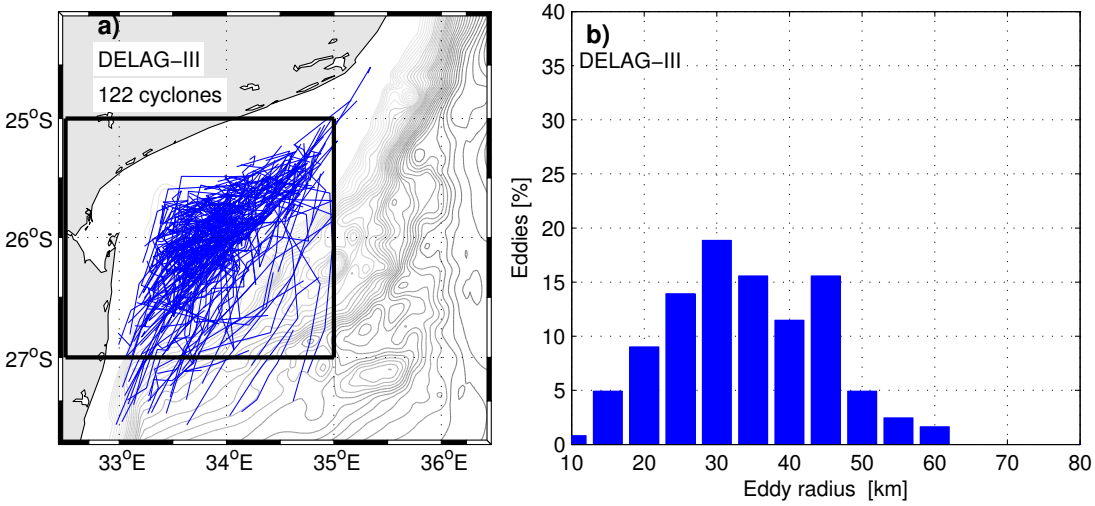

Figure 5.3.6: Trajectories of the lee eddies tracked in the internal domain of DELAG-III (blue lines). In a) the gray lines represent the contours of bathymetry. The radii distribution is shown in b).

Table 5.2: Statistics of cyclonic eddies tracked in the internal domains of the model no-tides (DELAG-III).

Model	VAR	AVERAGE	MIN	MAX	STD
DELAG-III	Radius (km)	33.58	10.65	58.78	±10.3
	Life span (days)	24.39	6.0	102	±21.08
	Amplitude (cm)	10.34	3.61	27.24	±4.8

A comparison with a reference solution computed at high resolution shows an agreement in the

refinement area as well as some improvements in the coarse grid area, (Debreu et al., 2012). Despite this, the realism of this representation is not well known, in the case of Delagoa Bight due to the absence of high resolution products for comparison. Meanwhile, it seems to be shedding light in the presence of smaller features, in a region where the circulation has been deemed complex, (Lutjeharms and Jorge da Silva, 1988; Lamont et al., 2010; Cossa et al., 2016) and not well understood. An important remark to be made concerning the relatively smaller average radius of the cyclonic features estimated here, is related to the increase in the reproduction of smaller cyclonic features in the high resolution simulations. This expresses the contribution of these features in the average. Imposing a minimum radius greater than $20\,km$ in the eddy detecting and tracking system, would deliver a greater average radius.

5.3.2 Cyclonic cores and small anticyclones in the Delagoa Bight

The possibility of the prevalence of more than one cyclonic features in the Delagoa Bight region has been speculated in the previous studies. Martin (1981) presumed that it was unlikely that such a vast area of the terrace could be filled with a single lee eddy. Nevertheless, he could not prove the presence of such features. Lutjeharms and Jorge da Silva (1988), used in situ and high resolution satellite data to investigate the Bight. They concluded that the circulation was complex. Perhaps the excessive cloud coverage in most of their images, as well as the low frequency of occurrence of such smaller features, hindered these authors from inferring them inside of the Bight.

Sequences of images consisting of currents overlaid on SSH are shown in Figure 5.3.7. The goal is to follow the development of cyclonic features (negative dipoles and three-poles) and assess their thermocline structure, when they are well established.

Initially, a well developed lee eddy indexed 335 on model date ($23Mar8$), is undergoing a destruction process (Figure 5.3.7a). The flow inside of the Bight is generally turbulent, although within the $500\,m$ and $1000\,m$ isobaths it is stable and southward. Northeast of the domain, a rim of an anticyclone from the north moves downstream. Part of the southward flow tends to be unstable as all the features inside the Bight move southward. Three days later, the cyclone indexed 335 disappears. On model date ($29Mar8$), new cyclones are generated inside of Delagoa Bight.

The first cyclone indexed 342, seems to have been originated by a quick reconstruction of 335, whereas 343 results from the diversion towards west of part of the steady southward flowing

boundary current as it interacts with the topography. Such westwards current bifurcates into a northward and southward flow along the coast, at 27^oS (Figure 5.3.7b). Offshore, the impact of the anticyclonic eddy is preeminent. Overall, that region is characterized by high SSH, which is associated with the merger of the anticyclones from the north and east. On model date ($5Apr8$), the features move southward. The westwards current diverts northward along the axis formed by the 34^oE meridian, towards north. Here, it diverts eastward following the usual path of the coastal counter-current (Figure 5.3.7c). Three days later, three cyclonic eddies are found in the Bight. It seems that the SSH increase offshore, promotes the intensification of the southward flowing current, which interacts with the topography and generates mesoscale features in the Bight. For instance, the cyclone indexed 346 is generated in that manner (Figure 5.3.7d). Shoreward of the three-pole, an inconsistent anticyclonic circulation is apparent. On model date ($8Apr8$) a merger of the cyclones indexed 342 and 346 resulted in a strong dipole in the Bight (Figure 5.3.7e). This dipole is composed of the cyclones indexed 343 and 346. It is a long lived dipole that undergoes several shifts in its positioning. These shifts are induced by the anticyclones as they reach the latitudes of the Bight. The fate of the dipole, and other features generated in the Bight, is whether a local dissipation or a southward propagation towards the Agulhas Current. Both processes are mainly promoted by the passing anticyclones. On model date ($11Jun8$) the fate of the dipole has been dictated by the mutual interactions with an anticyclonic eddy (Figure 5.3.7f).

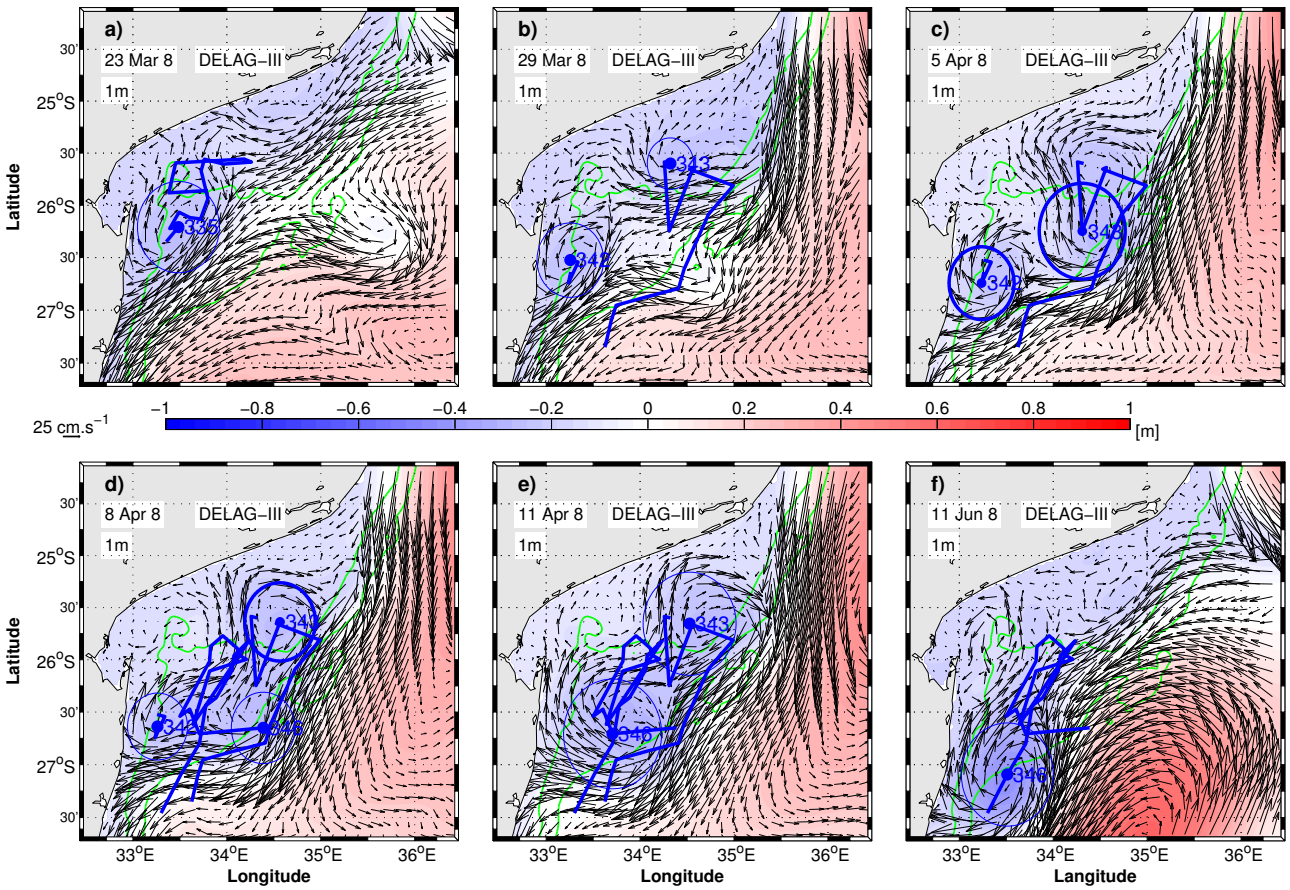

Figure 5.3.7: Sequence of cyclonic cores reproduced in the internal domain of the model without tides (DELAG-III), in the Delagoa Bight. The currents (black arrows), are overlaid on SSH. The blue circles indicate the sizes of cyclones as estimated by the eddy detecting and tracking system. The green lines are the 500 and 1000 m isobaths.

The thermocline structure of these cyclonic dipoles is very consistent (Figure 5.3.8). The stability of these dipoles appears to be associated with the high SSH promoted by the anticyclones found in the east and south of the Bight (Figure 5.3.8a,d). In the temperature field the dipole is characterized by two cyclones, one to the northeast of the domain, and the other to the southwest. These cyclonic dipoles are marked by the 16^oC isotherm, with the respective cores confined in the 18^oC isotherm (Figure 5.3.8b). The southward flowing current, now an authentic edge of the anticyclones, is marked by the 20 and 22^oC isotherms (Figure 5.3.8b). In the salinity field, the cyclonic dipoles are linked by an area (like eight) consisting of up-welled water masses promoted by the cyclones composing it, with the rest of the domain generally saltier (Figure 5.3.8c). This shows the importance of these features in the distribution of water masses in the Bight.

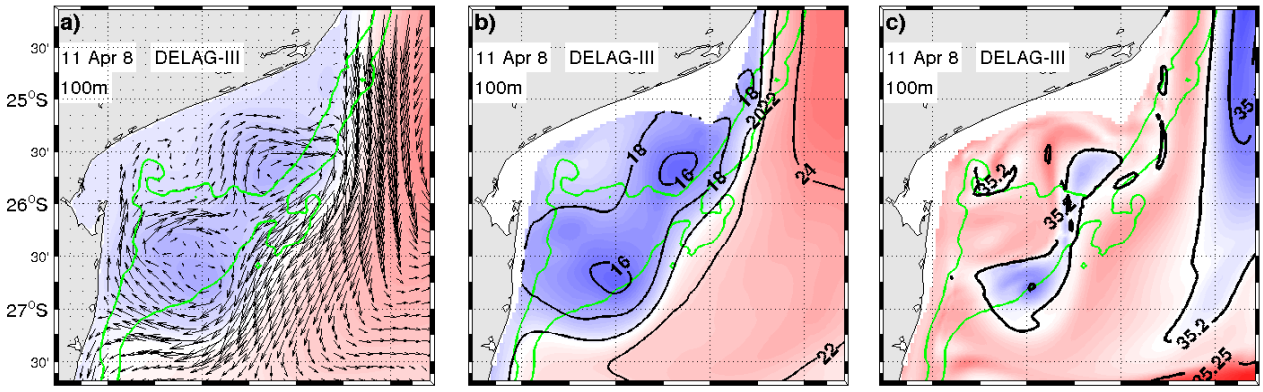

Figure 5.3.8: Cyclonic cores in Delagoa Bight, based on DELAG-III. Currents at 100 m overlaid on SSH in a) Temperature distribution at 100 m in b) and Salinity in c). The green lines are the 500 and 1000 m isobaths.

A summary containing the total number of cyclonic cores and anticyclonic cells found in the Bight in individual snapshots is presented in Table 5.3 for the child domain of the model without tides (DELAG-III). These small mesoscale features (radius greater than 10 km), are scarce in the simulations based on the coarse resolution. In the external domain of no-tides, 223 snapshots contain 2-cores (negative dipoles). Three cores were observed in 23 snapshots, whereas 4 cores and anticyclonic cells were not observed. In the internal domain, the occurrence of the features improves. Hence, simultaneous negative 4 cores were observed in 2 snapshots (2 times) The anticyclonic mesoscale features were observed only in 3 snapshots, for the whole length of the simulation. The eddy detecting and tracking system confirms that this corresponds to a single anticyclonic cell. The tidal simulation in appendix B.2 gives further aspects of these small features.

Table 5.3: Cyclonic cores and anticyclonic features in the Delagoa Bight

EXPERIMENT	DOMAIN	2 CORES	3 CORES	4 CORES	ANT. CELLS
DELAG-III	EXT.	223	23	-	-
	INT.	279	48	2	3(1)

5.4 Inhambane Cyclones

An important aspect of all the ROMS simulation used in this study was a systematic reproduction of cyclonic pulses by the passing anticyclones from the north of Mozambique Channel off Inhambane at approximately $35.4^oS, 23.87^oS$. Such cyclonic features develop into cyclonic eddies as they move southwards with the anticyclones that generate them, and may occasionally detach from them as both features move southward toward the northern Agulhas Current region. In a region where past studies such as Roberts et al. (2014), refer to the generation of dipoles by

the same anticyclones, the relatively higher resolution of these simulations allowed one to follow their propagation until they dissipate farther south. The features were dubbed Inhambane Pulses (Cyclones) considering their similarity with the Natal Pulses, known to be generated further south in the Agulhas Current, (Lutjeharms and Roberts, 1988). By considering the number of presences of these features in the model and AVISO snapshots, it has been demonstrated that they contain a seasonal signal, with the highest likelihood of occurrence falling within the forth to fifth initial months of the year (summer-autumn) in both model and AVISO, though they occur over the rest of the seasons (Figure 5.4.1). As a consequence, their absences are more common in Austral winter-spring season.

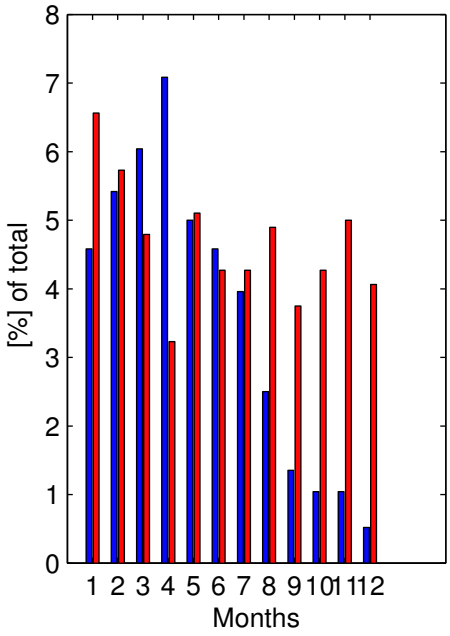

Figure 5.4.1: Percentage of occurrence of Inhambane cyclones in the model DELAG-I (red) and AVISO (blue).

Sequences of images based on DELAG-I experiment (no-tides) are shown in Figure 5.4.2. The arrival of an anticyclone from the north promotes a cyclonic circulation off Inhambane at $35.4^oS, 23.87^oS$ on model date ($17Mar8$), (Figure 5.4.2a). The feature forms a kind of a dipole structure with the ring generating it. During its southwards movement, it impacts the Delagoa Bight dynamics through modification of the angle of interaction of the southward flowing boundary current with the shelf off Inhaca. This kind of interaction had been considered crucial in the inception of the lee eddy Lutjeharms and Jorge da Silva (1988). A big ring off Ponta D'Ouro, locks the flow in the coast, contributing to the onset of the coastal counter-current, the coastal branch of the lee eddy. Some days after, on model date ($29Mar8$) (Figure 5.4.2b), the lee eddy is still established in spite of the fact that all the involved mesoscale features have moved southward. An interaction

of the Inhambane Cyclone with the lee eddy is noticeable in this sequence. It lasts for more than ten days, (Figure 5.4.2c,d). On model date ($2May8$), the Inhambane Cyclone (pulse) is detached from the coast and takes the form of cyclonic mesoscale eddy. The lee eddy is absent in the center of the the Bight, (Figure 5.4.2e,f). That situation lasts for more than two weeks.

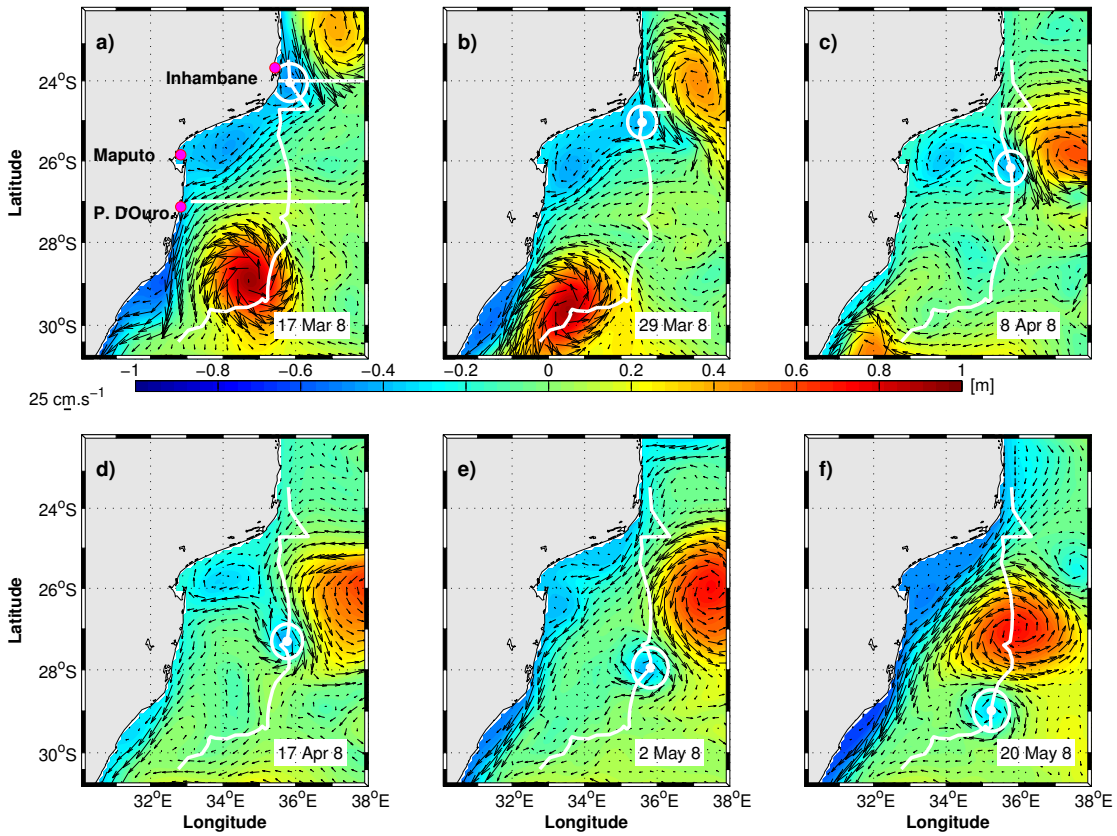

Figure 5.4.2: Track and positions of an Inhambane cyclones along the coast of Delagoa Bight. The circle shows the actual position of the pulse and the straight line represents the positions in which vertical cross sections are made.

To assess the thermocline structure of these pulses at the time of their generation and later, two positions were chosen to perform cross sections. The first is off Inhambane and the second is off Ponta D'Ouro, (Figure 5.4.2a). For the model without tides in Figure 5.4.3, the meridional velocity at the inception of the pulse in model date ($17Mar8$) shows a northward flow locked to the coast there. The southward flow is due to the coastal edge of the anticyclone. The speed of the northward counter-current is approximately $50\,cm/s$, (Figure 5.4.3a). It rises as a compensations of the water removed from the coast by the edge of the anticyclone. In temperature and salinity the doming of the isolines is not consistent perhaps due to the transient characteristic of these features, (Figure 5.4.3b-c). Off Ponta D'Ouro, the center of the pulse (cyclone) is located $250\,km$ from the coast. The associated northward speeds are close to $50\,cm/s$ above $300\,m$ depth. Towards the coast, at around $100\,km$ the line of zero meridional velocity separates the northward flow due to the pulse from the southward flowing coastal current, (Figure 5.4.3d). In temperature and

salinity, the expected doming of the isohalines is noticeable at 250 km from the coast, (Figure 5.4.3e,f). Considering that the tidal effect in the thermocline structure of the simulations used here are subtle, the impact of tides on the Inhambane Cyclones were included in the appendix B.1.2.

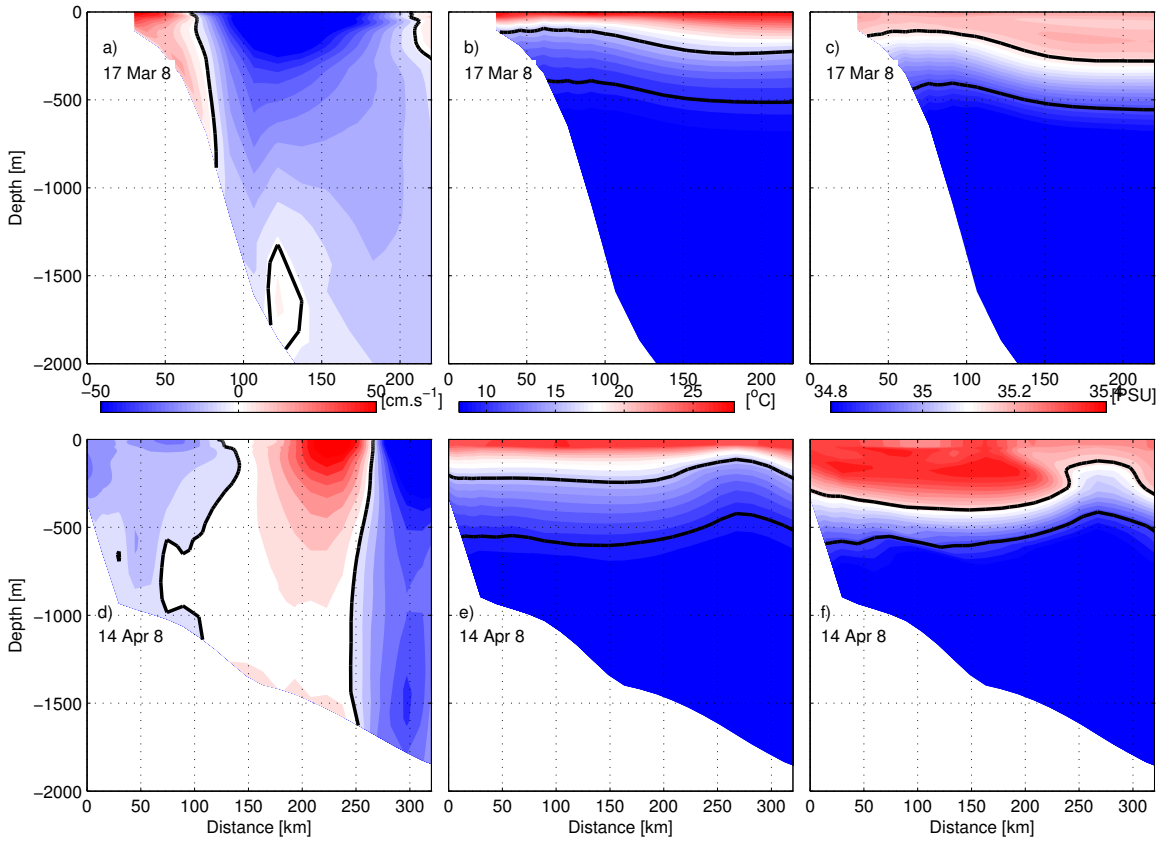

Figure 5.4.3: Inhambane cyclone vertical sections at Inhambane Section based on the model DELAG-I (first row), and at Ponta D'Ouro (second row). The fist column represents the meridional velocity a,d); the second represents the temperature b,e) and the last represents the salinity c,f). In velocity the black line denotes the zero meridional velocity. In temperature it denotes the isotherms of 10 and 16^oC, whereas in salinity it refers to the isohalines of 34.9 and 35.2psu

The pulse described above, interacts with the DBLE as it moves southward Figure 5.4.4. The associated transport is responsible in the shelf offshore interactions around the latitudes of the Bight. In the temperature distribution, the lee eddy, the pulse and the anticyclone are distinctively well marked (Figure 5.4.4b). In the salinity, the whole Bight is completely mixed, with salinity below 35.1 psu (Figure 5.4.4c). The interaction of the pulse with the lee eddy appears to be an important part of the Delagoa Bight dynamics.

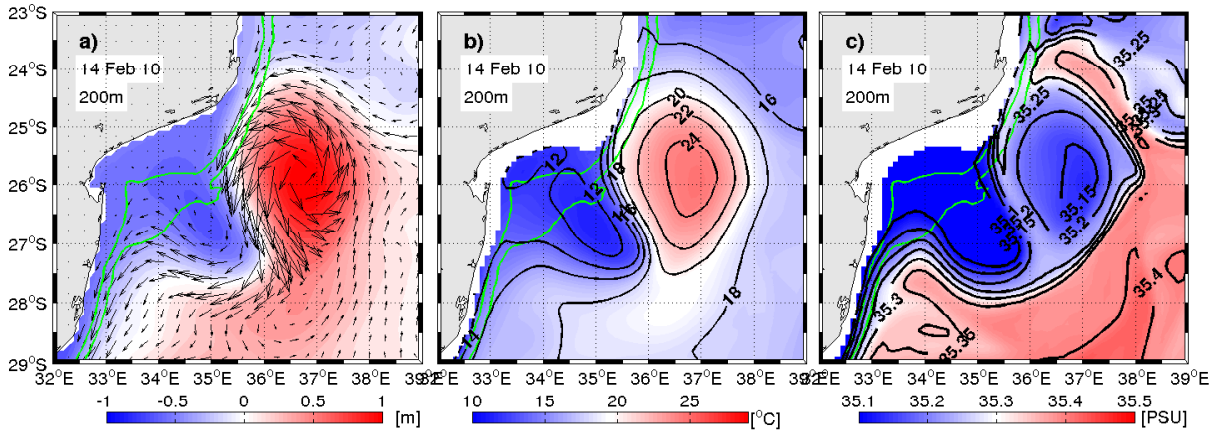

Figure 5.4.4: Impact of IC in the Delagoa Bight. Currents at 200 m overlaid on SSH a), temperature distribution in b) and salinity distribution c). The green lines are the 500 and 1000 m isobaths.

5.4.1 Inhambane Cyclones tracked in various sensitivity experiments

In this section the Inhambane Cyclones, are tracked from all available sensitivity experiments and observations. This is done with the aim of showing their trajectories and their behaviour within the local environment, which like the whole Mozambique Current is complex and variable. A total of 24 pulses, an equivalent to three pulses per annum, were detected in the model (DELAG-I). The eddy detecting and tracking system, reveals that their trajectories are quite variable (Figure 5.4.5). Most of the pulses propagate downstream toward the Agulhas Current, some intrude into the center of the Bight and dissipate there, whereas others recirculate with the spinning anticyclones, before moving downstream. The pulses that intrude into the Bight are likely to enhance the cyclonic circulation there. Overall, depending on their trajectory, they can impact the circulation inside of the Bight. These interactions may work to remove the lee eddy, to boost its inception or to exchange water masses between shelf and offshore. In Figure (5.4.5b), is illustrated the radii distribution of the Inhambane Cyclones tracked in the reference experiment (DELAG-I). In AVISO, 32 Inhambane Cyclones have been tracked (Figure 5.4.5c). Most of these pulses were not able to move out of the region in which they are generated. They do not recirculate, neither intrude into the Bight. The corresponding radii distributions are presented in Figure (5.4.5d).

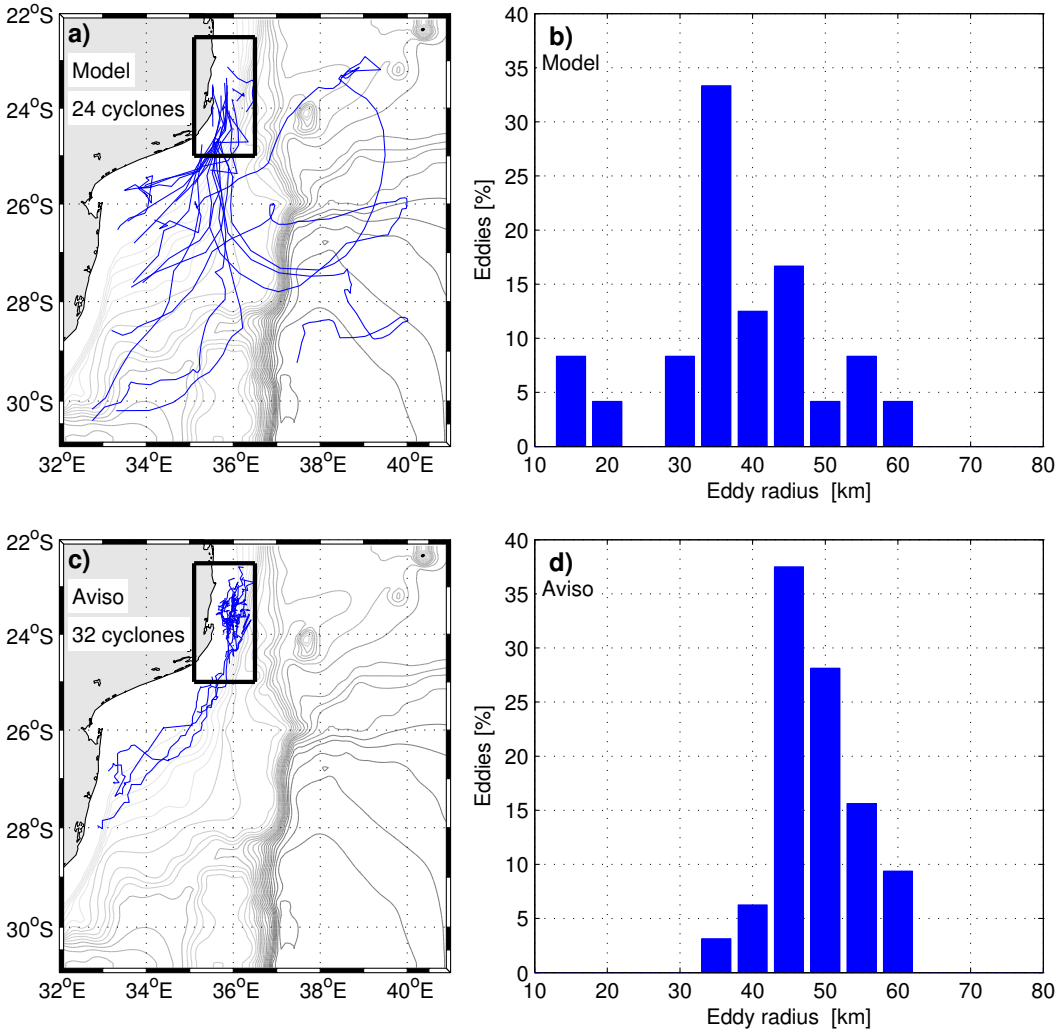

Figure 5.4.5: Tracked ICs in DELAG-I a) and AVISO b) in blue. The gray lines are contours of bathymetry. The corresponding radii distribution is given in c) and d) respectively.

Table 5.4: IC stats based on model DELAG-I, AVISO and DELAG-II

Model	VAR	AVERAGE	MIN	MAX	STD
DELAG-I	Radius (km)	37.63	14.75	59.03	±11.47
	Life span (days)	46.87	6	186	±56.10
	Amplitude (cm)	11.45	4.11	31.61	±7.90
AVISO	Radius (km)	46.65	35.59	60.21	±5.60
	Life span (days)	17.60	6	47	±12.60
	Amplitude (cm)	8.06	3.54	16.12	±5.57

The statistics of the Inhambane Cyclone based on the reference experiment (DELAG-I) and AVISO are presented in Table 5.4. For DELAG-I, the maximum radius of the pulses is 59.03 km. Its average lifetime is 46.87 $days$, with maximum lifetime of 186 $days$. This value is not so surprising if one considers the fact that they follow different trajectories, with some being relatively longer. This feature occasionally recirculates before ceasing in the northern Agulhas Current. In AVISO

the pulses are characterized by the same order of magnitude with those in the (DELAG-I), but the radii of these cyclones are relatively smaller in the model. A maximum lifespan of 47 *days* was estimated in AVISO. This is again because that in the model the pulses have some likelihood of recirculating, increasing the length of their trajectories and therefore the length of their life times. The Inhambane Cyclones tracked on the external domain of the model without tides (DELAG-III) are depicted in Figure 5.4.6. A total of 22 pulses were tracked in this simulation. Approximately 22.7% of these, move southward toward the northern Agulhas Current, with the majority of them wandering and fading inside of the generation zone, (Figure 5.4.6a). The radii distribution of these feature is presented in (Figure 5.4.6b).

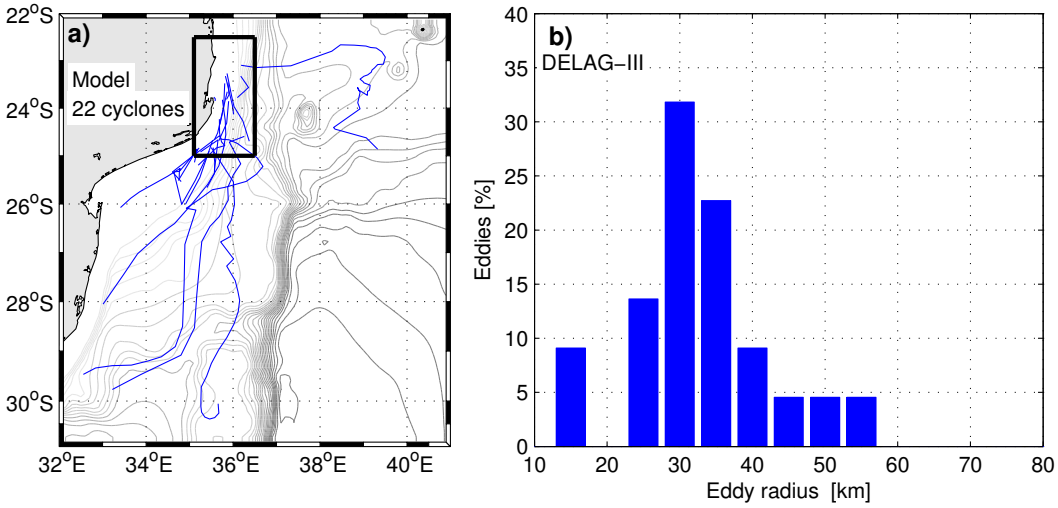

Figure 5.4.6: ICs tracked on the external domains of DELAG-III a) and DELAG-IV c) experiments. The respective radii distributions are presented in b) and d. The gray lines are contours of bathymetry.

The average and the maximum radii of the Inhambane Cyclones based on the external domain of the model without tides are presented in Table 5.5. They are characterized by an average radius of 32.86 *km*, with a maximum amplitude of 15.85 *cm* and maximum life-span of 99 *days*. Overall, the characteristics of the Inhambane Cyclones found in this simulations are generally close to previous ones, except the fact that the life time is very large in the reference experiment (DELAG-I). Their long life spans is explained by the relatively long trajectories associated with their recirculation.

Table 5.5: IC stats for the external domains of models DELAG-III and DELAG-IV

Model	VAR	AVERAGE	MIN	MAX	STD
DELAG-III	Radius (km)	32.86	15.00	53.99	±9.50
	Life span (days)	21.95	6	99	±27.56
	Amplitude (cm)	8.45	4.32	15.85	±3.17

5.5 Discussions and conclusions

The main objective of this chapter was to investigate the modelled Delagoa Bight lee eddy including its statistics, based on several ROMS numerical experiments and AVISO satellite observations. The impact of the passing anticyclonic eddies is revisited, mainly by considering the influence of the Inhambane Cyclones generated by the passing anticyclonic eddies from the north of Mozambique Channel, northeast of the Bight. These pulses were recently presented by Cossa et al. (2016). They are somewhat similar to the Natal Pulses (Lutjeharms and Roberts, 1988; van Leeuwen and et al., 2000; Tsugawa and Hasumi, 2010).

By considering the number of lee eddy occurrences (presences/absences) in the model snapshots, it was demonstrated that they are not season dependent in the Delagoa Bight. This is because that the southward flowing boundary current that sustains its onset is perturbed by the dynamics of the Mozambique Channel. Furthermore, the number of occurrence of presences is greater than the number of occurrence of absences in all simulations and observations. Regarding this, it can be underlined that the lee eddies presences in AVISO is somewhat greater in comparison with the modelled.

The addition of the nest, showed that the number of tracked cyclonic eddies in the Bight surpasses the cases of no-tides based on the coarse resolution model. In fact, in both the mother and the child domains of the nested experiments, the number of tracked eddies increases, with the internal domain exhibiting the greatest number of occurrences. The high resolution experiments tend to reproduce small scale features, with sizes less than the classic lee eddies. However, the realism of this representation needs to be confirmed. A biological devoted research, highlighted that the variability of phytoplankton biomass and primary production in the Bight was linked to high variability of the local hydrography, (Kyewalyanga et al., 2007). Other studies stated that the circulation in the Bight is complex (Lutjeharms and Jorge da Silva, 1988; Lamont et al., 2010). Modelling at high resolution with ROMS is generally known to improve the representation of the small scale processes (Penven et al., 2001; Debreu et al., 2012; Molemaker et al., 2015).

The thermocline structure of the lee eddy, has also been assessed based on these ROMS experiments. Vertical cross sections performed in the Delagoa Bight main section at 26^oS allowed one to show that the lee eddy presences/absences are well represented in all experiments. In the case of absence, the isolines are generally flat in agreement with in situ observations, (Lamont et al., 2010). A slight uprising of the isolines in both conditions of lee eddy present and absent was also

associated with the increase in the model resolution. In the horizontal sections, these conditions improve with increase of model resolution as well.

When the lee eddy is absent, a weak northward flow is found in the center of the domain. It seems to be due to the persistence of the counter-current in the lower levels despite the reversal of the northward branch of the lee eddy in the surface during absences. This northward current persists below $150\,m$. In the high resolution simulations this feature prevails from bottom to the surface under DBLE absent. It is associated with the prevalence of an anticyclonic circulation located at $25.75^oS, 33.5^oE$. Gründlingh et al. (1989) found an anticyclonic feature occupying the whole Bight, and refuted the possibility of a cyclonic eddy in the Bight. Because their satellite data had enough resolution, this feature seems to represent one of the aspects of the complex Delagoa Bight circulation. In the horizontal section, the thermocline structure is also well represented and shows an improvement in the representation of the lee eddy and its absences. The improvement of resolution is important in the representation of the thermocline structure in the Bight.

In association with the lee eddy, the transports of both the southward flowing current (formerly known as the Mozambique Current) and the coastal counter-current (the western branch of the lee eddy), were determined in section 5.2. It has been found that there is no correlation between these two currents. The eastern branch of the DBLE transports $21.67\,Sv$ southward, whereas the western branch consists of $1.24\,Sv$ toward the north (coastal counter-current). The southward transport based on this configuration does not show a big discrepancy with the transport of $18\,Sv$ calculated locally by (Lutjeharms, 2006a). The transport of coastal counter-current has never been estimated before. The oscillations noted in both appear to be due to the mesoscale activity in the surroundings, and to some degree their peaks tend to be close to the frequency of the passing anticyclones.

The eddy detecting and tracking system allowed the estimation of several parameters and associated statistics for the lee eddy. It has been found that the modelled average radius varies in the range of $34 - 43.2\,km$. The average life time is in the range of $23 - 27\,days$, whereas the amplitude varies between $8 - 12\,cm$. The maximum modelled radius vary in the range of $58 - 62\,km$. The amplitudes fall between $17 - 28\,cm$, whereas the maximum modelled life times lie between $63 - 126\,days$. These values are in agreement with the estimations based on AVISO, that show an average radius of $54\,km$, an average life time of $26\,days$ and an amplitude of $11\,cm$. The maximums in AVISO are $74\,km$, $116\,days$ and $20\,cm$, for the same parameters, respectively. Using drifters

data, (Lamont et al., 2010) found a lee eddy, which persisted for 6 *weeks* in the Bight, whereas Lutjeharms and Jorge da Silva (1988) estimated a diameter of 180 *km* for the lee eddy. Therefore the modelled maximum diameter based on Delagoa configurations is 124 *km*. This value is also close to 148 *km* estimated from AVISO altimetry. The long life times of the lee eddy found in both observations and model are associated to the proper characteristics of the lee eddy of existing for long time inside of the Bight, before it propagates southward. This subject will be discussed further in the next chapter. The southward advection of the lee eddy has also been discussed in literature (Lutjeharms and Jorge da Silva, 1988; Lamont et al., 2010).

The ROMS nested Delagoa Bight configurations allowed the determination of small mesoscale features not referred to in literature. These features consist of small cyclonic eddies existing simultaneously in the Bight, and occasionally of anticyclonic features. The anticyclonic features were found occupying the position $33.5^oE, 25.75^oS$, during the lee eddy absences in the Bight. Two to four cyclonic cores may be found cohabiting in the Bight. Nevertheless, the more the number of cores, the least their lifespan. This is because they tend to merge as a single eddy as they move southward, from their point of generation. When the lee eddy is present, which is the case most of the time, it occupies the whole terrace (Lutjeharms and Jorge da Silva, 1988). Therefore, the smaller features will not be there. The processes involved in the generation of the lee eddy and these small scale cyclonic and anticyclonic features are discussed in the next chapter. However, it can still be underscored that the most consistent multiple cores are generally characterized by two cyclones, whose thermocline structure is well established, hence distinguishable as separated eddies. They have been modelled cohabiting for more than 12 *days* (model days) in the Bight, before merging and moving toward the Agulhas Current. The fate of the cores, be it the merger or the southward dissipation, appears to be induced by the passing anticyclones.

By using the eddy detecting and tracking system the statistics of the anticyclonic features in the Delagoa Bight were determined. It has been demonstrated that these features are found in less that 31% of the total time of the model snapshots in the high resolution simulations. Their radii vary in the range of $27 - 43\,km$, and contain maximum life times of 12 *days*. Their amplitudes fall in the range of $4.82 - 8.56\,cm$. The anticyclonic feature found by Gründlingh et al. (1989) at $25.9S, 32.5^oE$ with a diameter of 70 *km*, agrees very well with the values found in this investigation. The complexity of the circulation in the Bight appears to be due to the complexity of the circulation in the Mozambique Channel, as noted in the model and satellite data.

The Inhambane Cyclones are cyclonic features somewhat similar to the Natal pulses (Lutjeharms and Roberts, 1988). Their occurrence show a seasonal cycle. They are generated off Inhambane at $24.7S, 35.4E$ by the passing anticyclones from the north of Mozambique Channel. By analysis of chlorophyll imagery Quartly and Srokosz (2004), found a cyclonic structure whose generation has been associated with a passing anticyclone, in this region. These features are consistent in ROMS Delagoa configurations. They are resolved as moving features with impact in the Delagoa Bight. When they move southward, can occasionally intrude into the center of Bight, as suggested by the eddy detecting and tracking system. The Inhambane Cyclone are characterized by strong thermocline structure. They appear to be deep reaching like the anticyclones that generate them. During the interaction with the Bight in Delagoa they are able to change completely the thermocline structure there, promoting the shelf offshore water masses exchanges. One of the most outstanding aspects of their properties is the recirculation, which is characterized by the northward movement offshore of the location of generation, before undergoing eventually a southward advection. Such recirculation seems to be driven by the merger of rings with the anticyclonic eddies from the east. Nevertheless, the rate of occurrence of such mergers is not well known statistically. Overall, they do advect southward towards the northern Agulhas Current. Roberts et al. (2014) investigated a dipole with an important contribution to the local Biology here. In this study it was noted that at times, the pulses can detach as single cyclonic features, and intrude into the Bight or move southward. The Inhambane Cyclone mean life times vary in the range of $19\,days$ to $46\,days$, whereas the maximums vary in the range of $84\,days$ to $90\,days$. In AVISO, it consists of an average life-time of $17\,days$ and a maximum of $47\,days$. The long life in the model is due to the recirculation. Their radii and amplitudes are of the same order of those of the lee eddy. Further details are shown in (Cossa et al., 2016).

Chapter 6

Location of generation of cyclonic eddies in the Delagoa Bight

6.1 Introduction

In the previous chapter it has been shown that the circulation in the Bight is complex, with the prevalence of mesoscale cyclonic and anticyclonic smaller features being common. It has been demonstrated that these small cells are found when the lee eddy, the most prominent feature of the Delagoa Bight circulation is absent, say, when it cannot fill the whole terrace, through analysis of model data sets of the nested configuration experiment. The statistics of these features were also determined using the eddy detecting and tracking system, Halo et al. (2014b).

This chapter, is designed to investigate the mechanism of generation of the lee eddy in the Delagoa Bight. This issue has been addressed in previous studies, (Lutjeharms and Jorge da Silva, 1988; Lamont et al., 2010). Based on Gill and Schumann (1979) model, Lutjeharms and Jorge da Silva (1988) presumed that the Mozambique Current, formerly considered as an inertial jet of permanent southwest-wards flowing boundary current in this region, had part of its water diverted northward as it impinges in the shallow valley between the coast and the Central Terrace, off Ponta D'Ouro. In another assertion, Lamont et al. (2010), suggested that the spawning of the Delagoa Bight lee eddy was due to a passing anticyclone from the north of the Mozambique Channel. Gründlingh et al. (1989) used satellite imagery to refute the prevalence of a cyclonic circulation in the Bight. They found an anticyclonic feature occupying the whole terrace, whose generation they ascribed to the instabilities of the southward flowing boundary current. The discrepancies in the interpretation

of the generation of the DBLE, as well as the less known possibility of occurrence of anticyclonic features led to the conception of this chapter. In this respect, the underlying physics will be examined, whereas the eddy detecting and tracking system will be used to find the exact location of the lee eddy generation.

Another reason that justifies the investigation of the Delagoa Bight lee eddy generation processes can be related to the high productivity, (Kyewalyanga et al., 2007; Barlow et al., 2008). Indeed, in Mozambique, it is recognized as the most important area in commercial fisheries after the Sofala Bank, (Dove, 2015). Its geographical location is peculiar, due to the merger of the southward flowing anticyclonic eddies from the north of Mozambique Channel and those from the south-east of Madagascar offshore of the Bight, (Cossa et al., 2016). Furthermore, it is dynamically linked with the Agulhas Current further south, because the cyclonic eddies generated there move southward towards the northern end of this current, (Lutjeharms and Jorge da Silva, 1988; Lutjeharms, 2006a; Lamont et al., 2010; Cossa et al., 2016). The circulation in this Bight, is considered to be of great relevance in the dynamics of the western side of the Inhaca Island ecosystem (Paula et al., 1998). Therefore, its full understanding is expected to help in the management of the ecosystem in this region.

The chapter is organized in the following manner: In section 6.2 the location and processes involved in the lee eddy generation are discussed based on analysis of the vorticity fields. As an extension, a discussion of the Inhambane Cyclone generation is also included. This feature which is investigated in the previous chapter, was discussed by Cossa et al. (2016). In section 6.3 the barotropic and baroclinic instabilities are assessed based on analyses of energy conversion terms. The last section of the chapter, is dedicated to the conclusion and discussions.

6.2 Locals and processes of generation of cyclonic eddies in the Delagoa Bight

6.2.1 Analysis of vorticity fields

The generation of the lee eddy is first assessed using the surface currents overlaid on surface relative vorticity. In this case, data emanated from the mother domain of the experience with tides and a two way nesting (DELAG-IV) is used, in contrast with the case without tides and

child domain that was used by Cossa et al. (2016). Tides and no-tides do not show considerable changes in the representation of the local dynamics, except in the speed of the flow as mentioned at the end of chapter 4.

Analyses of the model (DELAG-IV) snapshots and animations, allowed one to consider two conditions under which the onset of the lee eddy is possible. The first condition, is when the intensity of the southward flowing current is weak or moderate and the second condition, is when the mesoscale features are far away from the Bight, (Cossa et al., 2016). Despite the evolution introduced by nesting, and the subsequent development of smaller mesoscale features as mentioned in the previous chapter, and hence of the difficulty of separating the condition of lee eddy present from absent, these two criteria are maintained in these analyses.

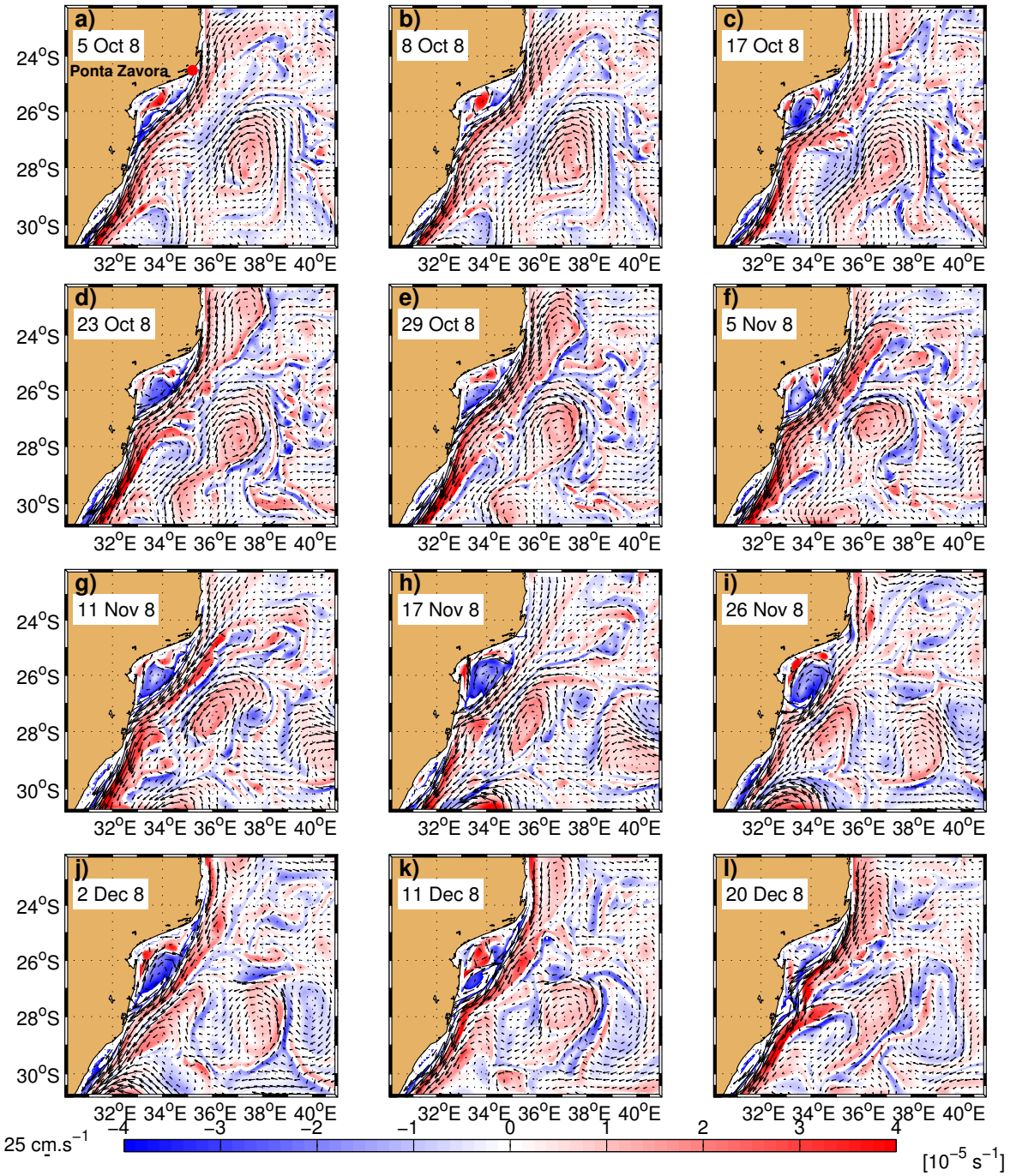

Figure 6.2.1: Simulated surface velocities overlaid on surface relative vorticity maps based on (DELAG-IV) (external domain) 3-days averages between 05 October year 8, and 20 December year 8. A Delagoa Bight lee eddy was present from 17 October to 23 November of year 8.

Initially the southward flowing current satisfies the first condition, Figure 6.2.1. It produces negative vorticity on its coastal edge, as it overshoots from the promontory in the coastline of Ponta Závora, around 24^oS. The generation of negative vorticity seems to be linked to the friction of the current with the shelf (D'Assaro, 1988; Magaldi et al., 2008), and also to the presence of the shallow Inharime Terrace past the promontory. On model date ($5Oct8$) (day 5 of month 10 of the model year 8), there is no significant organized negative vorticity inside of the Bight, indicative of the absence of the lee eddy in the Bight. The cyclonic vorticity observed south of 26^oS is due to

a previous cyclonic lee eddy, which has undergone dissipation as it enters the northern Agulhas Current region, where the speed of the current is high, whereas to the north of the domain the negative vorticity is still evolving (Figure 6.2.1a,b).

In contrast with the model without tides used by Cossa et al. (2016), this experience denotes a reduction in the sizes of the strips of negative vorticity usually spread inside of the Bight, possibly due to the increase of the speed of the flow noted at the coast in case of simulations with the tides, as demonstrated in chapter 4. Part of the southward flowing current is diverted by topography towards the coast, along the $500\,m$ isobath before it reaches 26^oS. This current flows northward inducing the development of a cell of negative vorticity northeast of the domain. The remainder of the current impinges into the coast off Ponta D'Ouro as it flows southward, enhancing the positive vorticity there. Due to the shallow depth and to the impact of the southward momentum here, the cell of negative vorticity developed to the north of 26^oS organizes quickly and slides southward toward the wider terrace in the center of the Bight, (Figure 6.2.1c).

An anticyclonic eddy from the east plays a role in the stability and strength of the lee eddy (negative vorticity), as it moves southwestwards towards the coast, off Ponta D'Ouro around 28^oS. As it reaches the coast, it seems to facilitate the organization of negative vorticity and hence, the growth of the lee eddy inside of the Bight (Figure 6.2.1d). On the other hand, on model date ($23Oct8$) the anticyclonic vorticity off Ponta Závora reflects the incoming of a small anticyclonic eddy, which forms a wodon like structure (Shi and Nof, 1994) as it interacts with the southward flowing current. Both anticyclonic features are crucial in the squashing of negative vorticity inside of the Bight, as shown in (Figure 6.2.1e). Because the southward flowing current persists, the production of negative vorticity in the northeastern sector of the Bight is continuous. Therefore the accumulated vorticity merges with the already existing negative vorticity and this contributes to the formation of the lee eddy, (Figures 6.2.1f-j).

Again, the positioning of an anticyclonic feature from the east seems to play a role. Finally, in Figures (6.2.1k-l) the process is reinitialized. It can be added that the complexity of the circulation in the Bight is due to the prevalence of small mesoscale features, and to the passing anticyclonic features. The sequences presented here, show that the interaction between the anticyclones with the southward flowing boundary current is the most important reason behind the development of cyclonic and anticyclonic cells when the lee eddy cannot fill the whole terrace (it is absent).

Regarding the second condition of the lee eddy generation, it depends on the angle at which

the southward current reaches the coast, off Ponta D'Ouro (Figures 6.2.1c-e). The anticyclones from the east act to reinforce this process. This process agrees with the mechanism proposed by Lutjeharms and Jorge da Silva (1988), in which the southward flowing boundary current which functions as an inertial jet, is likely to bifurcate as it impinges in the coast at 27^oS. Between both, the first condition seems to be the most predominant, and that is shown below using the eddy detecting and tracking system.

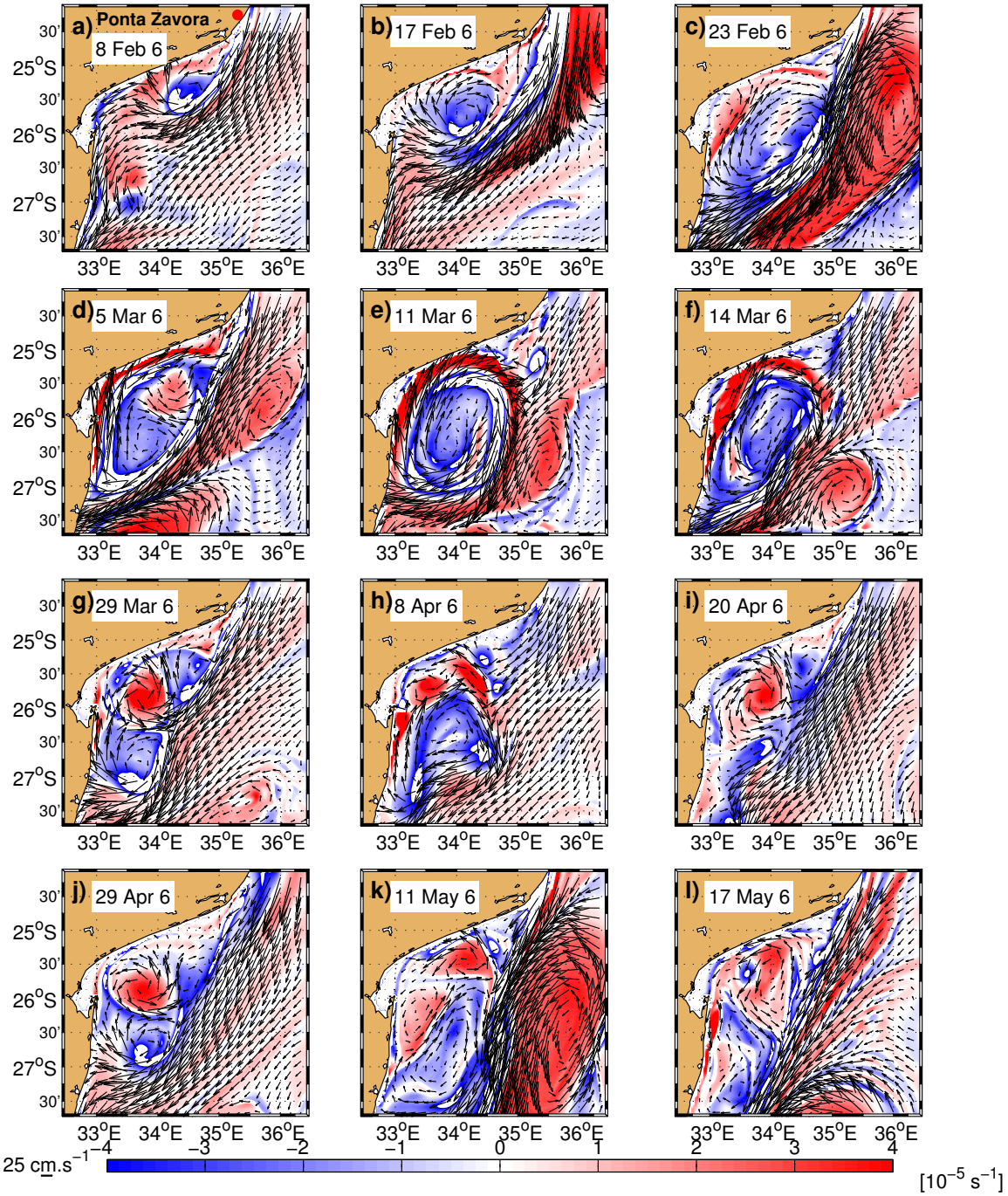

Figure 6.2.2: Simulated surface velocities overlaid on surface relative vorticity maps based on DELAG-IV (Internal domain) 3-days averages between 08 February and 17 May year 6. A Delagoa Bight lee eddy was present from 08 February to 17 May of model year 6.

To shed more light in the mechanisms involved in the generation of the DBLE, the same analysis

is carried out using data of the child domain of the same experiment (Figure 6.2.2). The resolution in this domain is roughly $3\,km$ ($\frac{1}{30}^o$), whereas in the mother it is $10\,km$ ($\frac{1}{10}^o$). This high resolution should improve the representation of the small processes occurring inside the Bight. On model date ($8Feb6$) (Figure 6.2.2a), the southward flowing current sweeps the whole domain, with part of its western edge diverting towards west to impinge into the coast, around 25.5^oS. This diversion is due to interaction of the current with the local bathymetry. Like in the previous case, this takes place in the northeastern sector of the Bight.

On model dates ($17-23Feb6$), (Figures 6.2.2b-c) the size of the lee eddy increases as the southward current is reinforced by an anticyclonic eddy from the north. This anticyclonic vorticity interacts with the negative vorticity (lee eddy), which is located in the center of the Bight, (Figures 6.2.2d-f). This condition is short lived. It reveals the fast shifts that characterize the circulation in the Bight, which basically consist of cells of cyclonic and anticyclonic vorticity that dominate the flow when the lee eddy cannot fill the whole terrace, (Figure 6.2.2g). The quick shifts of vorticity is induced the by merger of cyclonic vorticity caused by the southward momentum (Figure 6.2.2h), whereas a condition of no lee eddy is dominated by anticyclonic vorticity to the western side of the domain, exactly centered in the location where Gründlingh et al. (1989) found an anticyclonic eddy, that they affirmed was a single structure covering the whole Bight.

A strip of pronounced negative vorticity located in the center of the Bight, along the shoreward side of the southward flowing current, which forms a diagonal with the domain on model date ($20Apr6$) in (Figure 6.2.2i,j), reflects the presence of a northward flowing current in the center of the Bight, in association with the presence of this anticyclonic feature. Although not quite prominent, this feature was noted as an undercurrent lying below $200-300\,m$, in the composites when the lee eddy is absent as detailed in the previous chapter.

The separation of the modelled lee eddy presences from absences is subtle, due to the quick re-accumulation of negative vorticity northeast of the domain. Southwest of the Bight, the quick concentration of cyclonic vorticity is caused by the negative vorticity which develops on the western edge of the southward flowing current. This increases the likelihood of development of cyclonic features as the southwards flowing current impinges into the coast around Inhaca, in a mechanism similar to the one presented by Lutjeharms and Jorge da Silva (1988) (Figure 6.2.2j). This shows that this point is one of the locations where the lee eddy is generated. The fate of the cyclonic features generated here is a merger with those from the northeastern sector, because they generally

slide southward. Likewise, the fate of the merger is a southward propagation, toward the Agulhas Current. An anticyclonic eddy can occasionally interact with the resulting features (Figure 6.2.2k), before sweeping them southward to develop a condition of lee eddy absent in the Bight (Figure 6.2.2l). The absence of the lee eddy is characterized by strips of negative vorticity lying in the western side of the southward flowing current. These strips, reveal the prevalence of a complex regime of circulation inside of the Bight. When an anticyclonic feature is found interacting with the southward flowing current inside of the Bight, there is a likelihood of generation of upwelling in association with the interaction of two flows in opposite direction, (Figure 6.2.2i,l). Nevertheless, these regimes of circulation are short lived because the lee eddy occupies the whole domain once it is established.

In order to find the exact locations of the lee eddy generation in the Bight, several small regions were surveyed using the eddy detecting and tracking system, and the results are depicted in Figure 6.2.3. The external domain of the model with tides is chosen considering its size, which facilitates to follow the fate of the lee eddies as they move southward towards the Agulhas Current. Inside of the Bight, this experiment has been able to yield a total of 121 *cyclones*, equivalent to 15.125 *cyclones* per year, (Figure 6.2.3a). The realism of this mesoscale processes needs to be confirmed using in situ measurements. Nevertheless, the results based on the reference experiment show similarity with the observation, and were presented by Cossa et al. (2016). Therefore, the results found here can be ascribed to the high resolution, which allows to capture small scale features, not visible in the coarse resolution simulations and AVISO.

The survey in the central part of the domain where the lee eddy usually resides (Lutjeharms and Jorge da Silva, 1988; de Ruijter et al., 2006; Lamont et al., 2010; Dove, 2015), shows that 45.45% of the total number of cyclones reside in the wide terrace (red trajectories) in Figure (6.2.3a). Most of these eddies stay in the Bight for weeks before moving southward (Figure 6.2.3a). Their ratio of prevalence in the center is 6.875 $cyclones/year$. On tracking the eastern sector of the the Bight, (Figure 6.2.3b), 55.4% of the total were found. These eddies are generated in the northeastern sector of the Bight, and migrate to occupy wide terrace before moving southward. From the northeastern-most corner of this sector (Figure 6.2.3c) 23.1% of the total were tracked, whereas in the whole southwestern sector 24.8% were found. Therefore, it has been concluded that the majority of the lee eddies are generated in the northeastern sector of the Bight under weak to moderate conditions of the southward flowing current, which behaves as a boundary current in

most of the times, as demonstrated in chapter 4.

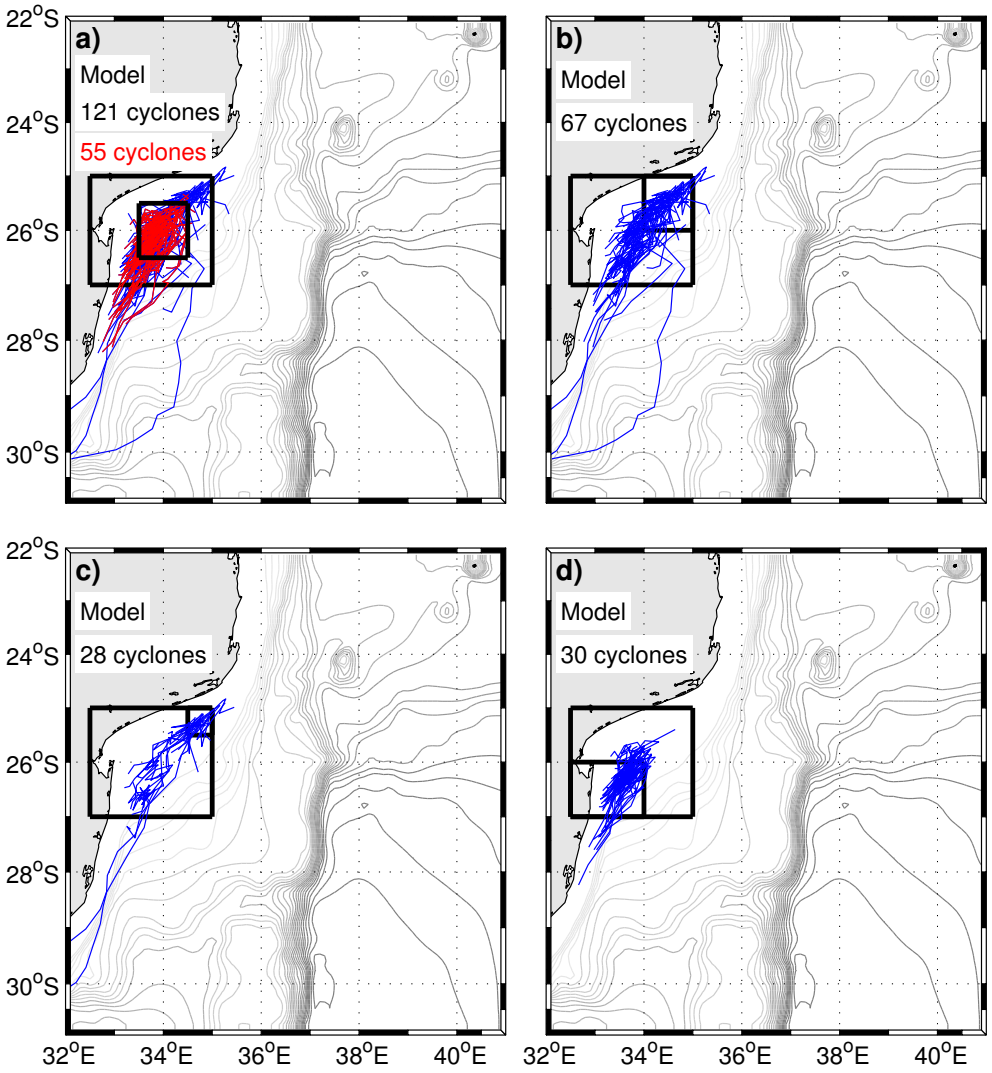

Figure 6.2.3: Trajectories of cyclonic eddies tracked in the external domain of the model with tides (DELAG-IV). In a) the whole domain (blue) and innermost part (red). In b) and c) are presented the lee eddies tracked in the northeastern sector of the Bight, whereas in d) are shown the tracks of the southwestern sector (blue) for all the cases. The gray lines in all maps are contours of the bottom topography.

To show the behaviour of the eddies generated in the northeastern sector of the Bight, an example of a long lived lee eddy generated there, is presented in Figure 6.2.4. On model date ($5Mar8$), its onset is at approximately $34.4^oE, 25^oS$ (Figure 6.2.4a). The southward flowing current in this phase, satisfies the conditions of moderate flow mentioned above. The lee eddy develops quickly to an aged phase as an anticyclone from the east moves towards the coast off Ponta D'Ouro, (Figures 6.2.4b-c). Overall, the prevalence of positive SSH southwest of the domain (around 28^oS) coincides with the establishment of the lee eddy in the center of the Bight (Figures 6.2.4d-e). This appears to show the importance of the eddies from the east in the establishment of the DBLE. From the north, a pulse moving with an anticyclonic feature interacts with the lee eddy (Figures 6.2.4c-e), and the latter is absorbed in the northern Agulhas Current, (Figure 6.2.4f).

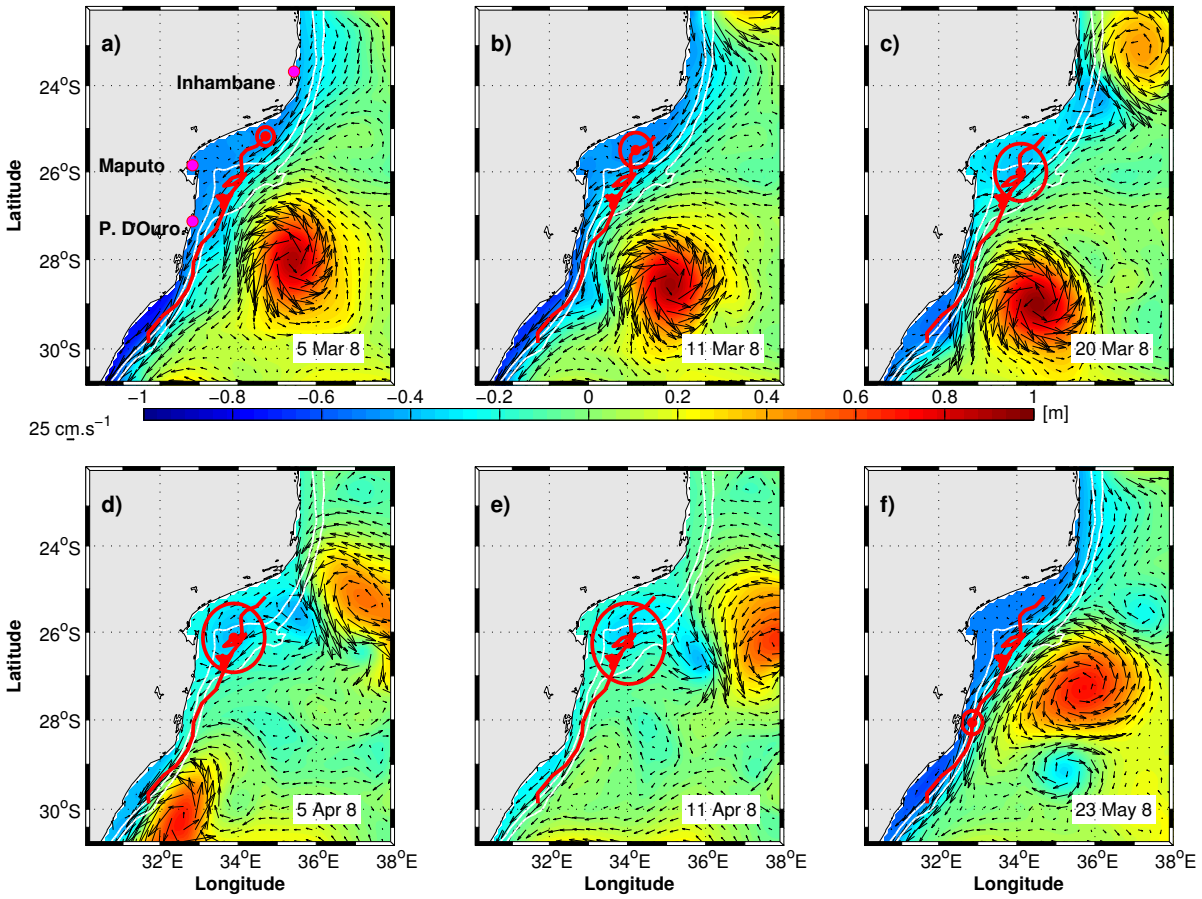

Figure 6.2.4: Model surface currents overlaid on SSH given as an example of a long lived DBLE generated in the northeastern sector of the Bight. The red line indicates its trajectory, whereas the circle shows its exact position of the eddy. The white lines represent the 500 and 1000 m isobaths.

Although, the thermocline structure of the lee eddy had been examined using composite analysis in the previous chapter, it is revisited resorting to the analysis of the characteristics of a long lived lee eddy generated in the northeastern sector of the Bight, Figure 6.2.5. The idea is to highlight that the cyclonic features generated there, move southward to form the classic in the wide terrace DBLE. The SSH overlaid on the surface currents is illustrated in Figure (6.2.5a). The red circle represents the size of the lee eddy, whereas the red line indicates its trajectory, as determined through the eddy detecting and tracking system. This trajectory confirms that this particular lee eddy, was generated in the northeastern sector of the Bight. It slides towards the center of the terrace, to occupies the whole area, before being swept southward through the edges of an anticyclonic eddy from the north (not shown).

The inception of the lee eddy was on model date ($11Oct5$) and disappeared on model date ($8Dec5$), with a total life time of 57 $days$. Its minimum radius varied in the range of 16.7 km at its onset to around 26.6 km at its last detectable moment in the northern Agulhas Current. Its maximum radius was 69.7 km on model date ($2Nov5$), as depicted in Figure (6.2.5a). Vertical cross sections

were performed in the main Delagoa Bight section at 26^oS. In the meridional velocity (Figure 6.2.5b), it has been inferred that the northward branch of the lee eddy flows at speeds above $25\,cm/s$. Although its intensity decreases with depth, it still presents speeds above $10\,cm/s$ at $400\,m$ depth. The center of the lee eddy is represented by the contour of zero meridional velocity (black line), which forms a vertical at approximately $100\,km$ from the coast. Towards offshore, the southward flowing coastal current is dominant, with speeds above $45\,cm/s$. An intrusion of water masses from the south at around $200\,km$ from the coast is noticeable (Figure 6.2.5b). The origin of this water is unknown. It is speculated that it derives from the northward flowing undercurrent, or from a northwards branch of a neighbouring mesoscale feature.

The temperature cross section (Figure 6.2.5c) shows a uniform distribution in the upper layer (above $50\,m$ depth), with a tendency of widening towards offshore. This layer is characterized by temperatures above 25^oC which is typical for the warmer seasons in the Bight. Below $75\,m$ depth, a region of accented vertical gradient reflects the modelled thermocline, under lee eddy presence. This gradient, grows towards offshore. The 10^oC and 16^oC isotherms (black contours) consist of strong doming, typical of cyclonic eddies, with peaks located in the usual center of the DBLE at $100\,km$ from the coast. In salinity, the halocline lies below $100\,m$ depth and consists of a much uniform gradient towards offshore. Both the $35.2\,psu$ and $35.2\,psu$ isohalines, mimic the doming associated with the lee eddy (Figure 6.2.5d). In the horizontal, the temperature field shows several concentric isotherms that highlight the preeminence of a cyclonic feature at $100\,m$ depth. The southward flowing current is characterized by a warmer strip encompassed in the 20^oC and 21^oC isotherms (Figure 6.2.5e). In the salinity field, the $35.15\,psu$ marks the lee eddy (Figure 6.2.5f). It presents lower salinity in the core, consistent with the upwelling of fresher water masses. The southeastern side of the domain is dominated by higher salinity, in comparison with the southward flowing current. Since the DBLE described using composite analyses in the previous chapter is similar to this cyclone, it can be reaffirmed that the lee eddy in the Delagoa Bight is mainly generated in the northeastern sector of the Bight.

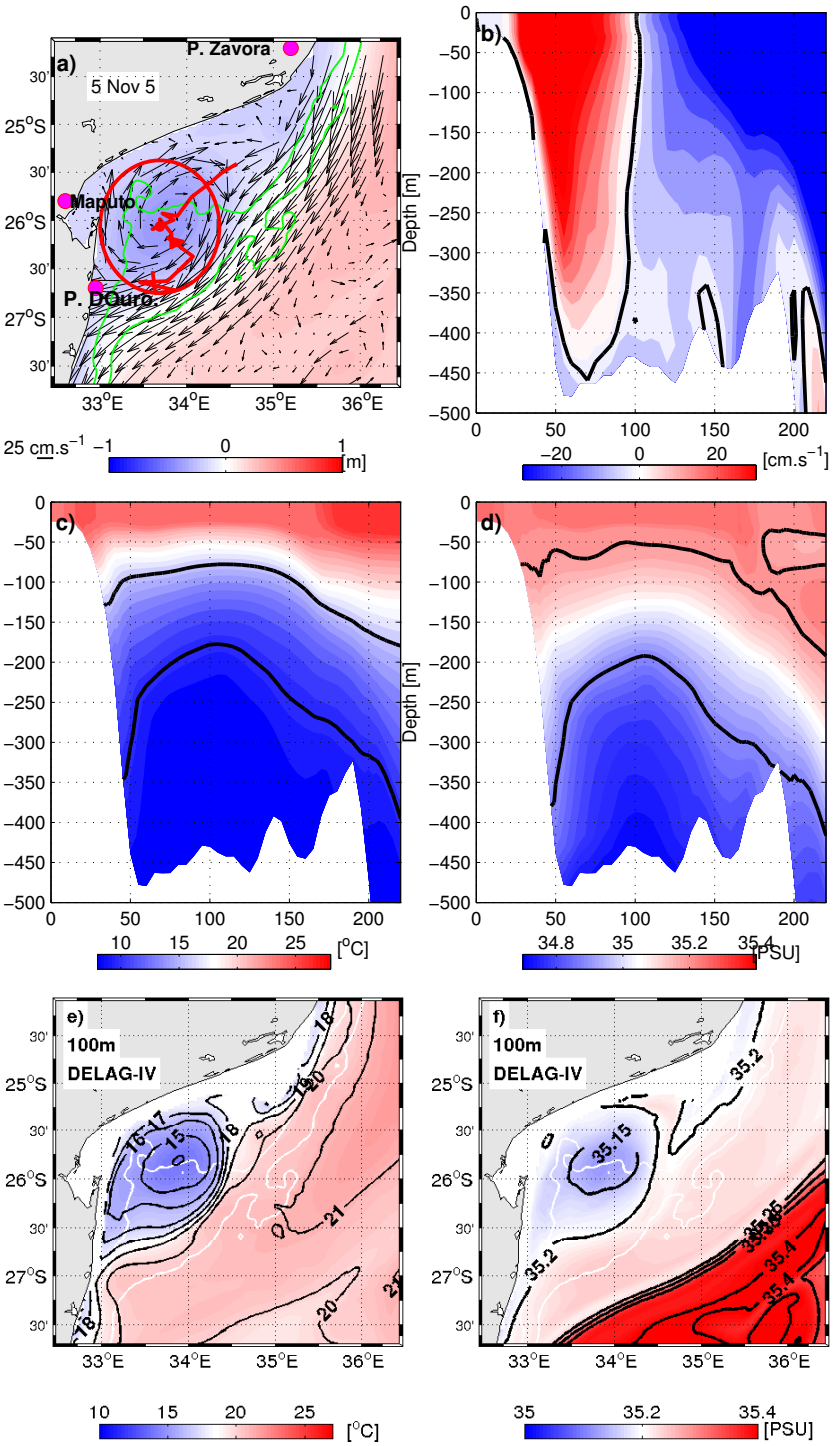

Figure 6.2.5: Characteristics of a single long lived lee eddy. In a) the surface currents are overlaid on SSH, with the red line indicating the trajectory and the size of the eddy (circle). The green (white) lines show the $500 - 1000m$ isobaths. The meridional velocity cross section is depicted in black in b). The temperature and salinity sections are in c) and d), respectively. In e) and f) are shown the horizontal sections of the same parameters.

The mechanism involved in the generation of the Inhambane Cyclones (pulses), is also analyzed exploring DELAG-II data, in Figure 6.2.6. The choice of the data is arbitrary and takes into account that there are no significant differences between tides and no tides simulations, in the way both represent the local dynamics. Before the onset of the pulse (Figure 6.2.6a), the region northeast of Ponta Závora is characterized by weak strips of negative and positive vorticity, that

reflect the approximation of an anticyclonic eddy from the north. In the Delagoa Bight the slight organized negative vorticity, shows the consistency of the lee eddy there. South of the domain the positive vorticity that abuts the coast at 27^oS, is due to the consistency of the southward flowing current and the flow from the east. The coastal counter-current is established and hence the lee eddy in the Bight. The angle between the southward flowing current with the coast, which favours the presence of an organized negative vorticity in the Bight is promoted by an incipient Inhambane Cyclone (Figure 6.2.6b). Off Inhambane, when the anticyclone interacts with the steep shelf, produces negative vorticity which tends to be extracted from it (Figure 6.2.6c). This process takes place because usually the anticyclones develop ringlets (satellite eddies) in their periphery (Nof, 1993). Therefore, their interaction with the shelf facilitates the extraction of negative vorticity and hence the formation of the pulse.

This pulse occasionally recirculates with the anticyclones as suggested by both the model snapshots and the eddy detecting and tracking system. The core of the ring is characterized by positive vorticity, whereas its periphery contains negative vorticity (Figure 6.2.6d-f). According to Nof (1993), caps of lighter water may be accumulated on the top of the ring, due to the interaction with the fresh coastal water or with a warm current. On being expelled, the lighter water promotes negative vorticity in the outer edge of the ring, which is collected from the ring as it interacts with the shelf.

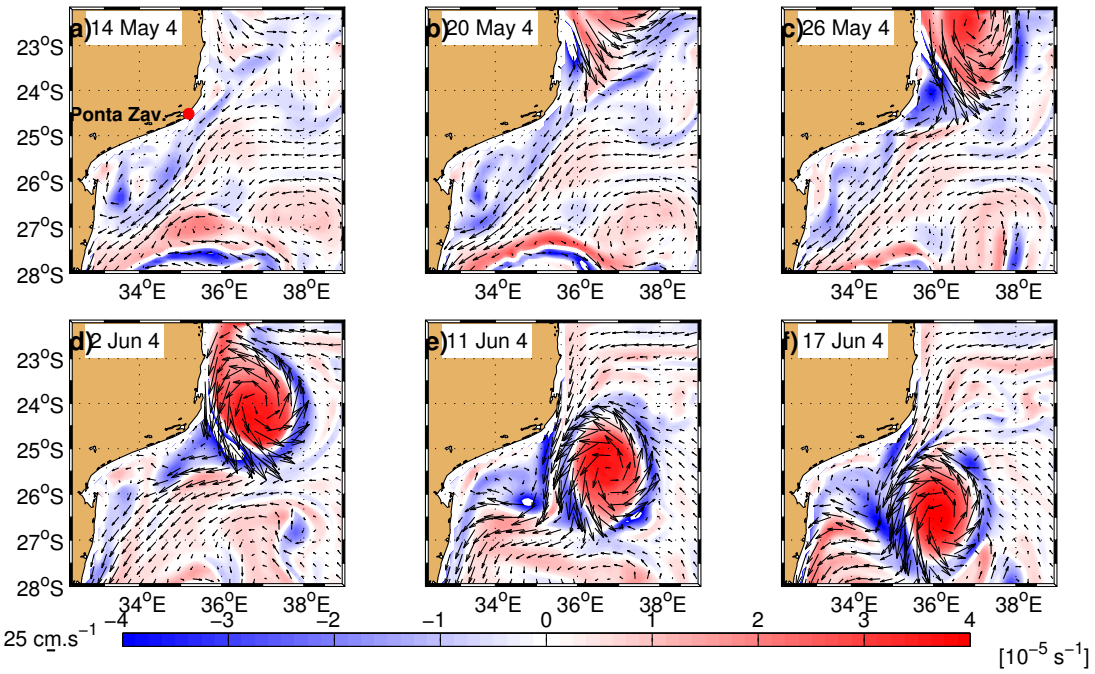

Figure 6.2.6: Relative vorticity associated to an Inhambane Cyclone, estimated using the data of the model with tides (DELAG-II).

6.3 Barotropic and Baroclinic instabilities

The analysis of the major components of the energy budget in geophysical fluid dynamics is an important tool for the investigation of the energy conversions processes in both the ocean and atmosphere sciences. Initially developed to tackle these problems in the atmosphere (Lorenz, 1951), its application was extended to the analysis of the dynamics in the ocean, (Miller and Lee, 1995; Oort et al., 1994, 1989; Orlanski and Cox, 1972). Basically, these analyses are useful because they show the interaction between the mean flow and the eddy field of the geophysical fluids, as well as the transfers that occur between the energy reservoirs (Azevedo et al., 2008). Such reservoirs are: the Mean Kinetic Energy (MKE), the EKE, the Mean Potential Energy (MPE) and the Eddy Potential Energy (EPE). The Lorentz diagram is a detailed way to represent the interactions between these reservoirs, and the exchange of energy across their boundaries (Azevedo et al., 2008). The conversion rates represented in the diagram can be summarized in the following set of equations:

$$T_1 = -\frac{g}{\rho_0} \iiint \overline{\rho' w'} dV \tag{6.3.1}$$

$$T_2 = -\frac{g}{\rho_0} \iiint \frac{\overline{u'\rho'}\frac{\partial \bar{\rho}}{\partial x} + \overline{v'\rho'}\frac{\partial \bar{\rho}}{\partial y}}{\frac{d\bar{\rho}}{dz}} dV \tag{6.3.2}$$

$$T_3 = -\frac{g}{\rho_0} \iiint \bar{w}.\bar{\rho} dV \tag{6.3.3}$$

$$T_4 = -\iiint [\overline{u'u'}\frac{\partial \bar{u}}{\partial x} + \overline{u'v'}\left(\frac{\partial \bar{u}}{\partial y} + \frac{\partial \bar{v}}{\partial x}\right) + \overline{v'v'}\frac{\partial \bar{v}}{\partial y}] dV \tag{6.3.4}$$

where T_1 represents the rate of conversion from the eddy potential to eddy kinetic energy. It explains the buoyancy production by the work performed by turbulent forces on the vertical stratification that leads into the changes on the potential energy (Cushman-Roisin and Beckers, 2011). T_2 is the rate of conversion of energy from the mean potential to eddy potential, T_3 indicates the conversion from the mean potential to the mean kinetic energy, and at last T_4 represents the conversion from the mean kinetic energy (of the mean flow) to the eddy kinetic energy (turbulence). It is known as the shear production term because it contains the shear of the large scale flow, (Cushman-Roisin and Beckers, 2011). In this set of equations u, v and w represent the zonal,

the meridional and the vertical components of the flow, respectively. g is the acceleration due to gravity, ρ is the sea water density, ρ_o is the sea water density of reference, and $\tilde{\rho}(z)$ is the reference state for the potential density. The derivative signs indicate the fluctuation of the parameters in relation to their means.

In order to investigate the processes involved in the generation of cyclonic eddies in the Bight T_1 and T_4 have been chosen. These terms, have been used in the region to examine the generation of eddies south of Madagascar (Halo et al., 2014b). Biastoch and Krauss (1999) used T_3 and T_4 to investigate the generation of the anticyclonic eddies of the northern Mozambique Channel, whereas Tsugawa and Hasumi (2010) used T_2 and T_4 to explain the generation of the Natal Pulses, some cyclonic meanders in the Agulhas Current (Lutjeharms and Roberts, 1988). In the North Atlantic (Beckmann et al., 1994) used the whole set of equations given above (6.3.1-6.3.4). Regarding the terms chosen for this investigation, it may be underlined that when T_1 is positive, the conversion rate is from eddy potential to eddy kinetic energy, and the signature in the maps suggests baroclinic instability. When, T_4 is positive the conversion rate is from mean kinetic to eddy kinetic energy and the signature indicates barotropic instability, (Halo et al., 2014b; Miller and Lee, 1995).

Two regions were selected for the evaluation of the conversion rates (Figure 6.3.1). Region I is located in the Delagoa terrace (Lamont et al., 2010; Lutjeharms and Jorge da Silva, 1988) where the lee eddy is usually found, whereas region II is located off Inhambane. The inclusion of the latter is mainly to assess the processes involved in the generation of the Inhambane pulses (Cossa et al., 2016). Both terms were integrated along the upper $500\,m$ of the water column. The results are depicted in Table 6.1.

For the model without tides (DELAG-I) in region I, $T_4 > 0$ and $T_1 < 0$. Therefore, in this case the eddy generation is by barotropic instabilities. This area is normally dominated by the lee eddy, (Lamont et al., 2010; Lutjeharms and Jorge da Silva, 1988). Therefore the formation of cyclonic eddies, and in particular the DBLE is through barotropic instabilities. According to the same model (DELAG-I), in region II the rates of energy conversion are such that $T_4 > 0$ and $T_1 > 0$. This implies eddy formation by both barotropic and baroclinic instabilities. Therefore, the Inhambane Cyclones found in the reference experiment (DELAG-I), may be generated by both barotropic and baroclinic instabilities. The lee eddy is likely to dissipate its energy into eddy potential locally, since $T_1 < 0$, Table 6.1.

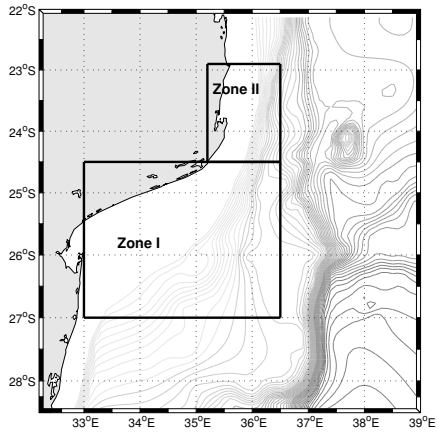

Figure 6.3.1: Zones used to estimate the energy conversion terms in the Delagoa region. Zone I, is in the center of the Bight whereas II is located off Inhambane. The gray lines are contours of bathymetry.

Table 6.1: Energy conversion terms T_4 and T_1, in regions I and II, for the model without tides (DELAG-I)

Model (DOMAIN)	REGION	T_4 $[m^3.s^{-3}]$	T_1 $[m^3.s^{-3}]$
DELAG-I	I	0.154×10^{-6}	-1.7×10^{-6}
DELAG-I	II	0.12×10^{-6}	3.34×10^{-6}

In Figure 6.3.2, the map of conversion rates T_4, from the mean kinetic to eddy kinetic, integrated along the upper $500\,m$ of the water column is shown, for the reference simulation (DELAG-I). The strip dominated by the southward flowing current and the anticyclonic eddies from the north, is characterized by positive rates ($T_4 > 0$). This signature highlights the importance of the barotropic instabilities in that area. Between the 500 and $1000\,m$ isobaths, and somewhat to the north of 26^oS, the maximum of conversion rates takes place. Along the coast of Inhambane, and off Ponta D'Ouro there are regions of negative conversion rates ($T_4 < 0$). In this case, there is eddy dissipation in the mean flow in those locations. Off Ponta D'Ouro, this negative rate seems to reflect the areas of dissipation of DBLEs as they move southward from their usual location in the center of the Bight, towards the Agulhas Current.

A recent work based on analysis of satellite observations and drifter trajectories, demonstrated that the northern Agulhas Current is a potential region for dissipation of cyclonic and anticyclonic eddies by entrainment in the main flow, (Braby et al., 2016). Therefore, our results appear to be concomitant with the processes that dominate the oceanic flow in that area. The zone off Inhambane is dominate by transient cyclonic pulses locally generated (Cossa et al., 2016). Therefore, the negative rates also seem the reflect the dissipation of eddies close to the position of generation of Inhambane Cyclones. The majority of these features, move southward with the anticyclones, (Cossa et al., 2016).

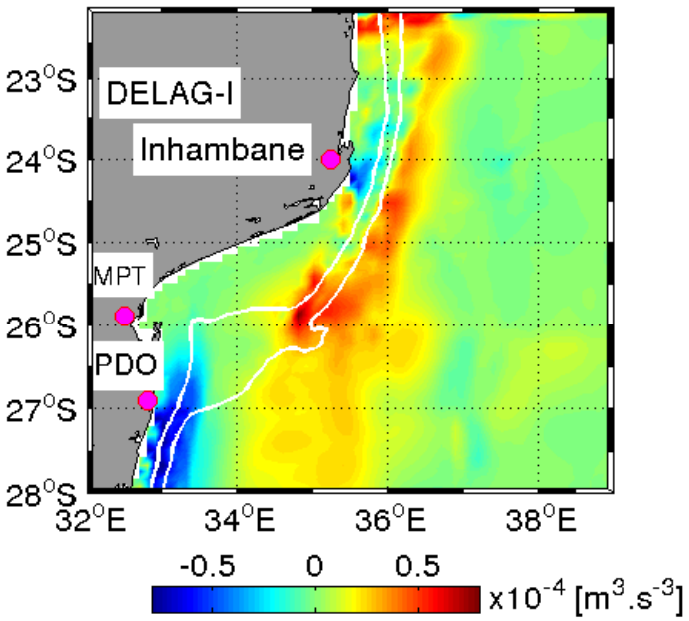

Figure 6.3.2: Energy conversion rates (T_4) integrated along the upper 500 m in the Delagoa Region, determined from the model without tides. The white lines represent the $500 - 1000\,m$ isobaths.

The mapped integrated conversion rate T_1 for DELAG-I is not significant, Figure 6.3.3. It is characterized by patchy areas of high rates along the 500 and 1000 m isobaths, which alternates with negative rates, suggestive of buoyancy production by the work of the eddies in the vertical, (Cushman-Roisin and Beckers, 2011) or by the opposite effect, the transformation from the eddy kinetic energy to eddy potential, (Figure 6.3.3). Offshore, it is characterized by positive conversions rates along the northern end of the Mozambique ridge, which extends towards the center of the domain. This seems to indicate the impact of the ridge. Overall, the distribution of T_1 suggests that the baroclinic instabilities are not the most important mechanism for the lee eddy generation in this region, at least from the stand point of these simulations. Indeed, the distribution of these conversion rates based on the other coarse resolution simulation shows similar patterns, as depicted in appendix B.3.1.

The effect of improving resolution is assessed through introduction of a child domain in the model without tides (DELAG-III). This allows one to recalculate both (T_4 and T_1) inside the region I defined in Figure 6.3.1. This is the region falling inside of the area covered by both the child and mother domains. The results are represented in Table 6.2. In this case both terms of integrated conversion rates are positive ($T_4 > 0$ and $T_1 > 0$), indicative of the prevalence of both barotropic and baroclinic instabilities. Comparisons between tables 6.2 and 6.1, show that the barotropic instabilities in region I, grow with improvement of resolution, whereas the baroclinic instabilities, which were weak in the reference experiment, also became important in the local generation of

mesoscale features.

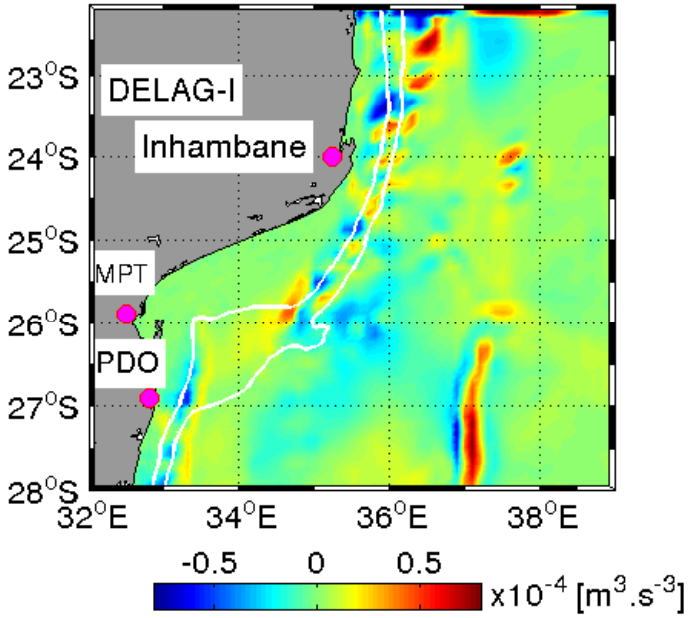

Figure 6.3.3: Eddy potential to eddy kinetic energy conversion rates (T_1) integrated along the upper layer ($500\,m$) in the Delagoa Region, determined from the model without tides (DELAG-I). The white lines represent the $500 - 1000\,m$ isobaths.

Table 6.2: Energy conversion terms T_4 and T_1, for DELAG-I and II in regions (I) and (II).

Model (DOMAIN)	REGION	T_4 $[m^3.s^{-3}]$	T_1 $[m^3.s^{-3}]$
Int. DELAG-III	I	0.13×10^{-6}	0.22×10^{-6}

The maps of conversions rates from the mean kinetic to eddy kinetic energy (T_4) in the case of the nested simulation without tides (DELAG-III), are given in Figure 6.3.4. In analogy with the coarse domain presented above, the rates of conversions are higher in the path of the southward flowing current. They tend to grow with resolution, by comparison with the non nested simulation portrayed above. The highest conversion rates occur between the 500 and $1000\,m$ isobaths, (Figure 6.3.4). Their maximum is concentrated in the $500\,m$ isobath north of 26^oS, suggestive of intense perturbation of the mean flow in there and therefore, conversion of the flow into eddy kinetic energy (turbulence) there. The rate of transfer from the mean flow to eddy kinetic energy, agrees with the diversion of part of the southward flowing current towards the coast analyzed in the previous sections, using the vorticity fields. Along the pathway of the coastal counter-current, the northward branch of the lee eddy, there is also a relative growth of T_4, with the increase of resolution. These higher rates of energy conversions from the mean kinetic to eddy kinetic show that the lee eddy, the dominant feature of the circulation in the Bight, is generated by barotropic instabilities. Along the shelf of Ponta D'Ouro at around 27^oS, the negative rates of

conversions indicates the conversion in the opposite direction, say, dissipation of eddies in that region. This is consistent with the lee eddies being absorbed by the mean flow as revealed by the eddy detecting and tracking system. These negative rates of conversions are also noticeable off Inhambane, indicative that some cyclonic eddies generated there may be absorbed in the mean flow in that region, (Figure6.3.4).

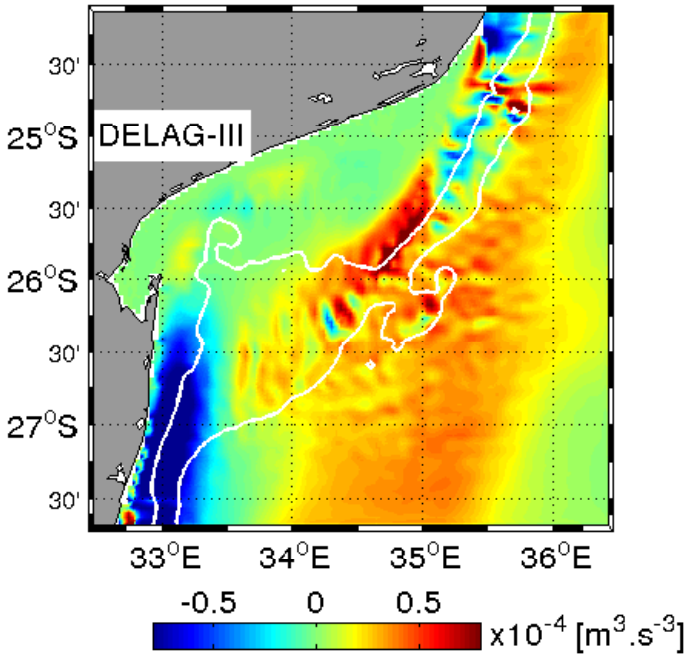

Figure 6.3.4: Energy conversion terms (T_4), integrated along the upper layer (500 m) in the Delagoa Region, for the child domain without tides (DELAG-III). The white lines represent the $500 - 1000\,m$ isobaths.

The rate of conversion from the mean potential to eddy potential energy based on the experiment with a nested domain without tides (DELAG-III), is presented in Figure, 6.3.5. It shows similarity with the description given for the coarse domain, presented above. It is characterized by higher values along the strip encompassed by the 500 and $1000\,m$ isobaths, suggestive of the increase of baroclinic instabilities with improvement of resolution along that strip (Figure 6.3.5). Therefore, the improvement of resolution, seems to have implications in the growth of baroclinic instabilities in the region. The addition of tidal forcing in the simulations doesn't show considerable changes in the aspects analyzed here, as shown in appendix B.3.2.

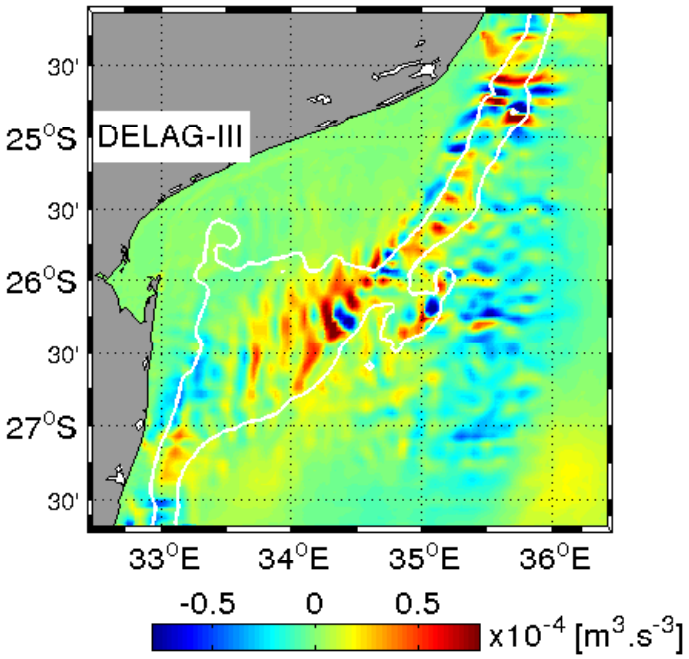

Figure 6.3.5: Rates of energy conversion from mean potential to eddy potential (T_1), integrated along the upper layer ($500\,m$) in the Delagoa Region, based on DELAG-III child domain. The white lines represent the $500 - 1000\,m$ isobaths..

To finalize the analyses, the seasonal variations of the energy conversion rates are assessed inside of the boxes of the map in Figure (6.3.1), as illustrated below (Figure 6.3.6). In Figure (6.3.6a) are presented the results for the reference experiment (DELAG-I) in zone I. The rate of conversion from the mean kinetic to eddy kinetic energy (T_4 in blue) is characterized by a higher value in spring (AMJ) season, with a decrease towards a minimum in autumn (OND). The rate of conversion from the mean potential to eddy potential (T_1 red) is generally negative. It consists of a maximum modulus in summer (JFM), which grows towards zero at the end of the year. These negative values are indicative of the irrelevance of Baroclinic Instability on the eddy activity in the Bight. Nevertheless, in this case there is a major likelihood for the lee eddy to convert into the mean flow, at the beginning of the year. When T_4 is positive, the conversion rate is from the mean flow to the eddy kinetic. Hence, the Barotropic Instability is the most important process involved in the generation of the lee eddy (Figure6.3.6a).

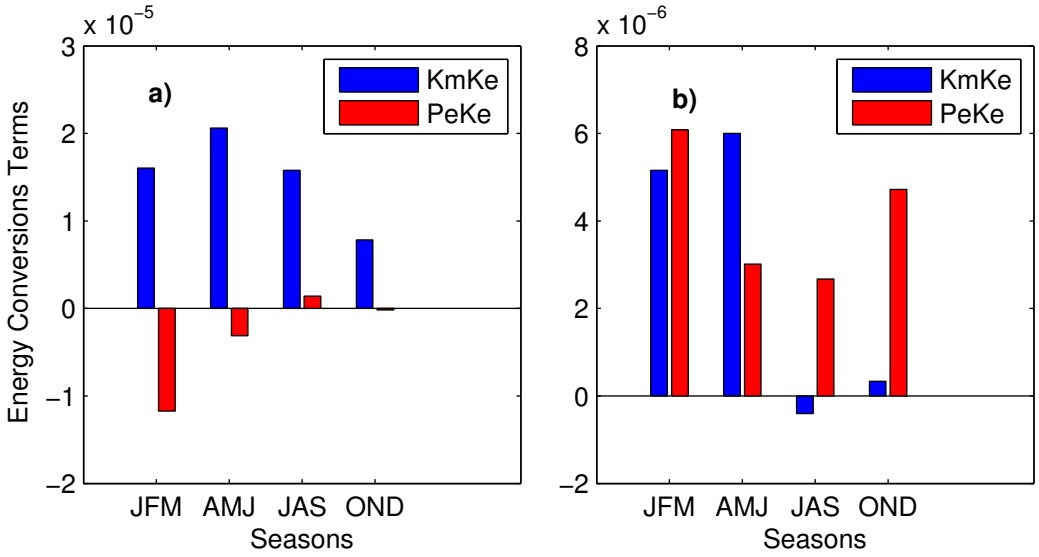

Figure 6.3.6: T_4 (blue) and T_1 (red) based on the DELAG-I, in regions I in a) and II in b).

In Figure (6.3.6b) are presented the conditions of the energy conversion rates in region II, where the Inhambane cyclones are generated, as estimated from DELAG-I simulation. Is was noted that the maximums of T_4 are in summer and spring. They are close to zero in the other seasons. This behaviour seems to reflect the seasonal cycle found in the transiting rings from the north, which generate this features. T_1 is positive in all seasons as well, and consists of maximum values in summer and autumn, with the minimum in spring and winter. The rates of conversion from the mean potential to eddy potential are more important in the development of Inhambane Cyclones by comparison with the conversion from the mean kinetic to eddy kinetic energy (Figure 6.3.6b). Therefore, for the Inhambane Cyclones the baroclinic instabilities are also important.

6.4 Discussions and conclusions

The main objective of this chapter is to discuss the mechanisms of generation of cyclonic features in the Delagoa Bight region, with incidence on their exact local of formation. Although some authors have discussed the subject (Lamont et al., 2010; Lutjeharms and Jorge da Silva, 1988), it has been noted that the circulation is complex and therefore not well understood. The advantage of a numerical model of resolving sufficiently well the processes in time and space is an opportunity to shed light into the Delagoa Bight circulation.

Analyses of vorticity fields in both the coarse and high resolution domains allowed to infer that the cyclonic features are generated in the northeastern sector of the Bight through production of negative vorticity by interaction of the southward flowing current with the promontory around

Ponta Závora. The interaction of a jet of uniform vorticity with the shelf of a promontory is known to generate (accumulate) negative vorticity in its side of contact with the shelf, which accumulates behind the cape as the jet overshoots there (Magaldi et al., 2008). This negative vorticity is likely to organize and form a cyclonic feature behind the cape. This behaviour has been noted in all of the simulations prepared for this work. Due to the relatively small space in the Inharime Terrace, such cyclonic vorticity slide downstream towards the large terrace at $26^oS, 36^oE$. The stability of the eddy here is promoted by the positioning of the anticyclonic eddies in the neighbourhood, and the presence of high SSH off Ponta D'Ouro appears to be one of the most important mechanisms in facilitating the DBLE stability, and hence its life time. Cossa et al. (2016) demonstrated the importance of the positioning of the anticyclones in the lee eddy prevalence in the Bight, using the reference experiment presented in their work. The thermocline structure of the lee eddies generated in the northeastern sector of the Bight is similar to those based on the composite analysis.

The eddy detecting and tracking system corroborate the fact that the majority of the lee eddy are generated in the northeastern sector of the Bight, with some formed close to the center of the Bight at $26^oS, 36^oE$ whereas others, in a relatively minor number, are formed in the southwestern sector of the Bight. The latter, are generated as the angle of the southward flowing current with the coast, allows its bifurcation as it impinges in the shelf off Ponta D'Ouro, in a mechanism similar to the one proposed by (Lutjeharms and Jorge da Silva, 1988) for the DBLEs generation. Although Lamont et al. (2010) refers to a generation of the lee eddy by a passing anticyclone, the model shows that they have a destructive effect when they transit along the latitudes of the Bight. They sweep the Bight with their edges, promoting absences. Nevertheless, these anticyclonic features, mainly from the north produce pulses which occasionally intrude into the Bight as revealed by the eddy detecting and tracking system.

The energy conversion rates integrated along the whole upper $500\,m$ allowed to infer that the Delagoa Bight is dominated by barotropic instabilities, with possible formation of baroclinic instabilities in the high resolution simulations. The region off Inhambane, known to be dominated by pulses (Cossa et al., 2016), is characterized by prevalence of both barotropic and baroclinic instabilities. Off Inhambane, the likelihood of eddy dissipation in the mean flow is small, but Off Ponta D'Ouro this is common and seems to explain the fate of the DBLEs in that region. Overall, region I is dominated by barotropic instabilities whereas in region II both forms seem to prevail.

Halo (2012) on investigating the Mozambique Channel eddies, noted high rates of energy conversion from the mean flow to eddy kinetic energy in this region (region I), and he also associated the generation of the DBLE with barotropic instabilities.

The mapping of the conversion rates is a very important tool used to examine the exact location of energy transference for a specific term. This has been used to estimate the areas of eddies generation in the Delagoa Bight region, and their respective dissipation to the south off Ponta D'Ouro. They helped to show that the whole region dominated by the southward flowing current between the 500 and 1000 m isobaths and even offshore is characterized by high rates of conversions from the mean flow to eddy kinetic energy (barotropic instabilities). The maximum of these conversion rates was found in a box located at $25 - 26.25^oS, 34 - 36^oE$ along the 500 m isobath. This area is mainly located in the northeastern sector of the Bight, consistent with the conclusions drawn based on the eddy detecting and tracking system. Analysis of model snapshots showed that this region is important even for the formation of anticyclonic features by instabilities of the southward flowing current as conjectured by (Gründlingh et al., 1989).

Off Inhaca at $26^oS, 33^oE$ the energy conversion rates from the mean flow to turbulence is also considerable. This is to do with the formation of the coastal counter current by bifurcation of the mean flow. Off Inhambane at $24.5^oS, 34.75^oE$ there are considerable rates of formation of turbulence by the mean flow, whereas north of this point there is prevalence of conversion in the opposite direction, say absorption of eddies in the mean flow. Off Ponta D'Ouro, and south of 26.25^oS the absorption of eddy kinetic energy by the mean flow reaches its maximums, consistent with the lee eddy moving southward following that route. All the sensitivity experiments used in this study, converge in this results with the highest resolution experiments improving the representation as expected.

In Delagoa Bight the baroclinic instabilities signature is generally patchy and found encompassed in the 500 and 1000 m isobaths. Its representation improves with the model resolution. Its maximum is found in the wide terrace below 26^oS. Due to their complex distribution, it is tricky to associate them with the prevalent features of the regional circulation. Therefore, the generation of eddies in the Delagoa Bight region is induced by barotropic instabilities. The most outstanding finding of this study was that the Bight is generally turbulent and dominated by cyclonic and even anticyclonic features, as presented in the previous chapter. It is hence summarized that these features are induced by barotropic instabilities of the southward flowing boundary current

and to the impact of the passing anticyclones.

The analyses of seasonality inside of the zones I (Delagoa Bight) and II (Inhambane) (Figure 6.3.1) has shown that there is seasonality in the rates of conversion in zone II. Such seasonality seems to be related to the influence of the passing anticyclones which are characterized by a seasonal signal, whereas in Delagoa there is no clear seasonality.

Chapter 7

Conclusions and the way forward

7.1 Conclusions

The investigation of the circulation in the Delagoa Bight, has been consistently increasing within the past five decades, with both in situ and satellite imagery contributing to the valuable knowledge accumulated so far. However, this study emerges as the first modelling approach designed to tackle the circulation in a region whose hydrodynamics is considered to be complex, (Lamont et al., 2010; Lutjeharms and Jorge da Silva, 1988). Several sensitivity experiments were performed including two at high resolution ($3km$), which allowed the representation of the mesoscale processes never dealt with in the previous studies. These simulations were validated against the WOA and AVISO observation, allowing one to carry out the investigation of the circulation in the Bight and surroundings. Since the chapters were drawn as stand alone unities, with the corresponding conclusions presented accordingly, here is given the synthesis of those conclusions, by dealing with the set of questions formulated in the literature review. The questions are presented sequentially, followed by the corresponding answers:

1. Does ROMS reproduce the mean regional circulation in the Delagoa Bight region?

- Are the presences and absences of the DBLE represented by ROMS?
- Are the main water masses represented? What is their source?
- Are there other relevant aspects of the regional circulation reproduced by ROMS?
- What is the impact of the mesoscale features from the north and east?

- What is the effect of increasing the model resolution?

ROMS has been able to simulate the regional circulation in the Delagoa Bight region. Comparisons of model results with the available data sets such as AVISO, WOA and Pathfinder SST, showed that the model represents reasonably well the main features of the regional circulation. These are: a consistent boundary current and the anticyclones from the north of Mozambique Channel and the east of Madagascar. The consistence of the southward flowing boundary current was ascribed to the merger of the flows from both the north and the east, along the latitudes of the Bight. Furthermore, the impact of the large scale oceanic circulation (South Indian Ocean Gyre) may also be relevant.

Some cyclonic meanders similar to Natal pulses (Lutjeharms and Roberts, 1988), not referred to in the previous studies, have been reproduced by ROMS. They are generated by the anticyclones from the north, off Inhambane. These features, propagate with the anticyclones towards the northern Agulhas Current. The fact that their trajectories are variable, helped to show their impact inside of the Delagoa Bight twofold: first as they pass from far away, they constitute a mechanism of inshore-offshore water masses exchange, with important influence in the thermocline structure; secondly, they may transfer water masses from the north or intrude into the wide terrace.

The lee eddy presences and absences in the Bight were also represented by ROMS. Analysis of averages showed that the lee eddy is the most dominant feature, for it shows up in all forms of averages, whereas the absences were poorly represented in both the coarse and high resolution simulations. This is associated with their short life time and presence of mesoscale features when the lee eddy cannot occupy the whole terrace in the Bight. In fact, according to the high resolution simulation, the mesoscale processes (cyclonic and anticyclonic eddies) dominate the flow when the lee eddy cannot fill the whole terrace.

The main water masses in the Bight are from the north. They generally enter the Bight through the northeastern sector off Ponta Závora. Their intrusion is through the southward flowing current or by the pulses as suggested by the eddy detecting and tracking system. Notwithstanding, several cyclonic and anticyclonic anomalies at the speed of the anticyclones are able to impact the Bight from the east, although they are mostly weak. This is because the anticyclones from the east generally move reasonably from far away of the Bight, reducing the flow of their water masses towards the Bight. Cyclonic eddies from the east show low probability of reaching the Bight, according to the eddy detecting and tracking system. In individual snapshots, it is also evident

that while the edges of the anticyclones from the north sweep the center of the Bight, those from the east do not because they move from far away towards the Agulhas Current.

The impact of the anticyclones has been viewed in several ways: first, their edges sweep the center of the Bight favouring the condition of lee eddy absent in the Bight; secondly, they do interact with the Bight through the pulses that they generate further north, and by promoting strong shelf offshore interaction in association with the pulses that they generate off Inhambane. Additionally, the positions of the anticyclones are essential in the establishment and consistency of the lee eddy in the Bight, because its stability appears to coincide with the presence of high SSH off Ponta D'Ouro (southwest of the Bight).

The increase of the grid resolution, resulted in the generation of smaller mesoscale features not referred to in the literature, namely cyclonic and anticyclonic cells, and even the possibility of occurrence of several simultaneous cyclonic cores in the Bight. Both the representation of the southward flowing boundary current and the coastal counter-current, seem to improve with the increase of the model resolution. This contributes into the enhancement of the upwelling in the center of the lee eddy, which is indeed more consistent in the high resolution simulation.

1. What is the mechanism controlling the DBLE generation?

- Is the cyclonic eddy generated by the southward flow, or by the passing anticyclones from the north of Mozambique Channel or from the east of Madagascar?
- Is the eddy generated by intruding cyclones?
- Where is the exact location of generation?

The lee eddy generation can be explained by three main mechanisms. All involve the southward flowing boundary current, which is consistent at the latitudes of the Bight. First, to the northeast it interacts with the shelf producing negative vorticity along the surface of contact with the shelf. Behind the promontory, south of Ponta Závora it overshoots accumulating negative vorticity behind the cape (Inharime terrace). This vorticity slides downwards towards the main terrace, and forms the lee eddy at $26^oS, 34^oE$. Seemingly its stability, depends on the positioning of the anticyclones, with the presence of anticyclonic circulation in the coast off Ponta D'Ouro, assuming an important role in the development of a strong coastal counter-current, capable to sustain the lee eddy in the Bight. It has been noted that the arrival of anticyclonic eddies whether from

the east or north in that region coincides with the presence of a consistent DBLE. The second mechanism involves the situations in which the lee eddies are generated in a manner similar to the one explained by Lutjeharms and Jorge da Silva (1988). Such condition is common when the pulses are still located far away from the Bight, say, around their location of generation. They tend to modify the angle of the boundary current, which bifurcates as it impinges in the coast around 27^oS. The last condition is by conversion of energy of the mean flow into turbulence (barotropic instabilities) that dominate the whole path of the southward flowing boundary current with incidence in the box limited by $25 - 26.25^oS; 34 - 36^oE$. This area is located along the $500\,m$ isobath. It is important to note that these instabilities also explain the generation, of the other small anticyclonic features found in Delagoa Bight. The intrusion of pulses through the northeastern sector of the Bight does not coincide with consistent lee eddies, in all the simulations. This is because the intrusion of pulses is immediately followed by the destructive impact of the anticyclones that generate these pulses. The passing anticyclones are relevant in the Delagoa Bight circulation. Those from the north, affect the Bight through their edges and tend to promote shelf offshore interaction. This effect is exacerbated by the pulses that occasionally move southward with them. Those from the east move towards the African coast off Ponta D'Ouro promoting a region of high SSH which seems to aid in the stability of the lee eddy as stated above.
The eddy detecting and tracking system allowed to demonstrate that the DBLEs are mainly generated in the northeastern sector of the Bight, although they are likely to be initiated anywhere along the path of the southward flowing current. Indeed, the most important area for the DBLEs inception is the northeastern sector, followed by the center and finally the southwestern sector.

1. Barotropic and baroclinic instabilities

- Why are the Barotropic instabilities more relevant than the baroclinic in this region?
- What is the fate of the DBLE?

The analysis of instabilities of the southward flowing boundary current has been carried out using several sensitivity experiments developed for this study. In the coarse resolution simulations it has been noted that the baroclinic instabilities are less relevant by comparison with the barotropic instabilities, say the latter dominates the instabilities in the Bight. By increasing the resolution, it has been noted that the baroclinic instabilities also become important in the region. Nevertheless, the fact they are only relevant in a relatively smaller area, by comparison with the maps of

barotropic instabilities, led one to conclude that the generation of cyclonic and anticyclonic features in this region is mainly by barotropic instabilities of the southward flowing boundary current. This conclusion agrees with Halo (2012) who associated the generation of cyclonic eddies in this region, with the barotropic instabilities. The presence of simulated anticyclonic mesoscale features in this region, also allows one to state that the anticyclonic eddies that were found occupying the whole region by Gründlingh et al. (1989), may be due to barotropic instabilities.

The DBLEs has been shown to move southward towards the northern Agulhas Current, (Cossa et al., 2016; Lamont et al., 2010; Lutjeharms and Jorge da Silva, 1988). The fate of these cyclonic eddies according to the analyses of instabilities, is the conversion of their turbulent form (EKE) into the mean flow (MKE) along the northern Natal Valley (Ponta D'Ouro). This was noted through the integrated mapped conversion rate (T_4) which shows negative values in this region. This behaviour agrees perfectly with the trajectories of the southward flowing current produced by the eddy detecting and tracking system. It may be underscored that these results agree with the previous studies, concerning the southward movement of the lee eddies. A recent observational study used a global data set of automatically tracked eddies in combination with surface drifters and satellite altimeter geostrophic currents, to show that both cyclonic and anticyclonic features from the Mozambique Channel and east of Madagascar are dissipated in the northern Agulhas Current, Braby et al. (2016). The region off Ponta D'Ouro where our simulations present negative rates for (T_4) appears to reflect the conversion of turbulence into the main flow, for both the anticyclones and the DBLEs.

7.2 Recommendations

The advantages of the high spacio-temporal resolution of the model outputs analyzed in this study allowed one to present outstanding results in the dynamics of the region, namely the presence of small cyclonic and anticyclonic features inside of the Delagoa Bight, although these results need to be re-evaluated using in situ observation. In the past, the condition of the lee eddy present/absent was tested using drifters launched in the center of the Bight where it usually resides, (Lamont et al., 2010). The same approach is proposed to reevaluate the location of generation of cyclonic features in the northeastern sector of the Bight. This would help in the confirmation of the results of this study. The behaviour of the currents, also needs to be revisited. A high resolution

simulation with a domain covering the whole Channel could help to explain the consistency of the southward flowing boundary current and its frequencies and behaviour at the latitudes of the Bight.

A ROMS inter-annual simulation forced with tides and river discharges would add invaluable information in the local dynamics. This statement is made because such simulation uses daily surface fluxes as initial condition at the surface and this is expected to improve the representation of the variability in the region. A tidal simulation has shown an increase in the speed close to the coast. These two factors and the addition of the river data are likely to bring more outcomes in the model outputs. The models with tides, also show potential of development of much smaller features than no-tidal simulations. The utilization of Self Organized Maps (SOMS) would improve our knowledge on the patterns that favor the present/absent conditions for the lee eddy. Furthermore, the experiments with tides would be useful in the understanding of the tidal impact in the innermost Maputo Bay. The impact of the internal tides, which are known to be very active in the Bight Cossa (2005), could also be investigated.

Bibliography

Arakawa, A. and Lamb, V. (1977). *Methods of Computational Physics*. New York: Academic Press.

Azevedo, L., Oliveira, L., Souza, J., Soares, I., and Mata, M. (2008). Os Processos de Conversão de Energias nos Oceanos: Uma revisão do diagrama de Lorenz. *Revista Brasileira de Geofísica*, 26(2):153–172.

Backeberg, B. and Reason, C. (2010). A connection between the South Equatorial Current north of Madagascar and the Mozambique Channel Eddies. *Geophysical Research Letters*, 37(4).

Bains, P. (1982). The Generation of internal Tides by Flat-bump Topography. *Deep Sea Research*, 20:179–205.

Barlow, R., Kyewalyanga, M., Sessions, H., van den Berg, M., and Morris, T. (2008). Phytoplankton pigments, functional types, and absorption properties in the Delagoa and Natal Bights of the Agulhas ecosystem. *Estuarine, Coastal and Shelf Science*, 80:201–211.

Barnier, B., Siefridt, L., and Marchesiello, P. (1995). Thermal forcing for a global ocean circulation model using a three-year climatology of ECMWF analyses . *Journal of Marine Systems*, 6(4):363–380.

Beal, L., Ffield, A., and Gordon, A. (2000). Spreading of Red Sea overflow waters in the Indian Ocean. *Journal of Geophysical Research: Oceans*, 105(C4):8549–8564.

Beckmann, A., Böning, C., Brüge, B., and Stammer, D. (1994). On the generation and role of eddy variability in the central North Atlantic Ocean. *Journal of Geophysical Research: Ocean*, 99(C10):20381–20391.

Beckmann, A. and Haidvogel, D. (1993). Numerical simulation of flow around a tall isolated seamount. Part I: Problem formulation and model accuracy. *Journal of Physical Oceanography*, 23(8):1736–1753.

Biastoch, A. and Krauss, W. (1999). The role of mesoscale eddies in the source regions of the Agulhas Current. *Journal of Physical Oceanography*, 29(9):2303–2317.

Biastoch, A., Reason, C., Lutjeharms, J., and Boebel, O. (1999). The importance of flow in the Mozambique Channel to seasonality in the greater Agulhas Current system. *Geophysical research letters*, 26(21):3321–3324.

Blayo, E. and Debreu, L. (1999). Adaptive Mesh Refinement for Finite-Difference Ocean Models: First Experiments . *Journal of Physical Oceanography*, 29(6):1239–1250.

Braby, L., Backeberg, B., Ansorge, I., Roberts, M., Krug, M., and Reason, C. (2016). Observed eddy dissipation in the Agulhas Current. *Geophysical Research Letters*, 43(15):8143–8150.

Buijsman, M., Uchiyama, Y., McWilliams, J., and Hill-Lindsay, C. (2012). Modeling semidiurnal internal tide variability in the Southern California Bight. *Journal of Physical Oceanography*, 42(1):62–77.

Chaigneau, A., Gizolme, A., and Grados, C. (2008). Mesoscale eddies off Peru in altimeter records: Identification algorithm and eddy spatio-temporal patterns. *Progress in Oceanography*, 79(2):106–119.

Chassignet, E., Arango, H., Dietrich, D., Haidvogel, D., Ma, C., Mehra, A., Paiva, A., and Sirkes, Z. (2000). DAMÉE-NAB : the base experiments. *Dynamics of Atmospheres and Oceans*, 32(3):155–183.

Chelton, D. and Freilich, M. (2005). Scatterometer-based assessment of 10-m wind analyses from the operational ECMWF and NCEP numerical weather prediction models. *Monthly Weather Review*, 133(2):409–429.

Chelton, D., Schlax, M., and Samelson, R. (2011). Global observations of nonlinear mesoscale eddies. *Science*, 334(6054):328–332.

Collins, C., Hermes, J., and Reason, C. (2014). Mesoscale activity in the Comoros Basin from satellite altimetry and a high-resolution ocean circulation model. *Journal of Geophysical Research: Oceans*, 119(8):4745–4760.

Conkright, M., Locarnini, R., Garcia, H., OBrien, T., Boyer, T., Stephens, C., and Antonov, J. (2002). *World Ocean Atlas 2001: Objective analyses, data statistics, and figures: CD-ROM documentation*. US Department of Commerce, National Oceanic and Atmospheric Administration, National Oceanographic Data Center, Ocean Climate Laboratory.

Cossa, O. (2005). Observacao por Satélites de Ondas Internas Solitárias no Canal de Moçambique. Master's thesis, Instituto de Oceanografia, Faculdade de Ciências-Universidade de Lisboa.

Cossa, O., Pous, S., Penven, P., Capet, X., and Reason, C. (2016). Modelling cyclonic eddies in the Delagoa Bight region . *Continental Shelf Research*, 119:14–29.

Cushman-Roisin, B. and Beckers, J. (2011). *Introduction to geophysical fluid dynamics: physical and numerical aspects*, volume 101. Academic Press.

Da Silva, A., Young, C., and Levitus, S. (1994). Atlas of surface marine data 1994, vol. 1, algorithms and procedures, NOAA Atlas NESDIS 6. *US Department of Commerce, NOAA, NESDIS, USA*, page 74.

Da Silva, J., New, A., and Magalhaes, J. (2009). Internal solitary waves in the Mozambique Channel: Observations and interpretation. *Journal of Geophysical Research: Oceans*, 114(C5).

D'Assaro, E. (1988). Generation of Submesoscale Vortices: A New mechanism. *Journal of Geophysical Research*, 93:6685–6693.

de Ruijter, W., Brummer, G., Drijfhout, S., Lutjeharms, J., Peeters, F., Ridderinkhof, H., van Aken, H., and van Leeuwen, P. (2006). Observations of the inter-ocean exchange around south africa. *Eos, Transactions American Geophysical Union*, 87(9):97–101.

de Ruijter, W., Ridderinkhof, H., Lutjeharms, J., Schouten, M., and Veth, C. (2002). Observation of the flow in the mozambique channel. *Geophysical Research Letters*, 29(10).

de Ruijter, W., Ridderinkhof, H., and Schouten, M. (2005). Variability of the southwest indian ocean. *Philosophical Transactions of the Royal Society of London A: Mathematical, Physical and Engineering Sciences*, 363(1826):63–76.

de Ruijter, W., van Aken, H., Beier, E., Lutjeharms, J., Matano, R., and Schouten, M. (2004). Eddies and dipoles around South Madagascar: formation, pathways and large-scale impact. *Deep Sea Research Part I: Oceanographic Research Papers*, 51(3):383–400.

Debreu, L. and Blayo, E. (2008). Two-way embedding algorithms: a review. *Ocean Dynamics*, 58(5-6):415–428.

Debreu, L., Marchesiello, P., Penven, P., and Cambon, G. (2012). Two-way nesting in split-explicit ocean models: algorithms, implementation and validation. *Ocean Modelling*, 49:1–21.

Demopoulos, A., Smith, C., and Tyler, P. (2003). *The Deep India Ocea Floor*. Elsevier, Amisterdam.

DiMarco, S., Chapman, P., Nowlin, W., Hacker, P., Donohue, K., Luther, M., Johnson, G., and Toole, J. (2002). Volume transport and property distributions of the Mozambique Channel. *Deep Sea Research Part II: Topical Studies in Oceanography*, 49(7):1481–1511.

Dove, V. (2015). *Seasonal and interannual variability of surface chlorophyll-a and Sea Surface Temperature in the Delgoa Bight, southern Mozambique, Masters Thesis, University of Cape Town.*

Egbert, G. and Erofeeva, S. (2002). Efficient inverse modeling of barotropic ocean tides. *Journal of Atmospheric and Oceanic Technology*, 19(2):183–204.

Egbert, G. and Ray, R. (2001). Estimates of M2 tidal energy dissipation from TOPEX/Poseidon altimeter data. *Journal of Geophysical Research: Oceans*, 106(C10):22475–22502.

Emery, W. (2001). Water types and water masses. *Encyclopedia of ocean sciences*, 6:3179–3187.

Emery, W. and Meincke, J. (1986). Global water masses-summary and review. *Oceanologica acta*, 9(4):383–391.

Ffield, A. (1997). GLR special section: WOCE Indian Ocean Expedition. *Geophysical Research Letters*, 24(21):2539–2540.

Ffield, A. and Toole, J. Wilson, D. (1997). Seasonal circulation in the south Indian Ocean. *Geophysical Research Letters*, (22):2773–2776.

Findlater, J. (1971). Mean monthly airflow at low levels over the western Indian Ocean. *Geophysical Memories*, 115(55).

Flather, R. (1976). A tidal model of the northwest European continental shelf. *Memoires de la Societe Royale des Sciences de Liege*, 10(6):141–164.

Garrett, C. (2003). Internal tides and ocean mixing. *Science*, 301(5641):1858–1859.

Garrett, C. and Laurent, L. (2002). Aspects of deep ocean mixing. *Journal of Oceanography*, 58(1):11–24.

Gill, A. and Schumann, E. (1979). Topographically induced changes in the structure of an inertial coastal jet: application to the Agulhas Current. *Journal of Physical Oceanography*, 9(5):975–991.

Gordon, A. (1986). Interocean exchange of thermocline water. *Journal of Geophysical Research*, 91(C4):5037–5046.

Gründlingh, M. (1995). Tracking eddies in the southeast Atlantic and southwest Indian oceans with TOPEX/POSEIDON. *Journal of Geophysical Research: Oceans*, 100(C12):24977–24986.

Gründlingh, M., Slinger, J., and Agenbag, J. (1989). The usefulness of nimbus CZCS imagery in the southwestern indian ocean. *South African Journal of Marine Science*, 8(1):261–269.

Haidvogel, D., Arango, H., Hedstrom, K., Beckmann, A., Malanotte-Rizzoli, P., and Shchepetkin, A. (2000). Model evaluation experiments in the North Atlantic Basin: simulations in nonlinear terrain-following coordinates. *Dynamics of Atmospheres and Oceans*, (3).

Hall, R., Huthnance, J. M., and Williams, R. G. (2011). Internal tides, nonlinear internal wave trains, and mixing in the Faroe _ Shetland Channel. *Journal of Geophysical Research: Oceans*, 116(C3):n/a–n/a.

Halo, I. (2012). *The Mozambique Channel Eddies: Characteristics and Mechanisms of formation*. UCT, PhD Thesis.

Halo, I., Backeberg, B., Penven, P., Ansorge, I., Reason, C., and Ulgren, J. (2014a). Eddy properties in the Mozambique Channel: A comparison between observations and two Numerical

Ocean Circulation Models. *Deep Sea Research Part II: Topical Studies in Oceanography*, 100:38–53.

Halo, I., Penven, P., Backeberg, B., Ansorge, I., Shillington, F., and Roman, R. (2014b). Mesoscale eddy variability in the southern extension of the East Madagascar Current: Seasonal cycle, energy conversion terms, and eddy mean properties. *Journal of Geophysical Research: Oceans*, 119(10):7324–7356.

Han, W. (2005). Origins and Dynamics of the 90-Day and 30-60-Day Variations in the Equatorial Indian Ocean. *Journal of physical oceanography*, 35(5):708–728.

Hancke, L., Roberts, M., and Ternon, J. (2014). Surface drifter trajectories highlight flow pathways in the Mozambique Channel. *Deep Sea Research Part II: Topical Studies in Oceanography*, 100:27–37.

Harlander, U., Ridderinkhof, H., Schouten, M., and de Ruijter, W. (2009). Long-term observations of transport, eddies, and Rossby waves in the Mozambique Channel. *Journal of Geophysical Research: Oceans*, 114(C2).

Hedstrȯm, K. (2009). *Technical Manual for a Coupled Sea-Ice/Ocean Circulation Model*. University of Alaska Fairbanks, Artic Region Supercomputing Center.

Hood, R., Bange, H., Beal, L., Beckley, L., Burkill, P., Cowie, G., Da-Adamo, N., Ganssen, G., Hendon, H., Hermes, J., et al. (2015). Tthe second International Indian Ocean Expedition (IIOE-2). *International Council for Science*.

IHO (1953). Limits of Oceans and Seas.

IOC (2013). International Indian Ocean Expedition 50th Anniversary Initiative (IIOE-2). *IOC:Unesco*.

Isern-Fontanet, J., Garcia-Ladona, E., and Font, J. (2003). Identification of marine eddies from altimetric maps. *Journal of Atmospheric and Oceanic Technology*, 20(5):772–778.

Jackson, C., Apel, J., et al. (2004). *Synthetic aperture radar: marine user's manual*. US Department of Commerce, National Oceanic and Atmospheric Administration, National Environmental Satellite, Data, and Information Serve, Office of Research and Applications.

Kantha, L., Rojsiraphisal, T., and Lopez, J. (2008). The North Indian Ocean circulation and its variability as seen in a numerical hindcast of the years 1993-2004. *Progress in Oceanography*, 76(1):111–147.

Kapilima, S. (2003). Tetonic and sedimentary evolution of the of the coastal basin of tanzania during the mesozoic times. *Tanzania Journal of Science*, 29(1):1–16.

Kolanski, J., Kaehler, S., and Jaquemet, S. (2012). Distribution and sources of particulate organic matter in a mesoscale eddy dipole in the Mozambique Channel (soth-west Indian Ocean): Insight from C nd N stable isotopes. 96:122–131.

Kurian, J., Colas, F., Capet, X., McWilliams, J., and Chelton, D. (2011). Eddy properties in the California current system. *Journal of Geophysical Research: Oceans*, 116(C8).

Kyewalyanga, M., Naik, R., Hedge, S., Mini, R., Barlow, R., and Roberts, M. (2007). Phytoplankton biomass and primary production in Delagoa Bight Mozambique: Application of remote sensing. *Estuarine, Coastal and Shelf Science*, 74(3):429–436.

Lamont, T., Roberts, M., Barlow, R., and van den Berg, M. (2010). Circulation patterns in the Delagoa Bight, Mozambique, and the influence of deep ocean eddies. *African Journal of Marine Science*, 32(3):553–562.

Large, W., McWilliums, J., and Doney, S. (1994). Oceanic Vertical Mixing: A review and model with nonlocal layer parameterization. *Review of Geophysics*, 32(4):363–403.

Lorenz, E. (1951). Available potential energy and the maintenance of the general circulation. *Tellus*, 3(3):205–207.

Lutjeharms, J. (2006a). *The Agulhas Current*. Springer-Verlag Berlin.

Lutjeharms, J. (2006b). The Ocean environment off southeastern Africa: a review. *South African Journal of Science*, 102(9-10):419–426.

Lutjeharms, J. (2007). Three decades of research on the greater Agulhas Current. *Ocean Science*, 3(1):129–147.

Lutjeharms, J., Biastoch, A., van der Werf, P., Redderinkhof, H., and de Ruijter, W. (2012). On the discontinuous nature of the mozambique current. *South African journal of science*, 108(1-2):1–5.

Lutjeharms, J. and Jorge da Silva, A. (1988). The Delagoa Bight Eddy. *Deep Sea Research Part A. Oceanographic Research Papers*, 35(4):619–634.

Lutjeharms, J. and Roberts, H. (1988). The natal pulse: an extreme transient of the agulhas current. *Journal of Geophysical Research*, 93:631–645.

Lutjeharms, J., Wedepohl, P., and Meeuwis, J. (2000). On the Surface drift of the East Madagascar and Mozambique currents . *South African Journal of Science*, 96(3).

MacNae, W. and Kalk, M. (1969). The Natural History of Inhaca Island: Mozambique. *Witwatersrand University Press, Johannesburg, South Africa.*

Madden, R. and Julian, P. (1972). Description of globalscale circulation cell in the tropics with a 40-50 day period. *Journal of the atmospheric sciences*, 29(6):1109–1123.

Magaldi, M., Ozgokmen, T., Griffa, A., Chassignet, E., Iskandarani, M., and Peters, H. (2008). Turbulent flow regimes behind a coastal cape in a stratified and rotating environment. *Ocean Modelling*, 25(1):65–82.

Manyilizu, M., Penven, P., and Reason, C. (2016). Annual cycle of the upper-ocean circulation and properties in the tropical western Indian Ocean. *African Journal of Marine Science*, 38(1):81–99.

Marchesiello, P., Debreu, L., and Couvelard, X. (2009). Spurious diapycnal mixing in terrain-following coordinate models: The problem and solution. *Ocean Modelling*, 26(3):156–169.

Marchesiello, P., McWilliams, J., and Shchepetkin, A. (2001). Open boundary conditions for long-term integration of regional oceanic models. *Ocean modelling*, 3(1):1–20.

Martin, A. (1981). The influence of the Agulhas Current on the physiographic development of the northernmost Natal Valley (SW Indian Ocean). *Marine Geology*, 39(3-4):259–276.

Matano, R., Beier, E., Strub, P., and Tokmakian, R. (2002). Large-Scale Forcing of the Agulhas Variability: The Seasonal Cycle. *Journal of Physical Oceanography*, 32(4):1228–1241.

McGillicuddy, D. and Robinson, A. (1997). Eddy-induced nutrient supply and new production in the Sargasso Sea. *Deep Sea Research Part I: Oceanographic Research Papers*, 44(8):1427–1450.

Miller, J. and Lee, T. (1995). Gulf Stream meanders in the South Atlantic Bight: 2. Momentum balances. *Journal of Geophysical Research: Oceans*, 100(C4):6705–6723.

Molemaker, M., McWilliums, J., and Dewar, W. (2015). Submesoscale Instability and Generation of Mesoscale Anticyclones near a Separation of the California Undercurrent. *Journal of Physical Oceanography*, 45(3):613–629.

Morales, R., Barton, E., and Heywood, K. (1996). Variability of water masses in the western indian ocean. *Journal of Geophysical Research*, 101(14):027–14.

Nash, J., Kelly, S., Shroyer, E., Moum, J., and Duda, T. (2012). The unpredictable nature of internal tides on continental shelves. *Journal of Physical Oceanography*, 42(11):1981–2000.

Nehama, F. and Reason, C. (2015). Modelling the zambezi river plume. *African Journal of Marine Science*, 37(4):593–604.

Nof, D. (1993). Generation of Ringlets. *Tellus A: Dynamic Meteorology and Oceanography*, 45(4):299–310.

Okubo, W. (1970). Horizontal dispersion of floatable particles in the vicinity of velocity singularities such as convergences. 17(3):445–454.

Omta, A., Lido, J., Garcon, V., Kooijman, S., and Dijkstra, H. (2009). The interpretation of satellite chlorophyll observation: The case of the Mozambique Channel. *Deep Sea Research Part I: Oceanographic Research Papers*, 56(6):974–988.

Oort, A., Anderson, L., Levitus, S., and Peixoto, J. (1994). Estimates of the Energy Cycles of the Oceans. *Journal of Geophysical Research*, 99(C4):7665–7682.

Oort, A., Ascher, S., Levitus, S., and Peixoto, J. (1989). New Estimates of the Available Potential Energy in the World Oceans. *Journal of Geophysical Research*, 94(C3):3187–3200.

Orlanski, I. and Cox, M. (1972). Baroclinic instability in ocean currents. *Geophysical & Astrophysical Fluid Dynamics*, 4(1):297–332.

Palastanga, P., van Leween, P., and de Ruijter, W. (2006). A link between low-frequency mesoscale eddy variability around Madagascar and the large-scale Indian Ocean variability. *Journal of Geophysical Research: Oceans*, 111(C9):n/a–n/a. C09029.

Palma, E. and Matano, R. (2000). On the implementation of open boundary conditions for a general circulation model: the three-dimensional case. *Journal of Geophysical Research: Oceans*, 105(C4):8605–8627.

Parson, L. and Evans, A. (2005). Seafloor topography and tectonic elements of the Western Indian Ocean . *Philosophical Transactions of the Royal Society of London A: Mathematical, Physical and Engineering Sciences*, 363(1826):15–24.

Paula, J., Pinto, I., Guambe, I., Monteiro, S., and Gove, D. (1998). Seasonal cycle of planktonic communities at Inhaca Island, southern Mozambique. *Journal of Plankton Research*, 20(11):2165–2178.

Penven, P., Echevin, V., Pasapera, J., Colas, F., and Tam, J. (2005). Average circulation, seasonal cycle, and mesoscale dynamics of the Peru Current System: A modeling approach. *Journal of Geophysical Research: Oceans*, 110(C10):n/a–n/a. C10021.

Penven, P., Lutjeharms, J., and Florenchie, P. (2006). Madagascar: A pacemaker for the Agulhas Current system? *Geophysical Research Letters*, 33(17):n/a–n/a. L17609.

Penven, P., Marchesiolo, P., Debreu, L., and J., L. (2008). Software tools for pre-and post-processing of oceanic regional simulations. *Environmental Modelling & Software*, 23(5):660–662.

Penven, P., Roy, C., Brundrit, G., de Verdière, A., Fréon, P., Lutjeharms, J., and Shillington, F. (2001). A Regional hydrodynamic model of upwelling in the Southern Benguela. *South African Journal of Science*, 97:472–475.

Penven, P. and Debreu, L. and Marchesiello P. and McWilliums, J.C. (2006). Evaluation and application of the ROMS 1-way embedding procedure to the central california upwelling system. *Ocean Modelling*.

Phillips, N. (1957). A coordinate system having some special advantages for numerical forecasting. *Journal of Meteorology*, 14(2):184–185.

Piton, B. et al. (1991). The Mozambique channel revisited. *Oceanologica Acta*, 14(6):549–558.

Proakis, J. and Dimitri, G. (1996). Digital Signal Processing. *New Jersey: Upper Saddle River. Printice Hall.*

Quartly, G., Buck, J., Srokosz, M., and Coward, A. (2006). Eddies around Madagascar - The retroflection re-considered. *Journal of Marine Systems*, 63(3):115–129.

Quartly, G. and Srokosz, M. (2002). Sst observations of the agulhas and east madagascar retroflections by the trmm microwave imager. *Journal of Physical Oceanography*, 32(5):1585–1592.

Quartly, G. and Srokosz, M. (2004). Eddies in the southern Mozambique Channel. *Deep Sea Research Part II: Topical Studies in Oceanography*, 51(1):69–83.

Reynolds, R. and Smith, T. (1994). Improved global global sea surface temperature analyses using potimum interpolation. *Journal of Climate*, 7(6):929–948.

Ridderinkhof, H. and de Ruijter, W. (2003). Moored current observations in the Mozambique Channel. *Deep Sea Research Part II: Topical Studies in Oceanography*, 50(12):1933–1955.

Ridderinkhof, W., Le Bars, D., Heydt, A., and Ruijter, W. (2013). Dipoles of the south east madagascar current. *Geophysical Research Letters*, 40(3):558–562.

Risien, C. and Chelton, D. (2008). A global climatology of surface wind and wind stress fields from eight years of QuikSCAT scatterometer data. *Journal of Physical Oceanography*, 38(11):2379–2413.

Roberts, M., Ribbink, A., Morris, T., van den Berg, M., Engelbrecht, D., and Harding, R. (2006). Oceanographic environment of the Sodwana Bay coelacants (Latimeria Chalumenae), South Africa. *South African journal of science*, 102(9-10):435–443.

Roberts, M., Ternon, J., and Morris, T. (2014). Interaction of dipole eddies with the western continental slope of the Mozambique Channel. *Deep Sea Research Part II: Topical Studies in Oceanography*, 100:54–67.

Roed, L. and Cooper, C. (1986). Open boundary conditions in numerical ocean models. In *Advanced physical oceanographic numerical modelling*, pages 411–436. Springer.

Sætre, R. (1985). Surface currents in the Mozambique Channel. *Deep Sea Research Part A. Oceanographic Research Papers*, 32(12):1457–1467.

Sætre, R. and Jorge da Silva, A. (1984). The circulation of the Mozambique Channel. *Deep Sea Research Part A. Oceanographic Research Papers*, 31(5):485–508.

Sangrá, P., Basterretxea, G., Pelegrí, J., and Aristeguí, J. (2001). Chlorophyll increase due to internal waves on the shelf break of Gran Canaria (Canary Islands). *Scientia Marina*, 65(S1):89–97.

Schott, F., Xie, S., and McCreary Jr., J. (2009). Indian Ocean Circulation and Climate Variability. *Review of Geophysics*, 47:2–46. RG1002.

Schott, F. A. and McCreary Jr., J. P. (2001). The Monsoon Circulation of the Indian Ocean. *Progress in Oceanography*, 51:1–123.

Schouten, M., de Ruijter, W., and Ridderinkhof, H. (2005). A seasonal intrusion of subtropical water in the Mozambique Channel. *Geophysical research letters*, 32(18).

Schouten, M., de Ruijter, W., Van, L., Dijkstra, P., and Redderinkhof, H. (2002). A teleconnections between the equatorial and southern Indian Ocean. *Geophysical Research Letters*, 29(16).

Schouten, M., de Ruijter, W., van Leeuwen, P., and Redderinkhof, H. (2003). Eddies and variability in the Mozambique Channel. *Deep Sea Research Part II: Topical Studies in Oceanography*, 50(12):1987–2003.

Senan, R., Senguta, D., and Goswami, B. (2003). Intraseasonal monsoon jets in the equatorial Indian Ocean. *Geophysical Research Letters*, 30(14):1–4.

Senguta, D., Senan, R., Goswami, B., and Jérôme, V. (2007). Intraseasonal Variability of Equatorial Indian Ocean Zonal Currents. *Journal of Climate*, 20:3037–3055.

Sete, C., Ruby, J., and Dove, V. (2002). Seasonal Variation of Tides, Currents, Salinity and Temperature along the Coast of Mozambique. *UNESCO*.

Shchepetkin, A. and McWilliams, J. (1998). Quasi-Monotone Advection Schemes Based on Explicit Locally Adaptive Dissipation. *Monthly Weather Review*, 126(6):1541–1580.

Shchepetkin, A. and McWilliams, J. (2003). A method for computing horizontal pressure-gradient force in an oceanic model with a nonaligned vertical coordinate. *Journal of Geophysical Research: Oceans*, 108(C3).

Shchepetkin, A. and McWilliams, J. (2009). Computational kernel algorithms for fine-scale, multiprocess, longtime oceanic simulations. *Handbook of Numerical Analysis*, 14:121–183.

Shchepetkin, A. and McWilliams, J. (2015). A regional oceanic modeling system (ROMS): a splicit-explicit, free-surface, topography-following-coordinate oceanic model. *Environmental Modelling & Software*, 73:201–217.

Shchepetkin, A. and McWilliams, J. C. (2009). 'Correction and commentary for Ocean forecasting in terrain-following coordinates: Formulation and skill assessment of the regional ocean modelling system by Haidvogel et al., J. Comp. Phys. 227, pp. 3595-3624'. *Journal of Computational Physics*, 228(24):8985–9000.

Shi, C. and Nof, D. (1994). The destruction of lenses and generation of Wodons. *Journal of Physical Oceanography*, 24(6):1120–1136.

Siedler, G., Rouault, M., Biastoch, A., Backeberg, B., Reason, C., and Lutjeharms, J. (2009). Modes of the southern extension of the East Madagascar Current. *Journal of Geophysical Research: Oceans*, 114(C1):n/a–n/a. C01005.

Song, Y. (1998). A General Pressure Gradient Formulation for Ocean Models. Part I: Scheme Design and Diagnostic Analysis. *Monthly Weather Review*, 126(12):3213–3230.

Song, Y. and Haidvogel, D. (1994). A semi-implicit Ocean circulation Model using a Generalized Topography-Following Coordinate system. *Journal of Computational Physics*, 115(1):228–244.

Soufflet, Y., Marchesiello, P., Lemarié, F., Jouanno, J., Capet, X., Debreu, L., and Benshila, R. (2016). On effective resolution in ocean models. *Ocean Modelling*, 98:36–50.

Souza, J., de Boyer, M., and Le Traon, P. (2011). Comparison between three implementations of automatic identification algorithsms for the quantification and characterization of mesiscale eddies in the South atlantic Ocean. *Ocean Science*, 7(3):317–334.

Stoica, P. and Randolf, M. (1997). Introduction to Spectral Analysis. *New Jersey: Upper Saddle River. Printice Hall.*

Swallow, J., Fieux, M., and Schott, F. (1998). The boundary currents east and north of Madagascar, Part I: Geostrophic currents and transports. *Journal of Geophysical Research*, 93(1):4951–4962.

Swart, N., Lutjeharms, J., Ridderinkhof, H., and de Ruijter, W. (2010). Observed Characteristics of Mozambique Channel Eddies. *Journal of Geophysical Research: Oceans*, 115(C9):1–14.

Ternon, J., Roberts, M., Morris, T., Hancke, L., and Backeberg, B. (2014). In situ measured structures of the eddy field in the mozambique channel. *Deep Sea Research Part II: Topical Studies in Oceanography*, 100:10–26.

Tew-Kai, E. and Marsac, F. (2009). Patterns of variability of sea surface chlorophyll in the Mozambique Channel: A quantitative approach. *Journal of Marine Systems*, 77(1):77–88.

Tomczak, M. and Godfrey, J. (2003). *Regional Oceanography: an Introduction* . Daya Publishing House Delhi, 2nd edition.

Tsugawa, M. and Hasumi, H. (2010). Generation and Growth Mechanism of the Natal Pulse. *Journal of Physical Oceanography*, 40(7):1597–1612.

van Leeuwen and, P., de Ruijter, W., and Lutjeharms, J. (2000). Natal pulses and the formation of agulhas rings. *Journal of Geophysical Research*, 105(C3):6425–6436.

Weiss, J. (1991). The dynamics of enstrophy transfer in two-dimensional hydrodynamics. *Physica D: Nonlinear Phenomena*, 48(2-3):273–294.

Weller, R., Baumgartner, M., Josey, S., Fischer, A., and Kindle, J. (1998). Atmospheric forcing in the Arabian sea during 1994-1995: observations and comparisons with climatology and models. *Deep Sea Research Part II: Topical Studies in Oceanography*, 45(10-11):1961–1999.

Wyrtki, K. (1971). *Oceanographic Atlas of the International Indian Ocean Expedition*. National Science Foundation, Whanshington, D.C.

Wyrtki, K. (1973). An equatorial jet in the Indian Ocean. *Science*, 181(4096):262–264.

You, Y. (1998). Intermediate water circulation and ventilation of the Indian Ocean derived from water-mass contributions. *Journal of Marine Research*, 56(5):1029–1067.

Zhao, Z., Alford, M., Lien, R., Gregg, M., and Carter, G. (2012). Internal tides and mixing in a submarine canyon with time-varying stratification. *Journal of Physical Oceanography*, 42(12):2121–2142.

Appendix A

The Vertical Sigma Coordinates (stretched)

A.1 Generalized sigma coordinates

The vertical sigma coordinate used in ROMS is presented in 3.2.18. Its form in ROMS, consists of the modification of the original coordinate developed by Song and Haidvogel (1994), as presented in A.1.1 below. This new construction is based on the combination of the expressions $z(x, y, \sigma, t) = S(x, y, \sigma) + \zeta(x, y, t)[1 + S(x, y, \sigma)/h(x, y)]$ and $S(x, y, \sigma) = h_c.\sigma + [h(x, y) - h_c].C(\sigma)$, see details in (Shchepetkin and McWilliams, 2015, 2009).

$$z = \zeta(1 + \sigma) + h_c.\sigma + (h - h_c).C(\sigma), -1 \leq \sigma \leq 0 \tag{A.1.1}$$

In A.1.1 $C(\sigma)$, is the non-dimensional monotonic vertical stretching function of Song and Haidvogel (1994) and ranges from $-1 \leq C(\sigma) \leq 0$, equation A.1.2.

$$C(\sigma) = (1 - \theta_b)\frac{sinh(\theta_s)}{sinh(\theta_b)} + \theta_b\frac{tanh[\theta_s(\sigma + 1/2)] - tanh[(1/2)\theta_s]}{2tanh[(1/2)\theta_s]} \tag{A.1.2}$$

where θ_s and θ_b are the surface and bottom control parameters. These, were designed to fall in the ranges $0 \leq \theta \leq 20$ and $0 \leq \theta_b \leq 1$. The depth h_c is a constant chosen to be the minimum depth of the bathymetry, or as the width of the surface of the bottom boundary layer in which the highest resolution is required, (Song and Haidvogel, 1994). In equation A.1.1, the first term is chosen to follow the free surface $\zeta(x, y, t)$. The second prevents possible linear instabilities, whereas the last term, is intended to stretch the interior coordinate and force them to follow the bottom topography, (Song and Haidvogel, 1994).

The full equations of motion in a sigma coordinates, are deducted considering the transformation

in the system of equations A.1.3, below.

$$\begin{cases} \hat{x} = x \\ \hat{y} = y \\ \sigma = \sigma(x, y, z) \\ z = z(x, y, \sigma) \\ \hat{t} = t \end{cases} \tag{A.1.3}$$

The variables with a super-script indicate the coordinate in the transformed coordinate. The chain rules for this transformation are:

$$\begin{cases} \left(\frac{\partial}{\partial x}\right)_z = \left(\frac{\partial}{\partial x}\right)_\sigma - \left(\frac{1}{H_z}\right)\left(\frac{\partial}{\partial x}\right)_\sigma \frac{\partial}{\partial \sigma} \\ \left(\frac{\partial}{\partial y}\right)_z = \left(\frac{\partial}{\partial y}\right)_\sigma - \left(\frac{1}{H_z}\right)\left(\frac{\partial}{\partial y}\right)_\sigma \frac{\partial}{\partial \sigma} \\ \frac{\partial}{\partial z} = \left(\frac{\partial \sigma}{\partial z}\right)\frac{\partial}{\partial \sigma} = \frac{1}{H_z}\frac{\partial}{\partial \sigma} \end{cases} \tag{A.1.4}$$

where $H_z = \frac{\partial z}{\partial \sigma}$. As as result of the geometric transformation, the momentum equations become more complicated:

$$\frac{\partial u}{\partial t} - fv + \vec{v}.\nabla u = -\frac{\partial \phi}{\partial x} - \left(\frac{g\rho}{\rho_o}\right)\frac{\partial z}{\partial x} - g\frac{\partial \zeta}{\partial x} + \frac{1}{H_z}\frac{\partial}{\partial \sigma}\left[\frac{K_m}{H_z}\frac{\partial u}{\partial \sigma}\right] + F_u + D_u \tag{A.1.5}$$

$$\frac{\partial v}{\partial t} + fu + \vec{v}.\nabla v = -\frac{\partial \phi}{\partial y} - \left(\frac{g\rho}{\rho_o}\right)\frac{\partial z}{\partial y} - g\frac{\partial \zeta}{\partial y} + \frac{1}{H_z}\frac{\partial}{\partial \sigma}\left[\frac{K_m}{H_z}\frac{\partial v}{\partial \sigma}\right] + F_v + D_v \tag{A.1.6}$$

$$\frac{\partial C}{\partial t} + \vec{v}\nabla C = \frac{1}{H_z}\frac{\partial}{\partial \sigma}\left[\frac{K_C}{H_C}\frac{\partial C}{\partial \sigma}\right] + F_T + D_T \tag{A.1.7}$$

$$\rho = \rho\left(T, S, P\right) \tag{A.1.8}$$

$$\frac{\partial \phi}{\partial \sigma} = \left(\frac{-gH_z\rho}{\rho_o}\right) \tag{A.1.9}$$

$$\frac{\partial H_z}{\partial t} + \frac{\partial (H_z u)}{\partial x} + \frac{\partial (H_z v)}{\partial y} + \frac{\partial (H_z \Omega)}{\partial \sigma} \tag{A.1.10}$$

where $\vec{v} = (u, v, \Omega)$ and $\vec{v}.\nabla = u\frac{\partial}{\partial x} + v\frac{\partial}{\partial y} + \Omega\frac{\partial}{\partial \sigma}$.

The vertical velocity in sigma coordinate is: $\Omega(x, y, \sigma, t) = \frac{1}{H_z}[w - \left(\frac{z+h}{\zeta+h}\right)\frac{\partial \zeta}{\partial t} - u\frac{\partial z}{\partial x} - v\frac{\partial z}{\partial y}]$ and $w = \frac{\partial z}{\partial t} + u\frac{\partial z}{\partial x} + v\frac{\partial z}{\partial y} + \Omega H_z$.

The boundary conditions for the dynamics equations in the stretched coordinate system becomes: on top the where $\sigma = 0$

$$\begin{cases} \left(\frac{K_m}{H_z}\right)\frac{\partial u}{\partial \sigma} = \tau_s^x(x, y, t) \\ \left(\frac{K_m}{H_z}\right)\frac{\partial v}{\partial \sigma} = \tau_s^y(x, y, t) \\ \left(\frac{K_C}{H_z}\right)\frac{\partial C}{\partial \sigma} = \frac{Q_C}{\rho_o c_p} \\ \Omega = 0 \end{cases}$$

in the bottom, $\sigma = -1$

$$\begin{cases} \left(\frac{K_m}{H_z}\right)\frac{\partial u}{\partial \sigma} = \tau_b^x(x, y, t) \\ \left(\frac{K_m}{H_z}\right)\frac{\partial v}{\partial \sigma} = \tau_b^y(x, y, t) \\ \left(\frac{K_C}{H_z}\right)\frac{\partial C}{\partial \sigma} = 0 \\ \Omega = 0 \end{cases}$$

these whole set of equations is presented in (Hedstrȯm, 2009).

A.2 The horizontal curvilinear coordinate

Representing the velocity components from the Cartesian system in the new curvilinear system by

$$\begin{cases} \vec{v}.\hat{\xi} = u \\ \vec{v}.\hat{\eta} = v \end{cases} \tag{A.2.1}$$

the equations of motion in chapter 3 which are from 3.2.1 to 3.2.6, may be rewritten as:

$$\frac{\partial}{\partial t}(\frac{H_z u}{mn}) + \frac{\partial}{\partial \xi}(\frac{H_z u^2}{n}) + \frac{\partial}{\partial \eta}(\frac{H_z uv}{m}) + \frac{\partial}{\partial \sigma}(\frac{H_z u\Omega}{mn}) \tag{A.2.2}$$

$$-\left\{\left(\frac{f}{mn}\right)+v\frac{\partial}{\partial\xi}\left(\frac{1}{n}\right)-u\frac{\partial}{\partial\eta}\left(\frac{1}{m}\right)\right\}H_z v=-\left(\frac{H_z}{n}\right)\left(\frac{\partial\phi}{\partial\xi}+\frac{g\rho}{\rho_o}\frac{\partial z}{\partial\xi}+g\frac{\partial\zeta}{\partial\xi}\right)$$

$$+\frac{1}{mn}\frac{\partial}{\partial\sigma}\left[\frac{K_m}{H_z}\frac{\partial u}{\partial\sigma}\right]+\frac{H_z}{mn}\left(F_u+D_u\right)$$

$$\frac{\partial}{\partial t}\left(\frac{H_z v}{mn}\right)+\frac{\partial}{\partial}\left(\frac{H_z uv}{n}\right)+\frac{\partial}{\partial\eta}\left(\frac{H_z u^2}{m}\right)+\frac{\partial}{\partial\sigma}\left(\frac{H_z v\Omega}{mn}\right) \tag{A.2.3}$$

$$+\left\{\left(\frac{f}{mn}\right)+v\frac{\partial}{\partial\xi}\left(\frac{1}{n}\right)-u\frac{\partial}{\partial\eta}\left(\frac{1}{m}\right)\right\}H_z u=-\left(\frac{H_z}{m}\right)\left(\frac{\partial\phi}{\partial\eta}+\frac{g\rho}{\rho_o}\frac{\partial z}{\partial\eta}+g\frac{\partial\zeta}{\partial\eta}\right)$$

$$\frac{1}{mn}\frac{\partial}{\partial\sigma}\left[\frac{K_m}{H_z}\frac{\partial v}{\partial\sigma}\right]+\frac{H_z}{mn}(F_v+D_v)$$

$$\frac{\partial}{\partial t}\left(\frac{H_z C}{mn}\right)+\frac{\partial}{\partial\xi}\left(\frac{H_z uC}{n}\right)+\frac{\partial}{\partial\eta}\left(\frac{H_z vC}{m}\right) \tag{A.2.4}$$

$$+\frac{\partial}{\partial\sigma}\left(\frac{H_z\Omega C}{mn}\right)=\frac{1}{mn}\frac{\partial}{\partial s}\left[\frac{K_C}{H_z}\frac{\partial C}{\partial\sigma}\right]+\frac{H_z}{mn}\left(F_C+D_C\right)$$

$$\rho=\rho\left(T,S,P\right) \tag{A.2.5}$$

$$\frac{\partial\phi}{\partial\sigma}=-\left(\frac{gH_z\rho}{\rho_o}\right) \tag{A.2.6}$$

$$\frac{\partial}{\partial t}\left(\frac{H_z}{mn}\right)+\frac{\partial}{\partial\xi}\left(\frac{H_z u}{n}\right)+\frac{\partial}{\partial\eta}\left(\frac{H_z v}{m}\right)+\frac{\partial}{\partial\sigma}\left(\frac{H_z\Omega}{mn}\right)=0 \tag{A.2.7}$$

All the boundary conditions formulated in the Cartesian framework remain unchanged, (Hedström, 2009).

A.3 Geostrophic velocity and Eddy Kinetic Energy

The zonal (u) and the meridional (v) components of the geostrophic flow were derived from both model SSH and altimetry through the relation $u=-\frac{g}{f}\frac{\partial\eta}{\partial y}$ and $v=\frac{g}{f}\frac{\partial\eta}{\partial x}$, where g is the acceleration

due to gravity, f is the Coriolis parameter and η is the SSH. The EKE is calculated from SSH derived geostrophic velocities, according to equation $EKE = \frac{1}{2}(u'^2 + v'^2)$, where $u' = u - \bar{u}$ and $v' = v - \bar{v}$ with $\bar{u}$ and $\bar{v}$ representing the temporal mean over the whole extension of the available data.

Appendix B

Impacts of Tides

B.1 Effect of tides in modelled DBLEs

When the model is forced with tides (DELAG-II), no significant changes occur in the representation of the circulation in the Bight, except the slight speed of the southward flowing current. Like in no-tides (DELAG-I), the lee eddy presences/absences do not show seasonality (Figure B.1.1). July and November show the highest peaks of the lee eddy establishment, but overall only 37% of the snapshots are dominated by the absence of the lee eddy. In analogy with no-tides, the thermocline structure will be reassessed using composites, following the criteria previously established in section 5.2.

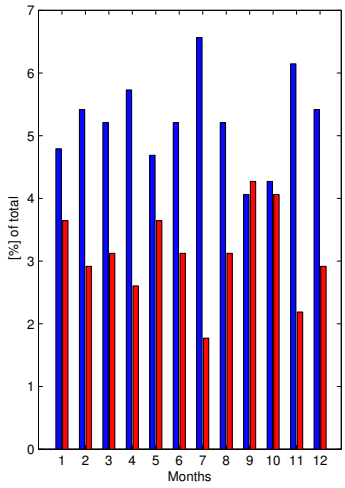

Figure B.1.1: Percentage of lee eddy presences (blue) and absences (red), in the model with tides (DELAG-II).

The representation of the DBLE and neighbouring features in the model parameters is given in Figure B.1.2. For the temperature, the DBLE at 50 m depth is traced by a wider contour of 22^oC isotherm, which reflects a slight enhancement of the upwelling in the center of the lee eddy, by

comparison with its counter-part without tides (Figure B.1.2), described in section 5.2, of the main text of this manuscript. It seems that the slight increase of the kinetic energy noted in the southwards flowing current in chapter 4, may be influential in the content of cooler water in the center of the lee eddy. The southwards flowing current is wider and reaches farther south, encompassed by the 24^oC isotherm. In salinity distribution where the lee eddy was not marked in the case of no tides at this depth, now it is conspicuous (Figure B.1.2b). For this experiment, the currents and the SSHs are enhanced in the center of the DBLE, (Figure B.1.2c). At $100\,m$ depth, the lee eddy representation is noticeable in all the parameters, (Figure B.1.2d-f). However, because there are no significant changes of properties below this depths in the Bight, by comparison with DELAG-I, the levels below are not shown here. In the Bight, the most substantial changes are generally known to occur in the upper layers, (Lutjeharms and Jorge da Silva, 1988; Lamont et al., 2010; Cossa et al., 2016).

In Figure B.1.3 is presented the condition when the DBLE is absent for DELAG-II at $50\,m$ depth. The northeastern part of the Bight is characterized by cooler water, suggestive of prevalence of a cyclonic circulation in that region, (Figure B.1.3a). In salinity the coastal intrusion of fresher water masses from the north is also noticeable, (Figure B.1.3b). The southwards flowing currents covers all the Bight including the coast. The northeastern part of the Bight shows lower SSH, that suggests an enhancement of cyclonic activity in that point by comparison with no tides described in the main text (Figure B.1.3c). In comparison with its counter-part without tides, the coastal zone is fresher (Figures B.1.3d-e). The anticyclonic area at $27.5^oS, 35.5^oE$ is also noticeable in this simulation (Figure B.1.3f).

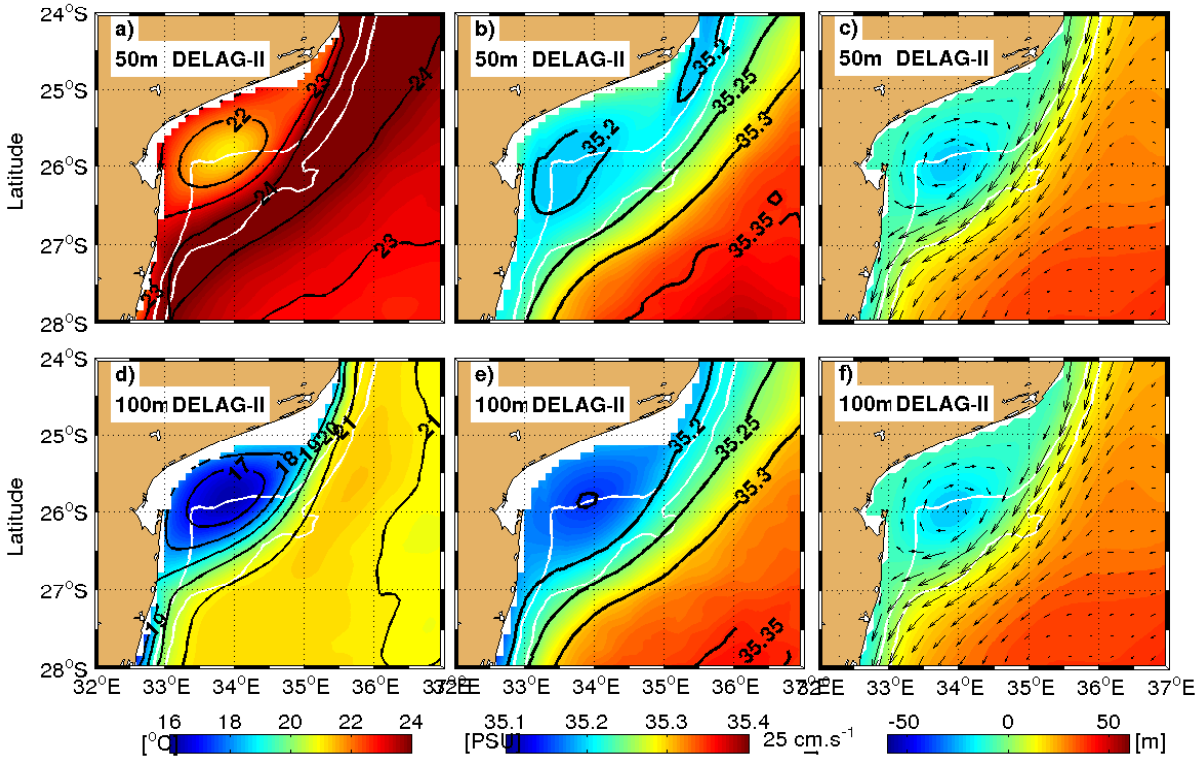

Figure B.1.2: Composite of the classic lee eddies in the Delagoa Bight, based on model DELAG-II. Horizontal section of Temperature a) Salinity and Currents overlaid on SSH c) at 50 m. The same variables are represented at 100 m, in d) e) and f), in the same order. The white lines are the isobaths of 500 and 1000 m.

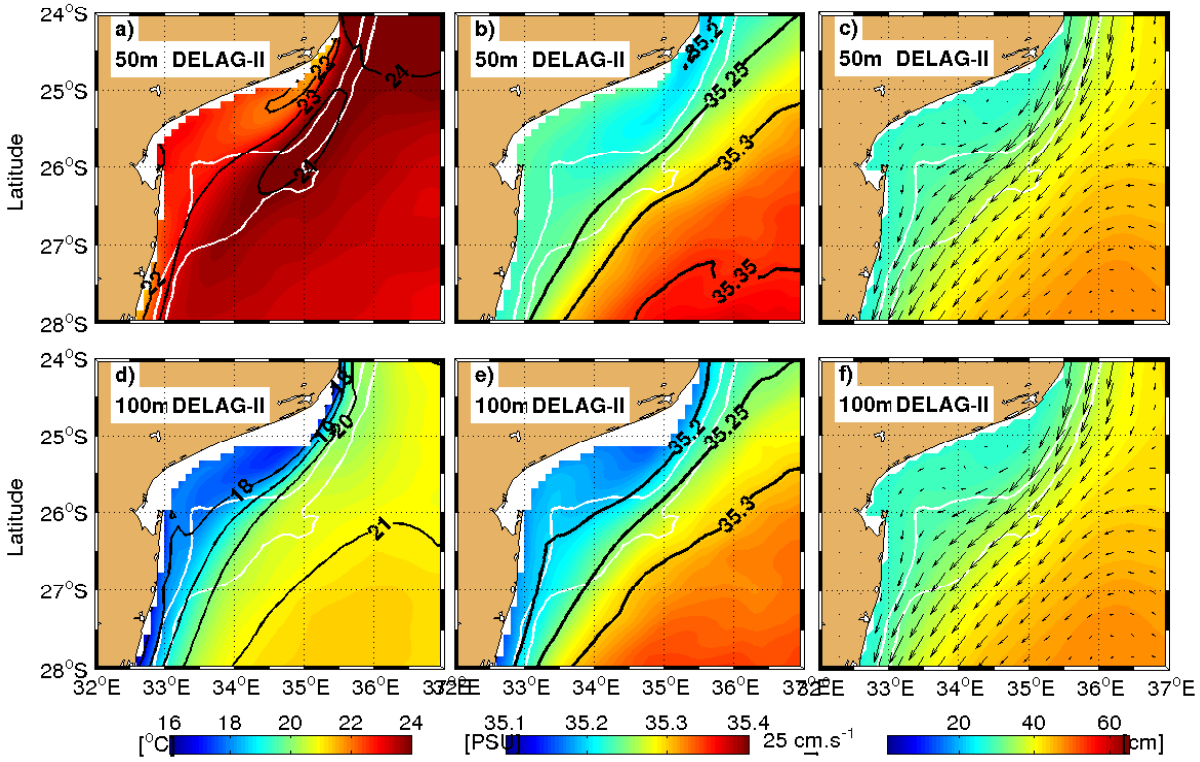

Figure B.1.3: Composite of the lee eddy absences based on model with tides (DELAG-II) in the Delagoa Bight. Horizontal section of Temperature a), Salinity b) and Currents overlaid on SSH c) at 50m. The same variables are represented at 100 m, in d) e) and f). The white lines are the isobaths of 500 and 1000 m.

In the case of the model with tides (DELAG-II), the difference between the composite of DBLE

present and absent at 100 m depth is given in Figure B.1.4. It generally shows all the features analysed in its counterpart without tides in the main manuscript (chapter 5, section 5.2). Meanwhile, in the northeastern zone of the domain the temperature field shows a positive difference between both composites, suggestive of transmission of intense heat flux from the north, when the lee eddy is present by comparison with the absences in this simulation (Figure B.1.4b). The salinity distribution also shows an enhancement in the transmission of fresher water masses from the north (Figure B.1.4c). Along the coast of Ponta do D'Ouro, the area where the southwards flowing current bifurcates to form the lee eddy is characterized by an increase in the anticyclonic impact (high SSH), in the composite with the lee eddy present than no lee eddy, (Figures B.1.4a-c). The anticyclonic feature at $27.5^oS, 35.5^oE$ when the lee eddy is absent, it induces a cyclonic difference there (Figure B.1.4a). For this simulation this difference if found further east. This means that the dominant anticyclonic feature for that region in the composite of DBLE absent, is more anticyclonic in comparison with the corresponding presences, and even with its counter-part no-tides. It is also interesting to underline that the huge strip in Figure (B.1.4c) reflects the increase of the southwards flowing current with tides.

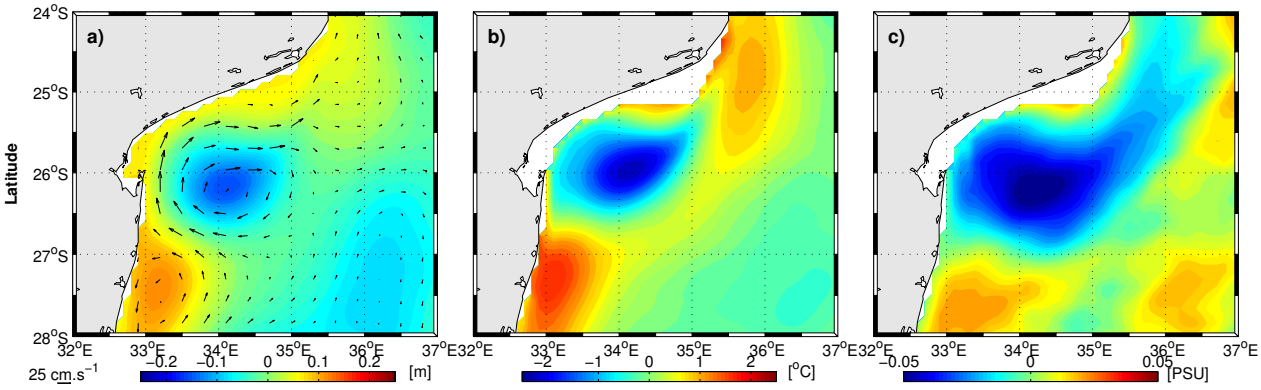

Figure B.1.4: Difference between the composite of lee eddy present and absent at 100 m in the model with tides (DELAG-II). In a) is presented currents on SSH, in b) the temperature and the salinity in c).

The cross sections for DELAG-II composites are shown in Figure B.1.5. The meridional velocity does not show important distinctive features besides of the offshore displacement of the DBLE center from $110 - 115\,km$, as indicated by the isotach of zero meridional velocity, (Figures B.1.5a) by comparison with its counterpart of the model without tides (DELAG-I). The temperature and salinity sections show an enhancement of the lee eddy representation. For instance, the 10^oC and 16^oC isotherms that fell below 100 m and 350 m depths in the model without tides (main text), lies above those depths, with their doming showing an upraise, (Figure B.1.5b). In the salinity section (Figure B.1.5c), the 34.9 psu and 35.2 psu isohalines also show an uprising from 430 m to

300 m depth and from 70 m to 50 m depth, respectively. In the composite of lee eddy absent, the line of zero meridional velocity also shows an increased doming. In the case of no-eddy, the dome was below 150 m depth, against 80 m depth in the case of tides (Figure B.1.5d). The no-eddy 10^oC and 16^oC isotherms upwell from 400 m and 150 m depths in the model with no-tides to 310 m and 140 m, respectively in the model with tides at 150 km from the coast (Figure B.1.5e). The 34.9 psu and 35.2 psu isohalines also upraise from 420 m to 350 m depth and from 130 m to 90 m depth, respectively (Figure B.1.5f).

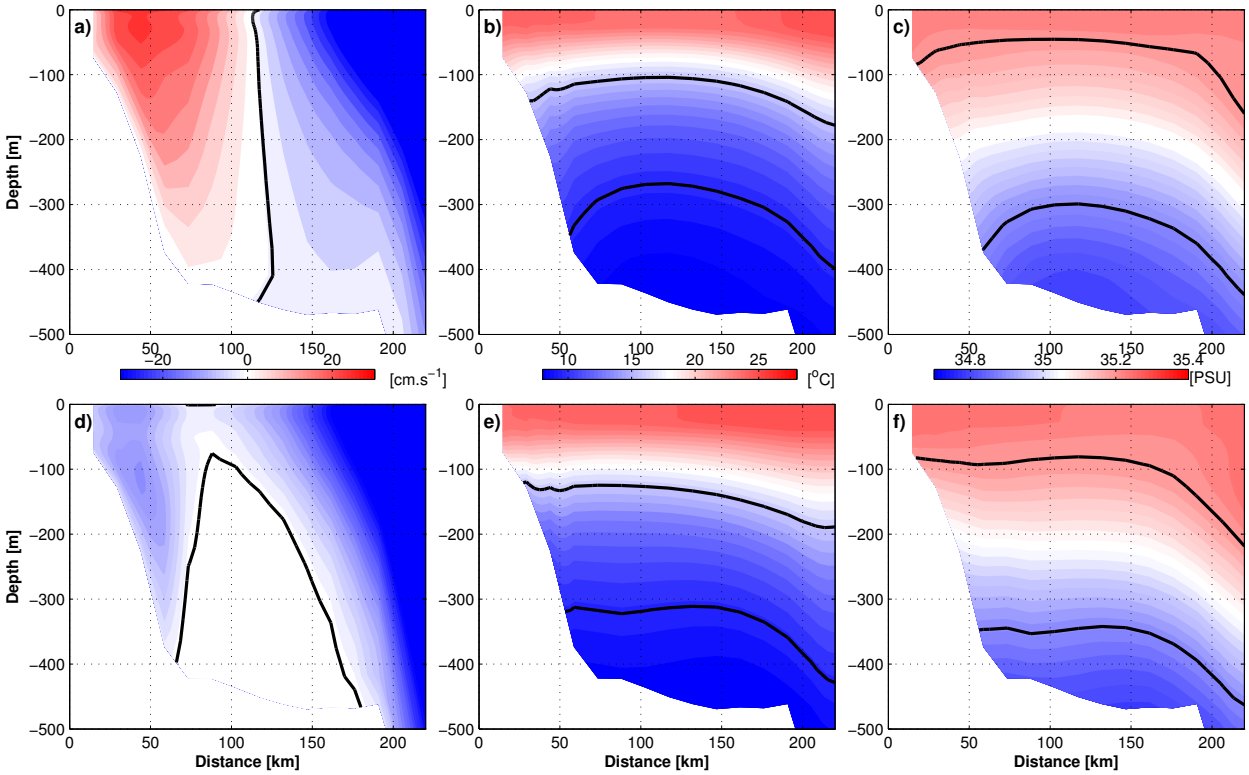

Figure B.1.5: Vertical sections of composites of modelled (DELAG-II) meridional currents (a and d), temperature (b and e) and salinity (c and f), across the main Delagoa Bight section, in the case of the presence (top) or absence (bottom) of a DBLE. Black lines indicate the zero isotach (a and c), 10 and 16°C isotherms (b and e) and 34.9 and 35.2 psu isohalines (c and f).

The lee eddies tracked in the model with tides (DELAG-II) were 82. This is equivalent to 10.25 cyclonic eddies per annum, Figure B.1.6. Their trajectories are concentrated in the area where the Delagoa Bight lee eddy is known to reside, (Lutjeharms and Jorge da Silva, 1988; Lamont et al., 2010), although are generated in specific location as it is discussed in chapter 6 of the main manuscript, (Figure B.1.6a). Their radii distribution is presented in Figure (B.1.6b). They grow from a minimum of 21.55 km to a maximum of 61.58 km, which is of the order of those estimated from its counterpart without tides (DELAG-II). The most striking aspect of this simulation is the increase in the life-span and amplitude of the lee eddy, indicative of the importance of the tides in improving the representation of parameters towards the observations, Table A1.

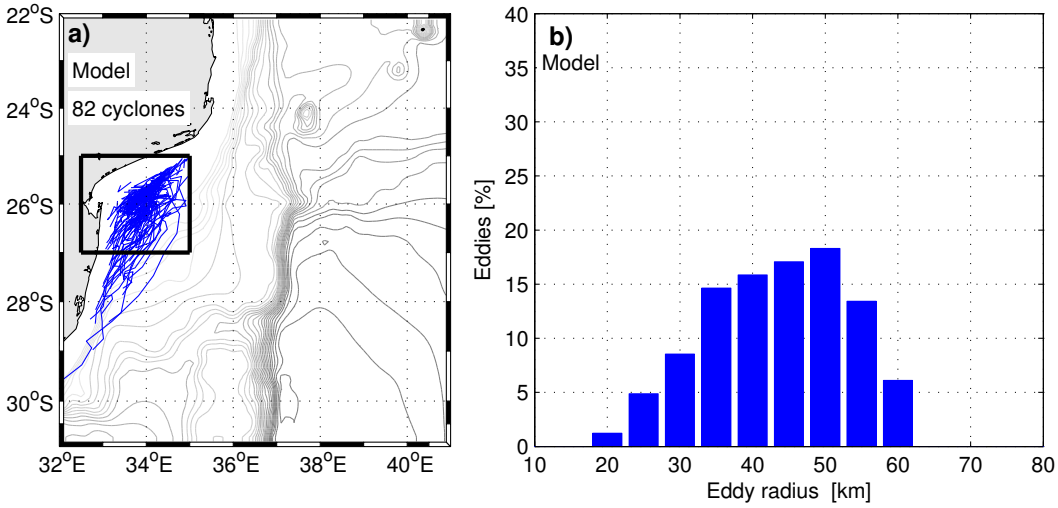

Figure B.1.6: Tracked lee eddies in the model with tides (DELAG-II) in a) and their radii distribution in b). The gray line represent the contours of topography.

Table A1: Stats of the lee eddy based on DELAG-II

Model	VAR	AVERAGE	MIN	MAX	STD
DELAG-II	Radius (km)	43.19	21.55	61.58	±9.57
	Life span (days)	27.21	6	84	±19.0
	Amplitude (cm)	9.65	3.7	19.24	±3.93

The integrated transport of both the southward flow and the coastal counter-current show an increase relative to the case without tides analysed before, (Figure B.1.7). For tides an average of $-21.67 \pm 7.58\,Sv$ was estimated for the southwards current. The reduction in the spread seems to reflect the stability of the current with the addition of tidal forcing. The average coastal counter-current is $1.24 \pm 2.4\,Sv$ towards the north, with a spread reduction by comparison with no-tides. The increase in both the currents by comparison with those estimated in no-tides is due to the increase of the southwards flowing boundary current with tides, as demonstrated in the previous chapter. Furthermore, the estimated transport for the southwards boundary current is in agreement with the $25\,Sv$ presented by Lutjeharms (2006a) for the region, (viz their Figure 3.30).

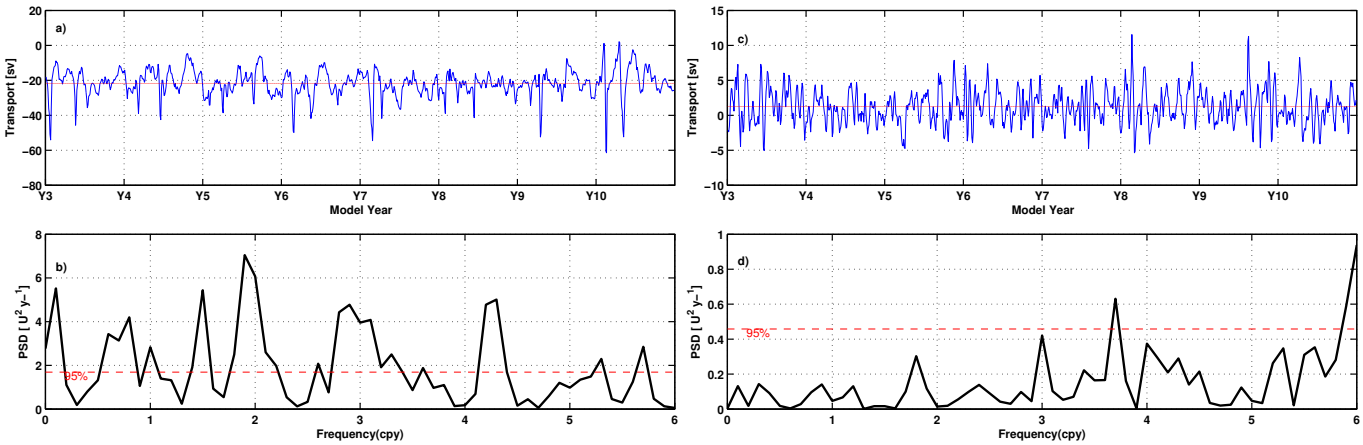

Figure B.1.7: Transports associated with the Southwards Current a), and the coastal counter current c) estimated from the model with tides (DELAG-II). The corresponding Power Spectra Density are shown in b) and d), respectively.

B.1.1 Effect of tides in the High Resolution Simulations

The model with tides (DELAG-IV), was conceived to investigate the simultaneous impact of forcing with tides and improvement of the resolution in the Delagoa Bight circulation. This procedure allows a better representation of the circulation and reproduction of small mesoscale features, not referred to in literature. In Figure B.1.8, are given the currents and the thermocline structure when the lee eddy is present, in the Delagoa Bight region. At 50 m depth (Figure B.1.8a), the lee eddy is conspicuous in a set of four isotherms in the range 20 to 23^oC. The southwards flowing boundary current, which is marked by the 24^oC isotherm is wider and links the northern Agulhas Current, Lutjeharms (2006a). This representation shows significant enhancements in comparison with DELAG-III (no-tides child). The salinity field shows an increase in the intrusion of fresher water from the north in the Bight. In the center, there is evidence of the increment of upwell of fresher water, (Figure B.1.8b). The wider negative SSH in the center of the Bight, confirms the enhancement associated with this experiment, (Figure B.1.8c). At 100 m depth, the lee eddy is characterized by 5 concentric isotherms lying in the range of 15 to 19^oC, (Figure B.1.8d). The wide 35.2 psu isohaline confining the lee eddy also reveals the presence of fresher water in its center, (Figure B.1.8e). The currents and the SSH are likewise enhanced in this experiment, (Figure B.1.8f).

At 200 m depth the 11, 12 and 13^oC isotherms mark the lee eddy, whereas the 15 and 16^oC isotherms show the southwards flow (Figure B.1.9a). This improvement in the representation of the lee eddy is also noted in the salinity field, through concentric isohalines (Figure B.1.9b). The lee eddy still covers a big area of the Bight and presents a consistent coastal counter-current

(Figure B.1.9c). At 400 m depth, the lee eddy covers only the area encompassed by the 500 and 1000 m isobaths. The temperature is below 10^oC. Seemingly this experiment appears to improve the representation of the upwelling in the center of the Bight. The 10 and 11^oC isotherms mark the edge of the southwards flowing current. The eastern side of the model is warmer, as usually (Figure B.1.9d). In the salinity field, the 34.8 psu confines the lee eddy, which seems contain more fresher water masses inside, by comparison with (DELAG-III). The southwards current is marked by a range of isohalines from 34.9 to 35 psu, (Figure B.1.9e). In currents, the lee eddy lies between the 500 and 1000 m isobaths (Figure B.1.9f).

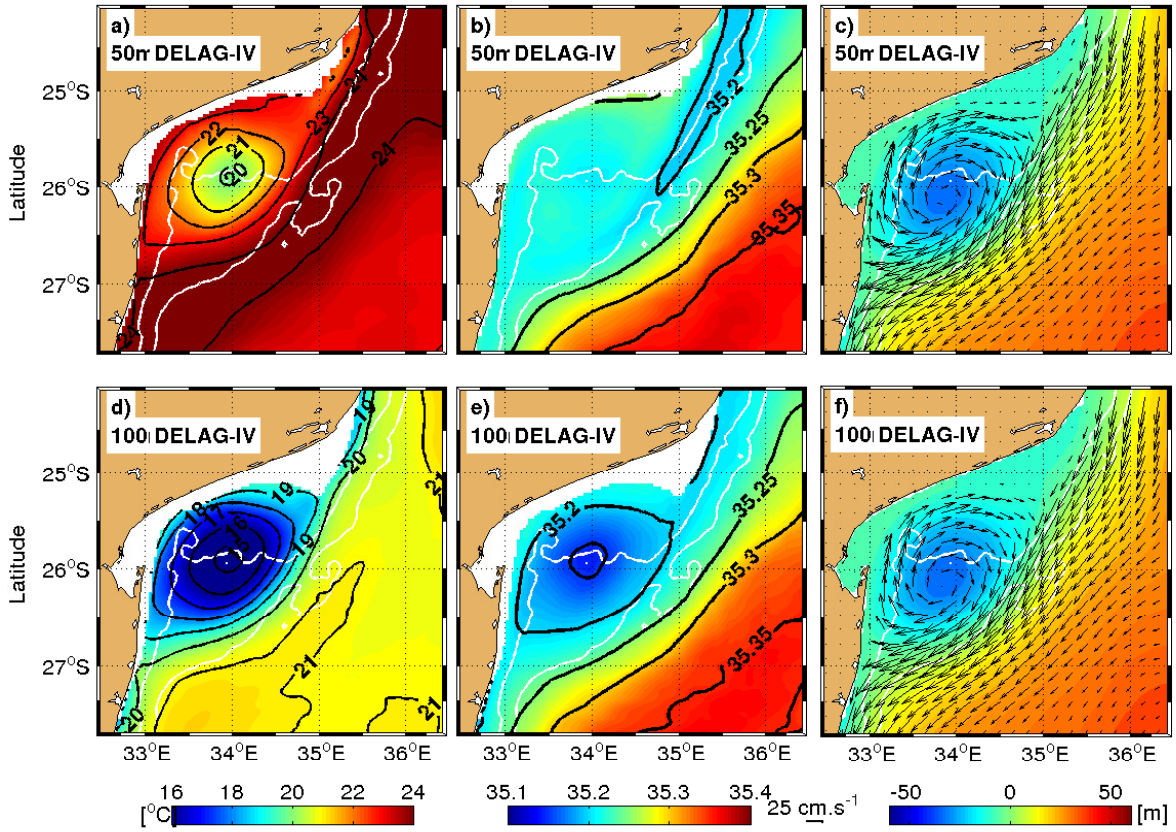

Figure B.1.8: Horizontal sections of the composite with the lee eddy present at 50 and 100 m, determined using the composite of the model with tides (DELAG-IV) in the Delagoa Bight. In a) and d) is shown the temperature distribution; in b and e) the salinity; and finally the currents on SSH in c) and f). The white lines are the isobaths of 500 and 1000 m.

The changes caused by addition of tidal forcing in the model appears to be substantiated first, by the slight increase in the speed of the southward flow, and by the enhancement of the fields, namely the temperature, salinity, SSH as well as the transports of fresher water masses from the north. In the case of lee eddy absent, Figure B.1.10 this enhancement is also evident. At 200 m, the water in the Bight is fresher and cooler in comparison with the eastern zone of the domain (Figure B.1.10a). The anticyclonic feature located at 25.75^oS, 33.5^oE is marked by the 35.1 psu, (Figure B.1.10). At 400 m, the zone between the 500 and 1000 m isobaths, is dominated by a

strip of fresher water, in association with the northwards flow, found in the middle of the Bight, that dominates the currents during the lee eddy absences, as diagnosed from vertical section in the previous analyses, (Figure B.1.10d). The $34.85\,psu$ marks the $25.75^oS, 33.5^oE$ anticyclonic feature.

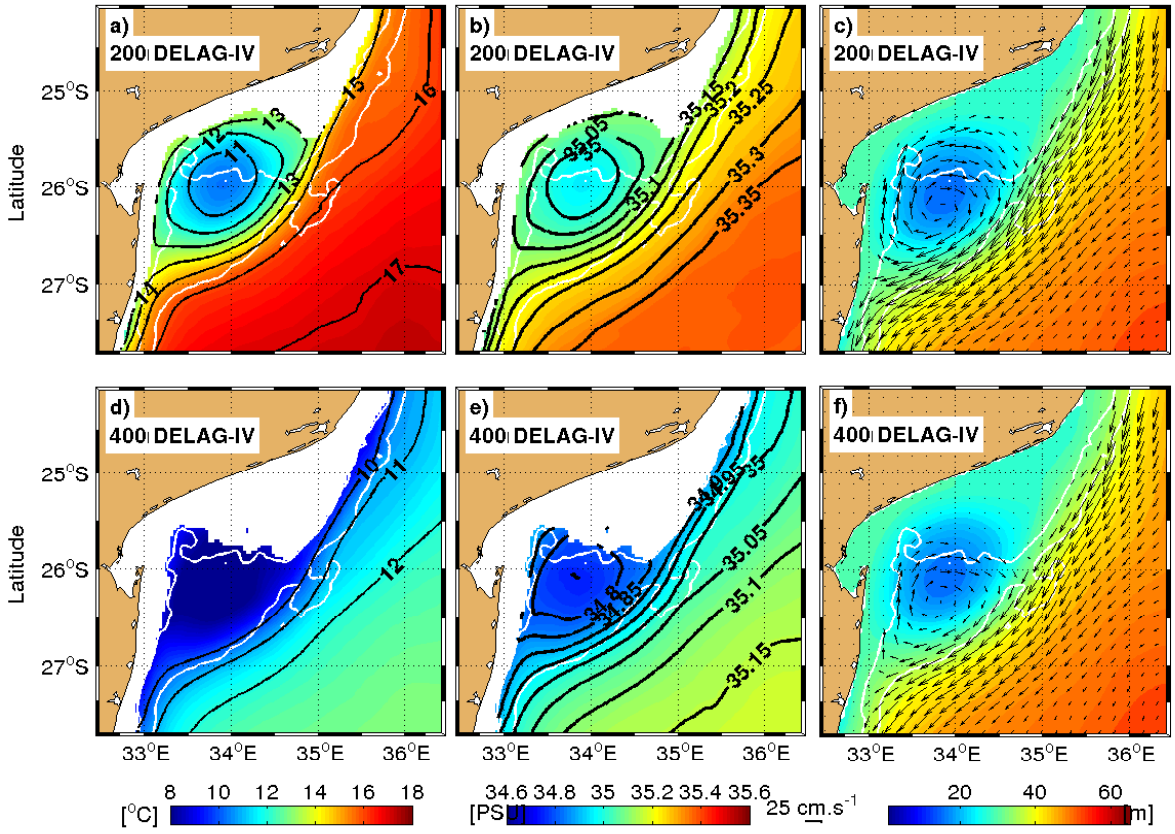

Figure B.1.9: Horizontal sections of lee eddy presence at 50 and $100\,m$, based on the composite of the model with tides (DELAG-IV) in the Delagoa Bight. In a) and d) is shown the temperature distribution; in b and e) the salinity; and finally the currents on SSH in c) and f). The white lines are the isobaths of 500 and $1000\,m$.

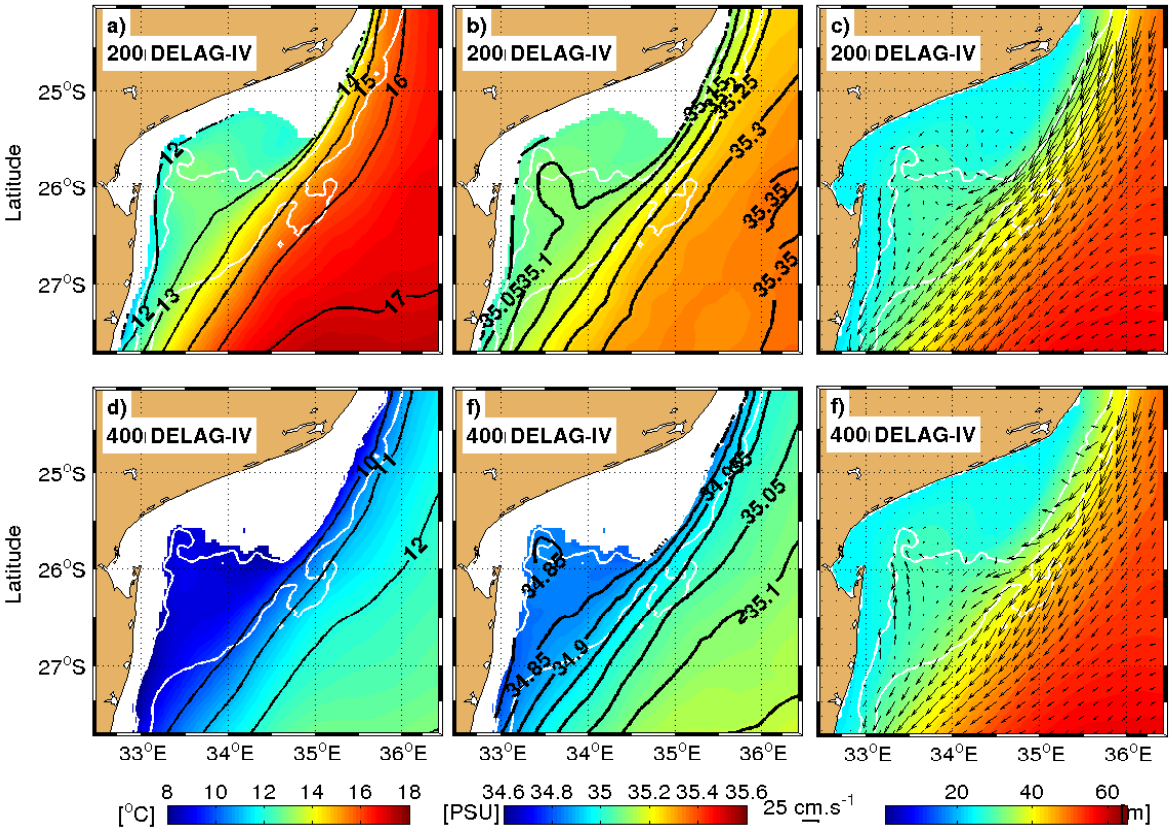

Figure B.1.10: Horizontal sections of the lee eddy absences at 50 and 100 m, based on the composite of the model without tides (DELAG-IV) in the Delagoa Bight. In a) and d) is shown the temperature distribution; in b and e) the salinity; and finally the currents on SSH in c and f). The white lines are the isobaths of 500 and 1000 m.

The difference of the composites in the case of DELAG-IV, is presented in Figure B.1.11. All the important features found in the previous cases are represented again, with some enhancements associated with both the tidal forcing and the increase of model resolution. In current and SSH, the northwards flowing counter-current is stronger in tides, north of the domain. The DBLE and the anticyclonic feature to the south (Ponta D'Ouro), are increased in comparison with the previous experiments (Figure B.1.11a). In temperature the features are noticeable as well, (Figure B.1.11b). The most outstanding characteristic is the enhanced strip describing the intrusion of water masses from the north in this experience. This feature is quite substantial by comparison with the same experiment without tides, (Figure B.1.11c).

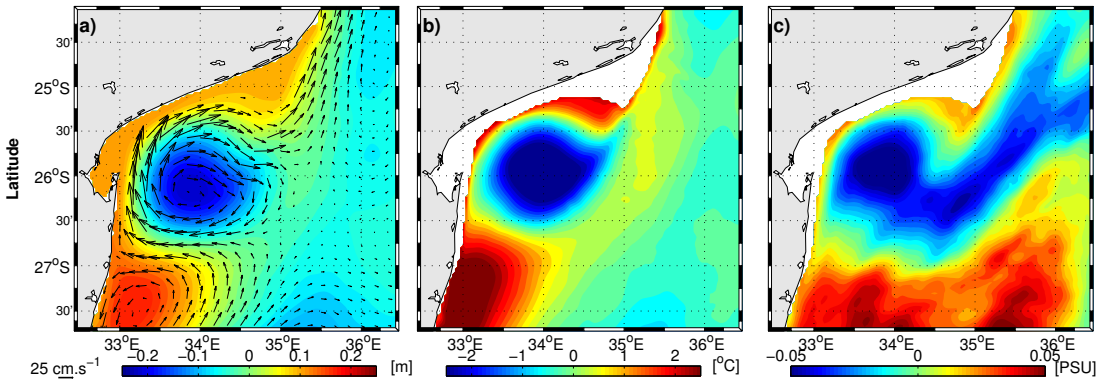

Figure B.1.11: Difference between the lee eddy composite of presences and absences in the model (DELAG-IV), at 100 m. In a) are presented the currents overlaid on SSH, in b) the temperature, and the salinity section in c).

The vertical cross section of the modelled DBLE, based on high resolutions experiment with tides (DELAG-IV), is given in Figure B.1.12. In case of presences, it shows an enhancement of the coastal counter-current as illustrated in the meridional velocity, which fills the shelf from the coast up to the center of the lee eddy at 110 km. In depth, it presents speeds above 25 $cm.s^{-1}$ which decreases up to 20 $cm.s^{-1}$ below 320 m depth, (Figure B.1.12a). The 10 and 16^oC isotherms in the center of the lee eddy are found at 220 m and 90 m depth respectively, which implies an upraising in the domes of the isotherms for this experiment, (Figure B.1.12b). In the salinity field, the 34.9 and 35.2 psu isohalines are found at 240 m and 65 m depth, respectively. The bulging noticed in the 35.2 psu is ascribed to the impact of the southwards flowing current which strengthens considerably, increasing the content of fresher water masses inside of the Bight in this experiment, (Figure B.1.12c). Under lee eddy absent, the counter-current reverses, Figure (B.1.12d). The reversed current has speeds below 20 $cm.s^{-1}$, which does not fill all the depth of the shelf. Between 70 km and 160 km, there is a counter-current whose highest speeds is in the upper level of the section, indicative of its strength by comparison with (DELAG-III) composite. This northwards current in the center of the Bight is promoted by anticyclonic features as mentioned before (Figure B.1.12d). The 10 and 16^oC isotherms are flat under lee eddy absences. They are found at 300 m and 120 m depths, respectively. This shows that the model with tides reproduces more bottom water, probably the AAIW, even under lee eddy absent in the Bight. The 34.9 psu isotherm is found slightly below the level of the 10^oC isotherm, whereas the 35.2 psu is above the level of the 16^oC isotherm. It also shows the bulging ascribed to the southwards flowing current, that feeds the Bight with fresher water masses.

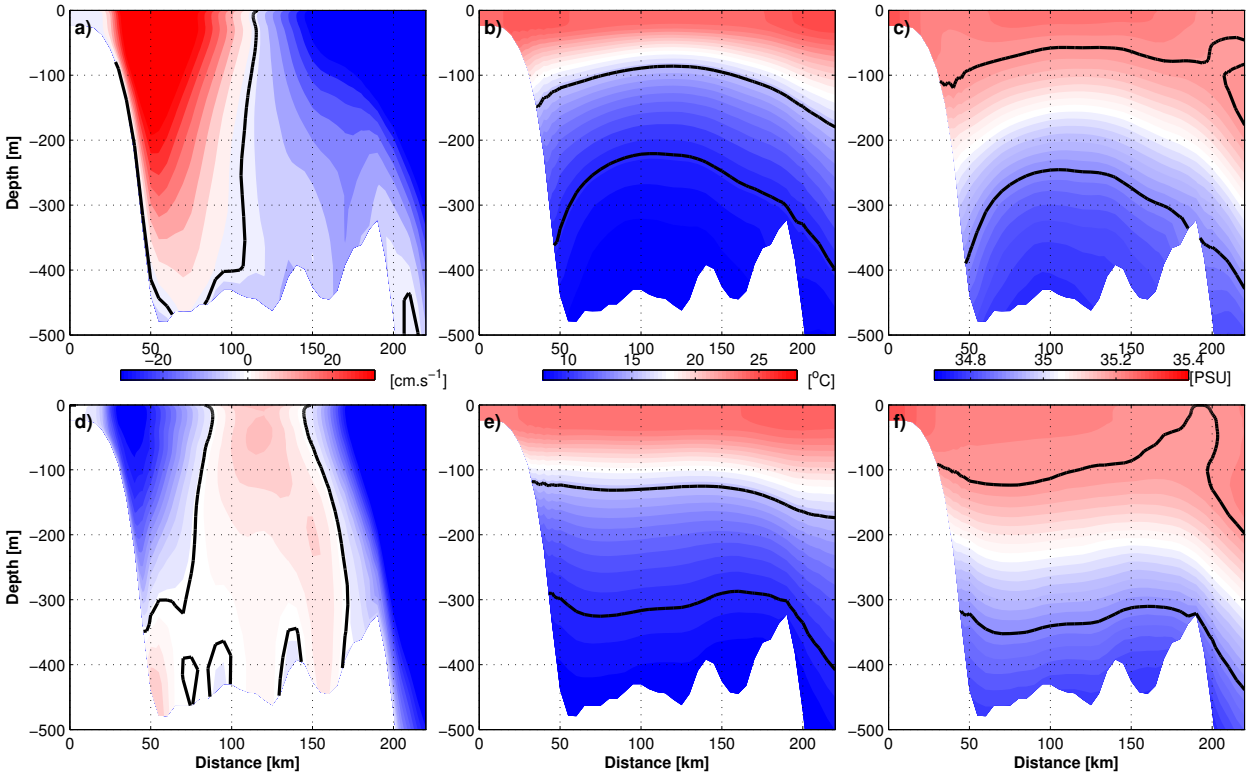

Figure B.1.12: Vertical sections of composites of modelled (DELAG-IV) meridional currents (a and d), temperature (b and e) and salinity (c and f), across the Delagoa Bight, in the case of the presence (top column) or absence (bottom). The black lines indicates the zero isotach (a and c), whereas in (b and e) it shows the 10 and 16 °C isotherms and finally the 34.9 and 35.2 psu isohalines in (c and f).

B.1.2 Effect of tides on the Inhambane Cyclones

In case of tides, the speed in the model has been demonstrated to increase mainly close to the coast. This change is expected to modify realistically the processes simulated in this region. The onset of an Inhambane Cyclone in the example considered here is on model date $17Jan10$ (Figure B.1.13a). In Delagoa Bight the lee eddy is absent. This seems to be due to the positioning of the anticyclones in the center of the domain. Furthermore, the anticyclonic eddy that usually controls the current off Ponta D'Ouro is absent. This condition is sufficient to hinder the development of the lee eddy in the Bight. On model dates $23Jan10$ and $2Feb10$, according to the illustration in (Figures B.1.13b-c), the anticyclonic dipole south of 26^oS moves but not enough to lock the flow from the north with the Mozambican coast (Figures B.1.13c). Therefore, the lee eddy in the Bight is still absent. Once the flow associated with this anticyclonic dipole is confined to the coast, the condition for the development of the coastal counter-current in the Bight is reached. On model dates $11Feb10$ and $14Feb10$, the SSH variations promoted by the positioning of these anticyclones favour the formation of the lee eddy (Figures B.1.13d-e). Furthermore, it interacts with the pulse impacting the thermocline structure inside of the Bight, as it is shown beneath. It is important to

highlight that once the rings are absorbed in the Agulhas Current, the lee eddy disappears again (Figure B.1.13f). Hence, the lee eddy onset may be induced by the positioning of the anticyclones. The sensitivity of Inhambane Cyclones thermocline structure to the tidal forcing is consistent, (Figure B.1.14). At the time of inception on model date $17Jan10$, the coastal northward counter-current off Inhambane is conspicuous in Figure (B.1.14a). Its speed is above $50\,cm/s$ and it presents the particularity of being deep reaching, demonstrative of the strength of the features with tides. In temperature and salinity there is a slight upwelling of the isolines in comparison with the case without tides (Figure B.1.14b-c). On model date $14Feb10$, the Inhambane Cyclones reaches 27^oC off Ponta D'Ouro. In meridional velocity, its center is found $200\,km$ away from the coast. The northwards velocity associated with the meander it promotes is enhanced in this simulation, by comparison with no-tides (DELAG-I) (Figure B.1.14d). The doming of the isolines is noted at $75\,km$ from the coast as well as at $200\,km$. Near the coast the doming is due to the interaction between the southwards flow with the northwards flowing counter-current induced by the western edge of the Inhambane Cyclones in that location. At $200\,km$, it is associated with the southwards branch of the pulse (Figure B.1.14e-f).

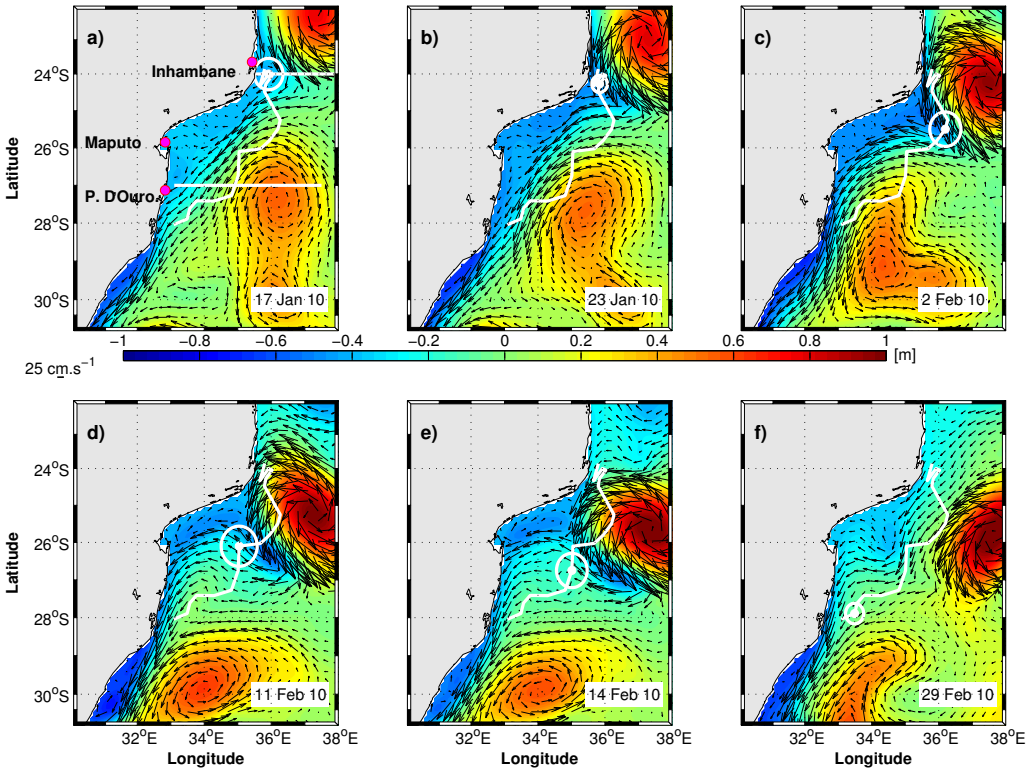

Figure B.1.13: Track and positions of an Inhambane cyclones along the coast (DELAG-II). The white circle shows the actual position of the pulse whereas the strait line represents the positions in which vertical cross sections are made. The trajectory is also in white line.

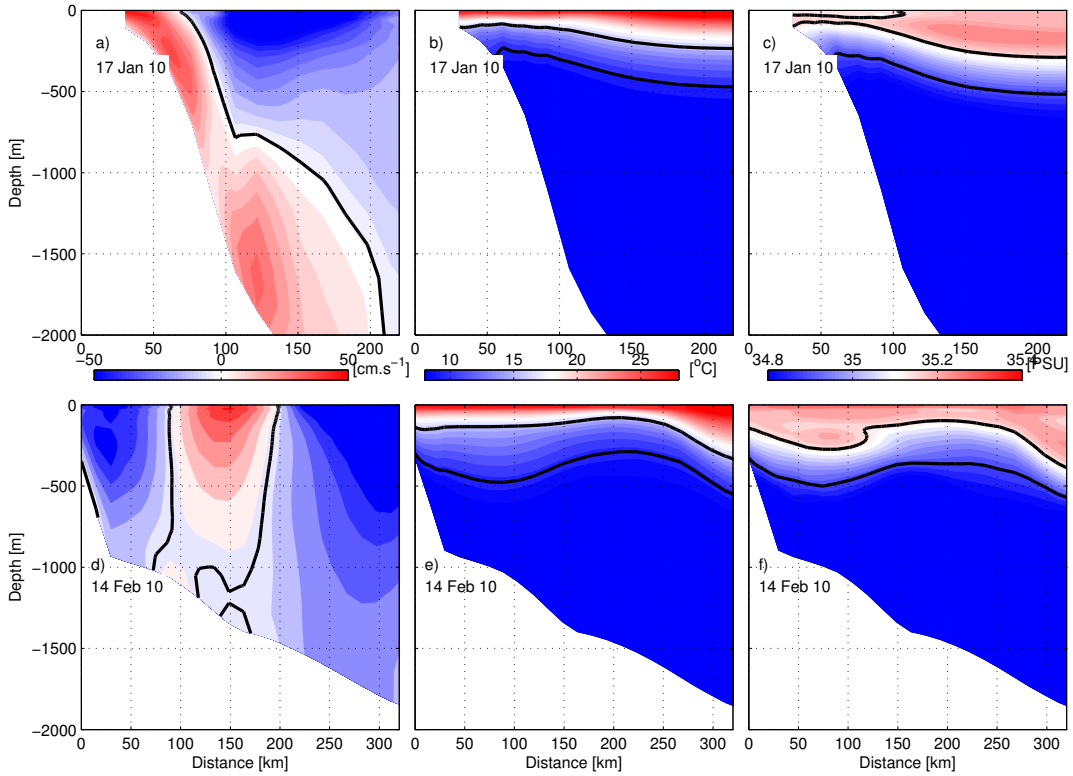

Figure B.1.14: Inhambane cyclone vertical sections at Inhambane Section based on the model DELAG-II (first row), and at Ponta D'Ouro (second row). The first column represents the meridional velocity (a,d); the second represents the temperature (b,e) and the last (c,f) represent the salinity field. In velocity the black line denotes the zero meridional velocity. In temperature it denotes the isotherms of 10 and 16^oC, whereas in salinity it refers to the isohalines of 34.9 and 35.2psu

In the model with tides Figure B.1.15, the pulse recirculation is weaker in comparison with no-tides shown above. This is possibly because of the increase of the speed of the southward flowing current along the shelf in the model with tides. Furthermore, the trajectories of the anticyclones from the east, that were overall northwestwards in no-tides, are adjusted towards south, to the point of becoming roughly westwards. The Inhambane Cyclones follow trajectories similar to those of no tides, but with a small caveat: most of them cease inside the area they are generated in conformity with AVISO observations (Figure B.1.15a). The respective radii distributions are presented in Figure (B.1.15b).

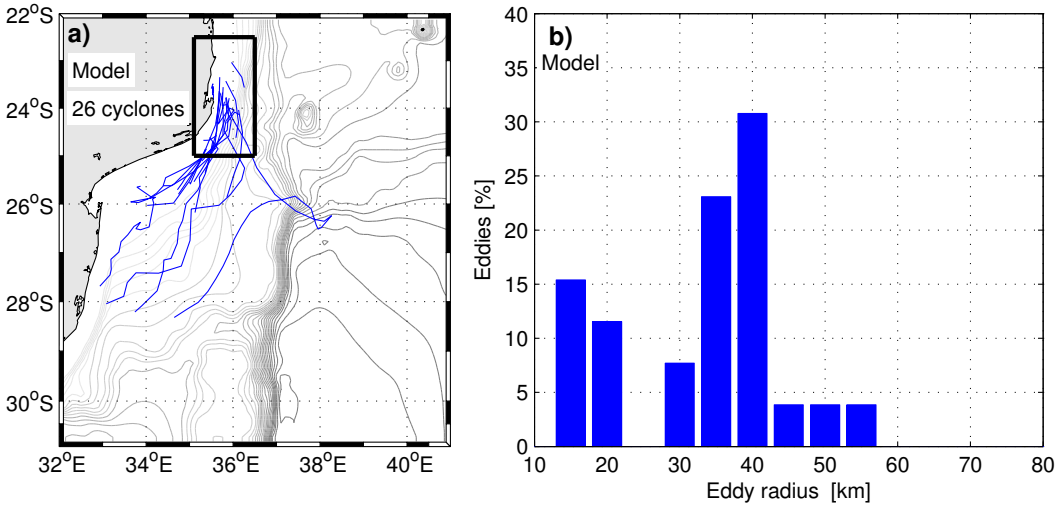

Figure B.1.15: Tracked ICs on the model with tides (DELAG-II) a) and their radii distributions b). The gray lines in a) are the contours of topography.

B.2 Anticyclonic eddies in the Delagoa Bight

In the model with tides, the number of the small mesoscale features increased, possibly due to the increase of the mean kinetic energy with tides close to the coast. The anticyclonic cells in the mother domain of the model with tides were found in 26 pictures, which correspond to 8 tracked features, Table 5.3. In the child domain, a total of 14 anticyclones were observed in 49 snapshots (Table A2). In Figure B.2.1 are given the results of the eddy detecting and tracking system based on DELAG-IV (tides), for both the mother (Figure B.2.1a,b) and child domains (Figure B.2.1c,d), respectively.

The modelled anticyclonic mesoscale features in the Delagoa Bight, Figure B.2.1 are characterized by an average radius of $32.35\,km$, in the external domain of the model with tides. The maximum life time of the anticyclone was $12\,days$, in both coarse and high resolution domains. Overall, the whole sets of parameters, including the amplitudes tend to increase in the internal domain, Table A2. These anticyclones are generally centered around $25.75^{o}S, 33.5^{o}E$ and appear during the lee eddy absences. Therefore, the northward current that prevails in the center of the Bight at approximately $100\,km$ from the coast, during the lee eddy absences seems to be due to this anticyclones. Cossa et al. (2016) found this counter-current at the same place, but as a kind of subsurface current. In the experiments with nest, this current is generally dominant from surface to bottom as indicated in the previous sections, which shows that the reversal of the coastal counter-current during absences promotes a northward currents, say a counter-current in the center of the Bight.

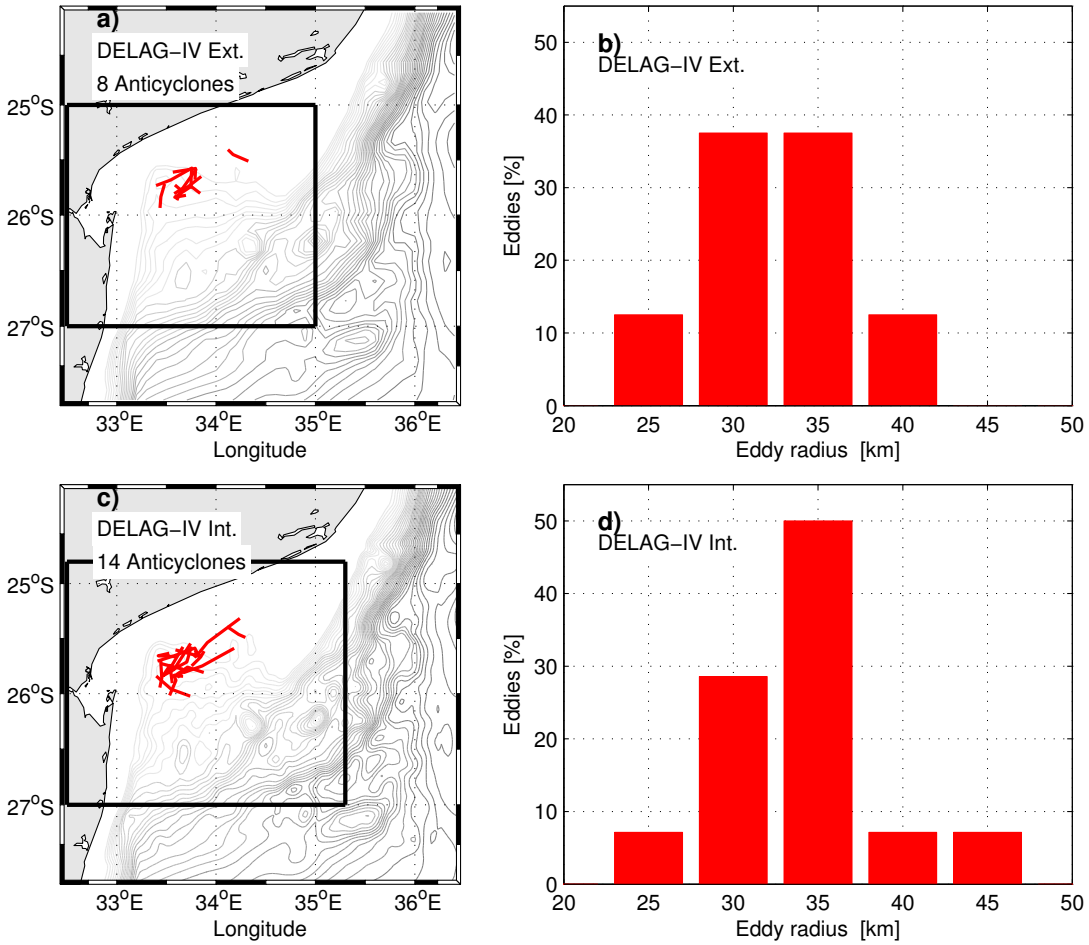

Figure B.2.1: Anticyclonic eddies tracked in the external and internal domains of the model with tides (DELAG-IV) in (a,c) (red), and the respective radii distributions in (b,d). The gray lines in a) are the contours of topography.

Table A2: Delagoa Bight anticyclonic eddies tracked in the inner domain of the model with tides

Model	VAR	AVERAGE	MIN	MAX	STD
DELAG-V Ext.	Radius (km)	32.35	27.24	38.67	±4.52
	Life span (days)	7.12	6.0	12	±2.23
	Amplitude (cm)	4.82	3.68	6.81	±0.97
DELAG-V Int.	Radius (km)	33.78	26.93	42.72	±4.65
	Life span (days)	7.92	6.0	12	±2.52
	Amplitude (cm)	5.53	3.96	8.56	±1.4

B.3 Barotropic and Baroclinic instabilities

B.3.1 Effect of tides on the instabilities

Addition of tidal forcing shows a very slight increase in the barotropic instabilities, by comparison with no-tides, as indicated in Figure B.3.1. Nevertheless, the distribution pattern for T_4 is similar to the one discussed in the main text, section 6.3. T_1 shows that the baroclinic instabilities, also

do not show great changes by comparison with its counter-part without tides, described in section 6.3, say the baroclinic instabilities are not relevant in the generation of mesoscale features, and hence the DBLE in this region is barotropic.

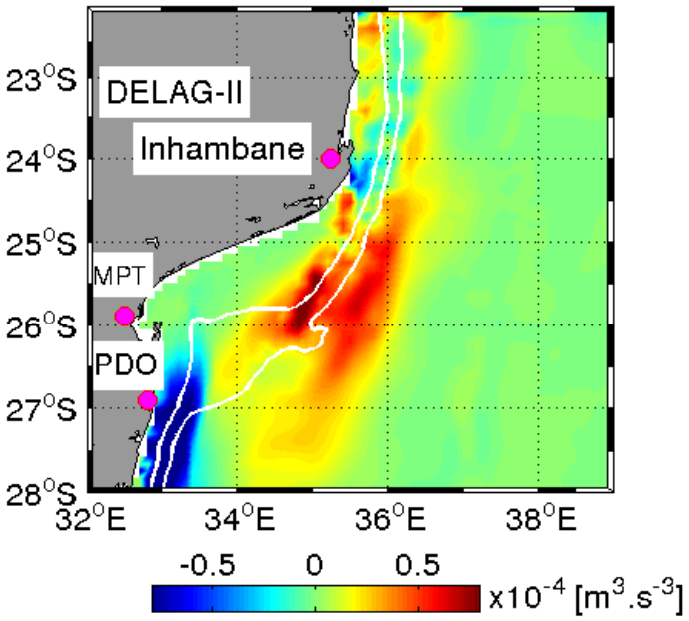

Figure B.3.1: Energy conversion rates (T_4) integrated along the upper layer 500 m in the Delagoa Region, determined from the model with tides (DELAG-II). The white lines are the 500 and 1000 m isobaths.

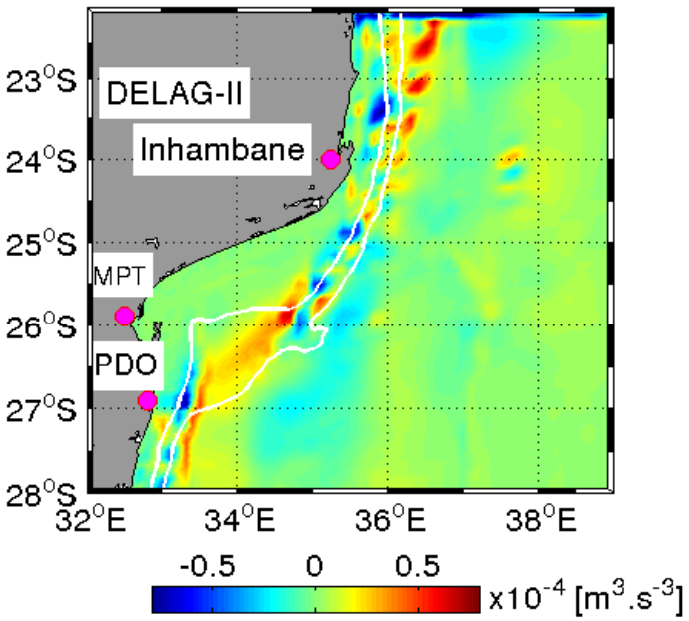

Figure B.3.2: Energy conversion rates (T_1) integrated along the upper layer 500 m in the Delagoa Region, determined from the model with tides (DELAG-II). The white lines are the 500 and 1000 m isobaths.

B.3.2 Simultaneous effect of tides and resolution on instabilities

The effect of changing resolution in the model has also been described in section 6.3. Addition of tides in high resolution simulation shows a very slight increase (not very significant) in the distribution of T_4 and T_1 as described in section 6.3. The results are given in Figures B.3.3 and B.3.4. The slight increase in this instabilities seems to be due increment of speed (kinetic energy) noted in the coast in case of tides, as discussed in chapter 4.

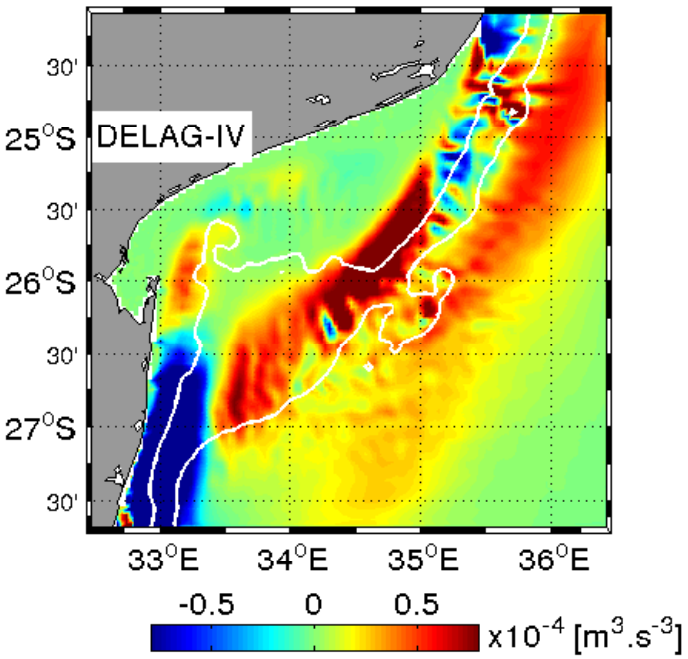

Figure B.3.3: Energy conversion rates (T_4) integrated along the upper layer 500 m in the Delagoa Region, determined from the model with tides (DELAG-IV). The white lines are the 500 and 1000 m isobaths.

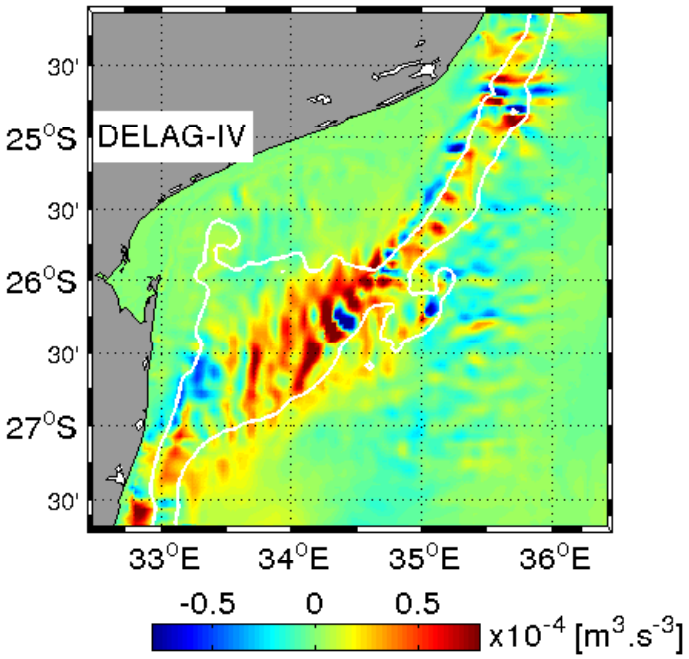

Figure B.3.4: Energy conversion rates (T_1) integrated along the upper layer ($500\,m$) in the Delagoa Region, determined from the model with tides. The white lines are the 500 and $1000\,m$ isobaths.